NONPARAMETRIC APPROACHES TO COMPUTATIONAL SENSITIVITY ANALYSIS OF TURBULENT PLANAR SHEAR LAYERS

by

Mohsen Zayernouri

A dissertation submitted to the faculty of
The University of Utah
in partial fulfillment of the requirements for the degree of

Doctor of Philosophy

Department of Mechanical Engineering

The University of Utah

December 2010

ProQuest LLC
789 East Eisenhower Parkway
P.O. Box 1346
Ann Arbor, MI 48106-1346

The University of Utah Graduate School

STATEMENT OF DISSERTATION APPROVAL

The dissertation of **Mohsen Zayernouri**

has been approved by the following supervisory committee members:

Meredith M. Metzger	, Chair	**04/30/2010** Date Approved
Partick McMurtry	, Member	**04/30/2010** Date Approved
Timothy Ameel	, Member	**04/30/2010** Date Approved
Rob Stoll	, Member	**04/30/2010** Date Approved
Philip Smith	, Member	**05/03/2010** Date Approved

and by **Timothy Ameel**, Chair of the Department of **Mechanical Engineering**

and by Charles A. Wight, Dean of The Graduate School.

ABSTRACT

Nonparametric approaches to computational sensitivity analysis, based on Complex Step Differentiation (CSD) and the Sensitivity Equation Method (SEM), have been used to examine parameter dependence in the incompressible, temporal, planar mixing layer. Both of these sensitivity approaches were implemented numerically in the context of Direct Numerical Simulation (DNS) and Large Eddy Simulation (LES), coupled with standard and dynamic Smagorinsky models, in order to examine the sensitivity of the flow to perturbations in Reynolds number, Prandtl number, initial conditions, and model coefficients. The DNS codes were run over a Reynolds number range $100 \leq Re_{\delta_0} \leq 1000$, where δ_0 represents the initial vortex thickness of the mixing layer; while the LES codes were run up to $Re_{\delta_0} = 2000$. In both cases, the partial differential equations governing the behavior of the flow are derived, discretized, and solved using an explicitly, unsteady, finite-volume based fractional step algorithm.

The unique aspect of the present work, compared to traditional parametric studies, is the fact that both CSD and SEM yield *spatiotemporally resolved* sensitivity fields. This allows one to investigate the local, instantaneous response of the flow field to infinitesimal changes in the design/flow parameters of interest, with application toward optimization and active control. In terms of the DNS of the temporal mixing layer, a *two-blade* pattern, which appears as a dominant feature in the sensitivity solution, provides new information that highlights the physical mechanisms leading to vortex thickness growth and enhanced molecular mixing with increasing Reynolds and Prandtl numbers.Through a "nearby flow" analysis, the sensitivity fields predict faster growth of the mixing layer with an increase the turbulence intensity in the inital conditions.

In this study, both *a priori* and *a posteriori* studies were conducted in the LES framework. The sensitivity solution allows one to extrapolate low Reynolds number *a priori* data to estimate the correct value of the model coefficients that should be used at higher Reynolds numbers. Results from the *a posteriori* study indicate that both

CSD and SEM in the context of LES are able to capture the essential, large-scale features of the coherent sensitivity structures at high Reynolds number.

Dedicated to my family:
my precious parents, Nasrin and Abdolkarim,
and my lovely brothers, Mehdi, Masoud, and Manouchehr.

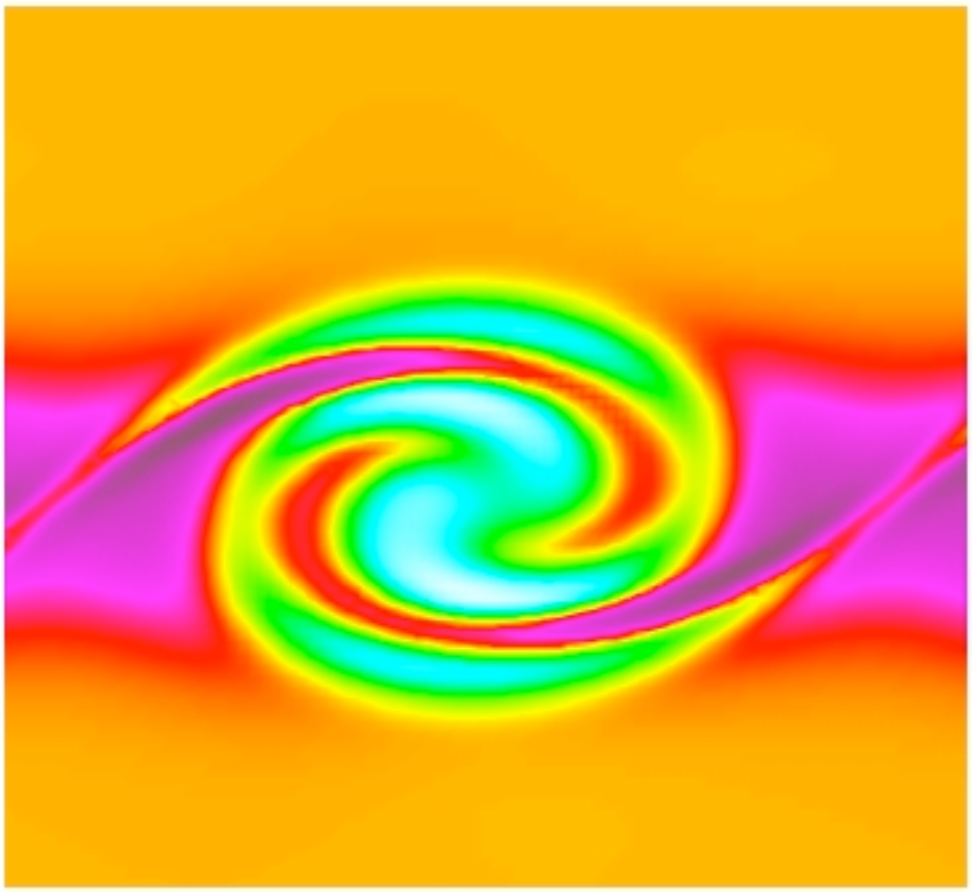

"The measurement of a turbulent flow is interestingly analogous to the process of knowing people and understanding their sensitivities! Necessarily, a long enough sampling-time is demanded to thoroughly capture the chaotic behavior of turbulence."

Mohsen Zayernouri

Summer of 2010

CONTENTS

LIST OF TABLES

ACKNOWLEDGEMENTS

I was so fortunate to have an incredibly knowledgeable and supportive advisory committee in my Ph.D. program. Here, I would like to acknowledge them one by one. First of all, I recognize my advisor Dr. Meredith M. Metzger for supporting me to work on the interesting field of computational sensitivity analysis. Besides, I would like to specially thank Prof. Patrick McMurtry for all of his help and support on this research. He was unquestionably the source of inspiration for me during my Ph.D. research. He taught me turbulence, and his advice regarding my research is unforgettable. Also, I was so lucky and grateful to be led and advised by Prof. Timothy Ameel, who is a great asset to the department. Special thanks to him for being a strong support to my study. In addition, I need to especially thank Dr. Rob Stoll for his wonderful impact on my research. Indeed, he added a lot to my dissertation by his deep understanding of the present work. He taught me large eddy simulation (LES), and even more important than that, he practically showed me how a man can be kind and generously supportive to others, with a huge sense of humanity and responsibility. Finally, I was so honored to have Prof. Philip Smith on my committee. He is undoubtedly a great asset to the department of Chemical Engineering. I learned a lot from him as a wonderful professor and advisor. At the end, I love to acknowledge my lovely family, dear teachers and instructors, kind staff of the department, and all of my friends who were always supporting and encouraging me to work hard. They really taught me how to be strong in difficult moments of my life.

CHAPTER 1

INTRODUCTION

Instantaneous, nonparametric sensitivity analysis remains an underdeveloped yet potentially powerful tool to control and optimize the functionality of thermo-fluid systems. For the particular case of fluid systems involving mixing processes, having faster and stronger mixing that translates into energy savings is highly desired. In fact, many engineering applications involving mixing, such as propulsion, combustion, and oil refinement, amongst others, operate below optimum performance levels due to a lack of understanding of (i) the physics of mixing occurring in these processes and (ii) the sensitivity of the mixing efficiency to the inlet conditions and geometric design of the mixing chamber. Instantaneous sensitivity analysis can predict flow response to perturbations in important design parameters without having to resort to parametric studies. This information may then be used to promote improvements in system design.

In this research, the evolution of sensitivity features in a canonical test case, namely the incompressible two-dimensional (2-D) planar mixing layer, will be numerically simulated using *nonparametric* approaches based on the Sensitivity Equation Method (SEM) and Complex-Step Differentiation (CSD). In SEM, the governing equations of fluid motion are first differentiated (with respect to the parameters of interest), then discretized and solved computationally to obtain the time-evolving fields of the sensitivity coefficients. In CSD, the governing equations are treated as complex as is the velocity field. In this method, the sensitivity coefficients are estimated by dividing the imaginary part of the velocity field by a very small perturbation in the parameter of interest. In the present study, SEM and CSD will be implemented in the context of Direct Numerical Simulation (DNS) at low Reynolds number and Large Eddy Simulation (LES) using the Smagorinsky model (both standard and dynamic) at higher Reynolds numbers. In DNS and LES, the primitive variables (velocity and

pressure) are solved concurrently with the sensitivity coefficients at each time step using an explicit, finite-volume-based, fractional-step scheme.

Specifically, this study utilizes SEM and CSD to examine the sensitivity of the velocity and vorticity to changes in some parameters of interest such as Reynolds number (based on the initial vortex thickness δ_0), the model parameter (namely, the length scale obtained as the product of Smagorinsky coefficient and filter width i.e., $l^* = C_s\Delta$) and initial conditions. The computational sensitivity analyses using SEM and CSD indicate that the sensitivity field of vorticity with respect to Reynolds number exhibits coherent structures similar to that observed in the actual vorticity field. Therefore, the sensitivity coefficients provide direct quantitative information about the growth/suppression of the coherent vortices in the flow with increasing Reynolds number. This study also incorporates a new step into the *a priori* study of the LES necessary to evaluate model coefficients. Sensitivities associated with the Smagorinsky coefficient, Subgrid Filter Scale (SFS) stresses, and SFS kinetic energy dissipation rate will be introduced as new quantities that can be used to assess the Reynolds number invariance of the LES model. Using SEM and CSD, it is also feasible to investigate the long-term effects of flow initialization on the coherent structures.

1.1 Significance

The primary objective of the present research lies in the implementation of SEM and CSD for the case of the 2-D turbulent planar mixing layer, and the interpretation of the sensitivity fields for predicting parameter dependence in the flow. In terms of scientific impact, these computational sensitivity analysis approaches offer a unique (and quantitatively accurate) view of the instantaneous sensitivity of individual coherent structures in the flow that cannot otherwise be captured by parametric studies. Because coherent structures constitute the most energetically significant features of any flow, SEM and CSD approaches toward sensitivity analysis will extend broadly to all areas of fluid dynamics including three-dimensional (3-D) flows. In this manner, computational sensitivity analysis has the potential to serve as the framework for design optimization or flow control algorithms, and could be incorporated relatively straightforwardly into commercial Computational Fluid Dynamics (CFD) software packages, such as Fluent. In addition, this dissertation outlines a paradigm shift

in turbulence model evaluation, which uses SEM or CSD to assess model-parameter dependence in the resultant flow field. The technique is demonstrated for the specific case of the standard Smagorinsky LES model, but can be applied generally to other turbulence models as well.

1.2 Background of Computational Sensitivity Analysis

Computational sensitivity analysis is a technique to quantify the dependencies of the flow to changes in parameters of interest without resorting to traditional parametric studies. This is done by explicitly solving the equations governing the sensitivity derivatives, which then yields spatio-temporal resolved sensitivity fields.

1.2.1 Sensitivity Analysis Techniques

A sensitivity coefficient is defined as the partial derivative of a field variable with respect to the design/flow parameter of interest. For instance, the sensitivity of the field variable u to a parameter P is expressed as

$$S_{u,P} = \frac{\partial u}{\partial P}. \tag{1.1}$$

The design/flow parameters can be fluid properties, geometric constraints, initial conditions, or any combination of these, such as nondimensional numbers that appear in the governing equations. There are several numerical techniques for performing sensitivity analysis including the Finite Difference Method (FDM), Automatic Differentiation Method (ADM), Complex-Step Differentiation (CSD), and Sensitivity Equation Method (SEM).

1.2.1.1 Finite Difference Method

In the finite difference method (which serves as the basis for typical parametric studies), sensitivity coefficients are approximated using a first order Taylor series expansion as

$$S_{u,P} = \frac{u(P + \Delta P) - u(P)}{\Delta P} + O(\Delta P), \tag{1.2}$$

where $u(P)$ and $u(P + \Delta P)$ represent two different numerical solutions obtained using parameter values P and $P + \Delta P$, respectively. Although this method is easy to implement, the accuracy of $S_{u,P}$ depends strongly on ΔP (Martins et al., 2000).

Finding the optimum step increment, ΔP, can require several independent runs (Sobieski, 1990). In addition, because of the unavoidable time mismatch between the two different solutions, sensitivity information derived from the finite difference method is necessarily limited to integral or statistical quantities, such as vortex thickness or mean velocity profiles. Local details of the sensitivity field, for example the response of coherent structures in the flow to instantaneous changes in the parameter of interest, cannot be captured with this method.

1.2.1.2 Automatic Differentiation Method

Automatic (or software) differentiation method utilizes a discretize-then-differentiate approach to computational sensitivity analysis. Specifically, this technique employs a script that automatically differentiates an existing numerical code line by line, creating a new code that outputs the desired sensitivities. Preprocessors of this type have been developed for a number of programming languages including MATLAB, C and Fortran (Bischof et al., 1996, 1997, 2003).

1.2.1.3 Complex Step Differentiation Method

The application of complex variables to approximate the first and higher derivatives of mathematically analytic functions was introduced first by Lyness (1967) and Lyness and Moler (1967). Many years later, this method was implemented by Squire and Trapp (1998) in order to estimate the derivatives of real functions.

In the complex-step method, the parameter of interest is initialized as $P + i\,\Delta P$; and, the governing fluid dynamic equations are treated as complex. Here, ΔP represents a very small perturbation step size (typically on the order of 10^{-16} or smaller). The governing equations are solved numerically using a computing language and algorithms capable of handling complex arithmetic; and, the resultant solution involves complex-valued field variables. The sensitivity coefficients are subsequently estimated by dividing the imaginary part of the field variable by the imaginary part of the parameter (Lyness, 1967), i.e.,

$$S_{u,P} = \frac{Im[u(P + i\Delta P)]}{\Delta P} + O(\Delta P^2). \tag{1.3}$$

Note, this derivative estimate is not subject to subtractive cancellation error, since it does not involve an explicit difference operator; and therefore, the complex-step

derivative remains essentially insensitive to the parameter step size (Martins et al., 2000; Kirkman and Metzger, 2008b), in contrast to the finite difference method.

1.2.1.4 Sensitivity Equation Method (SEM)

In SEM, the continuous governing equations, along with the initial and boundary conditions, are differentiated with respect to the flow/design parameter of interest. This approach yields a new set of equations describing the dynamics of the sensitivity coefficients. In a transient or unsteady flow, the sensitivity and governing equations must be solved concurrently at each time step, which at least doubles the computational expense. Nevertheless, SEM provides a relatively efficient and accurate technique for performing computational sensitivity analysis.

This method has been under development in the field of fluid mechanics since the late 1990s (Borggaard and Burns, 1997; Dowding and Blackwell, 1998; Gunzburger, 1999), motivated initially by the problem of optimal aerodynamic design. Most of the SEM literature to date discusses the implementation and application of SEM in the context of *finite element* discretization methods (Borggaard and Verma, 2000; Turgeon et al., 2000; Blackwell and Dowding, 2002; Stanley and Stewart, 2002; Turgeon et al., 2002, 2003; Duvigneau and Pelletier, 2006). Recently, Kirkman and Metzger (2008b,a) applied SEM to laminar and turbulent channel flow using a *finite-volume* based fractional step algorithm.

The solution obtained from SEM represents the time-resolved sensitivity of the flow to *infinitesimal* changes in the design/flow parameters of interest; and, as such, SEM constitutes a nonparametric approach toward sensitivity analysis. Importantly because of this, SEM provides a quantitative measure for interrogating how inherently unsteady coherent features of the turbulence are instantaneously affected by changes in the parameter(s) of interest (Kirkman and Metzger, 2008b, 2009).

1.3 Turbulent Free Sear Flows

Turbulent mixing occurs as a result of two primary mechanisms: molecular mixing and stirring. The former is associated with diffusion across small-scale structures; while, the latter characterizes advection by spatially-organized large scales or coherent structures, which can be either 3-D such as in the turbulent boundary layer (Kline

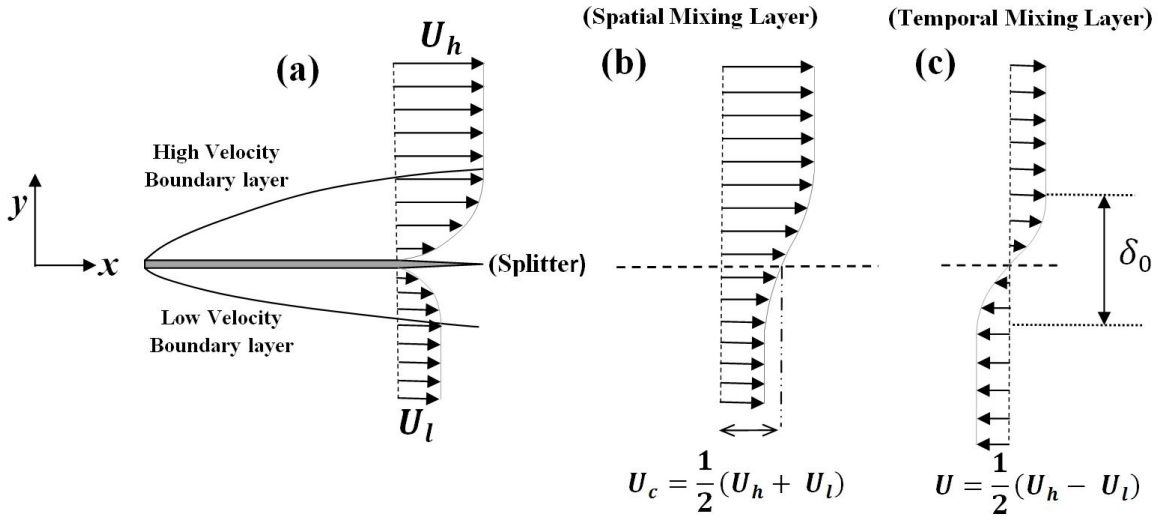

Figure 1.1. Schematic of the spatial and temporal mixing layer after the merging of two boundary layers (having different freestream velocities) separated by a splitter plate.

et al., 1967), or quasi 2-D like Kelvin-Helmholtz eddies in the mixing layer (Brown and Roshko, 1974).

In many practical applications, a plane mixing layer is generated when two boundary layers, with different free stream velocities U_h and U_l, merge behind a splitter plate, as shown in Fig. 1.1a. Aft of the splitter, the flow exhibits an intense velocity gradient along the y-axis and is highly rotational near the interface of the two streams. In a fixed reference frame, the flow is referred to as a "*spatial mixing layer*" (see Fig. 1.1b), which is convected by the characteristic convection velocity scale, $U_c = 1/2(U_h + U_l)$. In order to determine the inflow boundary condition of the spatial mixing layer, one needs information about the turbulent boundary layers at the downstream edge of the splitter. Also, one needs a fairly large computational domain in order to simulate the growth of the mixing layer. Therefore, simulation of the spatial mixing layer is numerically expensive.

To reduce computational costs, the present study considers the so-called "*temporal mixing layer*" instead. For velocity ratios, $0 << U_l/U_h < 1$, it is possible to treat a temporal mixing layer as a spatial mixing layer that moves along the x-axis with

a characteristic velocity scale of $U = 1/2(U_h - U_l)$, as shown in Fig. 1.1c. In this framework, periodic boundary conditions are used in the streamwise direction, which allows the computational domain to be much smaller and consequently the direct numerical simulations become more manageable.

As long as the turbulence intensity remains small, $u'/U << 1$, Taylor's hypothesis may be used to relate turbulence in the temporal mixing layer to that in the spatial mixing layer. In this manner, the initial conditions for the temporal mixing layer play the same role as the inflow conditions for the spatial mixing layer. For excessive values of u'/U, however, the evolution of the temporal mixing layer is not consistent with the expected behavior of the spatial mixing layer.

One of the first studies in the area of turbulent shear flows was performed by Liepmann and Laufer (1947), who showed experimentally that the laws governing the spread of turbulent free shear flows and their self-similar behavior can be obtained via integral boundary layer relations. Their experimental data also invalidated the conventional mixing-length theory of Prandtl as an adequate model for representing the dynamics of turbulent mixing layers. Further significant progress in terms of the fundamental physics of mixing layer flow did not appear until the 1970s (Spencer and Jones (1971); Champagne et al. (1976); Townsend (1976); Dimotakis and Brown (1976)). Experiments at this time provided evidence of a high correlation between the pressure and velocity fields (Spencer and Jones (1971)), accurate statistical measurements of the pressure and velocity to aid in developing models of the turbulent transport in mixing layers (Spencer and Jones (1971); Champagne et al. (1976)), and the importance of initial conditions on the long-time evolution of the flow toward a self-similar state (Champagne et al. (1976); Dimotakis and Brown (1976)). Townsend (1976, p.198) showed that, by substituting the self-preserving form of the mean velocity, Reynolds stress, and turbulent kinetic energy into the momentum and energy equations and examining the criteria that guarantees the equations are independent of the streamwise coordinate, the plane mixing layer will indeed achieve self-similar behavior provided (i) the characteristic velocity scale remains constant and (ii) the mixing layer thickness grows linearly in time.

Direct numerical simulation (DNS) of the self-similar behavior of the velocity field were first performed by Patel (1978) and continued with vigor in the early

1990s; (see for example Clarksean and McMurtry (1991); Rogers and Moser (1992); Moser and Rogers (1993)). Discrepancies between numerical and experimental studies continue to exist, however, due to the sensitivity of the flow to such parameters as the initial conditions (Rogers and Moser (1992)), geometry of the splitter (Dziomba and Fiedler (1985)), freestream velocity ratio (Mehta and Westphal (1986, 1989)), turbulent intensity of the freestreams (Patel, 1978), and the state of the upstream flows (i.e., laminar or turbulent inflow conditions) (Bell and Mehta, 1990).

The role of the initial (or upstream) conditions in establishing asymptotic behavior of the mixing layer using abundant experimental and DNS data, George and Davidson (2004) concluded that, even though the scaled mean velocity profiles collapsed, the streamwise (or temporal) variation of the scaling parameters and spreading rates of the mixing zone varied widely for different upstream (or initial) conditions. Therefore, experiments and numerical simulations that directly incorporate some type of sensitivity analysis are extremely prudent. Typical sensitivity analysis involves parametric studies wherein a series of experiments or numerical simulations are performed by varying the flow or design parameter(s) of interest in discrete increments about a baseline test case (Fathali et al., 2008). Although one can obtain quantitative information about the sensitivity of the flow to perturbations in the flow/design parameters with this type of method, the cost of running multiple simulations/experiments can be exorbitant, and the uncertainty in the resultant sensitivity derivatives depends largely on the perturbation step size used to increment the parameter values (Martins et al., 2000; Blackwell and Dowding, 2002).

1.4 Motivation

Analysis and control of unpredictable turbulent flows is a vital issue, especially when the turbulence involves spatially organized *coherent structures* that play an important role in mixing process or heat transfer, for example. The canonical mixing layer flow was chosen in the present study because of the major role of coherent vortices in evolution of the flow field. Simulation of the mixing layer in a temporal framework simplifies the problem with regard to its boundary conditions, and considerably reduces the computational cost when compared to the spatial mixing layer. However, the results of temporal mixing layer can be extended to the spatial coun-

terpart by satisfying the Taylor's hypothesis. Besides, the present study can be used to guide the application of computational sensitivity analysis in more complicated turbulent flows.

In this research, incorporation of SEM and CSD in the context of DNS and LES of the mixing layer will result in capturing the instantaneous sensitivity of coherent structures to the parameters of interest. The knowledge of instantaneous sensitivities in unsteady flows helps better understand how the dynamics of turbulent flows changes instantaneously with perturbations in the design parameters of interest.

In case of DNS, sensitivity analysis of the mixing layer to nondimensional parameters Reynolds number Re_{δ_0} and Prandtl number Pr is examined. The choice of Re_{δ_0} and Pr was made because they are important parameters that appear in the governing equations and affect the solution of the problem. The interpretation of these sensitivity fields can be used for the purpose of predicting the behavior of coherent vortices and scalar mixing in the shear layer at higher Re_{δ_0} and Pr. However, computational sensitivity analysis in the context of DNS is only feasible for a range of low-to-moderate Reynolds numbers and performing this technique at high Reynolds numbers is prohibited. Therefore, one needs to use LES in order to make the computational cost manageable. In case of LES of the mixing layer, sensitivities of the resolved flow to Re_{δ_0} and model parameter l^*, are examined at higher Reynolds numbers. The model parameter $l^* = C_s\Delta$, where C_s denotes the Smagorinsky model coefficient, and Δ is the grid spacing. This investigation clarifies the instantaneous effects of the LES model on the resolved structures in the mixing layer.

The present study introduces a new *diagnostic tool* in *a priori* study of LES models. Typically, LES models are evaluated, in an *a priori* study, in comparison with low Re_{δ_0} DNS data. Values for model coefficients are determined and an explicit assumption is made that these coefficients are independent of Re_{δ_0}. So that, the values of the model coefficients obtained from the low Re_{δ_0} *a priori* study are then used in subgrid scale modeling at high Re_{δ_0} LES. To test the validity of the underlying assumption, application of the LES sensitivity analysis in the context of an *a priori* study ends up with calculation of the sensitivity of the model coefficient(s), the SFS stresses and SFS kinetic energy dissipation introduced by the model to Re_{δ_0}.

Prior work in the literature has documented, via traditional parametric studies,

how the mixing layer is strongly sensitive to the initial conditions. Therefore, there is a potential for CSD or SEM to make a contribution in this area. Finally, CSD is introduced as a means to understand how the initial conditions of the problem affect the long-term evolution of the flow field including the formation of the coherent structures and their successive pairings.

1.5 Methodology

The Navier-Stokes equations governing the unsteady, incompressible flow with no body force can be written in nondimensional and fully conservative form as

$$\frac{\partial u_i}{\partial t} + \frac{\partial (u_i u_j)}{\partial x_j} = -\frac{\partial p}{\partial x_i} + \frac{1}{Re_L}\frac{\partial}{\partial x_j}\left[\left(\frac{\partial u_i}{\partial x_j} + \frac{\partial u_j}{\partial x_i}\right)\right], \tag{1.4}$$

which are solved under the constraint of conservation of mass, $\partial u_i/\partial x_i = 0$. Here, t is the nondimensional time based on L/U, x_i denotes the spatial coordinates nondimensionalized by the size of the domain L, u_i represents the velocity components nondimensionalized by a characteristic velocity, U, and, $Re_L = UL/\nu$ is the Reynolds number based on the physical domain size. The nondimensional vorticity ω is determined from its definition based on the velocity field rather than solving the vorticity equation explicitly. The momentum and corresponding sensitivity equations (shown in respective chapters) are solved concurrently in time using a variant of the fractional-step method originally formulated by Harlow and Welch (1965), and Chorin (1968) for the time-advancement of the Navier-Stokes equations and first implemented by Kim and Moin (1985), on a staggered grid. The spatial derivatives are discretized using second-order central differencing and the temporal derivatives are advanced explicitly in time using Adams-Bashforth time integration. Periodic boundary condition is applied along streamwise, x-axis, direction and free-slip condition is imposed along the top and bottom sides of the flow field. The DNS of mixing layer are performed over a Reynolds number range $100 \leq Re_{\delta_0} \leq 1000$ and LES codes were run up to $Re_{\delta_0} = 2000$.

1.6 Outline of Dissertation

The outline of dissertation is as follows. In Chap. 2, SEM is performed to examine the sensitivity of the planar mixing layer to Reynolds and Prandtl numbers using DNS at baseline $Re_{\delta_0} = 200$ and $Pr = 0.71$. In Chap. 3, *a posteriori* study of SEM and

CSD is done in the context of DNS and LES of the mixing layer at the baseline $Re_{\delta_0} = 500$ (up to $Re_{\delta_0} = 1000$ in the DNS study, and $Re_{\delta_0} = 2000$ in case of LES). In this chapter, probability density function (*pdf*) and grid convergence index (GCI) are used to compare the performance of SEM and CSD in capturing the coherent features in the sensitivity field of mixing layer. *A priori* study of Smagorinsky model is investigated in Chap. 4, and a new sensitivity-based criterion is introduced to further assess the performance of LES models. In Chap.5, the initial conditions for a temporal mixing layer are generated using two methods: (i) the stochastic method, and (ii) linear stability theory (LST). Sensitivity analysis of mixing layer to the pre-specified parameters in the initial conditions, namely initial integral length scale $\mathcal{L}$ (used in stochastic method), and noise factor c_{noise} (used in LST method) are performed using CSD.

CHAPTER 2

COHERENT SENSITIVITY FIELD OF A PLANAR MIXING LAYER

2.1 Abstract

Coherency in the topology of the instantaneous sensitivity fields of the planar mixing layer was captured using the Sensitivity Equation Method (SEM). The present results provide a means to examine how and to what extent perturbations in the Reynolds/Prandtl number *locally* alter the structure of the flow. Specifically, a *two-blade pattern* appears as a dominant feature in the sensitivity solution and highlights the physical mechanism leading to vortex thickness growth and enhanced molecular mixing with increasing Re_{δ_0} and Pr. SEM is a nonparametric approach in which the partial differential equations governing the evolution of the sensitivity coefficients are derived, discretized, and solved directly, in this work using an unsteady finite-volume-based fractional step algorithm. Numerical simulations were run at a baseline test case of $Re_{\delta_0} = 200$ and $Pr = 0.71$. An expression describing the sensitivity of vortex thickness to changes in Re_{δ_0} is also derived and validated using the concept of "nearby" flows.

2.2 Introduction

Computational sensitivity analysis provides a useful framework for physically understanding parameter dependencies in turbulent flows. This is achieved by directly solving the governing equations for the time-dependent sensitivity fields, which quantify how and to what extent coherent structures in the turbulence respond to infinitesimal changes in the design/flow parameters of interest. This contrasts typical parametric studies, which can only yield an integral measure of the average sensitivity of the flow to discrete changes in the design/flow parameters.

Indeed, computational sensitivity analysis not only reveals the temporal features of the sensitivity fields (Hristova et al., 2006), but also supplies the necessary gra-

dient information to actively control the performance and optimize the design of fluid systems (Stanley and Stewart, 2002; Turgeon et al., 2000). Sensitivity-based optimization involves a two-part procedure of computing the sensitivity coefficients (or derivatives) separately, using one of several techniques in the area of computational sensitivity analysis (see Sec. 1.2.1), and then substituting those derivatives into the appropriate minimization algorithm (Borggaard and Burns, 1997). This approach toward optimization may be preferred over adjoint methods (Gunzburger, 2002) because (i) sensitivity-based optimization is more intuitive to understand conceptually and easier to implement numerically for general-purpose design problems, and (ii) for the case of transient flows, the expense of adjoint methods, both in terms of CPU time and memory, becomes prohibitive (Mahieu et al., 2005).

The present study represents initial research in this direction as pertains directly to the implementation and evaluation of computational sensitivity analysis in the context of the canonical 2-D temporal mixing layer. The mixing layer was chosen as a reasonable test case because of the existence of well-defined coherent vortices, which are inherent features of any turbulent shear flow. Results from the present computational sensitivity analysis demonstrate an analogous coherency in the instantaneous sensitivity fields (i.e., sensitivity of the vorticity and temperature to infinitesimal changes in the Reynolds and Prandtl numbers). Interpretation of individual snapshots of the sensitivity fields leads to new insights into the physical mechanisms responsible for growth and enhanced mixing quality with increasing Reynolds and Prandtl numbers. In addition, results from the present study can be used to guide the application of computational sensitivity analysis in more complex turbulent flows exhibiting a larger range of scales.

2.2.1 Sensitivity Analysis of the Mixing Layer

Driven primarily by discrepancies between numerical and experimental studies, much work has already been done toward understanding sensitivities in the planar mixing layer. Previous research has investigated the sensitivity of the flow to such parameters as the initial conditions (Rogers and Moser, 1992), geometry of the splitter (Dziomba and Fiedler, 1985), freestream velocity ratio (Mehta and Westphal, 1986, 1989), turbulent intensity of the freestreams (Patel, 1978), and the state of the

upstream flows, i.e., laminar or turbulent inflow conditions (Bell and Mehta, 1990). The role of the initial (or upstream) conditions in establishing asymptotic behavior of the mixing layer was examined in-depth by George and Davidson (2004) using experimental and DNS data. The approach taken toward sensitivity analysis in all of this previous work involves parametric studies, wherein a series of experiments or numerical simulations are performed with the flow or design parameter(s) of interest varied in discrete increments about a baseline test case (Ko et al., 2008; Fathali et al., 2008). Although one can obtain quantitative sensitivity information from these types of parametric studies via a finite difference of integral or statistical quantities, running multiple simulations/experiments can be cumbersome and user-intensive; and, the uncertainty in the resultant sensitivity coefficients depends largely on the perturbation step size used to increment the parameter values (Martins et al., 2000; Blackwell and Dowding, 2002).

In contrast, the present study employs SEM in order to understand how the planar mixing layer responds to instantaneous, infinitesimal changes in the Reynolds and Prandtl numbers, which are known to enhance the mixing quality of the flow. The SEM results reveal regions within the coherent vortices that exhibit high/low sensitivity. Proper interpretation of these results leads to new insights on how the Reynolds and Prandtl numbers directly affect the instantaneous structure of the turbulence. This type of information cannot be obtained from traditional parametric studies and has potential broader impact to active control. Another important contribution of the present study is the practical implementation of SEM in the context of the finite-volume fractional-step algorithm. For this purpose, the present study builds off of the recent work of Kirkman and Metzger (2008b, 2009), who implemented SEM in a finite-volume, fractional-step code to examine sensitivities in laminar and turbulent channel flows. Whereas, most of the SEM literature to date discusses the implementation and application of SEM in the context of *finite element* discretization methods (Borggaard and Verma, 2000; Turgeon et al., 2000; Blackwell and Dowding, 2002; Stanley and Stewart, 2002; Turgeon et al., 2002, 2003; Duvigneau and Pelletier, 2006; Hristova et al., 2006).

The chapter outline is as follows. First, a brief overview of the governing equations of the fluid motion and corresponding sensitivity equations is provided. Here, tem-

perature is considered as a *passive* scalar. The finite-volume computational method and its extension to SEM is then discussed. Validation of the results for the vorticity and temperature fields and corresponding sensitivity coefficients are shown using the concept of *nearby flow*. The sensitivity of vorticity to changes in Reynolds number and the sensitivity of temperature to changes in both Prandtl and Reynolds number is examined. In addition, an expression describing the sensitivity of the vortex thickness to Reynolds number is derived using ensemble averaged SEM data and evaluated in comparison to results from a parametric study.

2.3 Problem Definition

The planar mixing layer was defined, and different types of this canonical test case were explained in Sec. 1.3. In fact, one of the challenges in numerical simulation of the mixing layer is the prescription of initial and boundary conditions that adequately describe the real flow. The process of defining the main features of the turbulence in the initial condition for the temporal mixing layer has been termed "super-grid modeling" (Grinstein, 2004). The most common method of super-grid modeling is to impose a pseudo-perturbation on a mean profile. Three strategies exist for constructing this perturbation. The first method utilizes a stochastic approach whereby the "turbulent" perturbations are comprised from random realizations having statistical equivalency to that of the actual turbulent flow field (Lee et al., 1992; Kondo et al., 1997; Smirnov et al., 2001; Fathali et al., 2008). This method will be implemented in Chap. 5. The second method uses the output from DNS and LES simulations that have been performed separately on an extended computational domain encompassing the splitter plate (Rogers and Moser, 1993; Li et al., 2000; Schlüter et al., 2003). The third, least expensive and simplest, method of initiating the turbulence follows from linear stability theory (Ragab and Wu, 1989). The present chapter adopts the last approach. Specifically, the nondimensional (by U) *initial* streamwise velocity profile, u_0, is introduced as a basic mean flow plus a noise function of the form

$$u_0(x,y) = \bar{u}_0(y) + c_{noise}\,\frac{\partial \psi}{\partial y}\,, \tag{2.1}$$

where

$$\psi(x,y) = \exp\left(-y^2 L^2/\delta_0^2\right)\,\left[\cos(8\pi x) + \cos(20\pi x)\right]\,. \tag{2.2}$$

Here, δ_0 denotes the initial vortex thickness, and x, y represent the spatial coordinates nondimensionalized by the size of the domain L. The nondimensional initial mean profile, $\bar{u}_0$, follows from Michalke (1964),

$$\bar{u}_0(y) = \tanh(2yL/\delta_0). \tag{2.3}$$

The factor $c_{noise} = 0.001$ is chosen to satisfy Taylor's hypothesis, which guarantees that velocity perturbations remain a small percentage of the mean velocity. Due to continuity, the initial vertical velocity, nondimensionalized by U, is

$$v_0(x, y) = -c_{noise} \frac{\partial \psi}{\partial x}\,. \tag{2.4}$$

The magnitude of δ_0 is calculated from the specified Reynolds number, $Re_{\delta_0} = \delta_0 U/\nu$. In the present study, the velocity ratio is taken as $U_l/U_h = 0.6$ following Bell and Mehta (1990), which leads to a characteristic velocity scale of $U = 2.0$ m/s. The value of viscosity ν is equivalent to that for air at standard conditions. The size of the domain L is selected according to linear stability theory, which states that for a given Reynolds number, Re_{δ_0}, a span of unstable longitudinal wavenumbers exists in the mixing layer that initiate instability and, thus, the onset of turbulence in the flow field. If this disturbance contains the whole range of unstable modes (the assumption used in this work), the largest amplitude wavenumber is the first one that appears in the velocity field. For $Re_{\delta_0} > 20$, the largest amplitude wavenumber is inviscid and therefore independent of Reynolds number (Betchov and Szewczyk, 1963). For the hyperbolic tangent velocity profile, (2.3), the wavelength, λ_a, corresponding to the most unstable mode, which also represents the length of each fundamental Kelvin-Helmholtz vortex, is approximately given by $\lambda_a \simeq 7\delta_0$ (Betchov and Szewczyk, 1963). Therefore, the length of the computational domain, L, is determined based on the number of the fundamental Kelvin-Helmholtz vortices, N, desired in the simulation, i.e.,

$$L = N\lambda_a \simeq 7N\delta_0. \tag{2.5}$$

In the present study, $N = 4$ so that $L/\delta_0 = 28$.

Since temperature is treated as a *passive* scalar and because the Prandtl number (Pr) is of order unity, the development of the thermal boundary layers aft of the splitter mirrors the momentum boundary layers shown in Fig. 1.1. Therefore,

initialization of the temperature field follows the same basic mean profile as the initial velocity field, i.e.,

$$T_0(y) = \tanh(2yL/\delta_0), \tag{2.6}$$

where T_0 represents the initial temperature nondimensionalized by the characteristic temperature scale, $\theta = 1/2(T_h - T_l)$. In the present study, the temperature associated with the high momentum stream is $T_h = 1$, while that for the low momentum stream is $T_l = -1$. This yields a characteristic temperature scale of $\theta = 1$. Note, perturbations in the temperature field are not required in order to initiate mixing of the passive scalar, as the initial turbulence in the velocity field suffices for this purpose. The baseline simulation in the present study corresponds to $Re_{\delta_0} = 200$, $Pr = 0.71$.

2.4 Governing Equations

2.4.1 Momentum, Continuity and Temperature Equations

The Navier-Stokes equations that govern unsteady, incompressible flow with uniform density distribution and no body force can be written in a nondimensional and fully conservative form as

$$\frac{\partial u_i}{\partial t} + \frac{\partial (u_i u_j)}{\partial x_j} = -\frac{\partial p}{\partial x_i} + \frac{1}{Re_L}\frac{\partial}{\partial x_j}\left(\frac{\partial u_i}{\partial x_j} + \frac{\partial u_j}{\partial x_i}\right), \tag{2.7}$$

which are solved under the constraint of conservation of mass,

$$\frac{\partial u_i}{\partial x_i} = 0. \tag{2.8}$$

Here, t represents time nondimensionalized by L/U, x_i denotes the spatial coordinates nondimensionalized by the size of the domain L, u_i represents the velocity components nondimensionalized by U, p denotes the pressure nondimensionalized by $1/2\,\rho U^2$, and Re_L ($\equiv UL/\nu$) is the Reynolds number based on the physical domain size. The nondimensional vorticity is determined from its definition based on the velocity field, i.e.,

$$w = \frac{\partial v}{\partial x} - \frac{\partial u}{\partial y}. \tag{2.9}$$

The equation describing temperature, uncoupled from momentum, is represented in nondimensional form by

$$\frac{\partial T}{\partial t} + \frac{\partial (T u_j)}{\partial x_j} = \frac{1}{Pr\, Re_L}\frac{\partial}{\partial x_j}\left(\frac{\partial T}{\partial x_j}\right), \tag{2.10}$$

where T is the temperature nondimensionalized by θ.

2.4.2 Sensitivity Equations

In the present study, sensitivity analysis is performed using the continuous sensitivity equation method (SEM). The purpose of this analysis is to quantify the sensitivity of the flow to changes in relevant design parameters. Indeed, Re_{δ_0} is a crucial design parameter for the momentum, continuity, and temperature equations, because it contains information about the initial conditions, geometry of the fundamental Kelvin-Helmholtz vortices, and physical properties of the working fluid. The Prandtl number (Pr) is another important parameter that affects the temperature equation. The continuous sensitivity equations are derived by differentiating the momentum and continuity equations with respect to Re_{δ_0}, and the temperature equation with respect to both Pr and Re_{δ_0}. The sensitivity equation for velocity, so derived, is

$$\begin{aligned}\frac{\partial S_{u_i}}{\partial t}+\frac{\partial (S_{u_i}u_j)}{\partial x_j} &= -\frac{\partial S_p}{\partial x_i}+\frac{1}{Re_L}\frac{\partial}{\partial x_j}\left(\frac{\partial S_{u_i}}{\partial x_j}+\frac{\partial S_{u_i}}{\partial x_i}\right) \\ &-\frac{\partial\left(u_i\, S_{u_j}\right)}{\partial x_j}-\frac{1}{(N\lambda_a/\delta_0)Re_{\delta_0}^2}\frac{\partial}{\partial x_j}\left(\frac{\partial u_i}{\partial x_j}+\frac{\partial u_j}{\partial x_i}\right),\end{aligned} \tag{2.11}$$

where S_{u_i} ($\equiv \partial u_i/\partial Re_{\delta_0}$) denotes the sensitivity of u_i to Re_{δ_0} and similarly, S_p ($\equiv \partial p/\partial Re_{\delta_0}$) denotes the sensitivity of p to Re_{δ_0}. The conversion between the Reynolds number based on the physical domain size and Reynolds number based on the initial vortex thickness is $Re_{\delta_0} = Re_L/(N\,\lambda_a)$, where N denotes the number of fundamental Kelvin-Helmholtz vortices in the domain and λ_a is the wavelength of each fundamental vortex. Note, equation (2.11) resembles the original governing equation (2.7) except for the last two terms on the right hand side, which represent respectively (i) stretching and orientation of the sensitivity and (ii) a source of sensitivity based on the Laplacian of the velocity field. The corresponding continuity equation for sensitivity is

$$\frac{\partial S_{u_i}}{\partial x_i} = 0. \tag{2.12}$$

The sensitivity of the vorticity to Reynolds number, S_ω, is determined by differentiating (2.9) with respect to Re_{δ_0},

$$S_\omega = \frac{\partial S_v}{\partial x} - \frac{\partial S_u}{\partial y}, \tag{2.13}$$

where S_v and S_u denote the y- and x-components of velocity sensitivity to changes in Re_{δ_0}. The equation describing the sensitivity of temperature to Pr is obtained by

differentiating (2.10) with respect to Pr,

$$\frac{\partial S_{T,Pr}}{\partial t} + \frac{\partial (S_{T,Pr}\, u_j)}{\partial x_j} = \frac{1}{Pr\, Re_L} \frac{\partial}{\partial x_j} \left(\frac{\partial S_{T,Pr}}{\partial x_j} \right) - \frac{1}{Pr^2 Re_L} \frac{\partial}{\partial x_j} \left(\frac{\partial T}{\partial x_j} \right), \quad (2.14)$$

where $S_{T,Pr}$ ($\equiv \partial T/\partial Pr$) denotes the sensitivity of T to Pr. Similarly, the sensitivity equation of temperature to Re_{δ_0} is obtained by differentiating (2.10) with respect to Re_{δ_0},

$$\frac{\partial S_{T,Re_{\delta_0}}}{\partial t} + \frac{\partial \left(S_{T,Re_{\delta_0}}\, u_j \right)}{\partial x_j} = \frac{1}{Pr\, Re_L} \frac{\partial}{\partial x_j} \left(\frac{\partial S_{T,Re_{\delta_0}}}{\partial x_j} \right) - \frac{\partial \left(T\, S_{u_j,Re_{\delta_0}} \right)}{\partial x_j} - \frac{1}{Pr(N\lambda_a/\delta_0) Re_{\delta_0}^2} \frac{\partial}{\partial x_j} \left(\frac{\partial T}{\partial x_j} \right), \quad (2.15)$$

where $S_{T,Re_{\delta_0}}$ ($\equiv \partial T/\partial Re_{\delta_0}$) represents the sensitivity of T to Re_{δ_0}. In both (2.14) and (2.15), source terms appear that drive $S_{T,Re_{\delta_0}}$ and $S_{T,Pr}$ due to the presence of the parameters in the original governing equations.

2.5 Numerical Method

2.5.1 Solution of the Momentum Equations

Equations (2.7) and (2.8) are solved by using a variant of the fractional-step method originally formulated by Harlow and Welch (1965) and Chorin (1968) for the time-advancement of the Navier-Stokes equations, and first implemented by Kim and Moin (1985) on a staggered grid. The fractional-step method is based on the Hodge decomposition in which the velocity field, $\hat{u}_i$, is decomposed into a divergence-free field, u_i, plus the gradient of a scalar potential, ϕ,

$$\hat{u}_i = u_i + \frac{\partial \phi}{\partial x_i}. \quad (2.16)$$

It is emphasized that the Hodge decomposition can be performed for any arbitrary vector field, such as S_{u_i}. The Hodge decomposition is implemented in two steps: (i) an intermediate velocity field, $\hat{u}_i$, is first obtained using the discretized equation

$$\frac{\hat{u}_i - u_i^n}{\Delta t} = \frac{3}{2} H_i^n - \frac{1}{2} H_i^{n-1}, \quad (2.17)$$

where

$$H_i = -\frac{\partial (u_i u_j)}{\partial x_i} + \frac{1}{Re_L} \frac{\partial}{\partial x_j} \left[\left(\frac{\partial u_i}{\partial x_j} + \frac{\partial u_j}{\partial x_i} \right) \right], \quad (2.18)$$

then, (ii) the intermediate velocity field calculated from the first step is projected onto a divergence-free velocity field using (2.16),

$$\frac{u_i^{n+1} - \hat{u}_i}{\Delta t} = -\frac{\partial \phi}{\partial x_i}, \tag{2.19}$$

where the superscript n represents the time step. Note, the intermediate velocity field will not satisfy (2.8) because the solution of the momentum equation for the intermediate velocity field is performed ignoring the pressure gradient term. Therefore, by taking the divergence of (2.19) and imposing continuity for the new time level $(n+1)$ an equation for the scalar potential follows

$$\frac{\partial^2 \phi}{\partial x_j \partial x_j} = \frac{1}{\Delta t}\frac{\partial \hat{u}_i}{\partial x_i}. \tag{2.20}$$

In this manner, the divergence of the intermediate velocity field is used as a source term for solving the gradient of the scalar potential. In order to solve (2.20), a finite volume based, *multigrid scheme* is used in which the coarse grid is half the resolution of the fine (original) staggered grid. In order to extract the pressure field, the scalar potential ϕ must be corrected as follows (Kim and Moin, 1985),

$$p = \phi - \frac{\Delta t}{2Re_L}\frac{\partial^2 \phi}{\partial x_j \partial x_j}. \tag{2.21}$$

The current fractional-step algorithm utilizes the finite volume method with a forward-staggered and uniform grid of resolution 300×300 in a square domain where $-0.5 < x < 0.5$ and $-0.5 < y < 0.5$. The spatial derivatives are discretized using second-order central differencing; and, the temporal derivatives are advanced explicitly in time using Adams-Bashforth time integration. Periodic boundary conditions are applied along the streamwise direction, x-direction, and free-slip conditions are imposed along the top and bottom boundaries.

2.5.2 Solution of the Temperature Equation

The temperature equation (2.10) is solved explicitly using the second order Adams-Bashforth method,

$$T^{n+1} = T^n + \Delta t\left(\frac{3}{2}\mathcal{H}^n - \frac{1}{2}\mathcal{H}^{n-1}\right), \tag{2.22}$$

where n represents the time level and

$$\mathcal{H} = -\frac{\partial (Tu_j)}{\partial x_j} + \frac{1}{Pr\, Re_L}\frac{\partial}{\partial x_j}\left(\frac{\partial T}{\partial x_j}\right). \tag{2.23}$$

At each time step, $\mathcal{H}$ is calculated on the staggered grid using central differencing.

2.5.3 Solution of the Sensitivity Equations

The governing equations for S_{u_i}, $S_{T,Pr}$, and $S_{T,Re_{\delta_0}}$ are similar to the momentum and temperature equations except for additional source terms, due to the presence of the parameters (Re_{δ_0} and Pr) in the Navier-Stokes and temperature equations. The solution procedure for the sensitivity equations is similar to (2.17) through (2.21) explained above. Specifically, the pressure sensitivity is obtained in a manner similar to (2.20) and (2.21),

$$\frac{\partial^2 S_\phi}{\partial x_j \partial x_j} = \frac{1}{\Delta t}\frac{\partial \hat{S}_{u_i}}{\partial x_i}, \tag{2.24}$$

where S_ϕ ($\equiv \partial\phi/\partial Re_{\delta_0}$) is the potential scalar sensitivity and $\hat{S}_{u_i}$ ($\equiv \partial\hat{u}_i/\partial Re_{\delta_0}$) is the intermediate velocity sensitivity. The sensitivity of pressure to perturbations in Re_{δ_0} is given by

$$S_p = S_\phi - \frac{\Delta t}{2Re_L}\frac{\partial^2 S_\phi}{\partial x_j \partial x_j} \tag{2.25}$$

Like the momentum equations, periodic boundary conditions are used along the streamwise direction, and free-slip conditions ($\partial S_{u_i}/\partial y = 0.0$) are employed along the top and bottom sides of the computational domain. A zero initial condition is appropriate for the velocity sensitivity field (i.e., $S_{u_i} = 0$ at $t = 0$) because neither u_0 nor v_0 depend on Re_{δ_0}; refer to (2.1) and (2.4) and recall that $L/\delta_0 \approx 28$ independent of Re_{δ_0}.

Finally, the sensitivity of temperature to Prandtl and Reynolds number is obtained by solving (2.14) and (2.15) using the same numerical scheme as that for the temperature equation, with the addition of the extra source term. Similarly, periodic boundary conditions are used in the streamwise direction; while, homogeneous Dirichlet boundary conditions are specified along the top and bottom boundaries. The initial temperature sensitivity field is also initialized to zero (i.e., $S_{T,Pr} = S_{T,Re_{\delta_0}} = 0.0$ at $t = 0$) since T_0 remains independent of both Re_{δ_0} and Pr; recall (2.6).

2.6 Validation of the DNS/SEM Solver

2.6.1 Validation of the Velocity Field

The grid independent solution of velocity field is obtained by successive simulations of the mixing layer at four differnt grid resolution 50×50, 100×100, 200×200 and 300×300. The total kinetic energy of velocity field (i.e., $K.E. = \frac{1}{2}u_i u_i$) is plotted versus time of the simulation in Fig. 2.1. The maximum error in capturing the $K.E.$

is only 0.2% at resolution 200×200 compared to the finest grid calculations (i.e., 300×300). However, in order to provide high resolution sensitivity features of the mixing layer we use the finest grid resolution in this chapter. Besides, the velocity field obtained from the numerical simulations is validated by comparing the self-similar mean profile to the analytical solution and experimental data of Champagne et al. (1976). The self-similar velocity is defined as

$$f(\xi) = \frac{1}{2}\left(\langle u \rangle - \frac{U_c}{U}\right), \tag{2.26}$$

where $\langle \cdot \rangle$ represents an ensemble average (along the x-axis) of the nondimensional streamwise velocity. Here, ξ denotes the self-similar vertical coordinate defined as

$$\xi = \frac{y - 1/2\,[y_{0.9} + y_{0.1}]}{y_{0.9} - y_{0.1}}, \tag{2.27}$$

where $y_{0.1}$ and $y_{0.9}$ represent the nondimensional vertical coordinates that satisfy the relation

$$\langle u(x, y_\alpha) \rangle = \frac{U_l}{U} + 2\,\alpha, \tag{2.28}$$

for $\alpha = 0.1$ and 0.9. Using the turbulent-viscosity hypothesis, an analytical solution to the momentum equation for the temporal mixing layer may be obtained following Pope (2000) as

$$f(\xi) = \frac{1}{2}\mathrm{erf}\left(\frac{\xi}{\sigma\sqrt{2}}\right), \tag{2.29}$$

where $\sigma = 0.3902$. Figure 2.2 compares the analytical solution (2.29) to the present DNS results from the baseline case of $Re_{\delta_0} = 200$ at three different nondimensional times t^* ($\equiv t\,L/\delta_0$) equal to 80, 140, and 200. Also shown are the experimental data of Champagne et al. (1976), acquired at a location of 59.5 cm away from a splitter plate. Excellent agreement exists between all profiles, but particularly between the present DNS and the analytical solution.

2.6.2 Validation of the Sensitivity Fields

One of the best ways to validate the sensitivity results is through a *nearby flow analysis* based on a truncated Taylor series (Colin et al., 2005; Hristova et al., 2006;

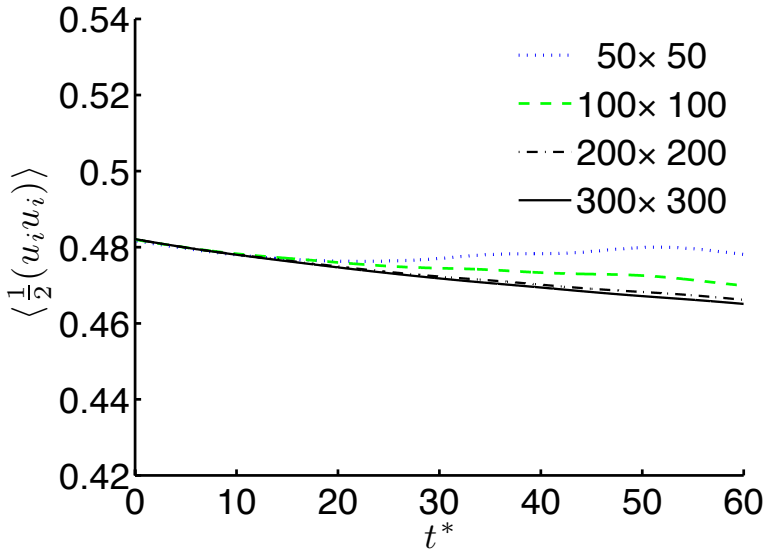

Figure 2.1. Grid independence study; the comparison between total kinetic energy of the velocity field obtained from four different grid resolution.

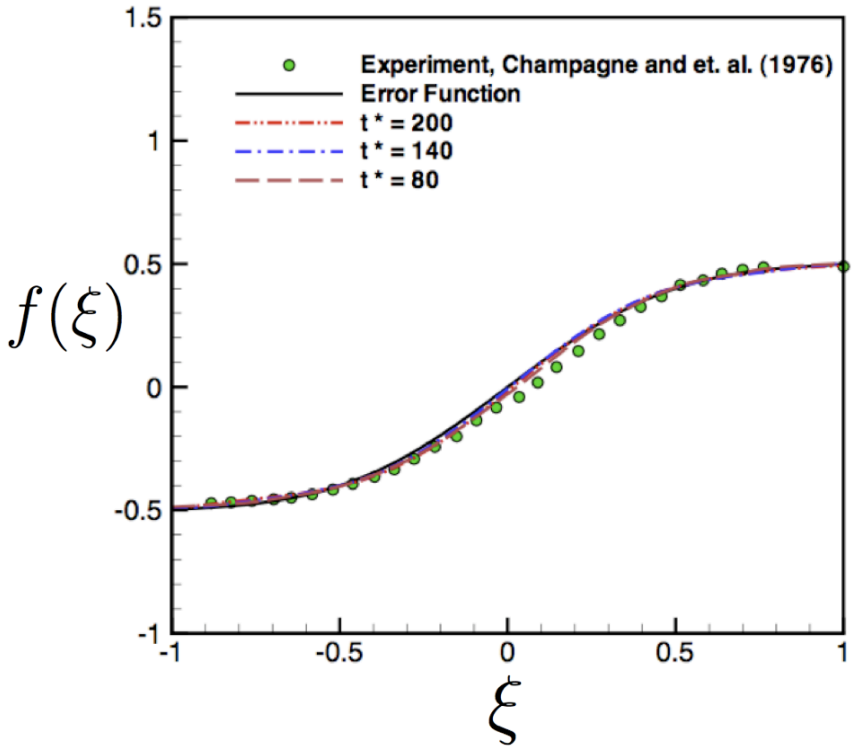

Figure 2.2. Self-similar profile of velocity at different time levels compared to the experimental data of Champagne et al. (1976) and the analytical similarity solution given in (2.29).

Duvigneau and Pelletier, 2006). A first-order Taylor series expansion of the vorticity about a baseline Reynolds number Re_{δ_0} yields

$$\omega\Big|_{Nearby} = \omega\Big|_{Re_{\delta_0}} + \frac{\partial\omega}{\partial Re_{\delta_0}}\Big|_{Re_{\delta_0}} \Delta Re_{\delta_0}\,, \tag{2.30}$$

where $\omega\big|_{Nearby}$ represents the vorticity at a *nearby* Reynolds number, specifically at $Re_{\delta_0}^{new} = Re_{\delta_0} + \Delta Re_{\delta_0}$. The derivative term in (2.30) is equivalent to the sensitivity coefficient evaluated at the baseline Reynolds number (i.e., $S_\omega\big|_{Re_{\delta_0}} \equiv \partial\omega/\partial Re_{\delta_0}\big|_{Re_{\delta_0}}$). This yields

$$\omega\Big|_{Nearby} = \omega\Big|_{Re_{\delta_0}} + S_\omega\Big|_{Re_{\delta_0}} \Delta Re_{\delta_0}. \tag{2.31}$$

Using (2.31), one can predict the flow field at a new Reynolds number, $Re_{\delta_0}^{new}$, given the vorticity and sensitivity results from a single simulation at the baseline Reynolds number Re_{δ_0}, as long as ΔRe_{δ_0} remains relatively small for purposes of the first-order Taylor series approximation. To validate the S_ω field, the nearby flow $\omega\big|_{Nearby}$ is calculated from (2.31) using the DNS/SEM results at $Re_{\delta_0} = 200$ and compared to the vorticity obtained from a separate DNS run at $Re_{\delta_0} = 240$ in order to verify that

$$\omega\Big|_{Nearby} \approx \omega\Big|^{\mathrm{DNS}}_{Re_{\delta_0}^{new}}\,. \tag{2.32}$$

Figure 2.3 compares $\omega\big|_{Nearby}$ along the centerline of the square domain at $t^* = 14$ to that directly simulated at $Re_{\delta_0} = 240$. The vorticity at the baseline Reynolds number of $Re_{\delta_0} = 200$ is also shown for reference. Here, $\Delta Re_{\delta_0} = 40$ in the nearby calculation, which reflects a 20% increase in Reynolds number. Figure 2.3 shows excellent agreement between the DNS at $Re_{\delta_0} = 240$ and the nearby flow calculation. This result gives a high-level of confidence that the SEM code is being solved correctly.

Validation of the temperature sensitivities ($S_{T,Pr}$ and $S_{T,Re_{\delta_0}}$) follows in a similar manner. The nearby flow for temperature is given by a first-order Taylor series of the form

$$\begin{aligned} T\Big|_{Nearby} = T\Big|_{(Re_{\delta_0},Pr)} &+ \left[S_{T,Re_{\delta_0}}\Big|_{(Re_{\delta_0},Pr)} \Delta Re_{\delta_0}\right] \\ &+ \left[S_{T,Pr}\Big|_{(Re_{\delta_0},Pr)} \Delta Pr\right], \end{aligned} \tag{2.33}$$

where the sensitivities are evaluated at the baseline Reynolds and Prandtl numbers of $Re_{\delta_0} = 200$ and $Pr = 0.71$. Therefore, two validations of the present SEM simulations

are performed, by comparing the nearby flow calculations obtained from the baseline DNS/SEM with results from separate DNS of the temperature field run using *new* parameter values: (Re_{δ_0}, Pr^{new}) and ($Re_{\delta_0}^{new}$, Pr), where $Pr^{new} \equiv Pr + \Delta Pr$.

In order to validate the sensitivity of temperature to Prandtl number ($S_{T,Pr}$) one can verify that

$$T\Big|_{Nearby} \approx T\Big|^{\text{DNS}}_{Re_{\delta_0},Pr^{new}} , \tag{2.34}$$

where the contribution from the first term in square brackets in (2.33) has been neglected, i.e., $\Delta Re_{\delta_0} = 0$. Figure 2.4 shows that, here too, the nearby flow prediction is nearly identical to the DNS at $Re_{\delta_0} = 200$, $Pr = 1.0$. In this case, $\Delta Pr = 0.29$, indicating a 40% increase in Prandtl number. The temperature along the centerline of the domain at $Re_{\delta_0} = 200, Pr = 0.71$ is also displayed for reference.

Similarly, validation of the sensitivity of temperature to Reynolds number ($S_{T,Re_{\delta_0}}$) is performed by comparing

$$T\Big|_{Nearby} \approx T\Big|^{\text{DNS}}_{Re_{\delta_0}^{new},Pr} , \tag{2.35}$$

where the contribution from the *second* term in square brackets in (2.33) is neglected, i.e., $\Delta Pr = 0$ in this case. Figure 2.5 shows that, indeed, the nearby flow prediction and the DNS at $Re_{\delta_0} = 240$, $Pr = 0.71$ are almost identical. Here $\Delta Re_{\delta_0} = 40$, indicating a 20% increase in Reynolds number. The temperature along the centerline of the domain at $Re_{\delta_0} = 200$, $Pr = 0.71$ is also displayed for reference.

Lastly, Fig. 2.6 presents the nearby flow prediction to simultaneous changes in both Reynolds and Prandtl numbers, where $\Delta Re_{\delta_0} = 40$ and $\Delta Pr = 0.29$. For comparison, the centerline temperature obtained from the DNS at $Re_{\delta_0} = 240$, $Pr = 1.0$ is also plotted, along with that from the baseline DNS simulation at $Re_{\delta_0} = 200$, $Pr = 0.71$. Figure 2.6 indicates good agreement between the nearby flow prediction and the actual DNS simulation at $Re_{\delta_0}^{new}$, Pr^{new}, despite the relatively large step size used for both the Reynolds and Prandtl numbers in the nearby flow calculation. The noticeable deviation at the peaks and valleys of T are likely due to (i) the coupling between $S_{T,Re_{\delta_0}}$ and $S_{T,Pr}$, which would appear in the second-order Taylor series approximation as a mixed derivative of the form $\partial^2 T/\partial Re_{\delta_0}\partial Pr$, and (ii) the nonlinear behavior of temperature to changes in Re_{δ_0}, which also might be better represented by using a second-order Taylor series approximation to calculate the nearby flow.

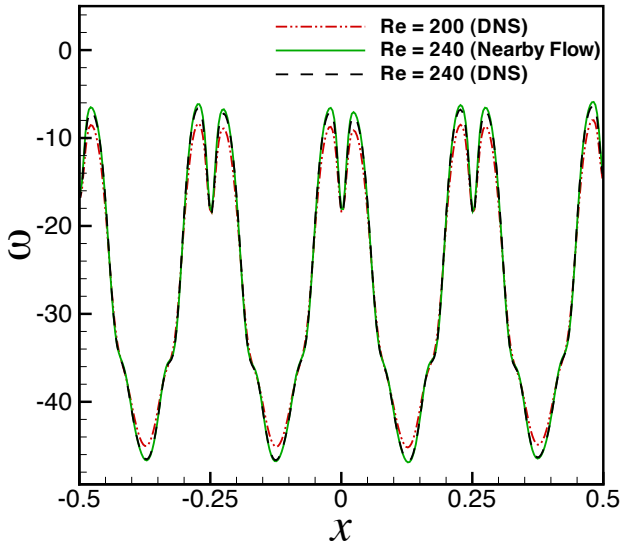

Figure 2.3. Vorticity along the centerline at $t^* = 14$. Three cases are shown: DNS at $Re_{\delta_0} = 200$, DNS at $Re_{\delta_0} = 240$ and the nearby flow prediction for $Re_{\delta_0} = 240$ using the SEM results at $Re_{\delta_0} = 200$.

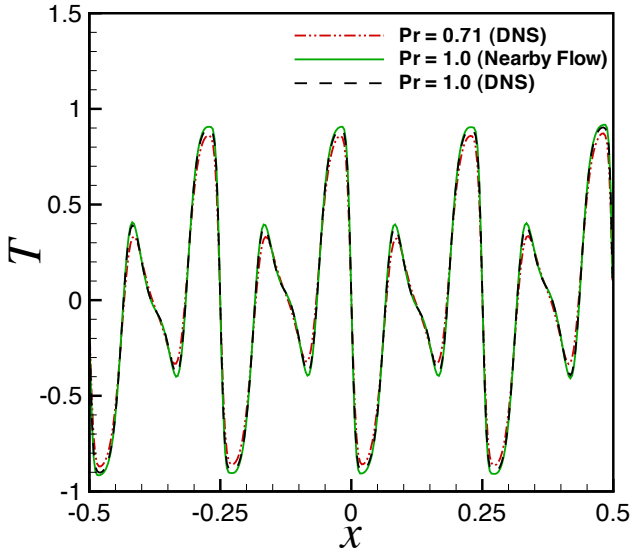

Figure 2.4. Temperature along the centerline at $t^* = 14$ and $Re_{\delta_0} = 200$. Three cases are shown: DNS at $Pr = 0.71$, DNS at $Pr = 1.0$ and the nearby flow prediction for $Pr = 1.0$ using the SEM results at $Pr = 0.71$.

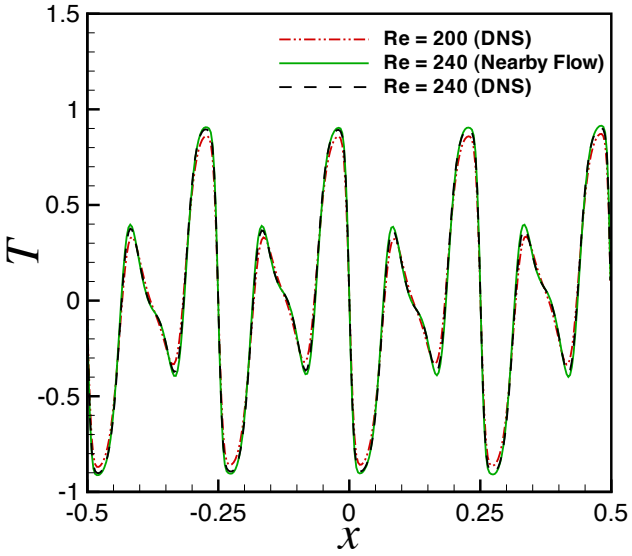

Figure 2.5. Temperature along the centerline at $t^* = 14$ and $Pr = 0.71$. Three cases are shown: DNS at $Re_{\delta_0} = 200$, DNS at $Re_{\delta_0} = 240$ and the nearby flow prediction for $Re_{\delta_0} = 240$ using the SEM results at $Re_{\delta_0} = 200$.

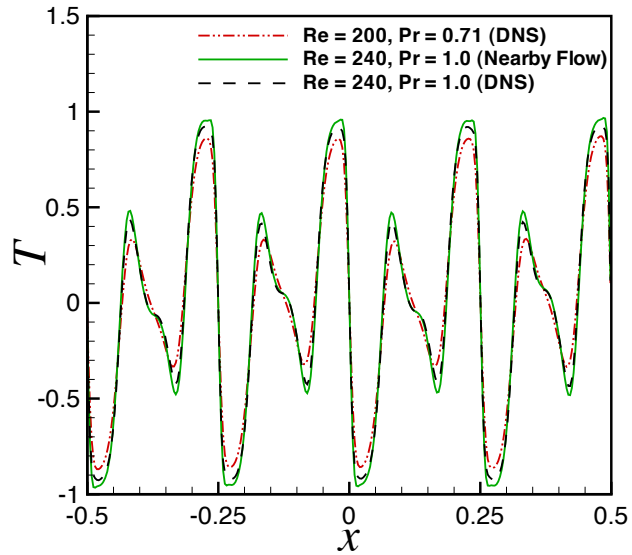

Figure 2.6. Temperature along the centerline at $t^* = 14$. Three cases are shown: DNS at $(Re_{\delta_0}, Pr) = (200, 0.71)$, DNS at $(Re_{\delta_0}, Pr) = (240, 1.0)$ and the nearby flow prediction for $(Re_{\delta_0}, Pr) = (240, 1.0)$ using the SEM results at $(Re_{\delta_0}, Pr) = (200, 0.71)$.

2.7 Results

Instantaneous snapshots of the vorticity and temperature fields, along with their corresponding sensitivity fields are presented from the baseline DNS/SEM simulation run at $Re_{\delta_0} = 200$, $Pr = 0.71$. Interpretations of the sensitivity fields S_ω, $S_{T,Pr}$, and $S_{T,Re_{\delta_0}}$ are given with particular emphasis on how to utilize the sensitivity results to *predict* the behavior of ω and T at higher Prandtl and Reynolds numbers. These interpretations/predictions are supported by comparing with results from three additional DNS run at slightly higher Reynolds and Prandtl numbers relative to the baseline case: ($Re_{\delta_0} = 240$, $Pr = 0.71$); ($Re_{\delta_0} = 200$, $Pr = 1.0$); and ($Re_{\delta_0} = 240$, $Pr = 1.0$).

As mentioned in Sec. 2.3, the domain size was chosen in order to produce four fundamental Kelvin-Helmholtz (K-H) vortices that span the streamwise extent of the domain. As time progresses, the fundamental K-H vortices pair, forming two larger vortices, which eventually pair a second time, forming a single vortex that fills approximately half of the area of the domain. After the second pairing, the flow begins to approach its saturation state. As the flow evolves, at least up to the second pairing, highly rotational fluid concentrated in the vortex cores gets redistributed into the surrounding nonvortical flow. As such, the vortex thickness (δ) provides a useful measure of tracking the growth of the mixing layer. The nondimensional vortex thickness is defined as

$$\frac{\delta(t)}{\delta_0} = \frac{2U/\delta_0}{[d\langle u\rangle/dy]_{max}}, \tag{2.36}$$

where $\langle\cdot\rangle$ represents an average along the x-direction.

Figure 2.7 shows δ/δ_0 plotted versus nondimensional time, t^* ($\equiv tL/\delta_0$) from the baseline DNS at $Re_{\delta_0} = 200$. The circles mark the four critical times corresponding to (i) formation of the fundamental vortices at $t^* = 14$, (ii) first pairing at $t^* = 40$, (iii) second pairing at $t^* = 60$ and (iv) fully saturated state at $t^* = 180$. As apparent, δ/δ_0 increases to a maximum value at the time of the second pairing, then decreases with oscillations that dampen out to a constant value upon reaching saturation.

The evolution of the temperature field follows in a similar manner to the vorticity. The probability density function (*pdf*) of the temperature is shown in Fig. 2.8 for the baseline case at $Re_{\delta_0} = 200$, $Pr = 0.71$. As apparent, the flow evolves from a completely unmixed state, where the *pdf* exhibits two narrow peaks at $T = 1$ and -1,

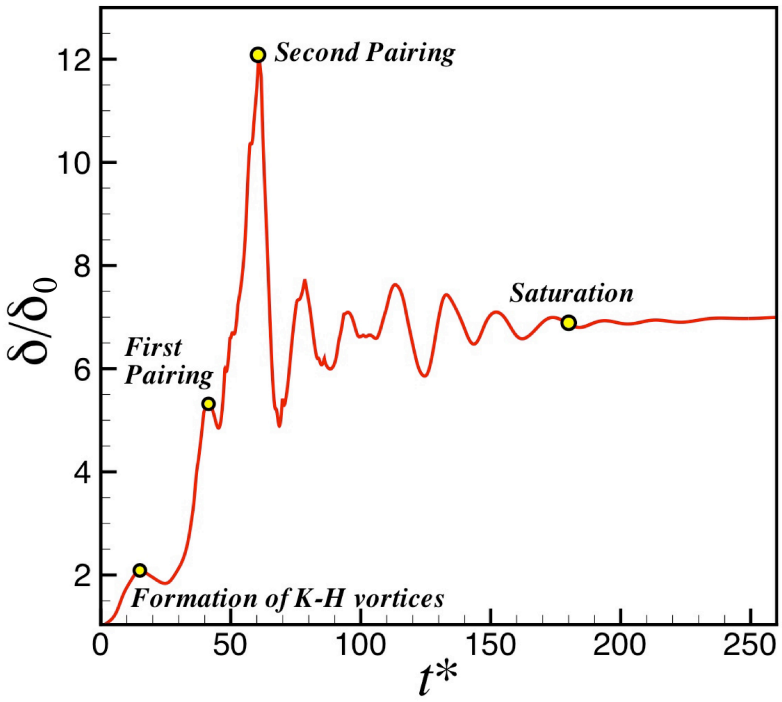

Figure 2.7. Nondimensional vorticity thickness, δ/δ_0, versus time, t^* from the DNS at $Re_{\delta_0} = 200$. The four primary stages of evolution are marked by circles.

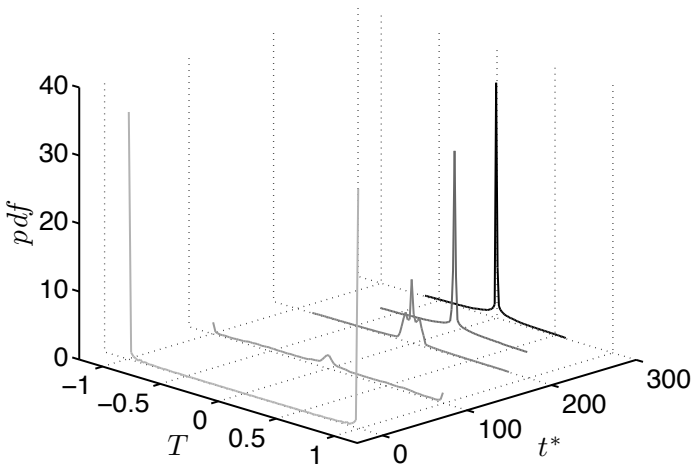

Figure 2.8. Evolution of the probability density function of the temperature field at different time levels from the baseline DNS at $Pr = 0.71$ and $Re_{\delta_0} = 200$.

to a nearly fully mixed state wherein the *pdf* exhibits a single peak at $T = 0$. The value of the *pdf* at $T = 0$ will be used (later) as a measure of the amount of molecular mixing that has transpired in the flow.

2.7.1 Sensitivity of Vorticity to Reynolds Number

As stated in Sec. 2.4.2, the Reynolds number is a critical parameter affecting the growth of the mixing layer. Therefore, three important questions are raised in this work: (a) how sensitive are the coherent vortex structures to changes in Reynolds number, (b) which regions of the coherent vortices are the most/least sensitive to Reynolds number, and (c) which mechanisms are responsible for these Reynolds number effects? Interpretation of the results focuses on addressing these open issues. Fig. 2.9, 2.10, 2.11, and 2.12 show four snapshots in the evolution of the vorticity (ω) and normalized sensitivity of the vorticity to Reynolds number, ($\bar{S}_\omega \equiv Re_{\delta_0} S_\omega$), from the baseline DNS/SEM at $Re_{\delta_0} = 200$ at nondimensional times corresponding to (i) the formation of four fundamental Kelvin-Helmholtz (K-H) vortices at $t^* = 14$, (ii) the first pairing at $t^* = 40$, (iii) the second paring at $t^* = 60$, and (iv) the saturation regime at $t^* = 250$, respectively. Dark regions in the vorticity contour plot at $t^* = 14$ represent areas of high negative vorticity concentrated around the vortex centers. The corresponding sensitivity of the vorticity field to changes in Reynolds number at the time of the formation of the four fundamental vortices is presented in Fig. 2.9. The structures in the sensitivity field appear to follow the same properties described by Lesieur (1997) for the *coherent vorticity* field, i.e., (i) the concentration of S_ω is high enough so that local roll-up of the surrounding S_ω is possible, (ii) these roll-up structures keep their shape approximately during a life time, longer than the local turnover time ω^{-1}, and (iii) the structures are unpredictable. Therefore by analogy, the sensitivity field will be referred to as the *coherent sensitivity* field in this free shear flow.

The coherent sensitivity field at $t^* = 14$ is characterized by roll-up laminae, each consisting of a pattern of dark (high negative S_ω) and light (high positive S_ω) bands that mimics (in size, shape, and location) the K-H vortices. These coherent sensitivity structures exist in a gray background of zero S_ω. This information can be used to predict the vorticity field at higher Reynolds number using a first-order Taylor series

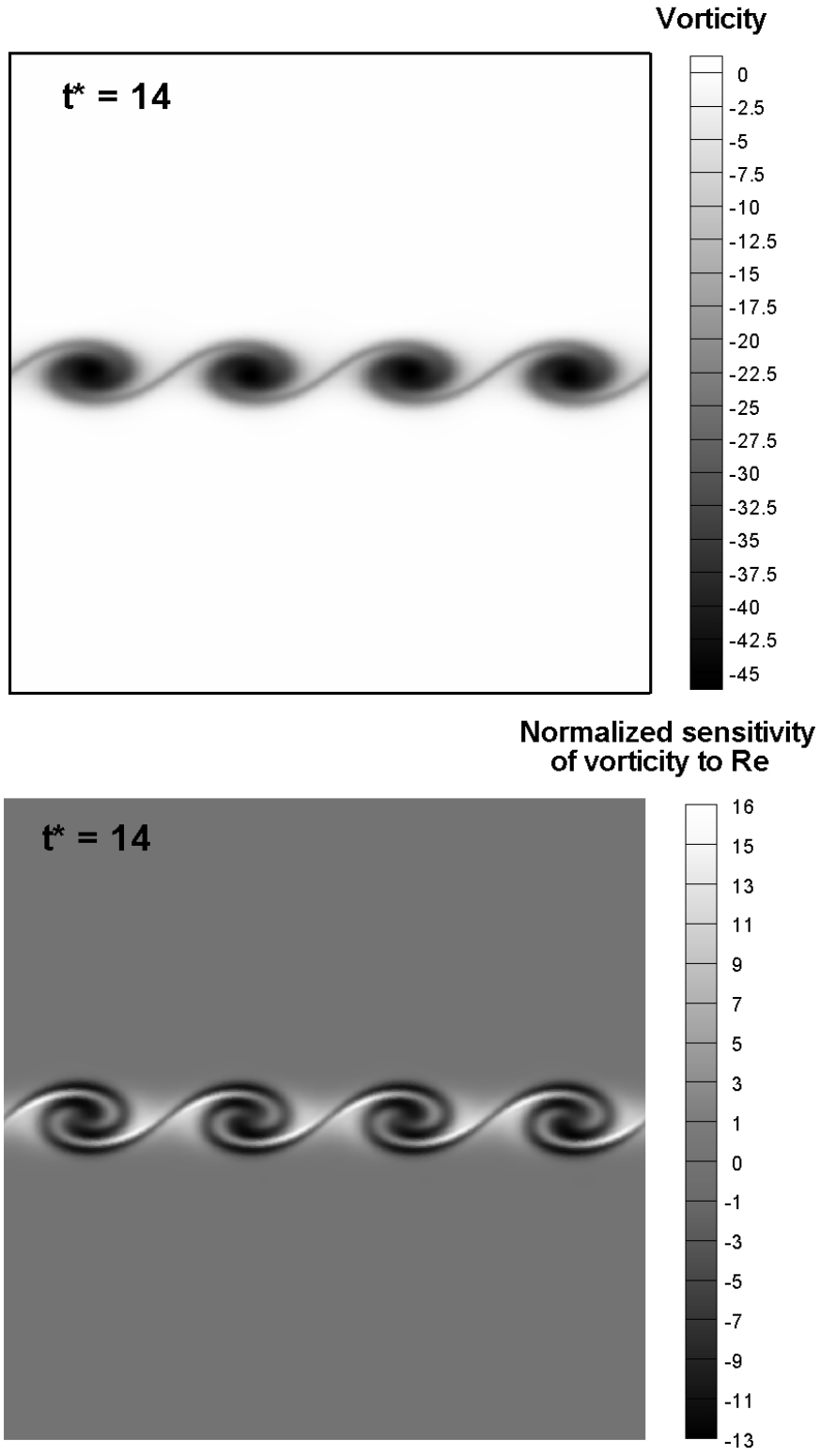

Figure 2.9. Vorticity field, ω, (top) and the normalized sensitivity of the vorticity to Reynolds number, $\bar{S}_\omega$ (bottom) at $Re_{\delta_0} = 200$, corresponding to the formation of fundamental Kelvin-Helmholtz vortices ($t^* = 14$).

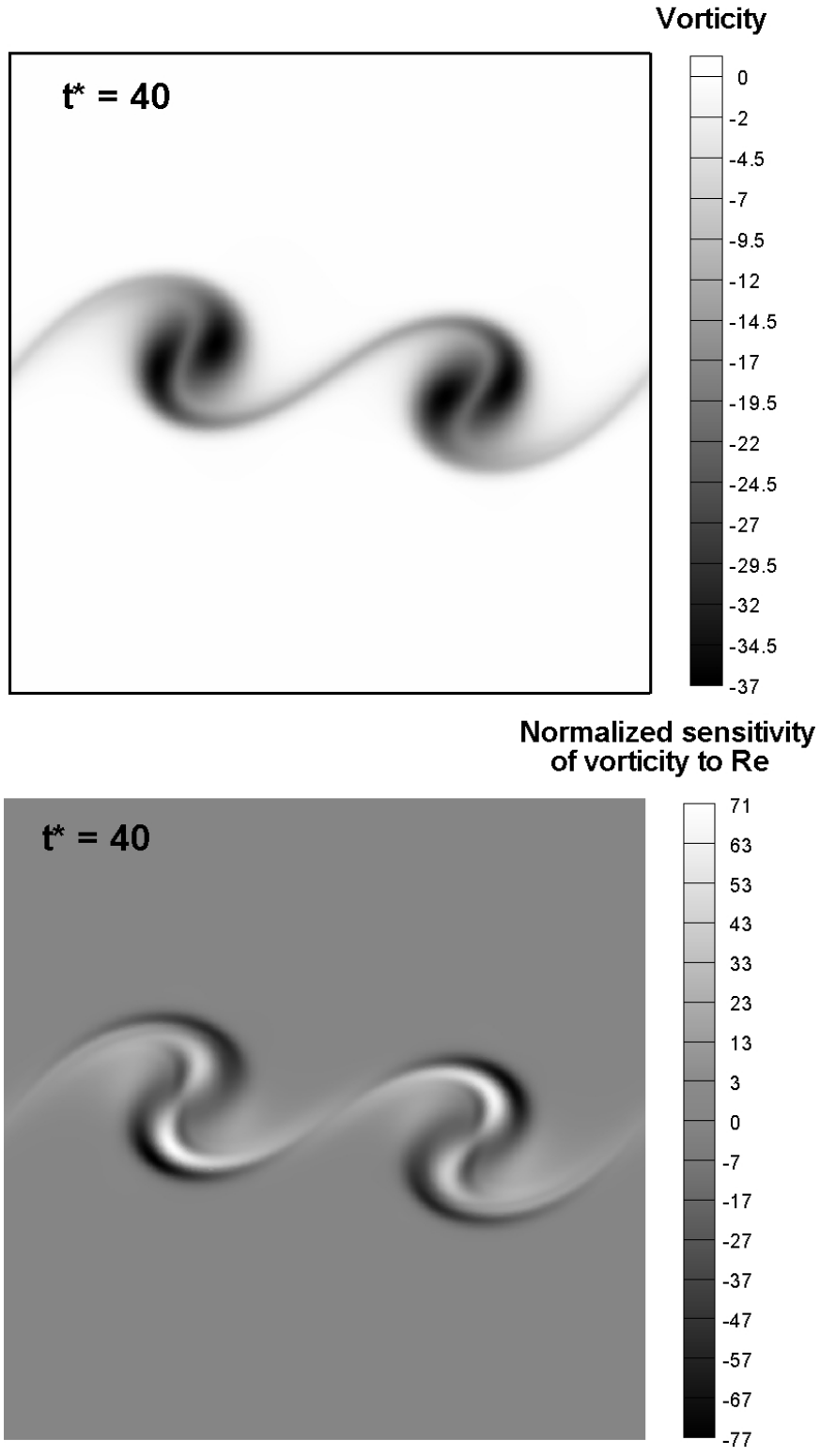

Figure 2.10. Vorticity field, ω, (top) and the normalized sensitivity of the vorticity to Reynolds number, $\bar{S}_\omega$ (bottom) at $Re_{\delta_0} = 200$, corresponding to the first pairing of fundamental Kelvin-Helmholtz vortices ($t^* = 40$).

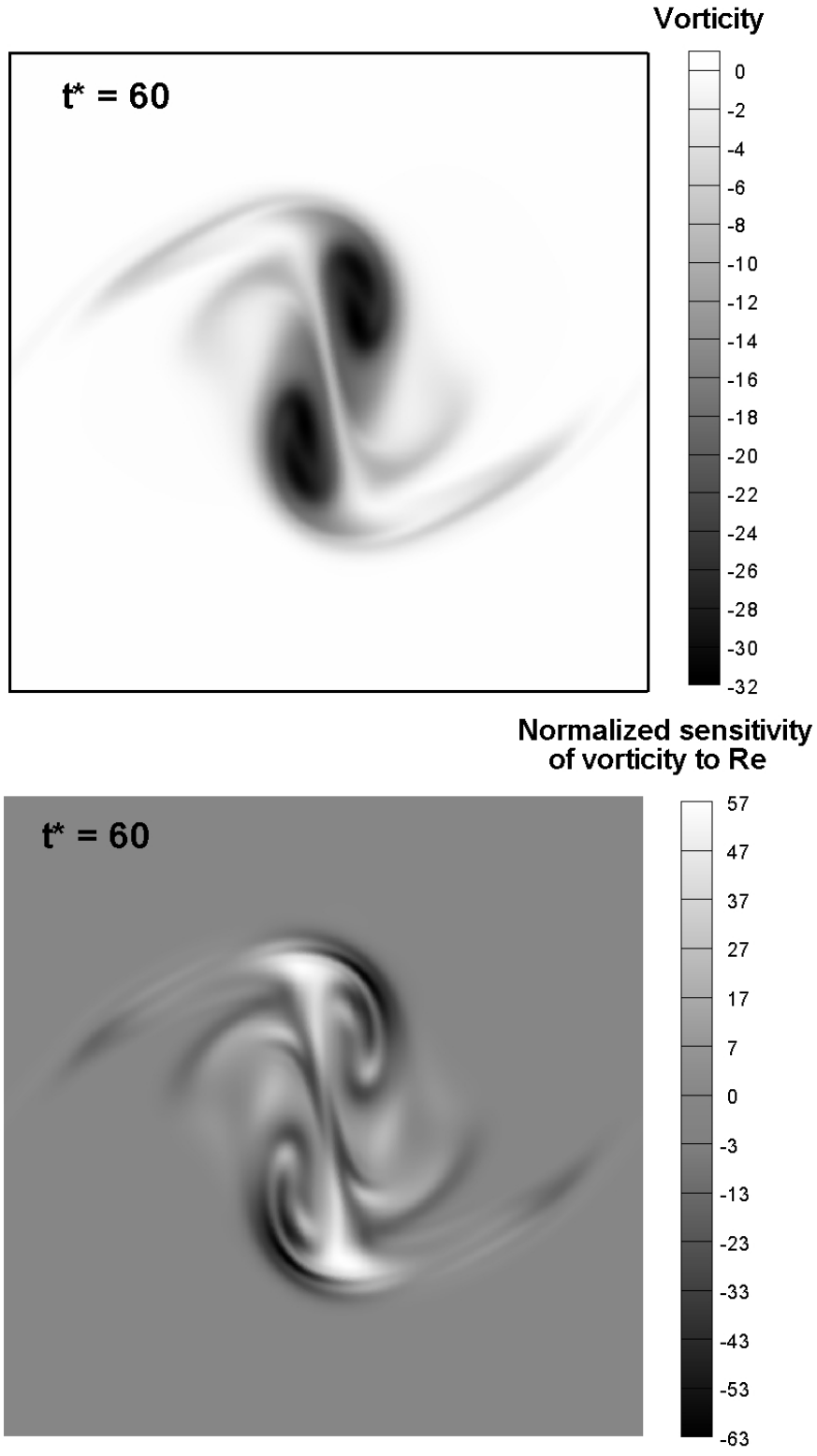

Figure 2.11. Vorticity field, ω, (top) and the normalized sensitivity of the vorticity to Reynolds number, $\tilde{S}_\omega$ (bottom) at $Re_{\delta_0} = 200$, corresponding to the second pairing of fundamental Kelvin-Helmholtz vortices ($t^* = 60$).

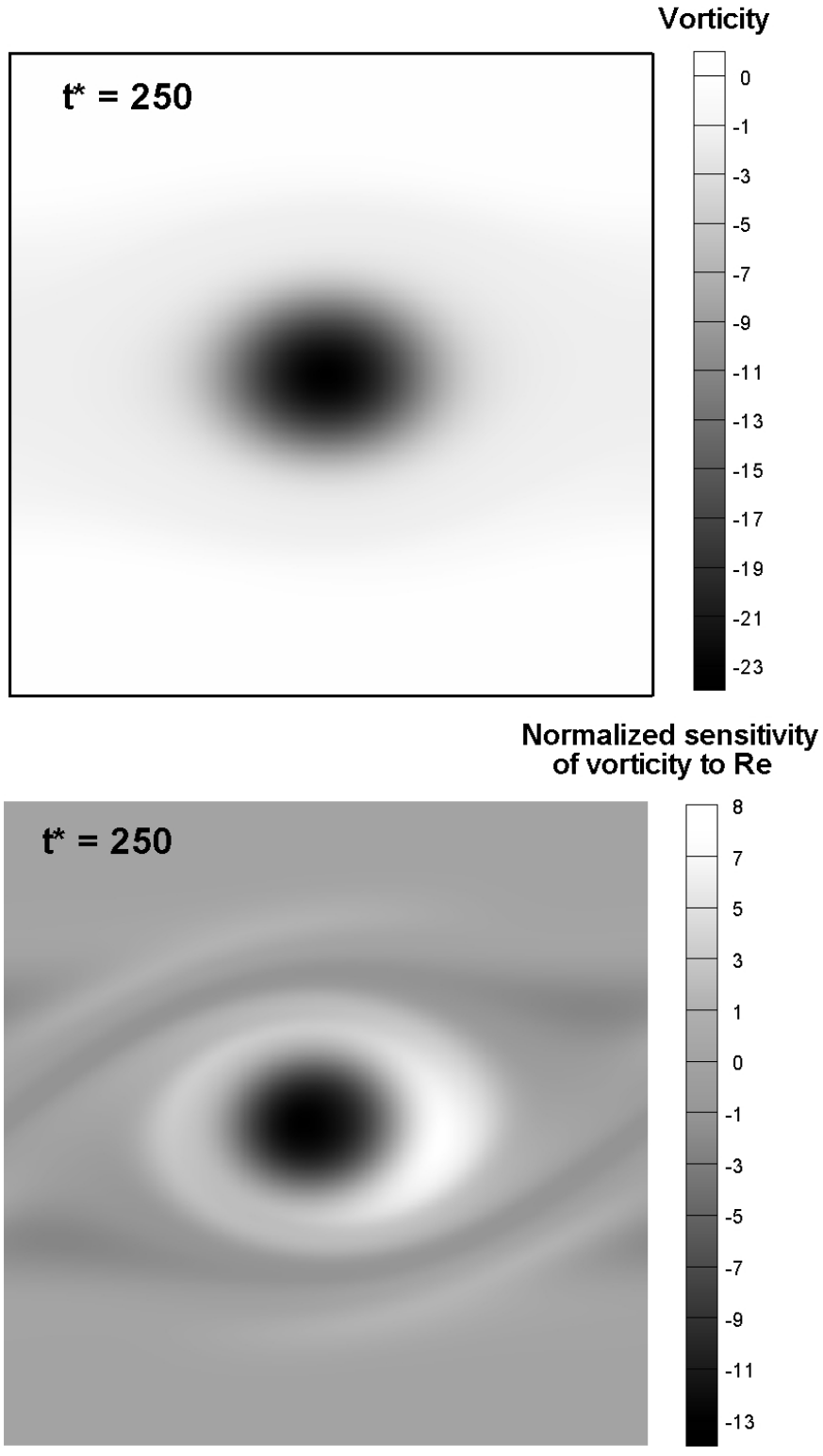

Figure 2.12. Vorticity field, ω, (top) and the normalized sensitivity of the vorticity to Reynolds number, $\bar{S}_\omega$ (bottom) at $Re_{\delta_0} = 200$, corresponding to the saturation state ($t^* = 250$).

$$\omega\Big|_{Re_{\delta_0}^{new}} \approx \omega\Big|_{Re_{\delta_0}} + S_\omega\Big|_{Re_{\delta_0}} \Delta Re_{\delta_0}. \tag{2.37}$$

Since $\omega \leq 0$ everywhere in the domain, amplification of vorticity magnitude at higher Re_{δ_0} can be achieved only in regions corresponding to negative S_ω (i.e., the dark bands of sensitivity). By comparing the contours of S_ω and ω side-by-side at $t^* = 14$, ones notices that the outer-most *dark bands* of the coherent sensitivity structures overlap the edges of the K-H vortices and extend slightly into the neighboring nonvortical regions of the flow. The dark bands of sensitivity continue to roll up inside the K-H vortices resulting in a large region of negative sensitivity in the central core of the K-H vortices. Based on these observations, one expects two outcomes at higher Re_{δ_0}: (i) the vorticity in the core of the K-H vortices will be more negative, and (ii) the periphery of the K-H vortices will expand resulting in growth of the vortex thickness with increasing Reynolds number. The axially symmetric topology of the dark bands of the coherent sensitivity structures implies an axially symmetric growth of the K-H vortices with increasing Reynolds number. The direction of maximum growth (i.e., the maximum gradient of S_ω) appears to coincide with the vertical axis. On the other hand, the *light bands* of high positive sensitivity appear collocated with the thin regions of lower magnitude vorticity that spiral into the K-H vortices due to entrainment. From (2.37), one predicts that these regions of lower magnitude vorticity inside the K-H vortices will tend even further toward zero at higher Reynolds number, which reflects a slight change in the internal structure of the K-H vortices as Re_{δ_0} increases. Note, due to the temporal nature of the flow, these predictions of the Reynolds number trend in ω are only valid for $t^* = 14$.

Figure 2.13 supports the above interpretations of the S_ω field by comparing the vorticity profile from the baseline DNS ($Re_{\delta_0} = 200$) with that from a separate DNS run at slightly higher Reynolds number ($Re_{\delta_0} = 240$). The vorticity profiles are taken through the center of one of the K-H vortices. The vertical dotted line in Fig. 2.13(a) indicates the exact location of the vorticity profiles relative to the corresponding coherent structure in the sensitivity field. The horizontal dashed ($--$) lines mark regions of high *negative* S_ω represented by the dark bands in (a); while, the horizontal dashed-dotted ($-\cdot-$) lines mark regions of high *positive* S_ω represented by the light bands in (a). One observes from the actual vorticity profiles in Fig. 2.13(b) that

$|\omega|$ increases with an increase in Re_{δ_0} in regions corresponding to the dark bands of S_ω; and conversely, $|\omega|$ decreases in regions corresponding to the light bands of S_ω. In order to highlight this, Table 2.1 lists the vorticity difference, $\Delta\omega$, between the two Reynolds number cases for each of the horizontal lines, where $\Delta\omega = \omega\big|^{DNS}_{Re_{\delta_0}=240} - \omega\big|^{DNS}_{Re_{\delta_0}=200}$. Furthermore, Fig. 2.13(b) shows that the outer boundaries of the K-H vortex (as defined by the distance between lines 1 and 6) increases with increasing Reynolds number, in agreement with the predictions from the S_ω contour as described in the previous paragraph.

The normalized sensitivity field at $t^* = 40$, corresponding to the first pairing of the fundamental vortices, is shown in Fig. 2.10. Again, the coherent sensitivity field mimics the same pairing behavior as the vorticity field. The regions of negative sensitivity (dark bands) along the periphery of the coherent sensitivity structure coupled with the lighter bands (of positive sensitivity) lining the inside of the structure form a *two-blade* pattern. The dark band along the outer edge of the two-blade pattern spans across the border of the coherent vortex, so that part of the dark sensitivity band lies in the high negative vorticity region of the vortex, while the outer portion of the two-blade pattern extends into the non-vortical region of the flow around the periphery of the vortex. This configuration of the sensitivity field predicts an increase in the growth of the mixing layer thickness at higher Reynolds number, similar to the interpretations of the sensitivity field at $t^* = 14$. In the first pairing, however, the magnitude of the normalized sensitivity has increased dramatically (about seven times that at $t^* = 14$). In addition, the direction of the maximum gradient of S_ω is no longer parallel to the vertical axis, but is rotated clockwise by approximately 45° with respect to the center of the two-blade structure.

The second pairing of the vortices and related sensitivity field at $t^* = 60$ are shown in Fig. 2.11. Again, regions of high negative sensitivity (dark bands) appear along the periphery of the coherent sensitivity structure, which resembles a larger version of the *two-blade* sensitivity pattern observed at $t^* = 40$. The small scale features apparent inside the heart of the larger two-blade structure result from the residual effect of the smaller two-blade sensitivity structures that formed in the first pairing. This highlights the coherency of the sensitivity field in the mixing layer. One can also observe that at this snapshot, the dark bands in S_ω are starting to vanish

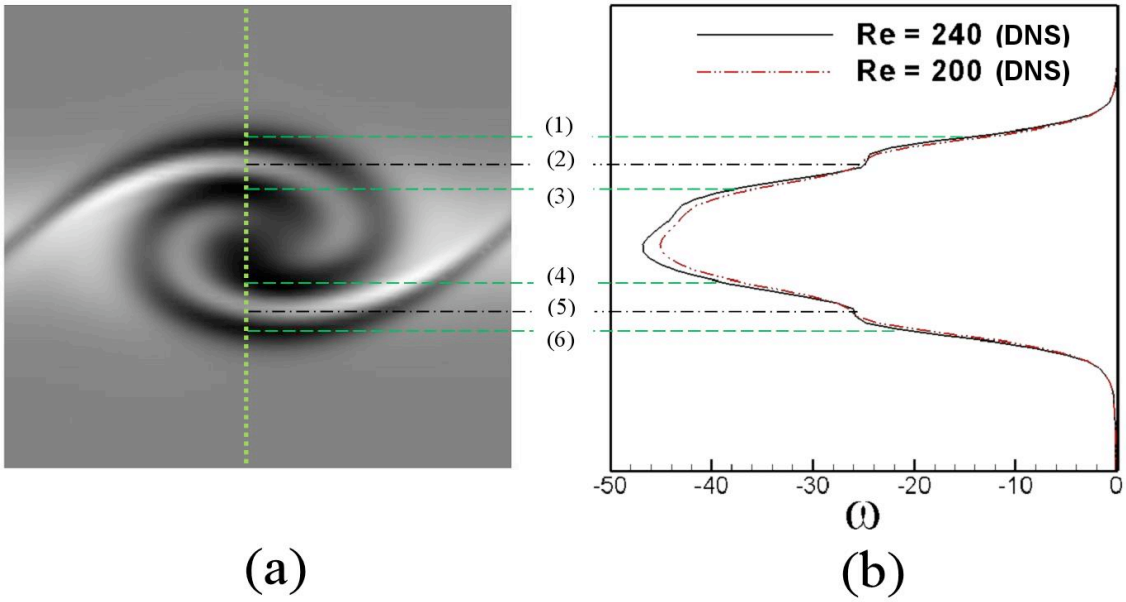

Figure 2.13. Interpretation of the light and dark bands in the coherent structure of S_ω at $t^* = 14$. (a) Enlarged region of one of the coherent sensitivity structures at $Re_{\delta_0} = 200$. (b) Vorticity profiles along the vertical dotted line in (a) from two different DNS simulations at $Re_{\delta_0} = 240$ and $Re_{\delta_0} = 200$. The horizontal dashed lines $(--)$ mark regions of *negative* S_ω (dark bands), while horizontal dashed-dotted lines $(- \cdot -)$ indicate regions of *positive* S_ω (light bands).

Table 2.1. Vorticity difference (between the DNS at $Re_{\delta_0} = 240$ and 200) at the same vertical locations numbered in figure 2.13.

line #:	(1)	(2)	(3)	(4)	(5)	(6)
$\Delta\omega$:	-1.83	0.53	-1.96	-1.97	0.47	-1.77

along the top and bottom rim of the larger two-blade structure. This implies that the vortex thickness will not change significantly with increasing Reynolds number at this normalized time. The reason for the halt in vortex thickness growth (with Reynolds number) stems from the fact that at the time of the second pairing, the coherent vortex has reached its maximum size in the computational domain. This will occur independent of Reynolds number because of the artificially imposed top/bottom boundary conditions, which serve to confine the subsequent evolution of the mixing layer beyond the second pairing.

Finally, the fully saturated fields of the vorticity and related sensitivity at $t^* = 250$ are presented in Fig. 2.12. At this snapshot, the sensitivity pattern can be described as a central dark region (of high negative sensitivity) encircled by a light ring (of high positive sensitivity). The dark region of sensitivity lies entirely within the boundaries of the saturated vortex (in the vorticity field). Based on (2.37), then, one predicts enhanced negative vorticity in the core of the saturated vortex at higher Reynolds number. Simultaneously, the light ring of positive sensitivity overlies the outer edge of the saturated vortex and extends into the neighboring areas having very low vorticity magnitude. This configuration indicates a reduction of vorticity magnitude around the periphery of the saturated vortex. Therefore, one would predict that at higher Reynolds number the saturated vortex will become smaller, with a higher concentration of vorticity magnitude in the core region.

2.7.2 Sensitivity of Temperature to Prandtl Number

The evolution of the passive temperature field and normalized sensitivity with respect to Prandtl number ($\bar{S}_{T,Pr} \equiv Pr\ S_{T,Pr}$) from the baseline DNS/SEM at $Re_{\delta_0} = 200$, $Pr = 0.71$ is shown in Fig. 2.14, 2.15, 2.16, and 2.17 at the same time levels as in Fig. 2.9 through 2.12 for the vorticity. Coherent structures are clearly evident in both the temperature and sensitivity fields. The evolution of the temperature field agrees well with previous work; see, for example, Lesieur et al. (1988). It should be noted that the temperature field has both positive and negative values, unlike the vorticity field which is negative throughout the entire domain for all times. Again, the sensitivity of temperature to Prandtl number (given a fixed Reynolds number) may be interpreted using the following first-order Taylor series approximation

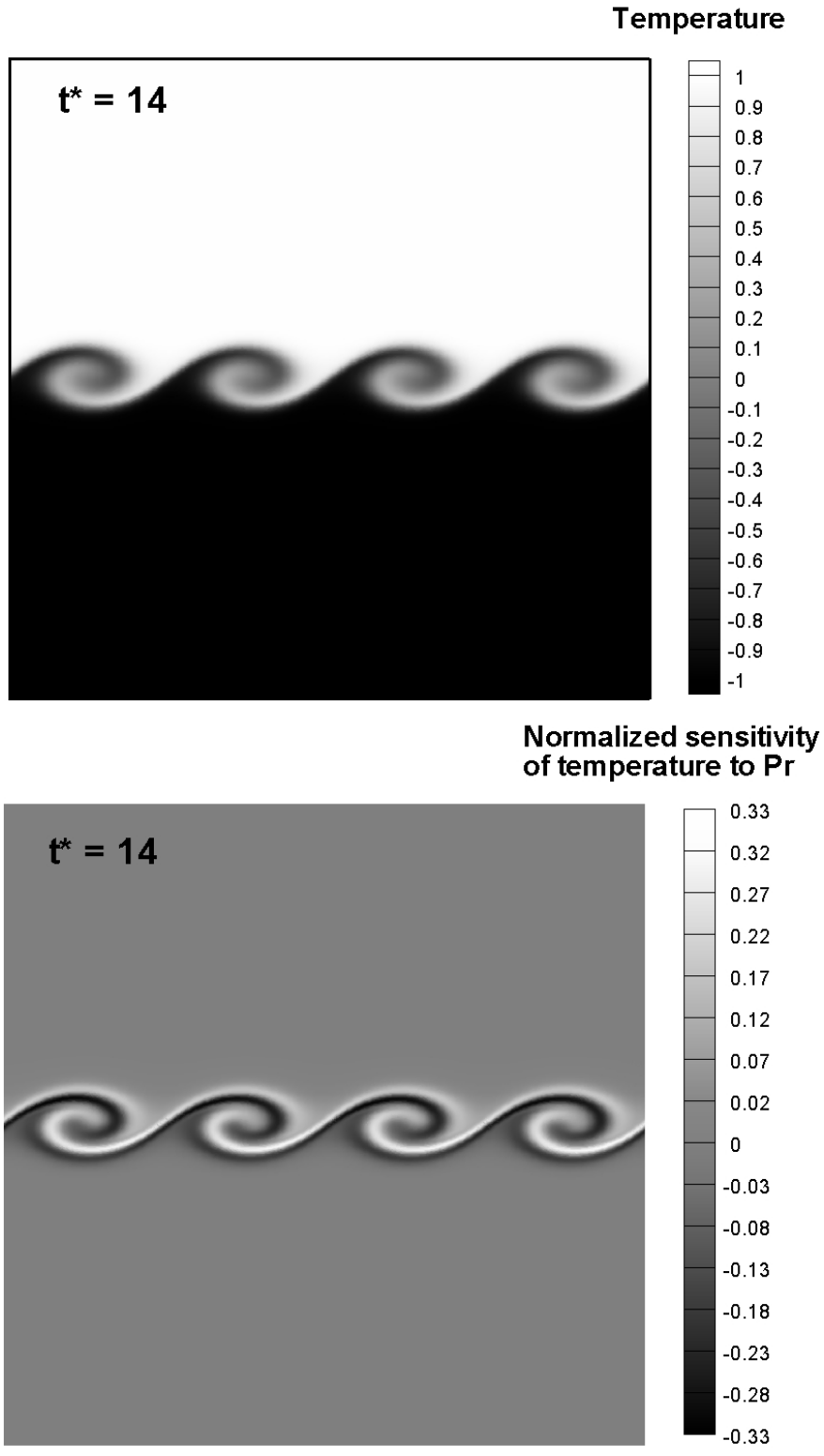

Figure 2.14. Temperature field, T, (top) and normalized sensitivity of the temperature to Prandtl number, $\bar{S}_{T,Pr}$, (bottom) at $Re_{\delta_0} = 200$, $Pr = 0.71$, corresponding to the formation of fundamental Kelvin-Helmholtz vortices ($t^* = 14$).

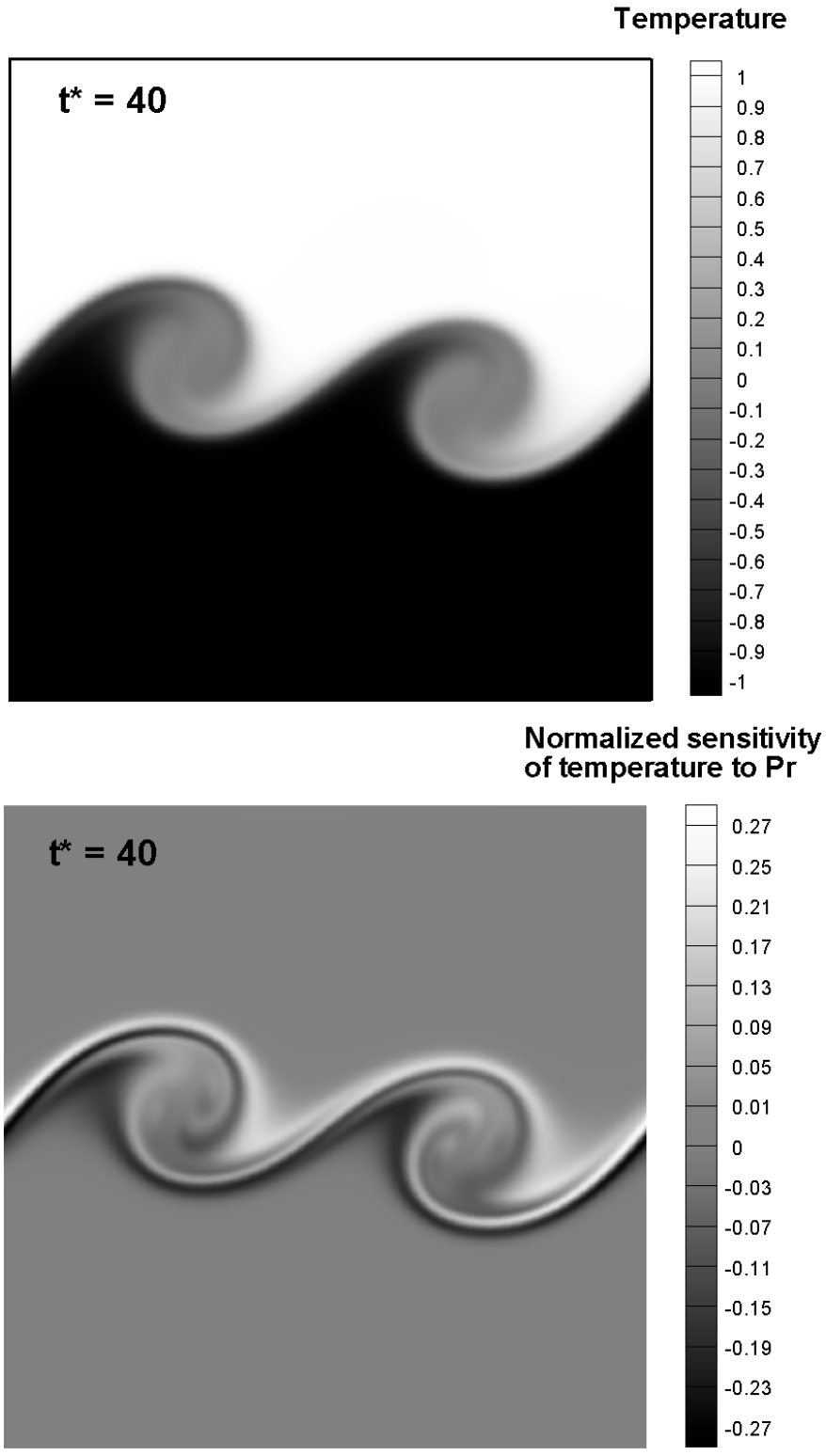

Figure 2.15. Temperature field, T, (top) and normalized sensitivity of the temperature to Prandtl number, $\bar{S}_{T,Pr}$, (bottom) at $Re_{\delta_0} = 200$, $Pr = 0.71$, corresponding to the first pairing of fundamental Kelvin-Helmholtz vortices ($t^* = 40$).

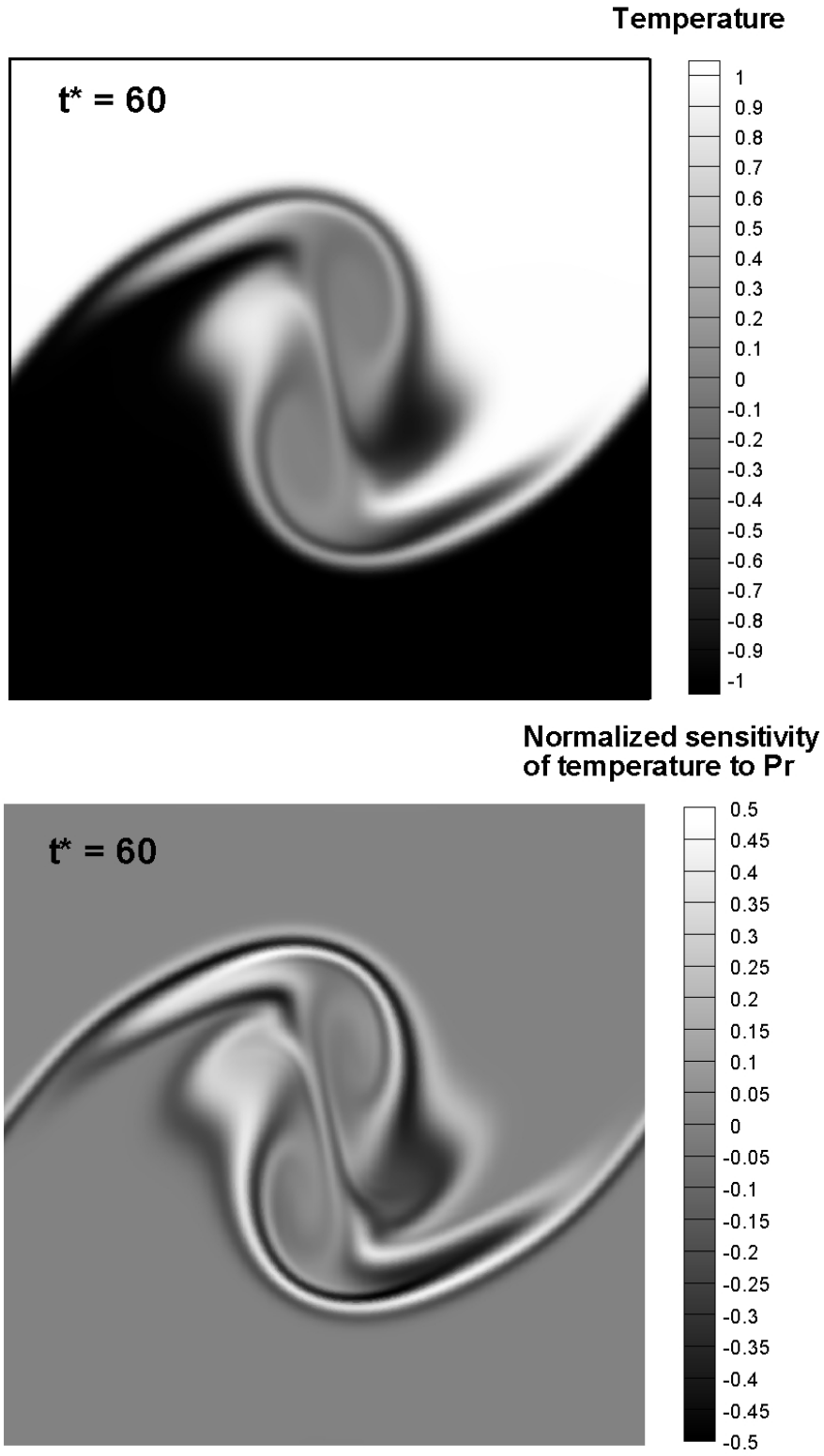

Figure 2.16. Temperature field, T, (top) and normalized sensitivity of the temperature to Prandtl number, $\bar{S}_{T,Pr}$, (bottom) at $Re_{\delta_0} = 200$, $Pr = 0.71$, corresponding to the second pairing of fundamental Kelvin-Helmholtz vortices ($t^* = 60$).

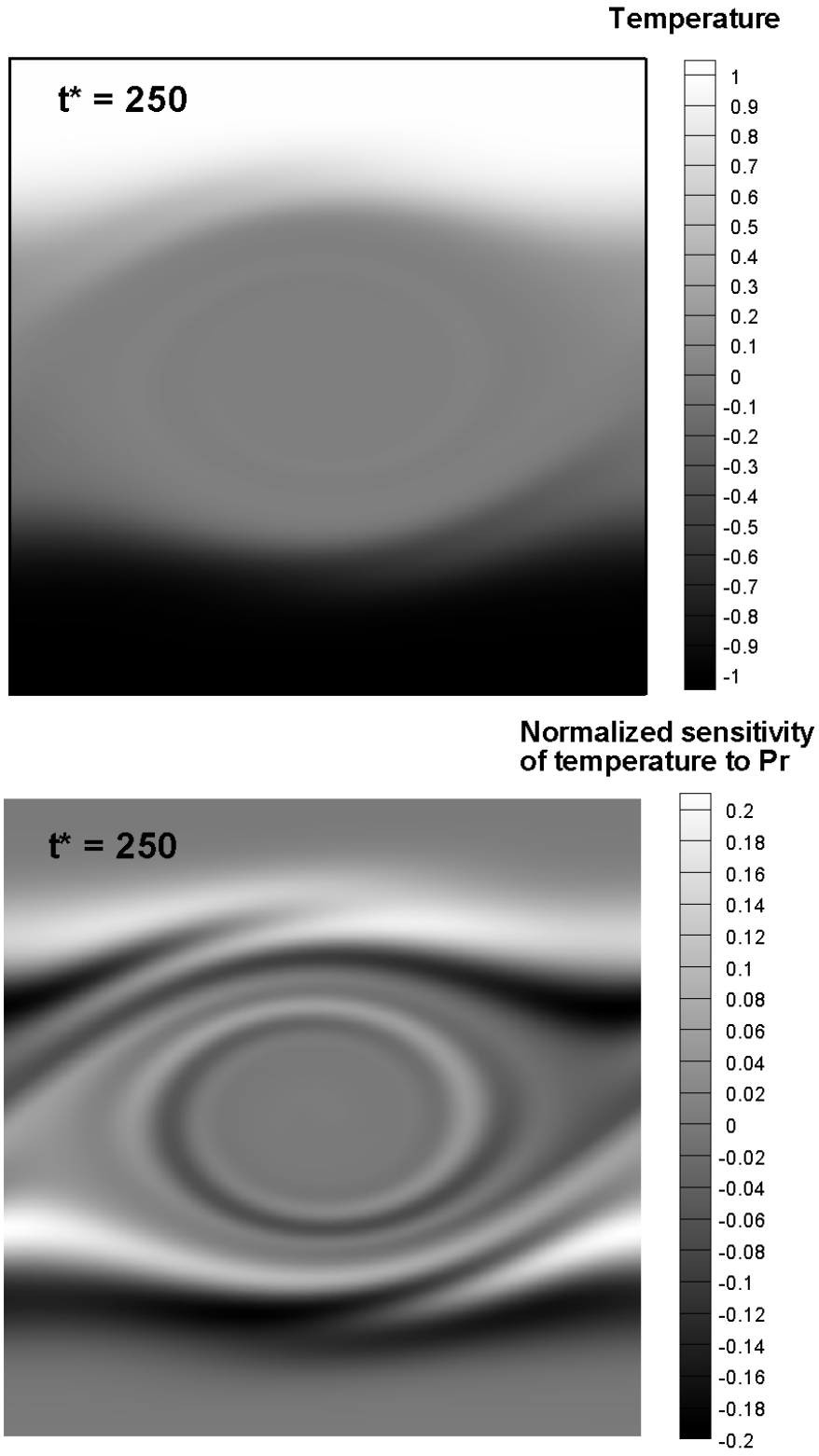

Figure 2.17. Temperature field, T, (top) and normalized sensitivity of the temperature to Prandtl number, $\bar{S}_{T,Pr}$, (bottom) at $Re_{\delta_0} = 200$, $Pr = 0.71$, corresponding to the saturation state ($t^* = 250$).

$$T\Big|_{Pr^{new}} \approx T\Big|_{Pr} + S_T\Big|_{Pr} \Delta Pr. \tag{2.38}$$

For time levels $0 \leq t^* \leq 60$ (up to the second pairing), the sensitivity pattern around the periphery of the coherent temperature structures is such that light (positive) bands of $\bar{S}_{T,Pr}$ correspond to regions of positive temperature, while dark (negative) bands of $\bar{S}_{T,Pr}$ correspond to regions of negative temperature. Based on these observations along with (2.38), the temperature at higher Pr is predicted to increase in regions of positive sensitivity, and decrease in regions of negative sensitivity. Because the light/dark (positive/negative) bands of sensitivity appear adjacent to each other, one can further predict an enhanced temperature gradient with increasing Pr along the interface between the light/dark bands of sensitivity, which primarily coincide with the outer edge of the coherent temperature structures.

This prediction is confirmed in Fig. 2.18 by examining the temperature difference, ΔT, calculated at $t^* = 14$ from two different DNS run at $Pr = 1.0$ and $Pr = 0.71$ with a fixed Reynolds number of $Re_{\delta_0} = 200$. The vertical dashed line in Fig. 2.18(a) indicates the location of the temperature difference profile relative to the coherent sensitivity structure. Similar to Fig. 2.13, the horizontal dashed $(--)$ lines mark regions of negative sensitivity, while the horizontal dashed-dotted $(- \cdot -)$ lines mark regions of positive sensitivity. As evident in Fig. 2.18(b), the value of the temperature at $Pr = 1.0$ increases by about 5–10% compared to that at $Pr = 0.71$ in the regions corresponding to the light bands of sensitivity. Conversely, the temperature decreases negatively by 5–10% in the regions corresponding to the dark bands of sensitivity. The ΔT data reveal an overall increase in the gradient of the temperature field at higher Prandtl number, especially around the periphery of the coherent temperature structure, consistent with the interpretations of the sensitivity contours from the DNS/SEM simulation at $Pr = 0.71$.

Inside the core of the coherent temperature structures, the value of T is observed to be very close to zero indicative of the effect of molecular mixing there. As t^* increases, the coherent temperature structures enlarge; and, the well-mixed core region (having zero temperature) grows accordingly. Hence, the probability of the occurrence of $T = 0$ in the domain increases with t^*. Consequently, by examining $S_{T,Pr}$ inside of the core of the coherent temperature structures, one can predict how perturbations in Pr affect the mixing quality of the flow. Specifically, the present $S_{T,Pr}$ data reveal

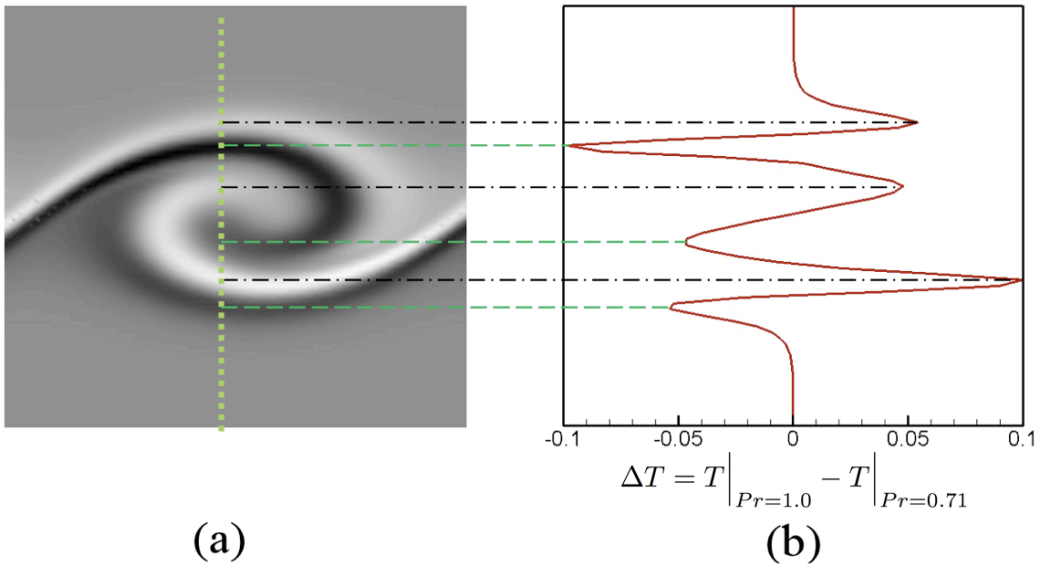

Figure 2.18. Interpretation of the light and dark bands in the coherent structure of $\bar{S}_{T,Pr}$ at $t^* = 14$. (a) Enlarged region of one of the coherent sensitivity structures at $Re_{\delta_0} = 200$, $Pr = 0.71$. (b) The difference in the temperature along the vertical dotted line in (a) from two different DNS at $Pr = 1.0$ and $Pr = 0.71$. The horizontal dashed lines $(--)$ mark regions of *negative* $\bar{S}_{T,Pr}$ (dark bands), while horizontal dashed-dotted lines $(- \cdot -)$ indicate regions of *positive* $\bar{S}_{T,Pr}$ (light bands).

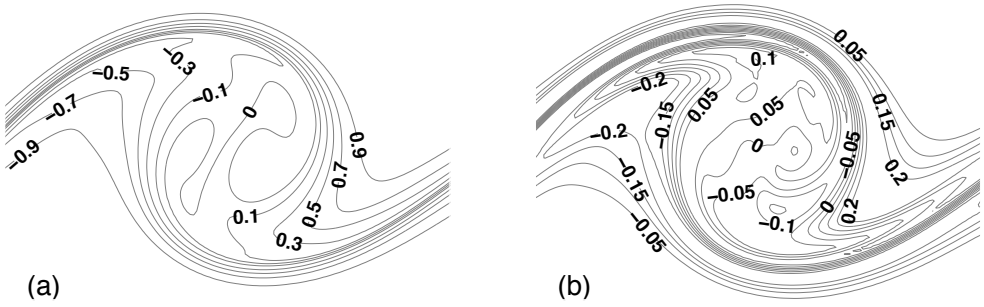

Figure 2.19. Contour lines of (a) temperature and (b) normalized sensitivity $\bar{S}_{T,Pr}$ for one of the vortices in the first pairing at $t^* = 40$.

that as Pr increases, the temperature *inside* the core of the coherent temperature structures will diverge from zero. Figure 2.19 highlights this by showing the contour lines of temperature and sensitivity for one of the coherent structures in the first pairing at $t^* = 40$. One can observe a homogenous temperature field with a value of $T = 0$ inside the core of the structure. In this same region, the contour lines of $S_{T,Pr}$ are nonzero, and vary between 0.05 and -0.05, with positive values in the upper core and negative values in the lower core. Combining these sensitivity results with the

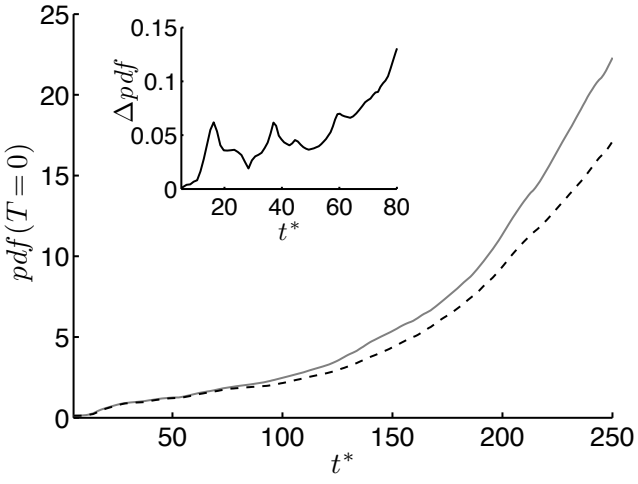

Figure 2.20. The value of the probability density function at $T = 0.0$ versus time, t^*, from two different simulations: — DNS at $Re_{\delta_0} = 200$, $Pr = 0.71$ and $--$DNS at $Re_{\delta_0} = 200$, $Pr = 1.0$. The inset highlights the difference between the two *pdf*s for $t^* \leq 80$, where Δpdf equals $pdf(T = 0)$ at $Pr = 0.71$ minus $pdf(T = 0)$ at $Pr = 1.0$.

Taylor series approximation in (2.38) leads to the prediction that at higher Pr the temperature field inside the core region will become nonhomogeneous. Therefore, the probability of occurrence of $T = 0$ will decrease at higher Prandtl number, translating into less efficient mixing.

This prediction based on an interpretation of the sensitivity field is supported in Fig. 2.20, which shows a plot of the *pdf* at $T = 0$ versus time t^* for two different DNS run at $Pr = 1.0$ and $Pr = 0.71$. The values of the *pdf* at $T = 0$ for the case of $Pr = 1.0$ are consistently lower than those at $Pr = 0.71$ for all t^*. Although, the difference remains small for $t^* < 60$ (up to the second pairing), because the ratio of the well-mixed area (having $T = 0$) over the total area of the domain grows significantly in time after the second pairing. For example, at $t^* = 250$ (in the saturation state), the region wherein $T = 0$ occupies almost one-third of the entire domain. The observed reduction in molecular mixing at $Pr = 1.0$ compared to that at $Pr = 0.71$ also agrees with the expected behavior based on an inspection of the nondimensional governing equation for temperature (2.10). Since the order of magnitude of the diffusion term scales like Pr^{-1}, it is expected that molecular mixing due to diffusion will decrease as Pr increases.

2.7.3 Sensitivity of Temperature to Reynolds Number

The evolution of the passive temperature field and corresponding normalized sensitivity of the temperature to the Reynolds number ($\bar{S}_{T,Re_{\delta_0}} \equiv S_{T,Re_{\delta_0}} Re_{\delta_0}$) is shown in Fig. 2.21, 2.22, 2.23, and 2.24 at the same time levels as in Fig. 2.9 through 2.12 for the vorticity. Note, the temperature fields in the top of Fig. 2.21 through 2.24 are identical to those shown in Fig. 2.14 through 2.17, and are duplicated here to allow direct comparison with $\bar{S}_{T,Re_{\delta_0}}$. Again, the sensitivity at a fixed Prandtl number may be used to predict the behavior at higher Re_{δ_0} using the following approximation

$$T\Big|_{Re_{\delta_0}^{new}} \approx T\Big|_{Re_{\delta_0}} + S_T\Big|_{Re_{\delta_0}} \Delta Re_{\delta_0}. \tag{2.39}$$

The normalized sensitivity of temperature to Re_{δ_0} at $t^* = 14$ is shown in the first row of Fig. 2.21. If the sensitivity and temperature fields are overlaid, one observes that the dark band of negative sensitivity along the top periphery of the coherent temperature structure extends into the positive temperature field in the upper half of the domain. Based on (2.39), it is expected that at higher Re_{δ_0}, the temperature along the top of the coherent structure will decrease, i.e., the region of negative temperature penetrates further into the upper domain causing growth of the coherent structure in the temperature field with increasing Reynolds number. A similar situation occurs in the lower half of the domain, where the white band of positive sensitivity along the bottom of the coherent temperature structure extends into the negative temperature field in the lower half of the domain, again indicating growth of the coherent temperature structure at higher Reynolds number. This is consistent with the interpretation of the sensitivity of the vorticity field to Reynolds number. Since the mixing layer thickness grows with Reynolds number, it is expected that the coherent structures in the passive temperature field will grow in a similar manner (Lesieur et al., 1988).

The above interpretation of $\bar{S}_{T,Re_{\delta_0}}$ is supported by the data in Fig. 2.25, which shows the vertical temperature profile at $t^* = 14$ from two DNS run at two different Reynolds numbers ($Re_{\delta_0} = 200$ and 240). The temperature profile at $Re_{\delta_0} = 240$ is broader than that at $Re_{\delta_0} = 200$, revealing an enlarged coherent temperature structure at higher Reynolds number. The sensitivity contours around the periphery of the coherent temperature structure corresponding to the first and second pairing

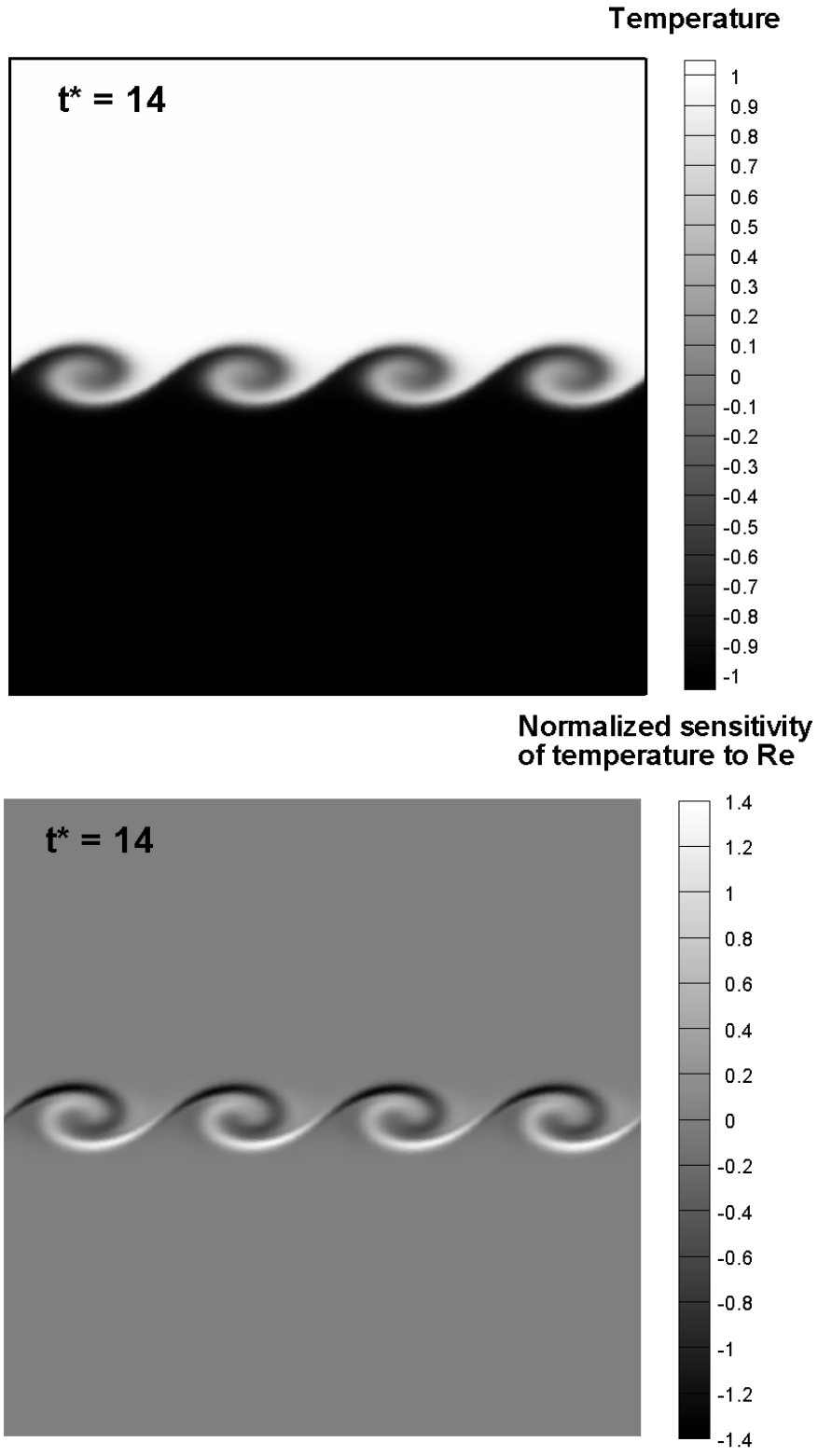

Figure 2.21. Temperature field, T, (top) and sensitivity of the temperature to Reynolds number, $\bar{S}_{T,Re_{\delta_0}}$, (bottom) at $Re_{\delta_0} = 200$, $Pr = 0.71$ corresponding to the formation of fundamental Kelvin-Helmholtz vortices ($t^* = 14$).

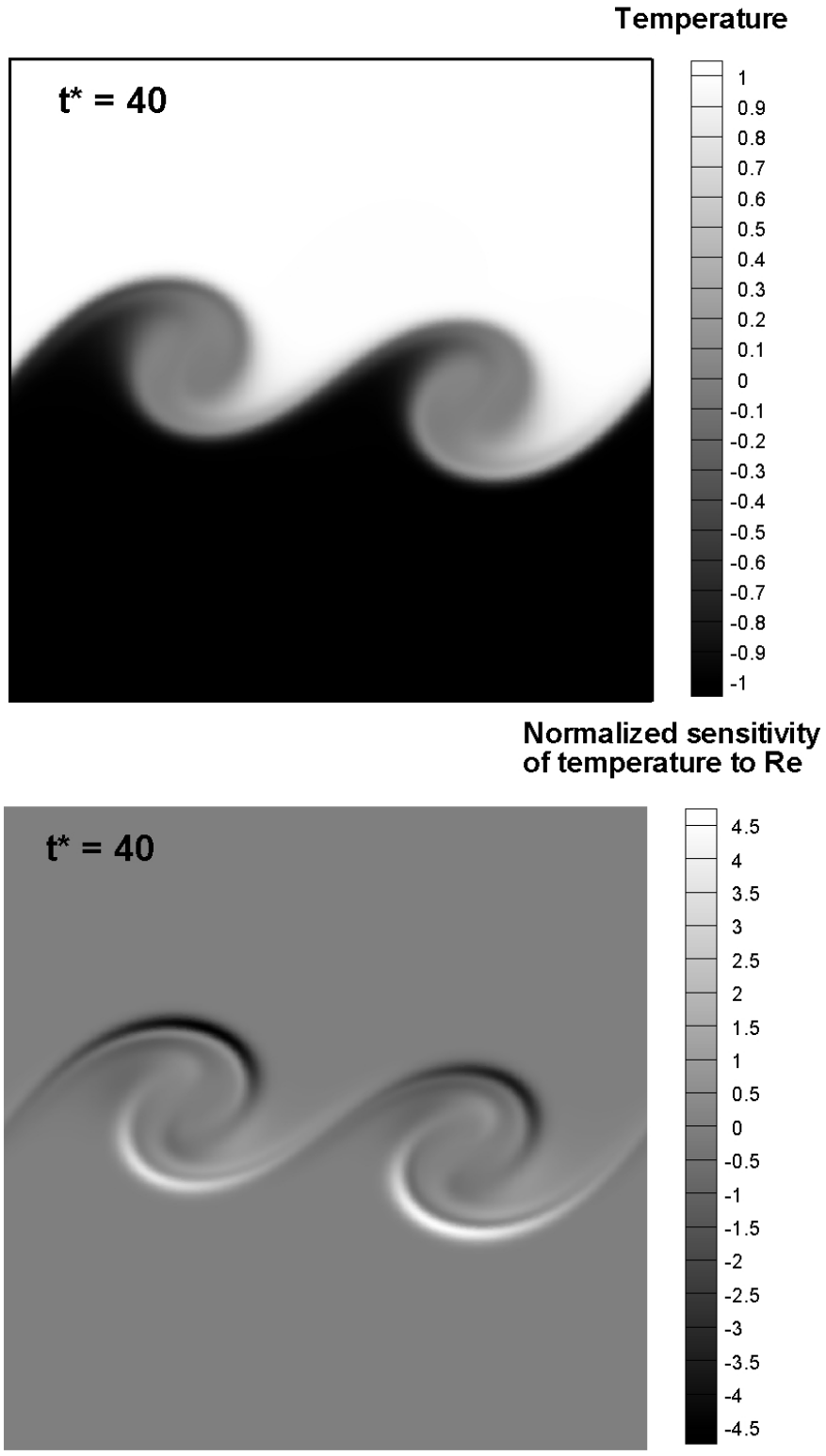

Figure 2.22. Temperature field, T, (top) and sensitivity of the temperature to Reynolds number, $\bar{S}_{T,Re_{\delta_0}}$, (bottom) at $Re_{\delta_0} = 200$, $Pr = 0.71$ corresponding to the first pairing of fundamental Kelvin-Helmholtz vortices ($t^* = 40$).

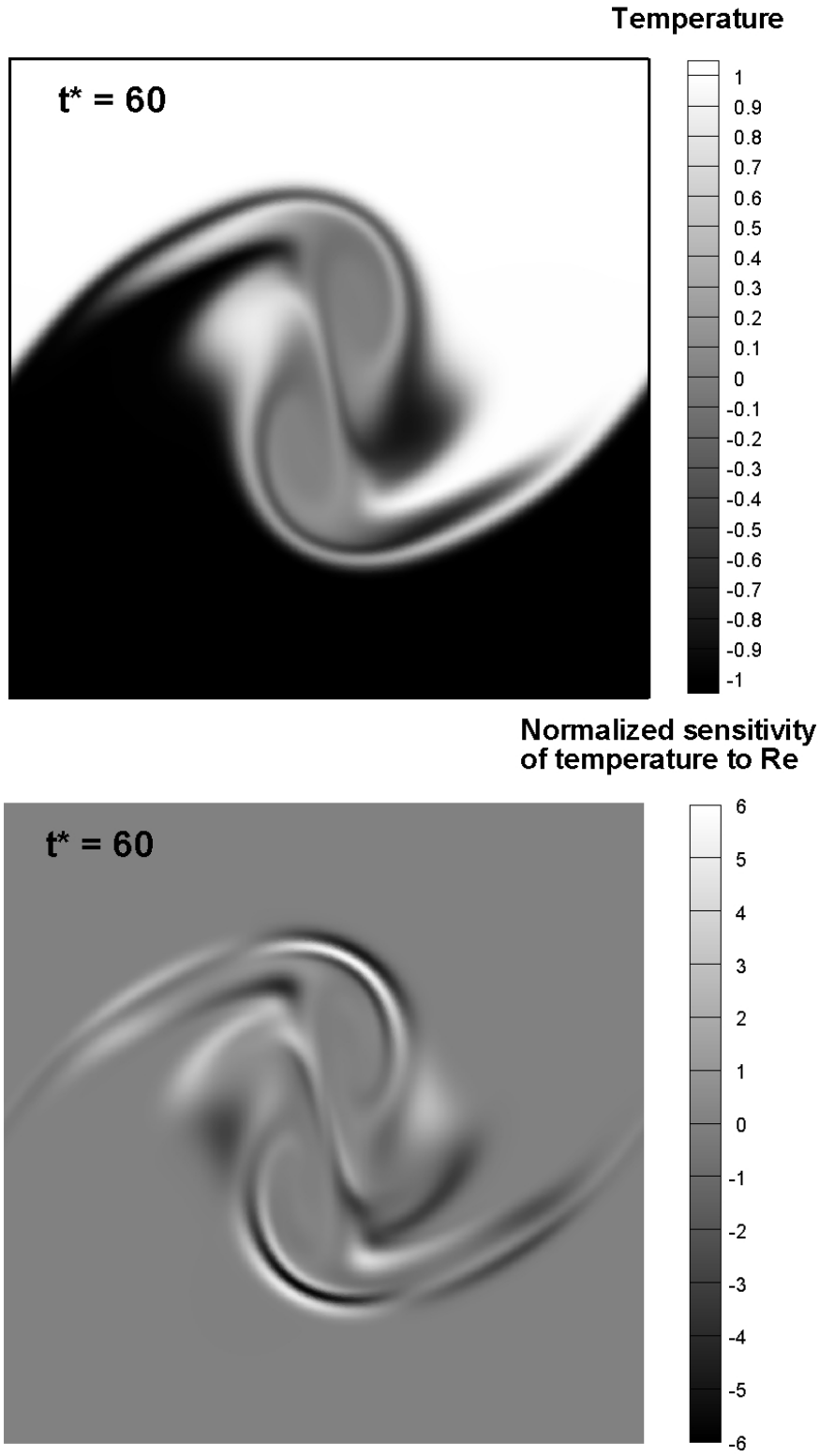

Figure 2.23. Temperature field, T, (top) and sensitivity of the temperature to Reynolds number, $\bar{S}_{T,Re_{\delta_0}}$, (bottom) at $Re_{\delta_0} = 200$, $Pr = 0.71$ corresponding to the second pairing of fundamental Kelvin-Helmholtz vortices ($t^* = 60$).

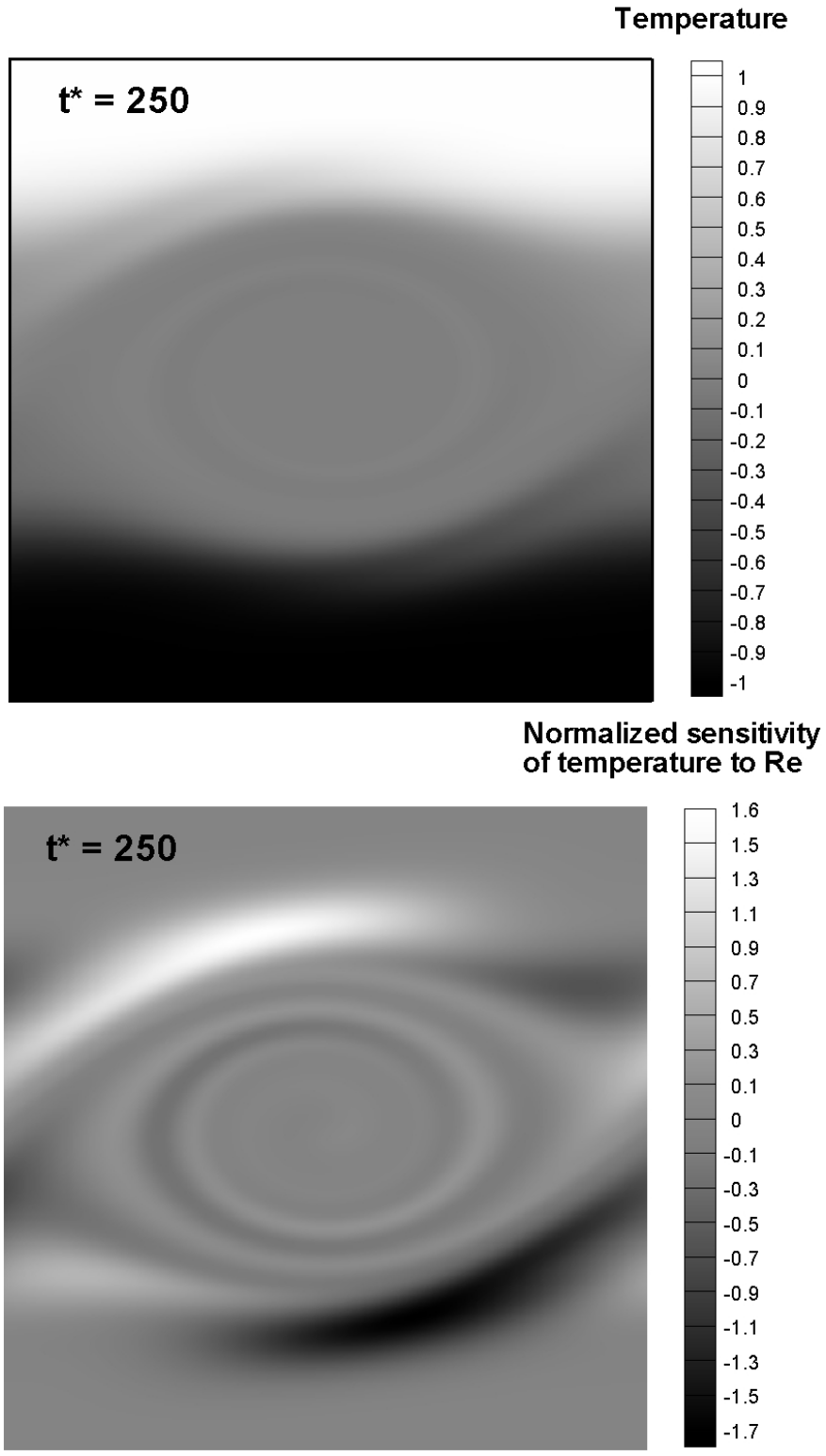

Figure 2.24. Temperature field, T, (top) and sensitivity of the temperature to Reynolds number, $\bar{S}_{T,Re_{\delta_0}}$, (bottom) at $Re_{\delta_0} = 200$, $Pr = 0.71$ corresponding to the saturation state ($t^* = 250$).

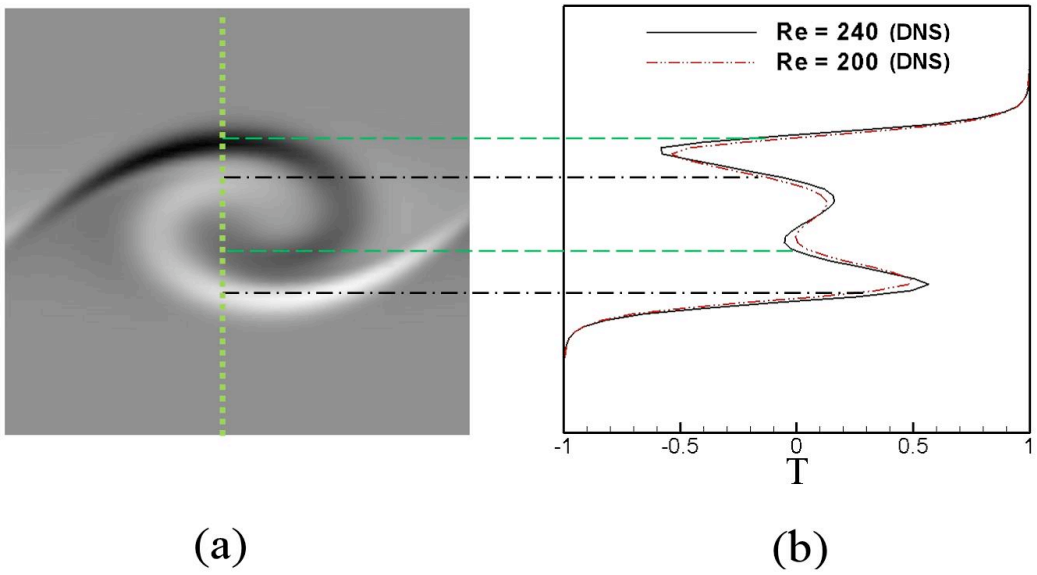

Figure 2.25. Interpretation of the light and dark bands in the coherent structure of $\bar{S}_{T,Re_{\delta_0}}$ at $t^* = 14$. (a) enlarged region of one of the coherent sensitivity structures at $Re_{\delta_0} = 200$, $Pr = 0.71$. (b) the vertical profile of temperature along the dotted line in (a) from two different DNS simulations at $Re_{\delta_0} = 240$ and $Re_{\delta_0} = 200$. The horizontal dashed lines $(--)$ mark regions of *negative* $\bar{S}_{T,Re_{\delta_0}}$ (dark bands), while horizontal dashed-dotted lines $(- \cdot -)$ indicate regions of *positive* $\bar{S}_{T,Re_{\delta_0}}$ (light bands).

(at $t^* = 40$ and 60) in Fig. 2.22 and 2.23, respectively, follow a similar pattern as that seen in the formation stage at $t^* = 14$.

Inside the core region where $T = 0$, the corresponding sensitivity is very close to zero for $t^* \leq 60$, unlike the situation observed for $S_{T,Pr}$. Therefore, the molecular mixing characteristics of the temperature field up to the second pairing are not expected to change with an increase in Reynolds number. Figure 2.26 confirms this by showing the value of the *pdf* at $T = 0$ as a function of t^* for two DNS runs at two different Reynolds numbers ($Re_{\delta_0} = 200$ and 240). For $t^* < 80$, no discernible difference in $pdf(T = 0)$ exists between the two Reynolds numbers. For $80 < t^* < 180$, the value of $pdf(T = 0)$ at $Re_{\delta_0} = 240$ remains slightly higher than that at $Re_{\delta_0} = 200$; while, for $t^* > 180$, the value of $pdf(T = 0)$ at $Re_{\delta_0} = 240$ falls well below that of $Re_{\delta_0} = 200$.

The long-time behavior of $pdf(T = 0)$ may be traced back to the evolution of the vorticity field. During the time period $80 < t^* < 180$, the vorticity field approaches saturation, and ultimately reaches its saturation state at approximately $t^* = 180$ (see

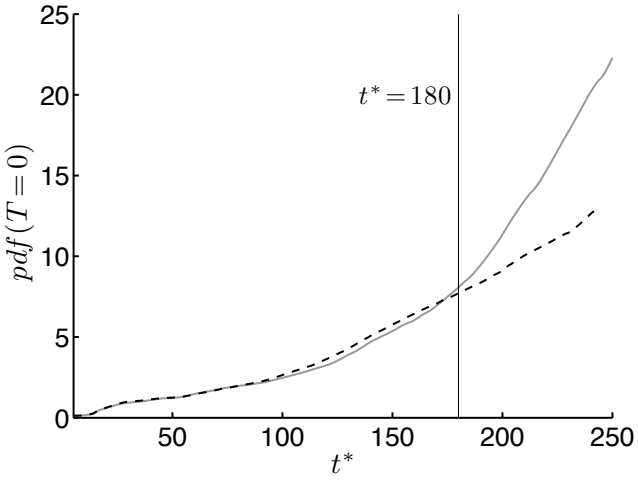

Figure 2.26. The value of the probability density function at $T = 0.0$ versus time, t^*, from two different simulations: — DNS at $Re_{\delta_0} = 200$ and −−DNS at $Re_{\delta_0} = 240$. In both cases, $Pr = 0.71$. The vertical line denotes the time whereupon the vorticity field first reaches its saturation state.

Fig. 2.7). This is the same time at which the two lines in Fig. 2.26 begin to diverge. When the vorticity field becomes fully saturated, the contribution of advection to the dynamics of the temperature field reduces significantly. Therefore, we expect diffusion to dominate the temperature equation (2.10) in the saturation state for $t^* > 180$. The order of magnitude of the diffusion term is given by $Re_{\delta_0}^{-1}$. As such, molecular mixing is expected to be less at higher Reynolds number, which would result in a lower value of $pdf(T = 0)$ at higher Re_{δ_0}, for a given Prandtl number.

2.7.4 Sensitivity of the Growth of the Vortex Thickness

In addition to obtaining the evolution of the sensitivities associated with the primitive variables, SEM also allows one to calculate the sensitivity of other important quantities of interest. For example, the sensitivity of the vortex thickness to changes in Reynolds number, S_{δ/δ_0}, can be determined by taking the partial derivative of (2.36) with respect to Re_{δ_0}, which yields

$$S_{\delta/\delta_0} = -\left(Re_{\delta_0}^{-1} + \frac{S_\zeta}{\zeta}\right)\left(\frac{\delta(t)}{\delta_0}\right), \tag{2.40}$$

where $\zeta = [d\langle u\rangle/dy]_{max}$ and $S_\zeta \equiv \partial\zeta/\partial Re_{\delta_0}$ (see Sec. A.1). In order to validate (2.40), the evolution of $\delta(t)/\delta_0$ from the DNS at $Re_{\delta_0} = 240$ is compared to that predicted by a nearby flow analysis using S_{δ/δ_0} obtained at Re_{δ_0}, i.e.,

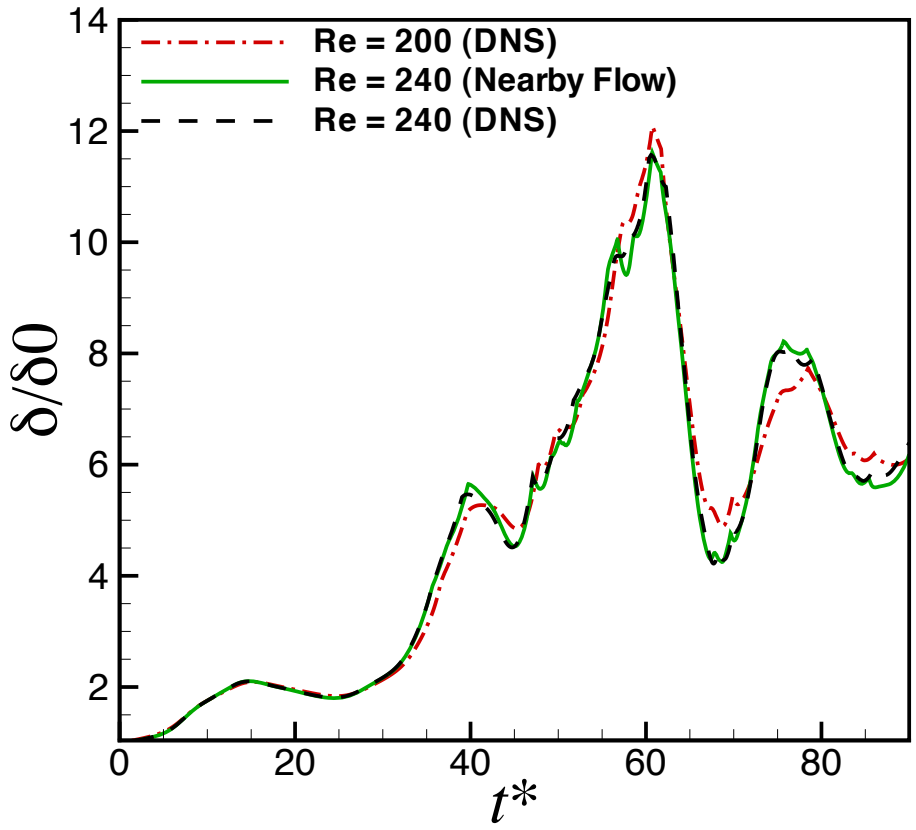

Figure 2.27. Nondimensional vortex thickness for three cases: DNS at $Re_{\delta_0} = 200$ $(- \cdot -)$, DNS at $Re_{\delta_0} = 240$ $(--)$, and the nearby flow prediction for $Re_{\delta_0} = 240$ using the SEM results at $Re_{\delta_0} = 200$ $(—)$.

$$\left[\delta(t)/\delta_0\right]\big|_{Nearby} = \left[\delta(t)/\delta_0\right]\big|_{Re_{\delta_0}} + \; S_{\delta/\delta_0}\, \Delta Re_{\delta_0}. \tag{2.41}$$

Substituting (2.40) in for S_{δ/δ_0} leads to the following relation

$$\left[\delta(t)/\delta_0\right]\big|_{Nearby} = \mathcal{A}(Re_{\delta_0}, t^*)\, \left[\delta(t)/\delta_0\right]\big|_{Re_{\delta_0}}, \tag{2.42}$$

where $\mathcal{A}(Re_{\delta_0}, t^*)$ represents an amplification factor defined according to

$$\mathcal{A}(Re_{\delta_0}, t^*) = 1 - \left(Re_{\delta_0}^{-1} + \frac{S_\zeta}{\zeta} \right) \Delta Re_{\delta_0}. \tag{2.43}$$

Figure 2.27 compares (2.42) from the DNS/SEM results at $Re_{\delta_0} = 200$ to that from the DNS at $Re_{\delta_0} = 240$. For reference, the evolution of the vortex thickness based on the DNS at $Re_{\delta_0} = 200$ is also shown. One observes excellent agreement between the nearby flow approximation and the actual DNS at $Re_{\delta_0} = 240$, thereby validating the sensitivity expression given in (2.40).

2.8 Conclusions

The continuous sensitivity equations with corresponding boundary and initial conditions were derived for the 2-D planar mixing layer by taking the partial derivative of the momentum and temperature equations (as well as their boundary/initial conditions) with respect to Re_{δ_0} and Pr. Direct numerical simulations (DNS) of the equations governing both the primitive variables and the sensitivity coefficients were performed using a finite-volume, fractional-step algorithm. This constitutes the basis of a nonparametric approach toward sensitivity analysis referred to as the Sensitivity Equation Method (SEM). Sensitivity results are presented from a baseline DNS/SEM simulation run at Re_{δ_0}=200 and Pr=0.71. Three sensitivity coefficients are examined: S_ω, sensitivity of the vorticity to changes in Reynolds number; $S_{T,Pr}$, sensitivity of temperature to changes in Prandtl number; and $S_{T,Re_{\delta_0}}$, sensitivity of temperature to changes in Reynolds number. An important advantage of SEM (over parametric studies) is that it yields temporally resolved sensitivity coefficients over the entire domain, and, as such, allows one to capture the coherency of the instantaneous sensitivity field. This information highlights the physical mechanisms responsible for Reynolds and Prandtl number effects on the evolution of the vorticity and temperature fields. In fact, a substantial effort has been spent in the present study on interpreting snapshots of the sensitivity fields from the baseline SEM simulation, toward making qualitative predictions of the behavior of the flow at higher Re_{δ_0} and Pr. The present study also introduces SEM as a powerful tool to obtain quantitative predictions of *nearby flows*, i.e., those with Re_{δ_0} and Pr values near the baseline case.

The SEM results reveal that coherent structures exist in the sensitivity field; and, these structures mimic those in the vorticity and temperature fields. Namely, the sensitivity field undergoes the same four main stages of evolution as the vorticity field: (i) the formation of the fundamental Kelvin-Helmholtz vortices, (ii) first pairing, (iii) second pairing, and (iv) saturation. The S_ω field, obtained from the baseline SEM, exhibits a two-blade pattern characterized by a highly negative band of S_ω along the outer edges of the vortices, coupled with a highly positive bands of S_ω inside the vortex cores. From this two-blade sensitivity pattern, one predicts growth in both the size and vorticity magnitude of the vortices at higher Re_{δ_0}. In terms of temperature, the contour pattern of $S_{T,Pr}$ leads to the prediction that the temperature inside the

core region of the vortices will become less homogeneous with increasing Pr, which translates into less scalar mixing at higher Pr. In contrast, $S_{T,Re_{\delta_0}}$ reveals negligible Reynolds number effect on scalar mixing, at least up to the second pairing. However, $S_{T,Re_{\delta_0}}$ does predict growth in the size of the coherent temperature structures with increasing Re_{δ_0}, as a direct consequence of the Reynolds number effect on the vorticity field. In addition, the normalized sensitivity coefficients show that the temperature field is an order of magnitude more sensitive to perturbations in Reynolds number compared to Prandtl number. Finally, an expression was derived for the sensitivity of the vortex thickness (δ/δ_0) to Re_{δ_0}. Evaluating this expression using the baseline SEM results yielded a successful prediction of δ/δ_0 at a 20% higher Re_{δ_0} compared to the baseline case.

The long-term vision of this work involves using SEM to aid in (i) understanding parameter-dependence in complex turbulent flows, (ii) design optimization of fluids engineering systems and devices, and (iii) active control of fluid flows. By examining the canonical 2-D temporal mixing layer, the present study represents one of the first steps in demonstrating the promise of SEM toward realizing these goals. Importantly, SEM has the capability to reveal the regions in an unsteady flow that are highly sensitive (or not) to the parameters of interest. The disadvantage, however, is the additional computational expense incurred to solve the discretized sensitivity equations. In reality, this costs no more (and possibly much less) than the alternative approach of performing a parameter study, which also inherently suffers from truncation errors in the finite difference operation used to estimate the sensitivity coefficients. Future work will include a direct comparison of the *complex-step method* to SEM in terms of ease of implementation, computational expense, and accuracy, as well as possible strategies to reduce the overall run time required to complete the computational sensitivity analysis.

CHAPTER 3

A POSTERIORI TESTS IN CAPTURING THE COHERENT SENSITIVITY FIELD OF A MIXING LAYER

3.1 Introduction

The performance of the sensitivity equation method (SEM) and complex-step differentiation (CSD) approach is evaluated for the case of incompressible, 2-D, temporal mixing layer. The aim of this *a posteriori* study is to discover how well these approaches practically capture the topology of the coherent sensitivity features in free shear flows due to perturbations in Reynolds number (Re_{δ_0}). Results from SEM and CSD, implemented in the context of both direct numerical simulations (DNS) and large eddy simulations (LES), were examined and compacted in terms of accuracy, computational expense, and ease of implementation. It is shown that CSD affords advantages over SEM in all of the aforementioned areas. The potential reasons underlying this difference in performance are discussed.

Because, computational sensitivity analysis in the DNS framework is expensive, it is prudent, for practical reasons, to examine alternative reliable and fast sensitivity analysis methods. Furthermore, DNS is limited to cases of relatively low-to-moderate Reynolds numbers (Re). Therefore, to overcome these challenges, the present study considers the implementation of computational sensitivity analysis in the context of Large Eddy Simulations (LES), which has the potential to both manage the high computational expense of SEM/CSD and also achieve high Re_{δ_0} solutions. The important unanswered scientific question is whether *computational sensitivity analysis in the LES framework can successfully reproduce the sensitivity features of the resolved flow*. In other words, to what extent is LES sensitivity analysis able to estimate the true physical sensitivity features of turbulent flows? In order to answer this question, *sensitivity-based a priori* and *a posteriori* studies should be performed following the

procedures used in typical LES *a priori* and *a posteriori* studies to demonstrate the performance of subfilter-scale (SFS) models (McMillan and Ferziger, 1979; Piomelli et al., 1988; Domoratdski et al., 1993; Hartel and Kleiser, 1993; Meneveau, 1993; Verman et al., 1995; Jimenez et al., 2001; Lu et al., 2007; Lu and Smith, 2008).

The main contribution of this chapter, is to perform an *a posteriori* study of two nonparametric, second-order accurate sensitivity analysis methods, namely Complex-Step Differentiation (CSD) and Sensitivity Equation Method (SEM) in the context of both DNS and LES. Results from CSD and SEM were compared at several grid resolutions both qualitatively, by visual inspection of the coherent structures in the sensitivity fields, and quantitatively using the probability density function estimates, apparent order of accuracy, the Grid Convergence Index (GCI), and computational time. In addition, CSD was implemented for the first time in the context of LES successfully using the standard and dynamic Smagorinsky models. The SEM sensitivity equations governing the sensitivity of *resolved* momentum were derived, and solved using the same LES models and numerics. Furthermore, the SEM analogous sensitivity equations governing the *filtered* sensitivity field were derived and the analogous *closure* problem for sensitivity was also introduced in this fashion. The DNS and LES simulations were run at baseline Reynolds number of $Re_{\delta_0} = 500$, up to $Re_{\delta_0} = 1000$ (for DNS) and $Re_{\delta_0} = 2000$ (for LES).

3.2 Temporal Planar Shear Layer

The present study considers the so-called *"temporal mixing layer"*. In this framework, periodic boundary conditions are used in the streamwise direction. The nondimensionalized *initial* streamwise velocity profile, u_0 is introduced as a basic mean flow plus a noise function of the form shown in (3.1), Michalke (1964),

$$u_0(x,y) = \underbrace{\tanh(2yL/\delta_0)}_{mean\ flow} + \underbrace{c_n \frac{\partial \psi}{\partial y}}_{noise}, \tag{3.1}$$

where,

$$\psi(x,y) = \exp\left(-y^2L^2/\delta_0^2\right)\left[\cos(8\pi x) + cos(20\pi x)\right]. \tag{3.2}$$

In (3.1) and (3.2), δ_0 denotes the initial vortex thickness, and x, y represent the spatial coordinates nondimensionalized by the size of the domain, (L). The factor

$c_n = 0.001$ is the noise factor chosen to satisfy Taylor's hypothesis. The process of defining the main features of the turbulence in the initial condition for the temporal mixing layer is termed "super-grid modeling" (Grinstein, 2004). The most common method of super-grid modeling is to impose a pseudo-perturbation on a mean profile. The least expensive and simplest method of initiating the turbulence follows from linear stability theory (LST), (Ragab and Wu, 1989), and the same is used in this study.

The size of the domain L is selected according to LST. For the hyperbolic tangent velocity profile, given in (3.1), the wavelength λ_a corresponding to the most unstable mode (which also represents the length of each fundamental Kelvin-Helmholtz vortex) is approximately given by $\lambda_a \simeq 7\delta_0$ (Betchov and Szewczyk, 1963). Therefore, the length of the computational domain L is determined based on the number of the fundamental Kelvin-Helmholtz vortices, N, desired in the simulation, i.e.,

$$L = N\lambda_a \simeq 7N\delta_0. \tag{3.3}$$

In the present study, $N = 4$ and $L/\delta_0 = 28$.

3.3 Direct Numerical Simulation

In direct numerical simulation (DNS) of the mixing layer, the Navier-Stokes equations that govern unsteady, incompressible flow with uniform density distribution and no body force can be written in a nondimensional and fully conservative form as

$$\frac{\partial u_i}{\partial t} + \frac{\partial (u_i u_j)}{\partial x_j} = -\frac{\partial p}{\partial x_i} + \frac{1}{Re_L}\frac{\partial}{\partial x_j}\left(\frac{\partial u_i}{\partial x_j} + \frac{\partial u_j}{\partial x_i}\right), \tag{3.4}$$

where are numerically solved under the constraint of continuity equation

$$\frac{\partial u_i}{\partial x_i} = 0. \tag{3.5}$$

In (3.4) and (3.5), t represents the time, x_i denotes the spatial coordinates, u_i represents the velocity components, p represents the pressure, and Re_L is the Reynolds number based on the physical domain size. The nondimensional vorticity is determined as

$$w = \frac{\partial v}{\partial x} - \frac{\partial u}{\partial y}. \tag{3.6}$$

3.3.1 Direct Sensitivity Analysis

In this chapter, the purpose of the sensitivity analysis is to initially quantify the sensitivity of the flow to changes in Re_{δ_0} (for DNS and LES) and the model parameter l^* (for LES). This is done using two second-order accurate sensitivity analysis approaches namely, *sensitivity equation method* (SEM) and *complex-step differentiation* (CSD).

3.3.1.1 Sensitivity Equation Method (SEM)

In SEM, the sensitivity and governing equations must be solved concurrently at each time step. The continuous sensitivity equations are derived by differentiating the momentum and continuity equations with respect to the parameter of interest, Re_{δ_0},

$$\begin{aligned}\frac{\partial \mathcal{S}_{u_i}}{\partial t} + \frac{\partial (\mathcal{S}_{u_i} u_j)}{\partial x_j} = -\frac{\partial \mathcal{S}_p}{\partial x_i} + \frac{1}{Re_L}\frac{\partial}{\partial x_j}\left(\frac{\partial \mathcal{S}_{u_i}}{\partial x_j} + \frac{\partial \mathcal{S}_{u_i}}{\partial x_i}\right) \\ -\frac{\partial \left(u_i\, \mathcal{S}_{u_j}\right)}{\partial x_j} - \frac{1}{(N\lambda_a/\delta_0) Re_{\delta_0}^2}\frac{\partial}{\partial x_j}\left(\frac{\partial u_i}{\partial x_j} + \frac{\partial u_j}{\partial x_i}\right),\end{aligned} \tag{3.7}$$

where $\mathcal{S}_{u_i}$ ($\equiv \partial u_i / \partial Re_{\delta_0}$) denotes the sensitivity of velocity component u_i to Re_{δ_0} and similarly, $\mathcal{S}_p$ ($\equiv \partial p / \partial Re_{\delta_0}$) denotes the sensitivity of pressure p to Re_{δ_0}. The Reynolds number based on the physical domain size is related to Reynolds number based on the initial vortex thickness as $Re_{\delta_0} = Re_L/(N\,\lambda_a)$, where N (here $N = 4$) denotes the number of fundamental Kelvin-Helmholtz vortices in the domain and λ_a is the wavelength of each fundamental vortex. The corresponding continuity sensitivity equation is obtained by differentiating (3.5) with respect to Re_{δ_0} giving,

$$\frac{\partial \mathcal{S}_{u_i}}{\partial x_i} = 0. \tag{3.8}$$

3.3.1.2 Complex-Step Differentiation Method (CSD)

The application of complex variables to approximate the first and higher derivatives of mathematically analytic functions was introduced first by Lyness (1967) and Lyness and Moler (1967), and later, implemented by Squire and Trapp (1998) to estimate the derivatives of real functions. Over the last decade, it has been shown that CSD is robust and accurate enough for use in computational fluid dynamics (CFD)(Anderson et al., 1999; Martins et al., 2000; Kirkman and Metzger, 2008b).

In the complex-step method, the governing equations (3.4) and (3.5) are treated as complex and, consequently, the velocity field $\mathcal{U}_j$ is obtained as a complex field. Additionally, the parameter of interest, in this case Re_{δ_0}, is defined as complex as

$$\mathcal{R}e_{\delta_0} = Re_{\delta_0} + i\Delta Re_{\delta_0}. \tag{3.9}$$

The real part of $\mathcal{R}e_{\delta_0}$ is the physical Reynolds number based on δ_0 introduced in the previous section, and the imaginary part ΔRe_{δ_0} represents the perturbation in the design parameter, typically chosen to be on the order of 10^{-16} (Martins et al., 2000). In CSD, the sensitivity coefficients are estimated by dividing the imaginary part of the calculated velocity field by the imaginary part of the parameter of interest (i.e., ΔRe_{δ_0}), as shown in (3.10).

$$\mathcal{S}_{\mathcal{U}_j} \approx \frac{Im[\mathcal{U}_j(Re_{\delta_0} + i\Delta Re_{\delta_0})]}{\Delta Re_{\delta_0}}. \tag{3.10}$$

Since this technique does not explicitly involve a difference operator, the estimate of the derivative is not subject to subtractive cancellation error. Therefore, the sensitivity coefficient obtained by complex-step differentiation is insensitive to actual value of the step size, i.e., ΔRe_{δ_0}, for small step sizes (Martins et al., 2000).

Finally, the sensitivity of the vorticity to Reynolds number, $\mathcal{S}_\omega$, is determined by differentiating (3.6) with respect to Re_{δ_0} as,

$$\mathcal{S}_\omega = \frac{\partial \mathcal{S}_v}{\partial x} - \frac{\partial \mathcal{S}_u}{\partial y}, \tag{3.11}$$

where $\mathcal{S}_v$ and $\mathcal{S}_u$ denote the y- and x-components of velocity sensitivity to changes in Re_{δ_0} obtain using SEM or CSD.

3.4 Large Eddy Simulation

Large eddy simulation (LES) is a technique to reduce the degrees of freedom of motion in turbulent flows in order to decrease the computational and time expenses associated with high Reynolds number simulations. The general idea in this approach is to resolve only large scales of motion and model the smaller (more universal) eddies. This scale separation is achieved in the momentum equations by applying a low-pass

kernel filter to the Navier-Stokes equations. The filter operation is defined as the convolution of a kernel filter to the function of interest as,

$$\tilde{\phi}(x,t) = G(x) \star \phi(x,t) = \int_{-\infty}^{-\infty} \phi(\xi,t) G(\xi - x) d\xi, \tag{3.12}$$

in which the kernel G is a smooth function associated with cutoff scales.The spatial kernel filter used in this research is tophat (Box) filter, defined by,

$$G(\mathbf{x} - \xi) = \begin{cases} \frac{1}{\Delta} & |\mathbf{x} - \xi| \leq \frac{\Delta}{2} \\ \\ 0 & otherwise \end{cases} \tag{3.13}$$

The spatially filtered Navier-Stokes equations that govern unsteady, incompressible flow with no body force are shown nondimensionally as

$$\frac{\partial \widetilde{u}_i}{\partial t} + \frac{\partial (\widetilde{u}_i \widetilde{u}_j)}{\partial x_j} = -\frac{\partial \widetilde{p}}{\partial x_i} + \frac{1}{Re_L} \frac{\partial}{\partial x_j} \left[\left(\frac{\partial \widetilde{u}_i}{\partial x_j} + \frac{\partial \widetilde{u}_j}{\partial x_i} \right) \right] - \frac{\partial \tau_{ij}}{\partial x_j}, \tag{3.14}$$

solved numerically under the constraint of the filtered continuity equation as

$$\frac{\partial \widetilde{u}_i}{\partial x_i} = 0. \tag{3.15}$$

In (3.14) and (3.15) the superscript tilde ($\tilde{\cdot}$) represents the filtering operation. The closure problem in LES is the subfilter-scale (SFS) stress tensor, τ_{ij}, which represents the dynamical interaction the resolved-scale eddies and SFS eddies, i.e.,

$$\tau_{ij} = \widetilde{u_i u_j} - \widetilde{u}_i \widetilde{u}_j, \tag{3.16}$$

In (3.16), $\widetilde{u_i u_j}$ remains as an unknown because it can not be computed directly. Therefore, LES requires a model for the behavior of the small scales that is based on the resolved (filtered) scales of motion (i.e., $\widetilde{u}_i$).

There are different classes of LES modeling in the literature such as *eddy-viscosity* models, *similarity* models, *stochastic* models, and *velocity reconstruction* models, which are very briefly explained here. Eddy-viscosity models employ an eddy-viscosity, which, like molecular viscosity, extracts energy from resolved scales in the simulation to model SFS stress (Deardorff, 1970). Based on the similarity models, the most active SFS are those close to the cut-off length scale. These models were first introduced by Bardina et al. (1980). In stochastic models, the general idea is that a random (stochastic) component is introduced into the SFS model. Usually, the nonlinear term

is combined with a eddy-viscosity model (Mason and Thomson, 1992). The velocity reconstruction of the SFS seeks to approximate the SFS stress through a direct reconstruction of the SFS. Two examples are the fractal method (Scotti and Meneveau, 1999) and the linear-eddy model (LEM) (Kerstein, 1988). The eddy-viscosity model performs reasonably well in modeling the SFS stresses in free shear flows and is also computationally cheaper when compared to other methods, and is hence employed in the present LES study.

3.4.1 Standard Smagorinsky Model

The Smagorinsky model (Smagorinsky, 1963) was originally developed for atmospheric applications and was first applied by Deardorff (1970) to LES work as

$$\tau_{ij} - \frac{1}{3}\delta_{ij}\tau_{kk} = -2\nu_\tau \widetilde{s}_{ij}, \tag{3.17}$$

in which, ν_τ in (3.17) is modeled by

$$\nu_\tau = (C_s\Delta)^2|\widetilde{S}| = (l^*)^2|\widetilde{S}|, \tag{3.18}$$

where $\widetilde{s}_{ij} = \frac{1}{2}(\partial\widetilde{u}_i/\partial x_j + \partial\widetilde{u}_j/\partial x_i)$ is the resolved strain-rate tensor, $|\widetilde{S}| = \sqrt{2\widetilde{s}_{ij}\widetilde{s}_{ij}}$, parameter $C_s(= 0.1$, suggested by Lesieur (1997) for the application of mixing layer) denotes the Smagorinsky coefficient, and Δ is the filter width basically obtained from the grid spacing.

3.4.2 Dynamic Smagorinsky Model

The dynamic model was first proposed by Germano et al. (1991) and essentially motivated by the notion of scale similarity. The dynamic model is a procedure to locally update the value of the Smagorinsky coefficient C_s based on the resolved scales. The dynamic model is based on Germano's identity, which states that the stress calculated at a test-filter with width $\widehat{\Delta}$ (usually $\widehat{\Delta} = 2\Delta$) scales as

$$L_{ij} = T_{ij} - \widehat{\tau}_{ij} = \widehat{\widetilde{u}_i\widetilde{u}_j} - \widehat{\widetilde{u}}_i\widehat{\widetilde{u}}_j, \tag{3.19}$$

where $T_{ij} = \widehat{\widetilde{u_i u_j}} - \widehat{\widetilde{u}}_i\widehat{\widetilde{u}}_j$ is the SFS stress at the test filter $\widehat{\Delta}$, and L_{ij} is the resolved stress (called *Leonard tensor*) that is evaluated based on the resolved scales. Note, the same test filter (tophat filter) of width $\widehat{\Delta} = 2\Delta$ is used to calculate $\widehat{\tau}_{ij}$ and $\widehat{\widetilde{u}}_i$.

The first assumption in the dynamic model is that T_{ij} can be modeled using the same Smagorinsky model at a larger length scale $\widehat{\Delta}$ as

$$T_{ij} - \frac{1}{3}\delta_{ij}T_{kk} = -2\left(C_s(\widehat{\Delta})\widehat{\Delta}\right)^2 |\widehat{\widetilde{S}}|\widehat{\widetilde{s}}_{ij}. \tag{3.20}$$

By substituting (3.17) and (3.20) into (3.19) and assuming that the Smagorisnky coefficient C_s is *insensitive* to filter width and does not change from Δ to $\widehat{\Delta}$ (scale invariance assumption), the following relation is obtained as

$$L_{ij} - \frac{1}{3}\delta_{ij}L_{kk} = C_s^2 M_{ij}, \tag{3.21}$$

in which

$$M_{ij} = 2\Delta^2\left(\widehat{|\widetilde{S}|\widetilde{S}_{ij}} - \alpha^2|\widehat{\widetilde{S}}|\widehat{\widetilde{S}}_{ij}\right), \tag{3.22}$$

where $\alpha = \widehat{\Delta}/\Delta = 2$. Following Lilly (Lilly, 1992) and minimizing the error in (3.21) with respect to C_s^2 in a least-square sense while also enforcing the Germano identity in an average sense over some region of statistical homogeneity (Ghosal et al., 1995), the Samgorinsky coefficient is dynamically calculated as

$$C_s^2 = \frac{\langle L_{ij}M_{ij}\rangle}{\langle M_{ij}M_{ij}\rangle}. \tag{3.23}$$

In the dynamic procedure, a homogeneous filter is typically applied.

3.4.3 Computational Sensitivity Analysis in the Context of LES

The sensitivity of the *resolved* vorticity $\widetilde{\omega}$ to $P_k = \{P_1, P_2\} = \{Re_{\delta_0}, l^*\}$, where $l^* = C_s\Delta$ (called SFS length scale), is obtained as

$$\mathcal{S}_{\widetilde{\omega},P_k} = \frac{\partial \mathcal{S}_{\widetilde{v},P_k}}{\partial x} - \frac{\partial \mathcal{S}_{\widetilde{u},P_k}}{\partial y}. \tag{3.24}$$

In (3.24), $S_{\widetilde{v},P_k}$ and $S_{\widetilde{u},P_k}$ represent the y and x-components of the resolved velocity sensitivities to perturbations in P_k obtained by SEM/LES or CSD/LES.

3.4.3.1 Sensitivity Equation Method in LES

There are two possible ways of deriving continuous sensitivity equations in the context of LES: (i) take the partial derivative of the already filtered momentum equations with respect to the parameter(s) of interest to obtain the sensitivity of the resolved velocity, i.e., $\mathcal{S}_{\widetilde{u}_i}$, or (ii) filter the direct momentum sensitivity equations

to obtain the resolved sensitivity of velocity, i.e., $\widetilde{\mathcal{S}}_{u_i}$. The present study considers the practical implementation of the first approach, and only outlines the appropriate equations for the second approach in the Appendix.

To implement the first approach, the sensitivity of the filtered momentum equations is derived by taking the partial derivative of (3.14) with respect to P_k (introduced in Sec. 3.4.3) as

$$\frac{\partial \mathcal{S}_{\widetilde{u}_i,P_k}}{\partial t} + \frac{\partial(\widetilde{u}_j \mathcal{S}_{\widetilde{u}_i,P_k})}{\partial x_j} = -\frac{\partial \mathcal{S}_{\widetilde{p},P_k}}{\partial x_i} + \frac{1}{Re_L}\frac{\partial}{\partial x_j}\left[\left(\frac{\partial \mathcal{S}_{\widetilde{u}_i,P_k}}{\partial x_j} + \frac{\partial \mathcal{S}_{\widetilde{u}_i,P_k}}{\partial x_i}\right)\right] - \frac{\partial(\mathcal{T}_{ijk})}{\partial x_j}, \tag{3.25}$$

where $l^* = C_s\Delta$ is called SFS length scale, $\mathcal{S}_{\widetilde{u}_i,P_1}$ $(\equiv \partial\widetilde{u}_i/\partial Re_{\delta_0})$ is the sensitivity of the resolved velocity to Re_{δ_0}, and $\mathcal{S}_{\widetilde{u}_i,P_2}$ $(\equiv \partial\widetilde{u}_i/\partial l^*)$ is the sensitivity of the resolved velocity to l^*. Similarly, $\mathcal{S}_{\widetilde{p},P_1}$ and $\mathcal{S}_{\widetilde{p},P_2}$ are sensitivities of resolved pressure to Re_{δ_0} and l^* respectively. As shown, this form of (3.25) looks similar to (3.14); however, in this case, $\mathcal{T}_{ijk}$ is given by

$$\mathcal{T}_{ijk} = \widetilde{u}_i \mathcal{S}_{\widetilde{u}_j,P_k} + \frac{\delta_{1k} 2\widetilde{s}_{ij}}{(N\lambda_a/\delta_0)Re_{\delta_0}^2} + \mathcal{S}_{\tau_{ij},P_k}, \tag{3.26}$$

where $\widetilde{u}_i\mathcal{S}_{\widetilde{u}_j}$ arises from differentiating the convection term using the chain rule, $\delta_{1k}2\widetilde{s}_{ij}/\left[(N\lambda_a/\delta_0)Re_{\delta_0}^2\right]$ represents a source term and appears because of the existence of Re_{δ_0} in the original, and $\mathcal{S}_{\tau_{ij},P_k}$ is the sensitivity of the SFS stress τ_{ij} to P_k. The term $\mathcal{S}_{\tau_{ij},P_k}$ is derived by taking the partial derivative of the eddy-viscosity model (3.18) with respect to P_k,

$$\mathcal{S}_{\tau_{ij},P_k} = -2\nu_\tau \widetilde{\Lambda}_{ijk}, \tag{3.27}$$

where $\widetilde{\Lambda}_{ijk}$ is obtained for each parameter P_k by considering the commutation property of the spatially homogeneous kernel filter,

$$\widetilde{\Lambda}_{ij1} = 2\mathcal{S}_{\widetilde{s}_{ij},Re_{\delta_0}} = \frac{\partial \mathcal{S}_{\widetilde{u}_i,Re_{\delta_0}}}{\partial x_j} + \frac{\partial \mathcal{S}_{\widetilde{u}_j,Re_{\delta_0}}}{\partial x_i} \tag{3.28}$$

$$\widetilde{\Lambda}_{ij2} = 2\left(\mathcal{S}_{\widetilde{s}_{ij},l^*} + \frac{1}{l^*}\widetilde{s}_{ij}\right) = \frac{\partial \mathcal{S}_{\widetilde{u}_i,l^*}}{\partial x_j} + \frac{\partial \mathcal{S}_{\widetilde{u}_j,l^*}}{\partial x_i} + \frac{2}{l^*}\widetilde{s}_{ij}. \tag{3.29}$$

3.4.3.2 Complex-Step Differentiation in LES

In order to implement the CSD in the LES framework, the only requirement is to initialize all dependent variables as complex and define the parameter(s) of interest as

complex, i.e., $P_k = P_k + i\Delta P_k$. The original governing equations (3.14) and (3.15) are then solved using complex arithmetic. The sensitivity of the resolved velocity to P_k is subsequently estimated by dividing the imaginary part of the calculated resolved complex velocity field by the small perturbation ΔP_k, as

$$\mathcal{S}_{\widetilde{u}_j} \approx \frac{Im[\widetilde{\mathcal{U}}_j(P_k + i\Delta P_k)]}{\Delta P_k}. \tag{3.30}$$

Note, care should be taken to ensure that the Smagorinsky coefficient C_s remains a real-valued number in both the standard and dynamic models, when Re_{δ_0} is the parameter of interest. This makes sense because defining the constant C_s as complex increase the number of arithmetic operations, and also generates some unwanted imaginary values for the modeled τ_{ij} at each time step.

3.5 Numerical Method

The numerical scheme used here for both the DNS and LES follows that presented in Chap.2, except for some minor differences as outlined below. The DNS and LES momentum equations (3.4) and (3.14) are solved by using a variant of the fractional-step method first implemented by Kim and Moin (1985) on a staggered grid. This numerical scheme was first originally formulated by Harlow and Welch (1965) and Chorin (1968) for the time-advancement of the Navier-Stokes equations. The fractional-step method is based on the Hodge decomposition in which the velocity field, u_i^*, is decomposed into a divergence-free field, u_i, plus the gradient of a scalar potential, ϕ,

$$u_i^* = u_i + \frac{\partial \phi}{\partial x_i}. \tag{3.31}$$

The Hodge decomposition is implemented in two steps: (i) an intermediate velocity field, u_i^*, is first obtained using the discretized equation as shown in (3.32),

$$\frac{u_i^* - u_i^n}{\Delta t} = \frac{3}{2}H_i^n - \frac{1}{2}H_i^{n-1}, \tag{3.32}$$

where,

$$H_i = -\frac{\partial (u_i u_j)}{\partial x_i} + \frac{1}{Re_L}\frac{\partial}{\partial x_j}\left[\left(\frac{\partial u_i}{\partial x_j} + \frac{\partial u_j}{\partial x_i}\right)\right], \tag{3.33}$$

and (ii) the intermediate velocity field calculated from the first step is projected onto a divergence-free velocity field using (3.31), as shown in (3.34).

$$\frac{u_i^{n+1} - u_i^*}{\Delta t} = -\frac{\partial \phi}{\partial x_i}, \tag{3.34}$$

In (3.34), the superscript n denotes the time step. The intermediate velocity field does not satisfy (3.5) because the solution of the momentum equation for the intermediate velocity field is performed ignoring the pressure gradient term. Therefore, an equation for the scalar potential can be derived as shown in (3.35) by taking the divergence of (3.34) and imposing continuity for the new time level $(n+1)$.

$$\frac{\partial^2 \phi}{\partial x_j \partial x_j} = \frac{1}{\Delta t} \frac{\partial u_i^*}{\partial x_i}. \tag{3.35}$$

A finite volume based, multigrid scheme is used to solve (3.35). In this approach, the coarse grid is half the resolution of the fine (original) staggered grid. In order to extract the pressure field, the scalar potential ϕ must be corrected following (Kim and Moin, 1985) as shown in (3.36).

$$p = \phi - \frac{\Delta t}{2Re_L} \frac{\partial^2 \phi}{\partial x_j \partial x_j}. \tag{3.36}$$

The current fractional-step algorithm utilizes the finite volume method with a forward-staggered uniform grid. The computational domain is a square, in which $-0.5 < x < 0.5$ and $-0.5 < y < 0.5$. The spatial derivatives are discretized using second-order central differencing, and the temporal derivatives are advanced explicitly in time using Adams-Bashforth time integration. Periodic boundary conditions are applied along the streamwise $x-$direction; and, free-slip conditions are imposed along the top and bottom boundaries.

In case of SEM, the governing equation for $\mathcal{S}_{u_i, Re_{\delta_0}}$ (3.7) and $S_{\widetilde{u}_i, Re_{\delta_0}}$ (3.25), are solved like the momentum equations except for additional source terms due to the presence of the parameter of interest in the original governing equations (3.4) and (3.14). Specifically, the pressure sensitivity is obtained in a manner similar to (3.35 and (3.36),

$$\frac{\partial^2 \mathcal{S}_{\phi, P_k}}{\partial x_j \partial x_j} = \frac{1}{\Delta t} \frac{\partial \mathcal{S}^*{}_{u_i, P_k}}{\partial x_i}, \tag{3.37}$$

where $\mathcal{S}_{\phi, P_k}$ $(\equiv \partial\phi / \partial P_k)$ is the potential scalar sensitivity and $\mathcal{S}^*{}_{u_i, P_k}$ $(\equiv \partial u_i^* / \partial P_k)$ is the intermediate velocity sensitivity. The sensitivity of pressure to perturbations in P_k is then given by (3.38).

$$\mathcal{S}_{p, P_k} = \mathcal{S}_{\phi, P_k} - \frac{\Delta t}{2Re_L} \frac{\partial^2 \mathcal{S}_{\phi, P_k}}{\partial x_j \partial x_j} \tag{3.38}$$

Similar to the momentum equations, periodic boundary conditions are used along the streamwise direction, and free-slip conditions ($\partial \mathcal{S}_{u_i, P_k} / \partial y = 0.0$ and $\partial \mathcal{S}_{\widetilde{u}_i, P_k} / \partial y = 0.0$)

Table 3.1. List of the DNS and LES sensitivity simulations run at different Re_{δ_0} and grid resolutions using CSD and SEM. CSD*/DNS is the reference (high resolution) sensitivity data used to compare CSD/DNS and SEM/DNS, also to be filtered and implemented in case of *a posteriori* study of CSD/LES and SEM/LES performance.

Method	Resolution	Re_{δ_0}
CSD/DNS	300×300	500
SEM/DNS	300×300	500
CSD*/DNS	350×350	500
CSD/LES	200×200	500
SEM/LES	200×200	500
Filtered CSD*/DNS	350×350	500
CSD/DNS (High Re_{δ_0})	512×512	1000
CSD/LES (High Re_{δ_0})	350×350	2000

are imposed along the top and bottom sides of the computational domain. Zero initial condition for the velocity sensitivity field (i.e., $\mathcal{S}_{u_i} = 0$ and $\mathcal{S}_{\widetilde{u}_i,P_k} = 0$ at $t = 0$) is considered because the initial velocity u_{0i} and the corresponding filtered field do not depend on P_k; see (3.1) and recall that $L/\delta_0 \approx 28$ independent of Re_{δ_0}. For this reason, in the case of CSD, the imaginary part of the velocity and pressure is initialized as zero.

As can be seen from the above discussion, the practical implementation of CSD in as existing CFD code is straightforward. In reality, converting a real CFD code to a complex one requires little effort in Fortran 90; one only needs to manipulate the declaration of the variables and make some minor changes in the convergence criterion of the Poisson solver. With regard to solving the complex Poisson equation, using the same multigrid scheme mentioned above, special care should be taken that the convergence criterion (here, set at 1×10^{-4}) is satisfied for *both* real and imaginary part of the complex velocity field at each time step.

3.6 Results

A posteriori study of the sensitivity analysis techniques, CSD and SEM, is performed in the DNS and LES frameworks. Table 3.1 provides brief information about all test cases examined in this study. For DNS, a grid resolution 300×300 is used at

baseline $Re_{\delta_0} = 500$ compared to a fine DNS sensitivity solution at a higher resolution 350×350. The LES simulations are run at the same $Re_{\delta_0} = 500$ but lower resolution 200×200 using the Smagorinsly model (both standard and dynamic).

The roll-up process of unsteady coherent structures in the mixing layer is shown in Fig. 3.1. The instantaneous snapshots of the vorticity field are obtained from the DNS simulation run at $Re_{\delta_0} = 500$. The snapshots reveal the evolution of the coherent vortices in the flow field from the formation of the four fundamental Kelvin-Helmholtz (K-H) vortices, followed by the first pairing into two larger vortices, and eventually the second pairing, which yields a single vortex nominally in the center of the domain.

3.6.1 Direct Sensitivity of Vorticity to Re_{δ_0}

The corresponding evolution of the sensitivity field of vorticity $\mathcal{S}_\omega$ obtained from the three DNS cases at SEM and CSD are shown in Fig. 3.2. In each case, the three instantaneous snapshots of $\mathcal{S}_\omega$ corresponding, from top-to-bottom, to (i) the formation of four fundamental K-H vortices, (ii) the first pairing, and (iii) the second paring. The left column represents the CSD results at 300×300. The right column shows the SEM results at 300×300. Finally, Fig. 3.3 indicates the fine-grid CSD results at a resolution of 350×350, which will be referred hereafter as CSD*. Note, the colorbar in Fig. 3.3 changes according to the stage of evolution, but is consistent across all three cases.

Although we solve the velocity field using exactly the same CFD scheme and with the same resolution, the velocity field is treated as complex in CSD in contrast to the SEM approach. Besides, applying the periodic boundary conditions along the homogenous direction (i.e., x-axis) may cause a time shift in the CSD and SEM simulations snapshots. In order to find the best match between snapshots of CSD and SEM to be used in our *pdf* analysis, we take all three important SEM snapshots for vorticity sensitivity corresponding to the formation, first pairing, and the second pairing of K-H vortices as the base cases. Then, we examine a number of the CSD snapshots in each case occurring in the time neighborhood of the SEM snapshots. By calculating the correlation coefficient between CSD and SEM sensitivity fields in each pair using (3.39), we find the best candidate snapshots with the maximum correlation coefficient.

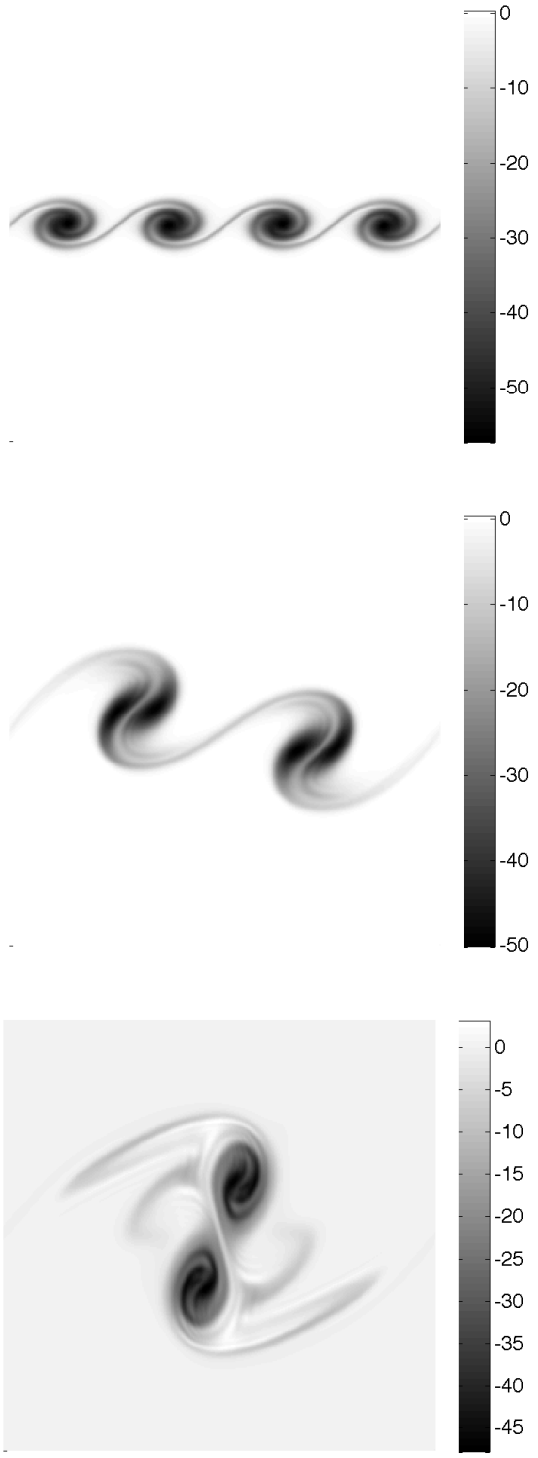

Figure 3.1. DNS vorticity field, ω, corresponding to the formation of fundamental Kelvin-Helmholtz vortices at nondimensional time $t^* = 13.8$ (top), first pairing (middle) at $t^* = 41.5$, and second pairing at $t^* = 57$ (bottom) at $Re_{\delta_0} = 500$ and resolution 300×300.

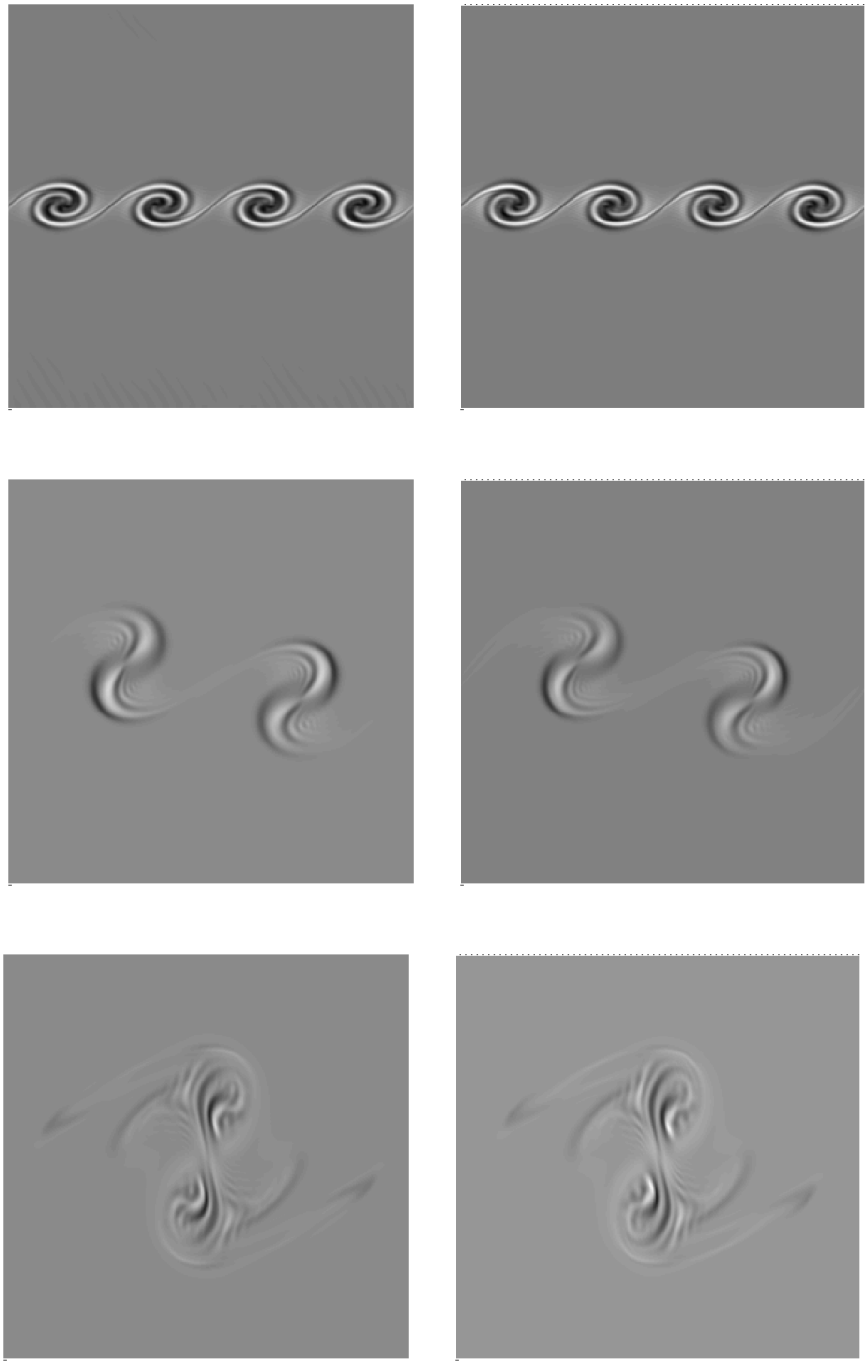

Figure 3.2. Sensitivity of vorticity to Reynolds number, $\mathcal{S}_\omega$, at $Re_\delta = 500$ from DNS. The rows show the formation of fundamental Kelvin-Helmholtz vortices, first pairing and second pairing process, using CSD at 300×300 (left column), SEM at 300×300 (right column).

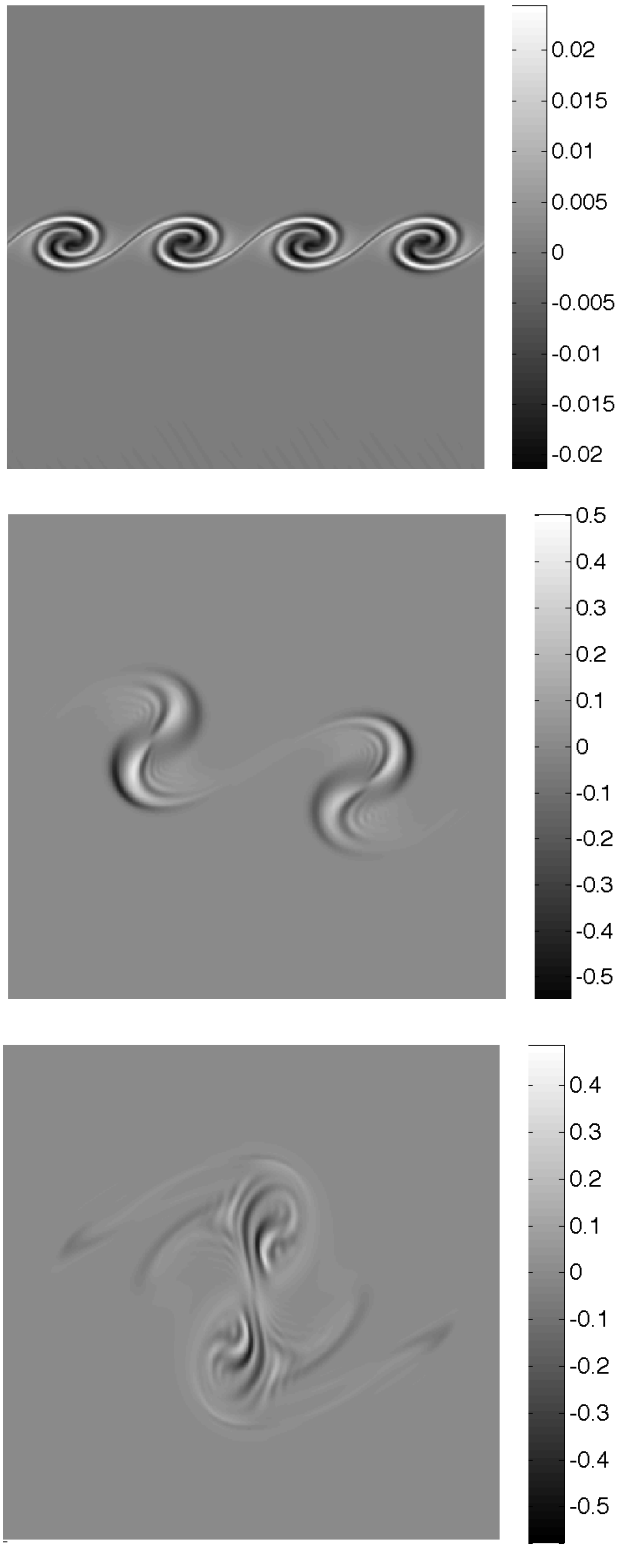

Figure 3.3. Sensitivity of vorticity to Reynolds number, $\mathcal{S}_\omega$, at $Re_\delta = 500$ from DNS. The rows show the formation of fundamental Kelvin-Helmholtz vortices, first pairing and second pairing process, using CSD* at 350×350.

$$\rho(\mathcal{S}_\omega^{CSD}, \mathcal{S}_\omega^{SEM}) = \frac{cov(\mathcal{S}_\omega^{CSD}, \mathcal{S}_\omega^{SEM})}{\sigma_{\mathcal{S}_\omega^{CSD}} \sigma_{\mathcal{S}_\omega^{SEM}}} \tag{3.39}$$

In (3.39), *cov* denotes the covariance and σ indicates the standard deviation. Figure 3.4 shows three plots of the correlation coefficient plotted against the time-lag corresponding to all three roll-up processes. In SEM, the snapshots are captured at $t^* = 13.8, 41.5$, and 57. It is shown that the appropriate matches of CSD snapshots are obtained at $t^* = 13.8, 40$, and 56.1, respectively, adopting the maximum correlation coefficients.

As seen in the top of Fig. 3.2, concentrated areas of high negative sensitivity (dark bands) exist around the periphery of each vortex during the formation of the four K-H vortices.

This feature of the sensitivity field was referred to in Chap.2 as the *coherent two-blade sensitivity structure*, and an extensive interpretation of the structure was provided in that chapter and only briefly recapitulated here. Because the vorticity is negative everywhere in the domain (see Fig. 3.1), spiraling sensitivity structure predicts that by increasing the Reynolds number the mixing layer evolves faster, by enforcing the nonvortical regions around the periphery of each vortex. As a result, each vortex becomes larger in terms of the size and mixing power at higher Reynolds number. This same two-blade structure of sensitivity is clearly observed in the first pairing of the vortices as well, shown in the right row of Fig. 3.2. By the second pairing a switch has occurred in the sensitivity pattern, which predicts more *homogenization* in the vorticity field at higher Re_{δ_0}, indicative of growth in the mixing layer leading to shorter time required to reach the self-similar state. This contrasts the DNS results at $Re_{\delta_0} = 200$ presented in Chap.2 wherein the two-blade structure was shown to exist over the entire roll-up process, including the second pairing. It has been observed, however, that for $Re_{\delta_0} \geqslant 350$, the topology of the sensitivity associated with the second pairing switches to that shown in Fig. 3.2.

A qualitative comparison of $\mathcal{S}_\omega$ based on visual inspection indicates good agreement between all cases. A quantitative assessment is somewhat more challenging because of the unsteady nature of the flow and the fact that the sensitivity solutions evolve at slightly different rates based on the sensitivity technique used and the resolution. As a result, the L_2 norm of the difference between two solutions, calculated

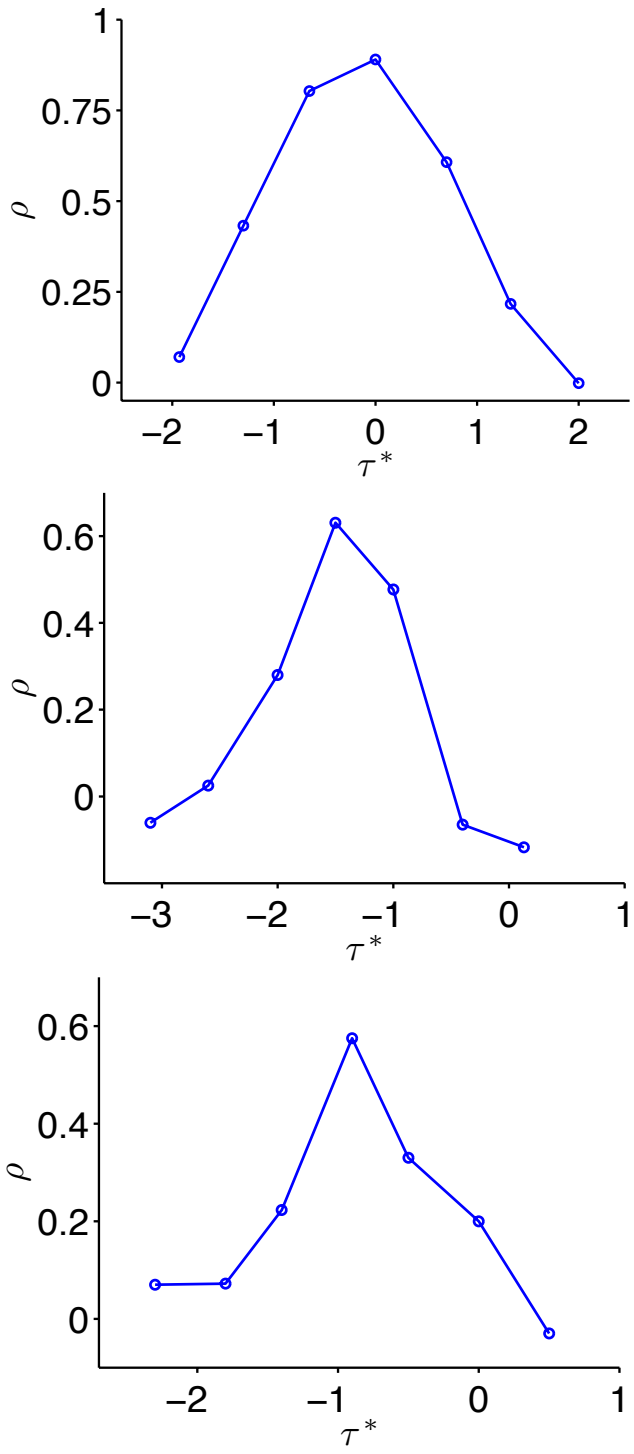

Figure 3.4. Correlation coefficient (ρ) between SEM and CSD versus simulation time-lag (τ^*). The SEM snapshots are considered as baseline (fixed), at simulation times corresponding to the formation snapshot at $t^* = 13.8$ (top), first pairing (middle) at $t^* = 41.5$, and second pairing at $t^* = 57$ (bottom), respectively. Correlation coefficient between each baseline SEM snapshot and those belonging to CSD captured in the time-neighborhood of each baseline SEM case is calculated.

as point-wise, tends to be artificially inflated, and as such does not yield a satisfactory measure of how similar or different the CSD and SEM solutions are relative to each other. Therefore, an integral measure was adopted in order to overcome this challenge and facilitate a quantitative comparison of the CSD and SEM solutions. Specifically, the bin-wise L_2 norm error in the *pdf* of sensitivity is calculated as

$$\epsilon^{ref.} = \frac{\|pdf^{CSD^*} - pdf\|}{\|pdf^{CSD^*}\|} \times 100, \tag{3.40}$$

in which pdf^{CSD^*} denotes the probability density function associated with CSD* solutions while *pdf* indicates that calculated either from CSD or SEM. Table 3.2 shows the percentage error obtained in this manner for the three main stages of evolution. At first glance, one notices that $\epsilon^{ref.}$ increases as the mixing layer evolves, not surprising given the transient nature of the flow. This behavior maybe compounded by the propagation and accumulation of error originating from the iterative Poisson solver(s) in each method.

Based on the values listed in Table 3.2, both methods yield identical *pdf*$'$s up to the formation stage (i.e., $\epsilon^{ref.} = 0.34\%$). Beyond this time in the evolution, CSD appears to more closely follow the fine-grid solution compared to SEM, in which the *pdf* error accelerates and reaches 6.3% by the time of the second pairing. To illustrate this difference, *pdf*$'$s of the sensitivity fields from CSD, SEM, and CSD* at the second pairing are shown in Fig. 3.5, in which the maximum percentage error in CSD and SEM *pdf*$'$s are 1.23% and 4.50%, compared to CSD*.

Alternatively, the Grid Convergence Index (GCI) of Roache (1997) is used to quantify the uncertainty and compare the accuracy of each sensitivity analysis approach in DNS case. Grid convergence index is defined as

$$GCI = \frac{F_s}{r^{\widehat{p}} - 1}\left|\frac{f_2 - f_1}{f_1}\right|, \tag{3.41}$$

where $F_S = 3$ indicates a factor of safety, and $\widehat{p}$ is the *apparent* order of accuracy of the scheme obtained as

$$\widehat{p} = \ln\left|\frac{f_3 - f_2}{f_2 - f_1}\right| \Big/ \ln(r), \tag{3.42}$$

where f_k denotes the numerical solution of the sensitivity field using k^{th} gird resolution, with $k = 1$ as the finest grid resolution, and r $(= 2)$ indicates the ratio of grid spacing between successive grid refinements. Three resolutions 50×50, 100×100, and

Table 3.2. The percentage of error $\epsilon^{ref.}$ between the *pdf* of the CSD/DNS and SEM/DNS compared to the fine-grid reference case, at grid resolution 350×350.

	Formation	1^{st} Pairing	2^{nd} Pairing
CSD/DNS:	0.34	0.5	0.53
SEM/DNS:	0.34	1.32	6.3

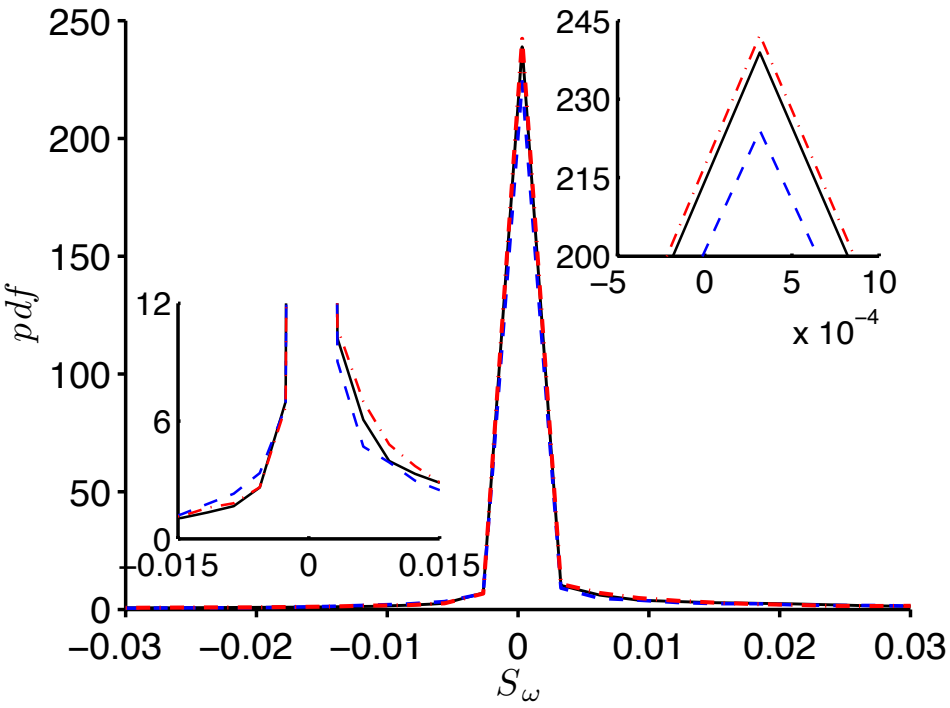

Figure 3.5. Probability density function (*pdf*) of $\mathcal{S}_\omega$ obtained from CSD shown by dash-dotted line $(- \cdot -)$, SEM indicated by dashed line $(--)$ and CSD* denoted by solid line $(-)$, at $Re_\delta = 500$, at time of the second pairing.

200×200 are used in simulation of f_3, f_2, and f_1, respectively. An ensemble averaged quantity $\overline{\langle \frac{1}{2}(\mathcal{S}^2_{u,Re_{\delta_0}} + \mathcal{S}^2_{v,Re_{\delta_0}})\rangle}$ is used in the uncertainty analysis (as f_k), where $\langle\cdot\rangle$ denotes the average over space, and superscript $\bar{\cdot}$ indicates the average over simulation time. Figure 3.6 shows the values of $\langle \frac{1}{2}(\mathcal{S}^2_{u,Re_{\delta_0}} + \mathcal{S}^2_{v,Re_{\delta_0}})\rangle$ versus nondimensional time of the simulation. In fact, it shows how the solution of sensitivity field (to Re_{δ_0}) tends to the converged grid independent solution used in this uncertainty study. Table 3.3 illustrates the apparent order of accuracy $\widehat{p}$ and also GCI for CSD/DNS and SEM/DNS. It is shown that the apparent order of accuracy for CSD is 3.09, as opposed to 2.040 for SEM. In fact, the higher apparent accuracy of CSD when compared to SEM implies that CSD performs better in capturing the sensitivity field at the same resolution. The fact that the obtained apparent accuracy for CSD is one order higher than its formal accuracy can be addressed to the choice of coarsest grid (50×50) and its performance at this resolution. Furthermore, the corresponding GCIs for CSD/DNS and SEM/DNS are obtained equal to 0.036 and 0.196, respectively, as shown in Table 3.3. It implies more than five times less uncertainty in the performance of CSD. This can be explained by this fact that, there is no additional sensitivity equation to be solved in CSD, in addition to the momentum equations.

This significant advantage of CSD over SEM can be attributed to two interrelated factors. On the one hand, there is just one Poisson equation (albeit complex) associated with the momentum equation that needs to be solved in CSD. In contrast, there is an *extra* Poisson equation associated with the sensitivity field in SEM that must be solved. In the results shown thus far, both CSD and SEM used the same convergence criterion in order to prevent biasing the comparison. However, it was found, by trial and error, that the iterative Poisson solver in SEM required a tighter convergence criterion compared to that used in CSD to yield the same results. The reason for thid id believed to stem from additional errors incurred in the SEM solver due to the presence of the source term involves the second derivative of the velocity field, which when evaluated numerically introduces noise into the solution. This especially occurs in regions of the velocity field exhibiting a high change in gradients, as would be the case near the periphery of the coherent vortices.

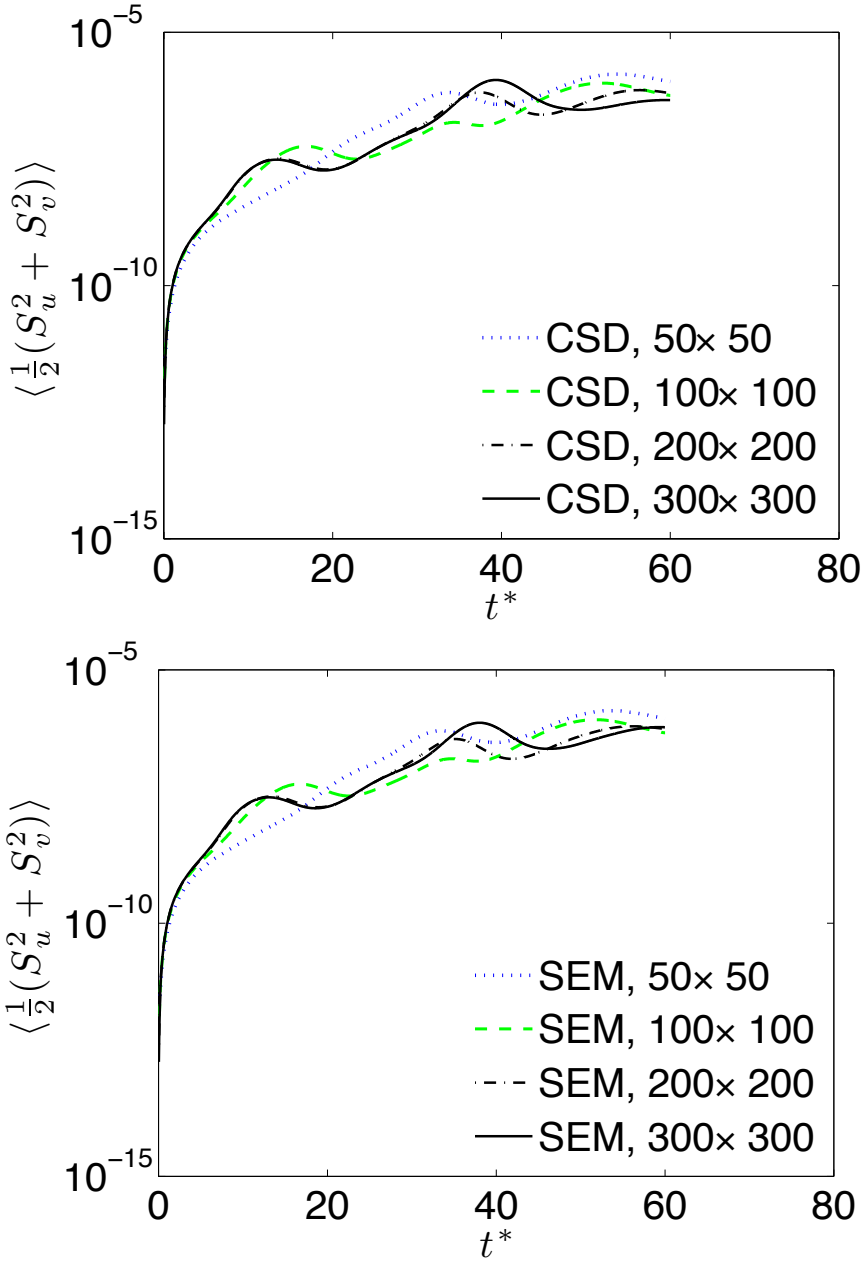

Figure 3.6. Comparison between CSD (left) and SEM (right) values of $\langle \frac{1}{2}(\mathcal{S}^2_{u,Re_{\delta_0}} + \mathcal{S}^2_{v,Re_{\delta_0}}) \rangle$ as a local spatial averaged quantity used in GCI.

Table 3.3. Comparison between the apparent order of accuracy and GCI of CSD and SEM in directly capturing the sensitivity coefficients.

	$\widehat{p}$	GCI
CSD/DNS:	3.09	0.036
SEM/DNS:	2.040	0.196

3.6.2 Sensitivity of the Resolved Vorticity to Re_{δ_0}

The question of interest here is whether the sensitivity pattern of the resolved vorticity field, $\mathcal{S}_{\widetilde{u}_i,Re_{\delta_0}}$, can reliably mimic and approximate the topology of the sensitivity field observed in the DNS data. If so, then LES might be a promising cost effective solution for computational sensitivity analysis at higher Re_{δ_0}. Figure 3.7 shows snapshots of the instantaneous sensitivity of the resolved vorticity to changes in Re_{δ_0} (i.e., $\mathcal{S}_{\widetilde{\omega},Re_{\delta_0}}$) at $Re_{\delta_0} = 500$ from LES using the standard Smagorinsky model. Again, the three snapshots correspond to: (i) the formation, (ii) the first pairing, and (iii) the second paring of the four K-H vortices. Similar to Fig. 3.2, the left column represents the sensitivity field obtained from CSD/LES, while the right column shows the sensitivity field from SEM/LES. The CSD/LES and SEM/LES simulations are both performed at a resolution of 200×200 and shown with the same colorbar. Finally, Fig. 3.8 indicates the *filtered DNS sensitivity field*, denoted as $\widetilde{\mathcal{S}}_{\omega,Re_{\delta_0}}$, at 350×350 resolution but then filtered to a 200×200 grid. Note, a separate colorbar is used for the filtered DNS sensitivity because the ranges were quite different than that from the LES runs, especially in the first pairing.

Interestingly, Fig. 3.7 reveals that the sensitivity of the resolved vorticity to Re_{δ_0} obtained from LES using the standard Smagorinsky model exhibits similar features and properties as that observed in the filtered DNS data up to the second pairing. However, the magnitude of the filtered DNS sensitivity field in general remains higher than that computed from the LES. The relative percentage differences in the range of the resolved sensitivity field corresponding to the three snapshots in Fig. 3.7, are 33%, 80%, and 50% compared to the filtered DNS data shown in Fig. 3.8. At this point, it is unclear why the maximum difference in the magnitudes occurs during the first pairing. However, one may speculate that this is due to the high curvature in the velocity field that exist during this stage in the evolution, which translates into a high source term in the LES sensitivity equations that can not be adequately resolved or modeled in the present framework. Qualitatively, though, the sensitivity structures are at least presented in the first pairing. The ability of the LES to capture the fine-scale details (thin striated dark and light bands of high and low sensitivity) degrades significantly by the time of the second pairing. This is likely due to the limitations in the Smagorinsky model, which adopts a constant model coefficient, C_s.

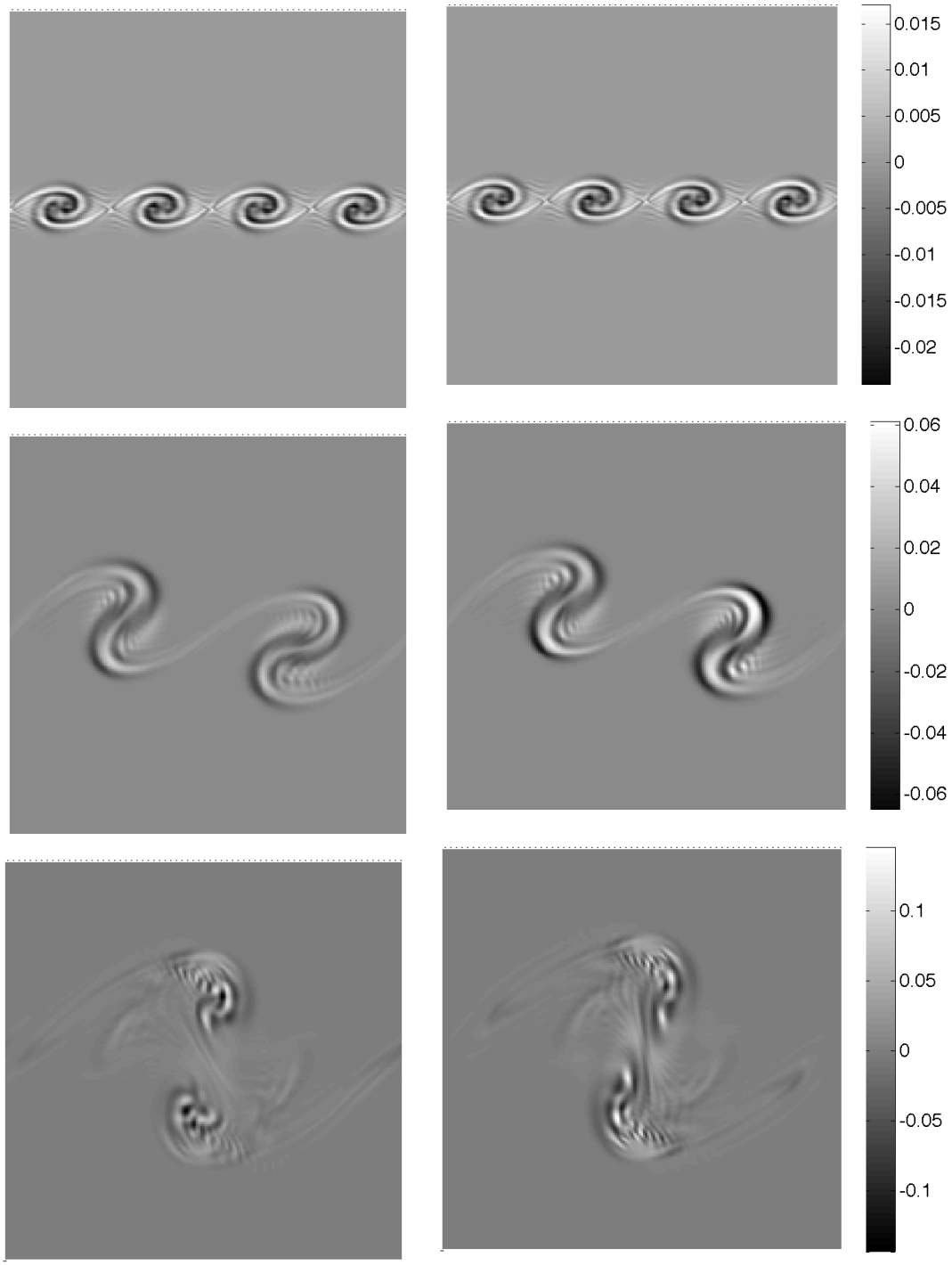

Figure 3.7. Sensitivity of the resolved vorticity to Reynolds number, $\mathcal{S}_{\widetilde{\omega},Re_{\delta_0}}$, at $Re_\delta = 500$ and resolution 200×200: CSD/LES (left column), SEM/LES (right column). Both LES cases (left and right columns) utilizes the standard Smagorinsky model.

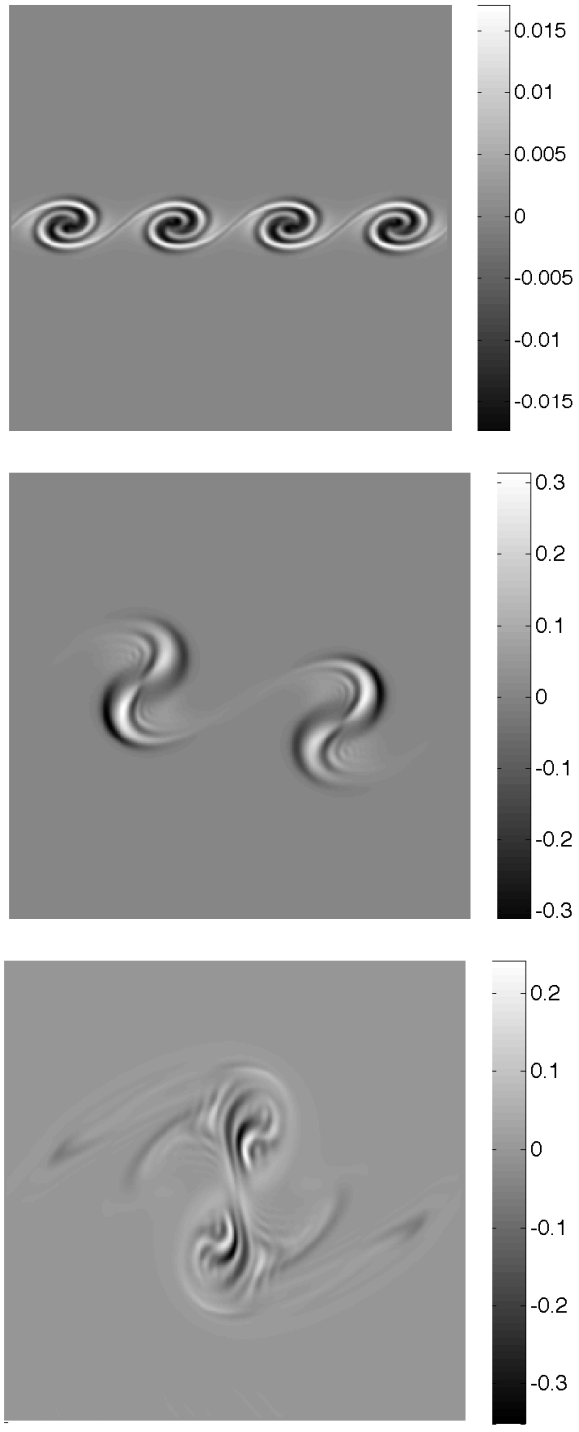

Figure 3.8. Filtered sensitivity of the vorticity to Reynolds number, $\widetilde{\mathcal{S}}_{\omega,Re_{\delta_0}}$, at $Re_\delta = 500$.

Table 3.4. The percentage of error $\epsilon^{ref.}$ between the *pdf* of the CSD/LES and SEM/LES, obtained from standard Smagorinsky model at resolution 200×200, compared to the filtered fine-grid reference case, at grid resolution 350×350

	Formation	1^{st} Pairing	2^{nd} Pairing
CSD/LES(standard):	0.84	8.1	6.1
SEM/LES(standard):	0.84	18.2	5.1

In order to qualitatively compare CSD/LES to SEM/LES, again the relative error in the *pdf*'s is calculated as

$$\epsilon = \frac{\|pdf^{\widetilde{DNS}} - pdf^{LES}\|}{\|pdf^{\widetilde{DNS}}\|} \times 100, \tag{3.43}$$

where $pdf^{\widetilde{DNS}}$ denotes the probability density function associated with the filtered CSD*. Table 3.4 lists the percentage error between the *pdf*'s of CSD/LES and SEM/LES shown in Fig. 3.9 with respect to the filtered DNS sensitivity field. In terms of ϵ, both methods perform the same in the formation stage. The error grows in each approach, albeit faster for the case of the SEM/LES, reaching a maximum at the time of the first pairing, and decreasing slightly by the time of the second pairing, consistent with the visual observation described above.

The dynamic Smagorinsky model, explained in Sec. 3.4.2, is also examined in order to determine whether increasing the sophistication of the LES model yields a resolved velocity field that matches more closely with the filtered DNS results. Figure 3.10 presents the comparison between the CSD/LES and SEM/LES for the case of the dynamic Smagorinsky model using a grid resolution of 200×200. Visually, there is no dramatic difference between the performance of the standard and dynamic LES models relative to each other. However, in terms of the error in the *pdf*'s shown in Fig. 3.11, as calculated using (3.43), the dynamic model produces less error in the first pairing compared to the standard model (see Table 3.5). Specifically, SEM/LES with the dynamic model shows a 14% error reduction in the first pairing, compared to that obtained from the standard model; while CSD/LES achieves a 4% reduction in error by implementing the dynamic model. The error in the formation and second stages remains essentially equivalent to that calculated from the standard model.

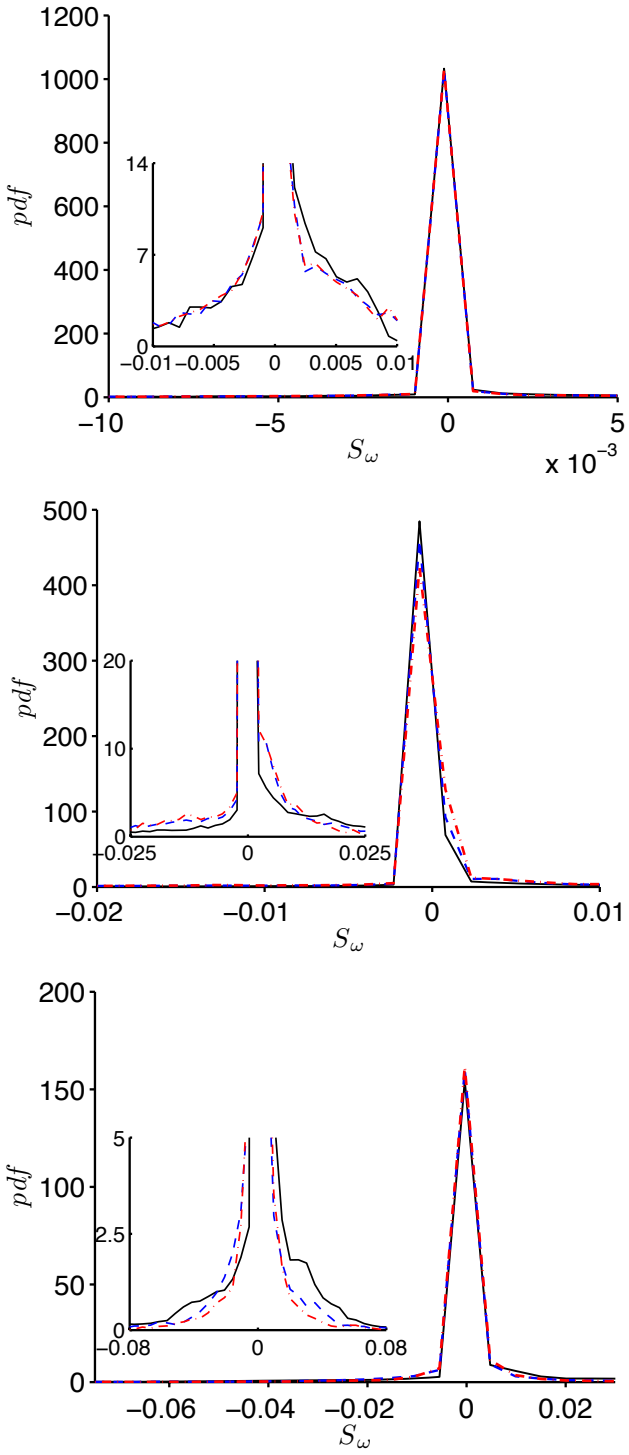

Figure 3.9. The comparison between the pdf's of the $\mathcal{S}_{\widetilde{\omega},Re_{\delta_0}}$ for the the three stages: formation (top), first pairing (middle) and second pairing (bottom), obtained from CSD/LES shown by dash-dotted line $(- \cdot -)$, SEM/LES indicated by dashed line $(--)$ and filtered CSD* denoted by solid line $(-)$. In the CSD/LES and SEM/LES caluculations, the standard Smagorinky model is employed.

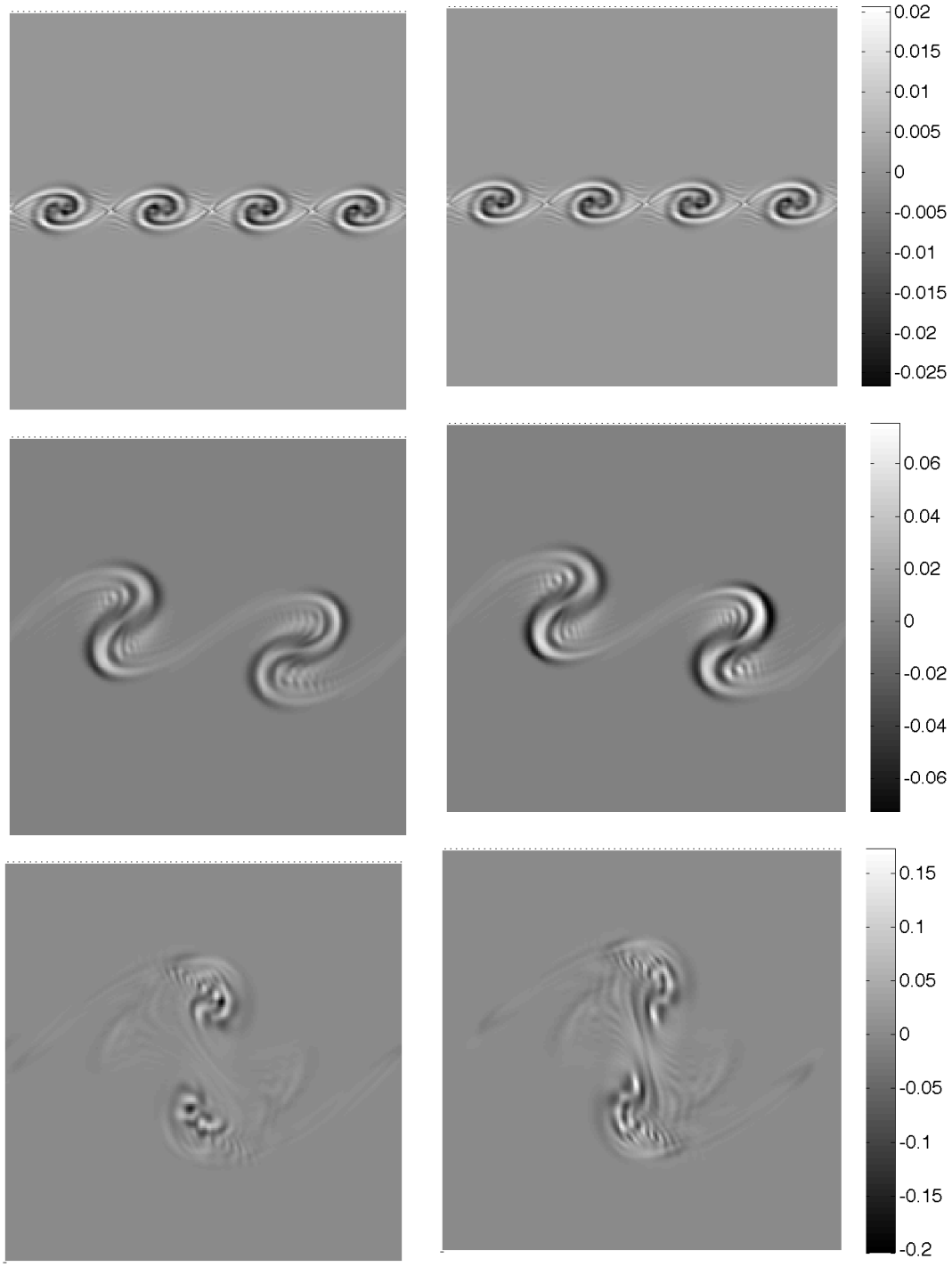

Figure 3.10. Sensitivity of the resolved vorticity to Reynolds number, $\mathcal{S}_{\widetilde{\omega},Re_{\delta_0}}$, at $Re_\delta = 500$ and resolution 200×200: CSD/LES (left column), SEM/LES (right column). Both LES cases (left and right columns) utilizes the dynamic Smagorinsky model.

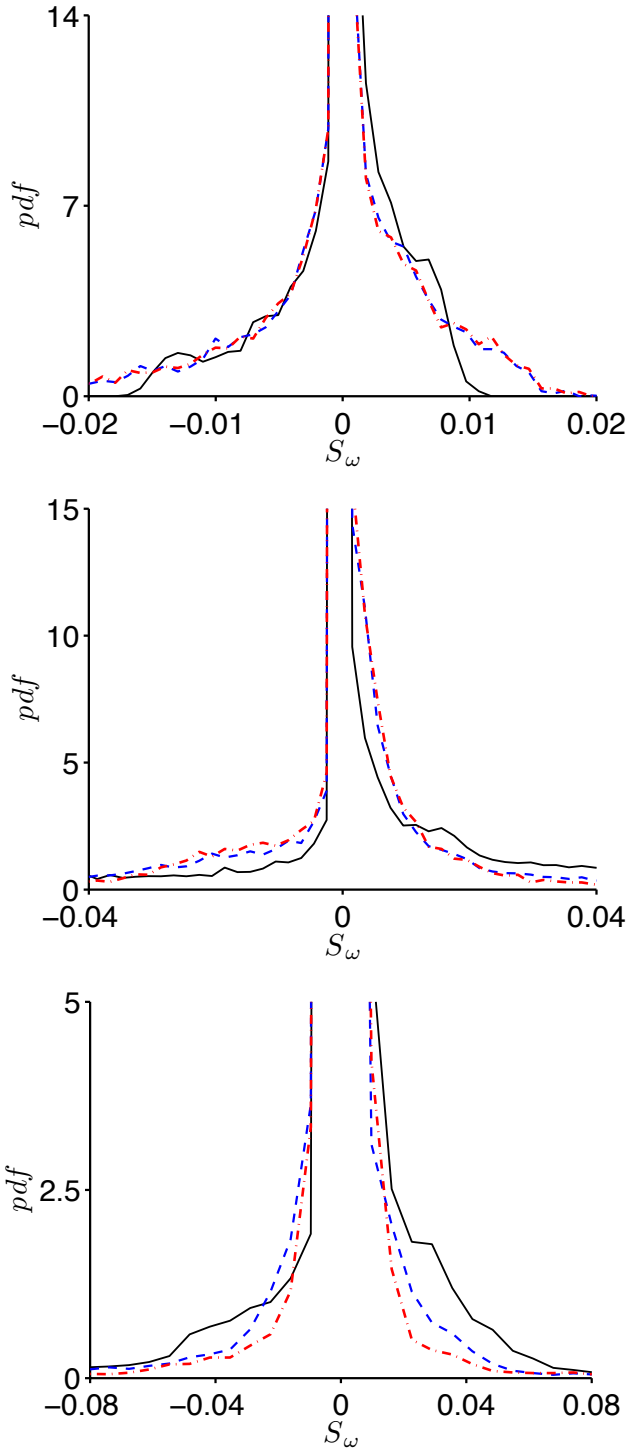

Figure 3.11. Comparison between $pdf^{'}s$ of $\mathcal{S}_{\widetilde{\omega},Re_{\delta_0}}$ from CSD/LES shown by dash-dotted line $(-\cdot-)$, SEM/LES indicated by dashed line $(--)$ at $Re_\delta = 500$ and resolution 200×200, and filtered CSD* denoted by solid line $(-)$ utilizing the dynamic Smagorinsky model.

Table 3.5. The percentage of error $\epsilon^{ref.}$ between the *pdf* of the CSD/LES and SEM/LES, obtained from dynamic Smagorinsky model at resolution 200×200, compared to the filtered fine-grid reference case, at grid resolution 350×350.

	Formation	1^{st} Pairing	2^{nd} Pairing
CSD/LES(dynamic):	0.9	4	7.5
CSD/LES(dynamic):	0.9	3.9	6.5

3.6.3 Computational Time

The comparison between the computational time required for each sensitivity method is another relevant resource of performance, and one may argue that it is even more important than accuracy in terms of assessing the feasibility of practically incorporating computational sensitivity analysis into optimization and control strategies.

Figure 3.12 shows CPU time plotted versus the nondimensional time t^*, corresponding to the evolution of the flow. Here, all CPU times have been normalized by the CPU time of the SEM/DNS at $t* = 60$. Near the beginning of the simulation SEM requires substantially more CPU time compared to CSD. for $t^* = 10$, after the formation stage; however, CPU time for both CSD and SEM appears to increase linearly with t^* at nearly the same rate implying that both methods computationally cost the same as far as computing time after the formation stage. This is true for both DNS and LES.

This observation underscores the fact that SEM is much more time consuming than CSD at initial time levels. This behavior most likely originates from the nature of the multigrid technique used to solve the sensitivity Poisson equation in SEM, which demands many iterations to converge from the zero-valued initialization at the beginning of the simulations. In the case of CSD, on the other hand, the CPU time spent per time-step in the simulation remains nearly constant for the entire duration of the run.

On the whole, using the same convergence criterion in the Poisson solver for each method, CSD is shown to be surprisingly five times faster than SEM in the case of DNS, 4.4 times faster than SEM in the case of LES using Standard Model, and 4.1 times faster than SEM in the case of LES using Dynamic Model, at the end

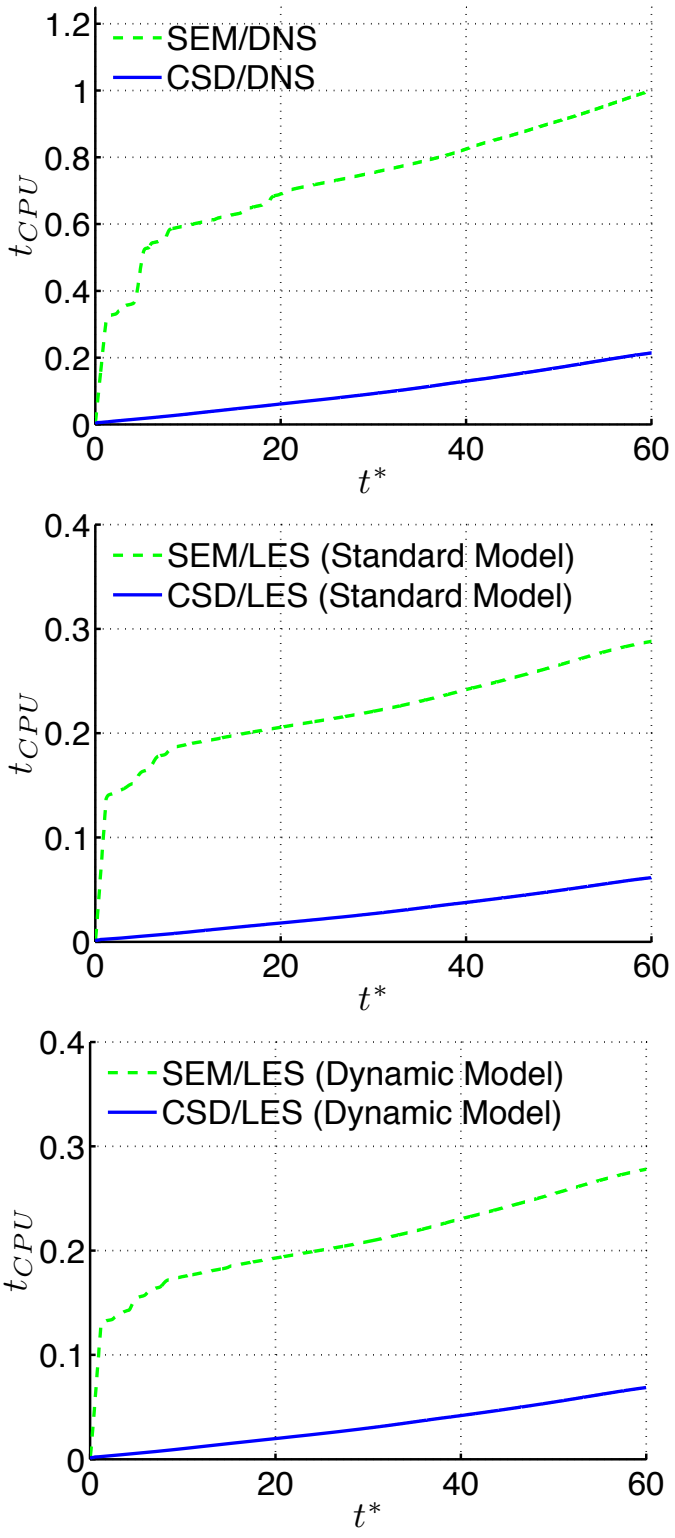

Figure 3.12. Comparison between CPU time required for SEM and CSD sensitivity calculations from DNS (top), standard Smagorinsky Model (middle) and dynamic model (bottom). All CPU times have been normalized by the CPU time of the SEM/DNS at $t^* = 60$.

of the simulations. It must be acknowledged though that different Poisson solvers may affect the overall computational time differently. So that, depending on the particular Poisson solver chosen, it may be possible to significantly decrease the CPU time required for SEM. This remains an open question.

The results in Fig. 3.12 also reveal that for the case of SEM, the SEM/LES code runs in $\approx 27\%$ of the time required for the SEM/DNS code. Little apparent difference in CPU time exists between the standard and dynamic models.

3.6.4 Sensitivity of the Resolved Vorticity to SFS Length Scale

The sensitivity of the resolved vorticity to SFS length scale l^*, i.e., $\mathcal{S}_{\omega,l^*}$, at $Re_{\delta_0} = 500$ and using a grid resolution of 200×200, are shown in Fig. 3.13 and 3.14 for both CSD and SEM, respectively. The information in $\mathcal{S}_{\omega,l^*}$ reveals how perturbations in the choice of the Smagorinsky constant C_s and/or filter-width Δ (i.e., the grid resolution) affects the evolution of coherent structures in the mixing layer. In the Smagorinsky model, C_s is a modulation factor for the filter-width; therefore, it makes more sense to examine the sensitivity of the product of C_s and Δ rather than the sensitivity of each separately.

Figures 3.13 and 3.14 show the three snapshots of vorticity sensitivity to l^* corresponding to the formation of the four K-H vortices, first pairing, and finally second pairing. In this case, the same two-blade structure is observed as before, except with the opposite sign, i.e., light and dark bands are reversed compared to the case observed in $\mathcal{S}_\omega$ (see Fig. 3.2).

Therefore, the interpretation of the $\mathcal{S}_{\omega,l^*}$ sensitivity field is that an increase in l^* serves to decrease the growth of mixing layer. This can be related to the fact that the eddy-viscosity ν_τ is proportionally to l^{*2} (see 3.18); and, as a result, an increase in l^* translates into an increase in the eddy-viscosity. Considering the momentum equations (3.4) with the Reynolds number expressed in terms of the total viscosity (i.e.,$Re_{\delta_0} = U\delta_0/\nu_{total}$, where $\nu_{total} = \nu + \nu_\tau$), it is clear that Re_{δ_0} decreases inversely proportional to ν_{total} (or ν_τ). Thus, as the SFS length scale l^* increases,the effective Reynolds number decreases, which would be expected to be accompanied by a reduction in the growth of the mixing layer, based on the previous interpretation of $\mathcal{S}_\omega$ outlined in Chap. 2. Specifically, using the first-order Taylor expansion, as shown

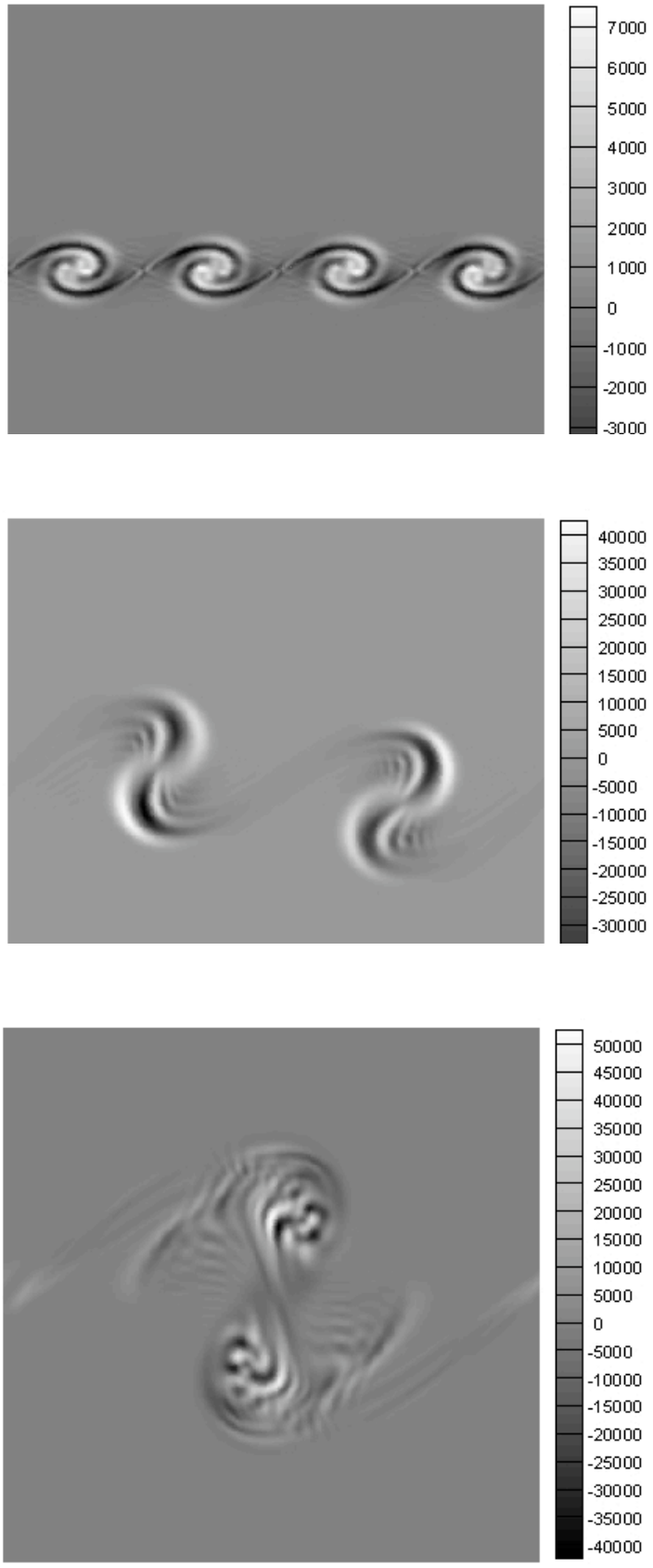

Figure 3.13. $\mathcal{S}_{\widetilde{\omega},Re_{\delta_0}}$ using CSD and the standard model, at $Re_\delta = 500$.

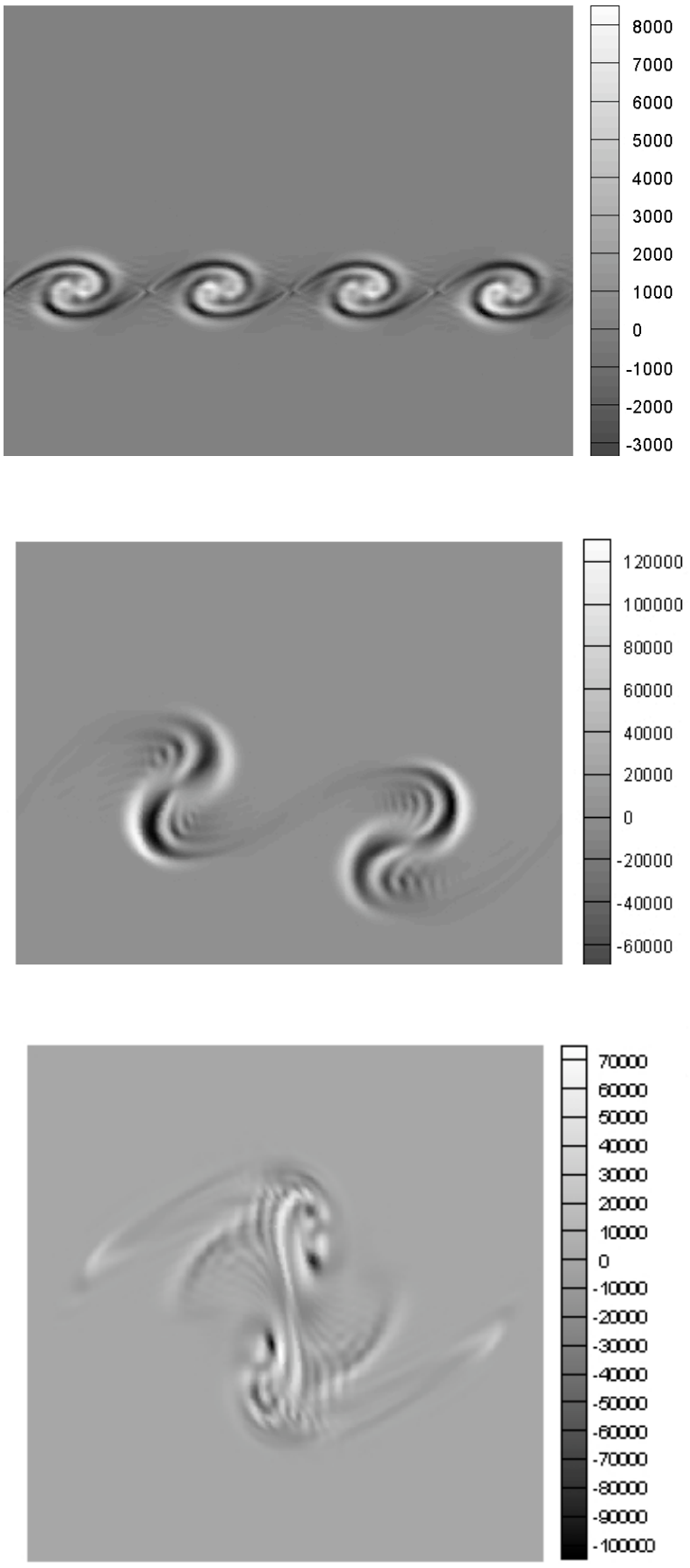

Figure 3.14. $\mathcal{S}_{\widetilde{\omega},Re_{\delta_0}}$ using SEM and the standard model, at $Re_\delta = 500$.

in Sec. 2.6.2, one can deduce that the highly positive areas of sensitivity (white bands) around the periphery of each vortex indicate that the vorticity in this region will become less negative with an increase in l^* , leading to a reduction in the size of the vortices.

The comparison between the CSD and SEM results shows that both methods qualitatively produce the same sensitivity pattern up to the second pairing. However, a noticeable disparity exists between CSD and SEM regarding the range of $\mathcal{S}_{\omega,l^*}$ with SEM/LES consistently yielding higher magnitude of sensitivity at each stage in the evolution of the flow.

The larger magnitudes of $\mathcal{S}_{\omega,l^*}$ is surmised to be an overestimation of the sensitivity due to the existence of the source term in SEM, which can amplify noise in the solution because of the numerical gradient of u_i.

3.7 Coherency of the Sensitivity Field at Higher Re_{δ_0}

In order to examine whether the two-blade structures in the vorticity sensitivity field observed at Re_{δ_0} persists at higher Reynolds numbers, CSD/DNS was performed at $Re_\delta = 1000$ and using a grid resolution of 512×512 along with CSD/LES at $Re_\delta = 2000$ using a grid resolution of 350×350. Results are shown in Fig. 3.15 and 3.16 respectively. The comparison between the DNS and LES sensitivity fields presented in Sec. 3.6.1 and Sec. 3.6.2 at $Re_\delta = 500$ and those observed in Fig. 3.15 and 3.16 at higher Re_δ reveals that: (i) the same coherent two-blade sensitivity feature is apparent at higher Re_{δ_0} in both the DNS and LES data sets, (ii) the order of magnitude of the sensitivity of vorticity to Re_δ decreases with increasing Re_δ retaining the pattern of the sensitivity field, and (iii) the structures in the coherent sensitivity field exhibit thinner lamellae of light (positive) and dark (negative) sensitivity, indicative of higher sensitivity gradients in the sensitivity fields of mixing layer at higher Re_{δ_0}.

3.8 Filtered Momentum Sensitivity Equation

The filtered momentum sensitivity equationa is obtained by filtering (3.7) using a low-pass filter as that in (3.12) giving

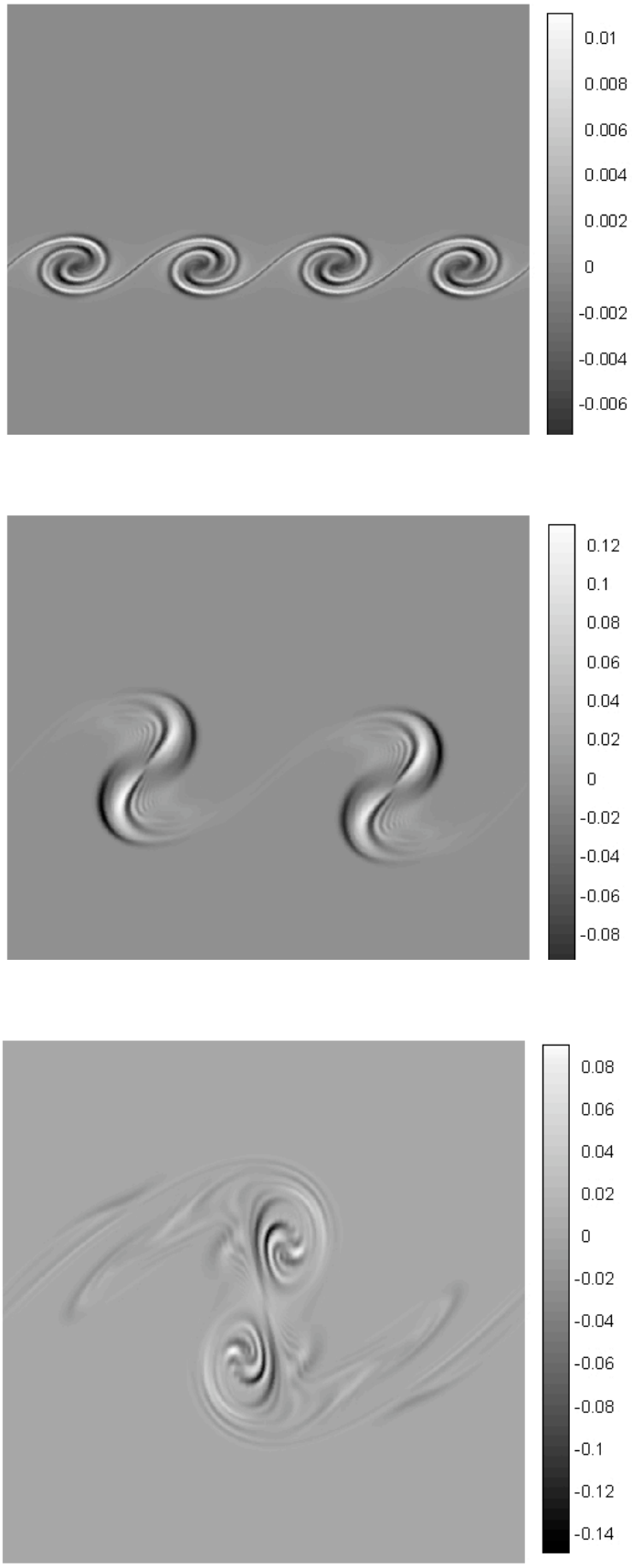

Figure 3.15. Direct $\mathcal{S}_\omega$, at $Re_\delta = 1000$, using CSD/DNS at 512×512 resolution.

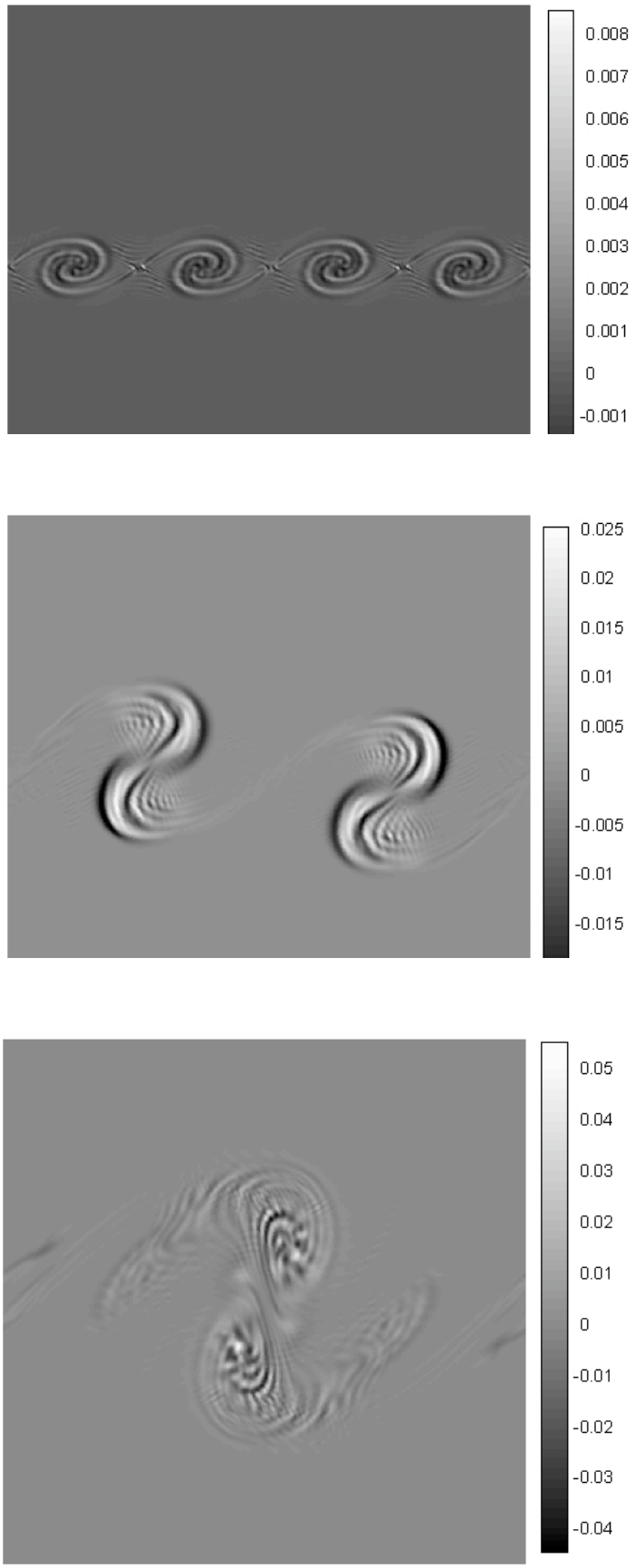

Figure 3.16. $\mathcal{S}_{\widetilde{\omega},Re_{\delta_0}}$, at $Re_\delta = 2000$ using CSD/LES at 350×350 resolution.

$$\frac{\partial \widetilde{\mathcal{S}}_{u_i}}{\partial t} + \frac{\partial\left(\widetilde{\mathcal{S}}_{u_i}\widetilde{u}_j\right)}{\partial x_j} = -\frac{\partial \widetilde{\mathcal{S}}_p}{\partial x_i} + \frac{1}{Re_L}\frac{\partial}{\partial x_j}\left(\frac{\partial \widetilde{\mathcal{S}}_{u_i}}{\partial x_j} + \frac{\partial \widetilde{\mathcal{S}}_{u_i}}{\partial x_i}\right) \tag{3.44}$$
$$-\frac{1}{(N\lambda_a/\delta_0)Re_{\delta_0}^2}\frac{\partial}{\partial x_j}\left(\frac{\partial \widetilde{u}_i}{\partial x_j} + \frac{\partial \widetilde{u}_j}{\partial x_i}\right) - \frac{\partial\left(\widetilde{u}_i\,\widetilde{\mathcal{S}}_{u_j}\right)}{\partial x_j} - \frac{\partial \mathcal{S}_{\tau_{ij}}}{\partial x_j}.$$

Equation, (3.44) includes an unclosed term, $\mathcal{S}_{\tau_{ij}}$, which looks like the SFS stress tensor τ_{ij} that appears in (3.14), and may be written as

$$\mathcal{S}_{\tau_{ij},Re_{\delta_0}} \equiv \partial(\widetilde{u_i u_j} - \widetilde{u}_i\widetilde{u}_j)/\partial Re_{\delta_0} = \mathcal{L}_{ij} - \mathcal{L}_{ij}^T, \tag{3.45}$$

where

$$\mathcal{L}_{ij} = \widetilde{\mathcal{S}_{u_i} u_j} - \widetilde{\mathcal{S}}_{u_i}\widetilde{u}_j \tag{3.46}$$

Note, the solution of (3.44) yields the *resolved* sensitivity of velocity, $\widetilde{\mathcal{S}}_{u_i,Re_{\delta_0}}$, as opposed to the solution of (3.25), which yields the sensitivity of the *resolved* velocity, $\mathcal{S}_{\widetilde{u}_i,Re_{\delta_0}}$. The difference, of course, stems from whether the filter is applied before differentiating with respect to Re_{δ_0} or after. The performance of $\widetilde{\mathcal{S}}_{u_i,Re_{\delta_0}}$ depends on the sub-grid scale model used to model $\mathcal{L}_{ij}$. If this can be done accurately, then the hypothesis is that $\widetilde{\mathcal{S}}_{u_i,Re_{\delta_0}}$ approaches $\widetilde{\mathcal{S}}_{u_i,Re_{\delta_0}}$. Indeed, the closure problem here requires serious thought. Because (3.44) contains additional source terms compared to the analogous filtered momentum equations (3.14), it is not clear that a Smagorinsky-type model will extend straightforwardly for $\mathcal{L}$. Therefore, this approach has not been pursued further in the present study.

3.9 Concluding Remarks

A posteriori study of two nonparametric sensitivity analysis methods namely complex-step differentiation (CSD) and sensitivity equation method (SEM) was performed. This is done in the context of two-dimensional temporal mixing layer. The simulations were run at a baseline $Re_{\delta_0} = 500$ by direct numerical simulation (DNS) and large eddy simulation (LES), using standard and dynamic Smagorinsky model, using the same numerics.

The *two-blade sensitivity structure* in the sensitivity of vorticity (to Re_{δ_0}) reported in Chap. 2 was re-captured and generalized to higher Reynolds numbers with some modifications. It was shown that the coherent pattern of the sensitivity field (to Re_{δ_0}) undergoes a switch to another chaotic structure at the second pairing snapshot and

$Re_{\delta_0} \geqslant 350$. The generalized sensitivity feature implies a faster self-similar, and fully developed turbulent state in the mixing layer at higher Reynolds numbers.

A posteriori study revealed that both CSD and SEM methods show excellent agreement in capturing the instantaneous sensitivity fields until the first pairing in DNS study. This was performed qualitatively using visual inspection, and quantitatively by comparing the probability density functions (*pdf*) of the sensitivity fields, compared to fine-grid sensitivity results. The error in the *pdf*s increases with simulation time in both methods. CSD performed better than SEM with about 5.8% less error in the *pdf* of sensitivity field at the second pairing compared to SEM. In addition, GCI of Roache (1997) was also used to measure the uncertainty and the apparent order of accuracy of each scheme. The GCI showed that CSD performs better than SEM in capturing the sensitivity features (to Re_{δ_0}) with one order higher accuracy and 16% less uncertainty.

In this study, CSD was successfully implemented in the context of LES using the standard and dynamic Smagorinsky models for the first time. It was shown that coherent sensitivity structures for the resolved vorticity (to Re_{δ_0}) exist in LES of the mixing layer. Both CSD/LES and SEM/LES methods were successfully able to reproduce the coherent two-blade structure in the sensitivity of resolved vorticity. The trade-off in performing the computational sensitivity analysis in the LES framework was an underestimation in the range of sensitivity compared to the filtered DNS data.

The comparison of the *pdf*$'$s in the LES sensitivity fields using the standard Smagorinsky model showed that the error in the *pdf*$'$s relative to the filtered fine-grid DNS data, increases in both methods up to a maximum error at the first pairing process. Afterwards, the error decreases till the end of the simulation as opposed to what is observed in DNS. It was reported that although CSD/LES and SEM/LES perform identically until the formation snapshot, there is a significant difference between their performances. In fact, CSD/LES simulates the coherent sensitivity field with 10.1% less error compared to SEM/LES when the standard model is used. However, both approaches meet the same order of error at the second pairing process.

Implementation of the dynamic model leads to improvement in the range of the sensitivity field compared to the filtered DNS data. Indeed, the *pdf* error variation has a similar behavior when compared to the DNS study. In this context, the error

increases as flow evolves in both CSD/LES and SEM/LES methods. In addition, the peak of *pdf* error was decreased from 8.1% to 4% in CSD/LES and from 18.2% to 3.9% in SEM/LES by replacing the standard model with dynamic Smagorinsky model.

It was shown that the implementation of CSD is very easier than SEM, without resorting to solve any extra sensitivity equation. Besides, it was presented that CSD solution was five times faster than SEM in DNS case and more than 4 times faster than SEM in LES studies.

Furthermore, the sensitivity field of resolved vorticity (to SFS length scale l^*), at $Re_{\delta_0} = 500$ were obtained using CSD and SEM. It was shown that the interpretation of the sensitivity of vorticity to l^* is consistent with decreasing $Re_{\delta_)}$. It was represented that increasing the l^* results in a decrease in the growth of the mixing layer.

CHAPTER 4

A PRIORI STUDY OF THE SMAGORINSKY MODEL

4.1 Introduction

The *a priori* study refers to the process of evaluating the performance of a subfilter scale (SFS) model in an offline mode. As such, *a priori* studies do not involve the calculation or analysis of actual LES data. Rather, an *a priori* study utilizes experimental or low-to-moderate Reynolds number DNS data to compare filtered DNS quantities with those calculated based on the SFS model. In a general sense, the objectives of the *a priori* study threefold: (i) providing a framework to establish new and testing existing LES subfilter scale (SFS) model, (ii) determining appropriate values of the LES model coefficients, and (iii) improving the understanding of the physics associated with kinetic energy transfer at the filter scale. *A priori* studies are usually conducted using experimental data or direct numerical simulations (DNS) of well-studied canonical flows, such as isotropic turbulence, channel flows and free shear flows (McMillan and Ferziger, 1979; Piomelli et al., 1988; Domoratdski et al., 1993; Hartel and Kleiser, 1993; Meneveau, 1993; Verman et al., 1995; Jimenez et al., 2001; Lu et al., 2007).

This chapter describes an *a priori* study of the standard Smagorinsky model for the case of the incompressible planar mixing layer. The new contribution here involves the additional computation of the sensitivity of the SFS model to changes in Reynolds number. This is significant because typical *a priori* studies using DNS data are performed at relatively low Reynolds numbers, but the resultant value(s) of the model coefficients are assumed to be valid at much higher Reynolds numbers. The present computational sensitivity analysis provides a quantitative means of assessing the validity of this underlying assumption. The results are shown using SEM only.

4.2 Traditional *A Priori* Study

As introduced in Chap.3, the idea behind LES is to decrease the number of degrees of freedom in the dynamical equations governing the behavior of the flow. This is achieved by filtering the high wavenumbers in the flow field using a convolution filter kernel (Sagaut, 2006),

$$\tilde{\phi}(x,t) = G(x) \star \phi(x,t) = \int_{-\infty}^{-\infty} \phi(\xi,t) G(\xi - x) d\xi. \tag{4.1}$$

In this research, a tophat (or box) filter is used, of the form

$$G(\mathbf{x} - \xi) = \begin{cases} \frac{1}{\Delta} & |\mathbf{x} - \xi| \leq \frac{\Delta}{2}, \\ 0 & otherwise, \end{cases} \tag{4.2}$$

where Δ denotes the filter width. In the standard Smagorinsky model, Δ is typically chosen as $\Delta = (dx\, dy)^{1/2}$ in 2D sense (Verman et al., 1995).

The spatially filtered Navier-Stokes equations that govern unsteady, incompressible flow with no body force can be written nondimensionally as

$$\frac{\partial \widetilde{u}_i}{\partial t} + \frac{\partial (\widetilde{u}_i \widetilde{u}_j)}{\partial x_j} = -\frac{\partial \widetilde{p}}{\partial x_i} + \frac{1}{Re_L} \frac{\partial}{\partial x_j} \left[\left(\frac{\partial \widetilde{u}_i}{\partial x_j} + \frac{\partial \widetilde{u}_j}{\partial x_i} \right) \right] - \frac{\partial \tau_{ij}}{\partial x_j}, \tag{4.3}$$

where $\tilde{.}$ represents the resolved quantity obtained by taking the convolution of the governing equations (2.7) to the Kernel filter. The subfilter-scale stress tensor, τ_{ij}, is

$$\tau_{ij} = \widetilde{u_i u_j} - \widetilde{u}_i \widetilde{u}_j. \tag{4.4}$$

In fact, $\widetilde{u_i u_j}$ can not be computed directly, so τ_{ij} represents the closure problem in LES. The proposed work examines the standard Smagorinsky model, wherein τ_{ij} is modeled as

$$\tau_{ij}^M = -2\nu_\tau \widetilde{s}_{ij}. \tag{4.5}$$

Note, the superscript M stands for *model*. Here, ν_τ represents the eddy-viscosity, and $\tilde{s}_{ij}$ denotes the resolved strain rate tensor, defined mathematically as

$$\nu_\tau = (C_s \Delta)^2 \sqrt{2 \widetilde{s}_{ij} \widetilde{s}_{ij}} \quad \text{and} \quad \widetilde{s}_{ij} = \frac{1}{2} \left(\frac{\partial \widetilde{u}_i}{\partial x_j} + \frac{\partial \widetilde{u}_j}{\partial x_i} \right). \tag{4.6}$$

The parameter C_s^2 is the Smagorinsky coefficient. One way to determine C_s^2 is an *a priori* study by matching the spatially averaged SFS kinetic energy dissipation rate

extracted from the filtered DNS data, $\Pi(\equiv -\tilde{s}_{ij}\tau_{ij})$, with that modeled from the SFS model, $\Pi^M(\equiv -\tilde{s}_{ij}\tau^M_{ij})$. This leads to

$$C_s^2 \longrightarrow \langle C_s^2 \rangle = \frac{\langle -\widetilde{s}_{ij}\tau_{ij} \rangle}{\langle \Delta^2 (2\widetilde{s}_{ij}\widetilde{s}_{ij})^{3/2} \rangle} \tag{4.7}$$

Note, $\langle \cdot \rangle$ denotes a spatial average over the domain. In (4.7), the model coefficient $\langle C_s^2 \rangle$ is obtained as a spatially averaged (constant) quantity for the entire of the domain, which is in accordance with the assumption of the standard Smagorinsky model.

Because DNS data are limited to low-to-intermediate Re_{δ_0}, whereas LES has been developed to simulate high Re_{δ_0} flows, the value of $\langle C_s^2 \rangle$ obtained from (4.7) is *assumed* to be independent of Re_{δ_0} in the traditional *a priori* study. The present study describes a methodology to evaluate the premise of this assumption using computational sensitivity analysis, which could extend generally to any *a priori* study, regardless of the actual SFS model or test flow under consideration.

4.3 Incorporation of SEM in the *A Priori* Study

SEM provides a powerful tool to determine the Re_{δ_0} dependency of $\langle C_s^2 \rangle$ by means of calculating $\mathcal{S}_{\langle C_s^2 \rangle, Re_{\delta_0}}$ $(\equiv \partial \langle C_s^2 \rangle / \partial Re_{\delta_0})$. Taking the partial derivative of $\langle C_s^2 \rangle$ with respect to Re_{δ_0} yields

$$\mathcal{S}_{\langle C_s^2 \rangle, Re_{\delta_0}} = \frac{\langle \mathcal{S}_{\Pi, Re_{\delta_0}} + 3\tau^M_{ij}\mathcal{S}_{\widetilde{s}_{ij}, Re_{\delta_0}} \rangle}{\langle \Delta^2 (2\widetilde{s}_{ij}\widetilde{s}_{ij})^{3/2} \rangle}, \tag{4.8}$$

where $\mathcal{S}_{\widetilde{s}_{ij}, Re_{\delta_0}} (\equiv \partial \widetilde{s}_{ij} / \partial Re_{\delta_0})$ is the sensitivity of the *filtered strain rate* tensor to Re_{δ_0} and $\mathcal{S}_{\Pi, Re_{\delta_0}} (\equiv \partial \Pi / \partial Re_{\delta_0})$ is the sensitivity of the kinetic energy dissipation rate to Re_{δ_0}. Because the filtering operator is commutative, therefore

$$\mathcal{S}_{\widetilde{s}_{ij}, Re_{\delta_0}} = \widetilde{\mathcal{S}}_{s_{ij}, Re_{\delta_0}} = \frac{1}{2}(\partial \widetilde{\mathcal{S}}_{u_i, Re_{\delta_0}} / \partial x_j + \partial \widetilde{\mathcal{S}}_{u_j, Re_{\delta_0}} / \partial x_i) \tag{4.9}$$

where $\widetilde{\mathcal{S}}_{u_i, Re_{\delta_0}}$ represents the resolved sensitivity of the velocity to Reynolds number obtained by filtering the SEM results from Sec. 2.4.2. similarly, the sensitivity of kinetic energy dissipation rate to Re_{δ_0} is obtained from the filtered DNS data as

$$\mathcal{S}_{\Pi, Re_{\delta_0}} = -\frac{\partial (\widetilde{s}_{ij}\tau_{ij})}{\partial Re_\delta} = -\left(\widetilde{s}_{ij}\mathcal{S}_{\tau_{ij}, Re_{\delta_0}} + \tau_{ij}\widetilde{\mathcal{S}}_{s_{ij}, Re_{\delta_0}} \right). \tag{4.10}$$

In the case of the standard Smagorinsky model it is assumed that $\mathcal{S}_{\langle C_s^2 \rangle, Re_{\delta_0}} \approx 0$.

4.4 Sensitivity of the Modeled SFS Stress Tensor

Another aspect of typical *a priori* studies involves evaluation the correlation between the physical and modeled SFS stress tensor, i.e., the correlation between τ_{ij} and τ_{ij}^M. Of course a faithful and accurate model should exhibit a high correlation between τ_{ij} and τ_{ij}^M in order to help ensure that the LES reproduces the important physical features of the flow. It is also proposed that the model should demonstrate good correlation between $\mathcal{S}_{\tau_{ij},Re_{\delta_0}}$ and $\mathcal{S}_{\tau_{ij}^M,Re_{\delta_0}}$. The sensitivity of the modeled SFS stress tensor obtained using the standard Smagorinsky model can be written as

$$\mathcal{S}_{\tau_{ij}^M,Re_{\delta_0}} = \frac{\partial(-2\nu_\tau \widetilde{s}_{ij})}{\partial Re_{\delta_0}} = -2\nu_\tau \widetilde{\Gamma}_{ij}, \tag{4.11}$$

where ν_τ is the same eddy-viscosity given in (3.18), and

$$\widetilde{\Gamma}_{ij} = 2\,\widetilde{\mathcal{S}}_{s_{ij},Re_{\delta_0}} + \left(\frac{1}{\langle C_s^2\rangle}\mathcal{S}_{\langle C_s^2\rangle,Re_{\delta_0}}\right)\widetilde{s}_{ij}. \tag{4.12}$$

4.5 Results

4.5.1 Smagorinsky Coefficient

As mentioned earlier, one of the main objectives of the *a priori* study is to determine the appropriate value(s) to use for the LES model coefficient(s). In the present study, this involves tuning the Smagorinsky model coefficient C_s^2 as an unknown parameter and modulation factor for the filter-width. In fact, the wrong choice of the model parameter may cause the LES to extract an improper amount of energy from the larger, energy-containing scales of the fluid motion, which affects the evolution of the mixing layer and statistics of the turbulence within the shear layer. The spatially-averaged Smagorinsky coefficient $\langle C_s^2\rangle$ obtained based on (4.7) at $Re_{\delta_0} = 100$, 300 and 500 is shown in Fig. 4.1. Note, to avoid the singularity problem in calculation of $\langle C_s^2\rangle$ using (4.7), and corresponding modeled SFS stress tensor using (4.11), the *a priori* study is begun at $t^* = 5$. However, the *a priori* study algorithm is decoupled from the flow solver, and the LES model is evaluated in a passive sense. Therefore, this time delay does not affect the DNS solution.

The standard Smagorinsky model requires the use of a constant coefficient, variations in the magnitude and sign of $\langle C_s^2\rangle$ as a function of t^* are viewed as adverse qualities of the model. Several observations can be made regarding Fig. 4.1. First of all, the Smagorinsky coefficient $\langle C_s^2\rangle$ versus time t^* is neither constant nor always

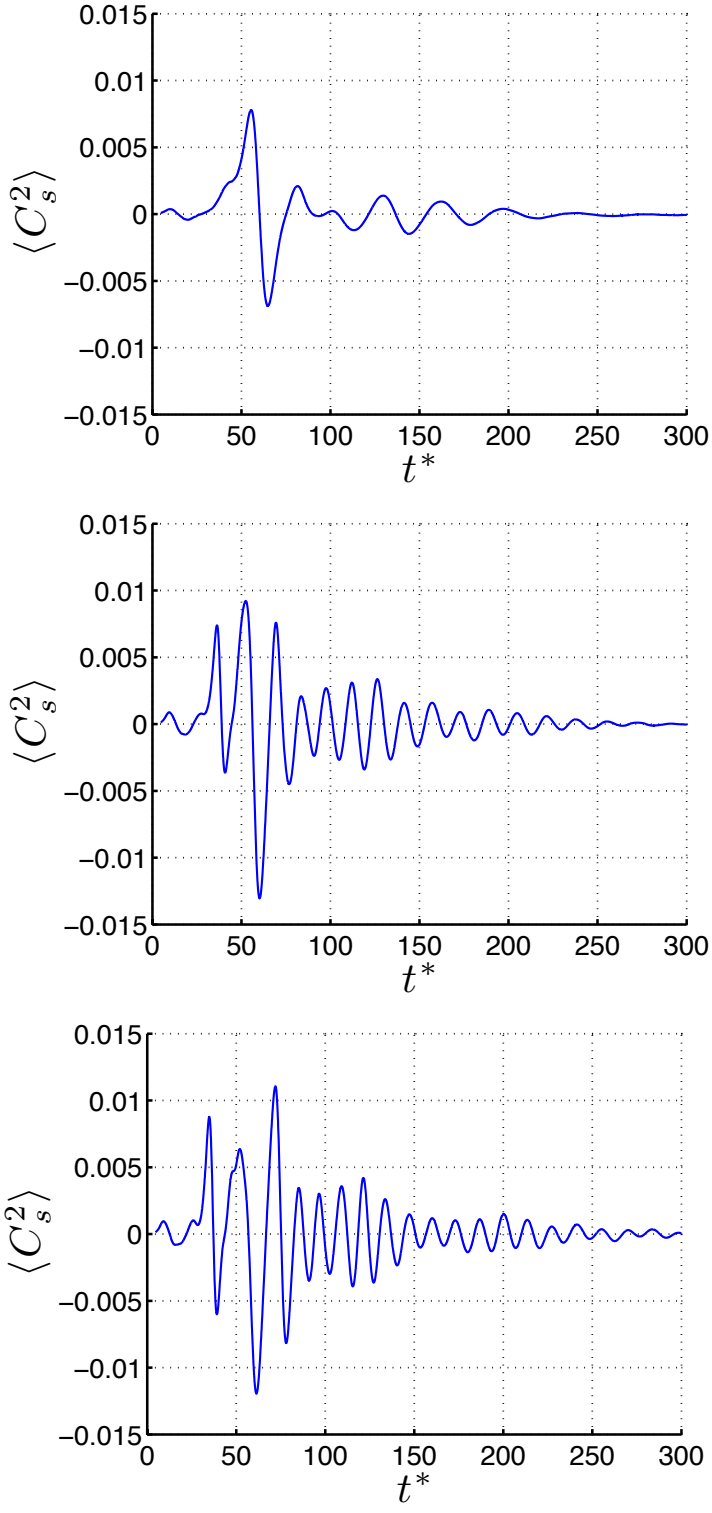

Figure 4.1. The spatially-averaged Smagorinsky constant, $\langle C_s^2 \rangle$, as a function of time evolution of the flow at $Re_{\delta_0} = 100, 300$ and 500, from top to bottom, respectively, and using the same resolution of 350×350.

positive. Indeed, it oscillates about $\langle C_s^2 \rangle = 0$ with a noticeably higher frequency after the occurrence of the second pairing at $t^* \approx 60$. Second of all, The frequency of all oscillations in $\langle C_s^2 \rangle$ also appears to increases with Re_{δ_0}, which indicates a reduction in the time-scales of the SFS kinetic energy dissipation at higher Reynolds numbers. Besides, the global maximum and minimum of $\langle C_s^2 \rangle$ occurs in the neighborhood of the second pairing, implying the strongest interaction between the SFS and the larger scales of the motion at this stage in the evolution. Finally, as the flow approaches the asymptotic state, the oscillations in $\langle C_s^2 \rangle$ dampen and the time required to reach a steady-state value increases with Re_{δ_0}.

4.5.2 Kinetic Energy Dissipation Rate

Another important aspect of an *a priori* study is to better understand the physics underlying the energy transfer between the larger and smaller scales of the motion. This can be achieved by studying the kinetic energy dissipation rate of the turbulence obtained from the filtered DNS data sets. The spatially averaged values of kinetic energy dissipation rate $\langle \Pi \rangle$ obtained from the filtered DNS data set, and corresponding values calculated from the model $\langle \Pi^M \rangle$ are shown in Fig. 4.2. The values extracted by the model are obtained using an ensemble-averaged Smagorinsky coefficient based on Fig. 4.1. The fact of the matter remains that all of the observations made above for $\langle C_s^2 \rangle$ are a consequence of the evolution of real energy transfer between the SFS and resolved scales, and the lack of ability of the standard model to adequately capture this process.

The most important difference in this regard stems from the failure of the standard model to present *back scatter* in the form of negative values of $\langle \Pi \rangle$. This occurs because $\langle \Pi^M \rangle$ remains positive definite, by definition, i.e., $\langle \Pi^M \rangle = -\widetilde{s}_{ij}\tau_{ij} = -\widetilde{s}_{ij}(-2\nu_\tau \widetilde{s}_{ij}) = 2(\widetilde{s}_{ij})^2 (C_s\Delta)^2 (2\widetilde{s}_{ij}\widetilde{s}_{ij})^{1/2}$. Thus, the standard model only succeeds in driving a forward energy cascade from large to small motions; whereas, the reverse (i.e., back scatter) is prevented altogether. At this point, one may argue that the standard Smagorinsky model does a poor job reproducing the dynamics of the kinetic energy dissipation rate in the planar mixing layer and thus should be dismissed in favor of a more appropriate model. However, because of the simplicity of the standard Smagorinsky model, it is a useful test case to adopt for purpose of demonstrating the

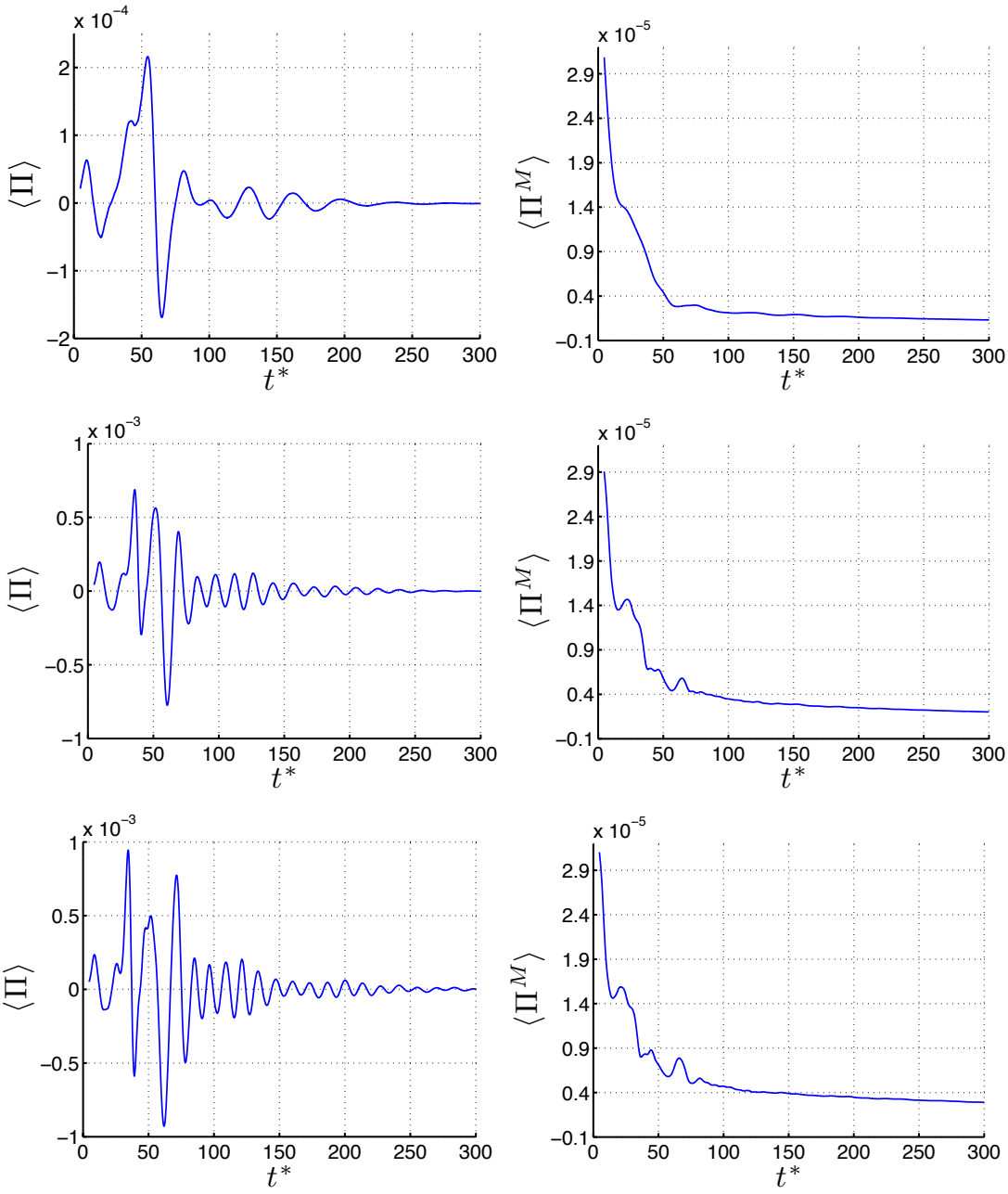

Figure 4.2. Spatially-averaged kinetic energy dissipation rate obtained from filtered DNS simulation, $\langle \Pi \rangle$, (left column), and that calculated from the Smagorinsky model, $\langle \Pi^M \rangle$, (right column). The first, second and the third row correspond to $Re_{\delta_0} = 100, 300$ and 500, respectively.

implementation of SEM in the LES framework.

Because coherent vortical structures constitute such a predominant feature of the mixing layer, they undoubtedly play a significant role in driving the subgrid scale energy dissipation. This, in fact, provides an attractive reason for using the mixing layer as a canonical test case in the *a priori* study. Figures 4.3 and 4.4 show the local distribution of Π and corresponding sensitivity of Π to Re_{δ_0} for $Re_{\delta_0} = 100$, also, Fig. 4.5 and 4.6 show the local distribution of Π and corresponding sensitivity of Π to Re_{δ_0} for $Re_{\delta_0} = 300$, and, Fig. 4.7 and 4.8 show the local distribution of Π and corresponding sensitivity of Π to Re_{δ_0} for $Re_{\delta_0} = 500$. In each figure, the top, middle, and bottom rows represent the formation stage, first pairing, and pairing, respectively.

The coherency observed in $\mathcal{S}_{\Pi,Re_{\delta_0}}$ mimics that captured in the Π field. It is apparent that by increasing Re_{δ_0} the dark (negative) and light (positive) laminates of the $\mathcal{S}_{\Pi,Re_{\delta_0}}$ sensitivity field becomes thinner. Although some similarities exist between the two-blade structure observed in $\mathcal{S}_{\omega,Re_{\delta_0}}$ and the patterns in the $\mathcal{S}_{\Pi,Re_{\delta_0}}$ fields, two major differences are noted.

The first dissimilarity is that the periphery of each vortex in $\mathcal{S}_{\Pi,Re_{\delta_0}}$ is not the place at which the maximum (negative) sensitivity occurs. The other difference is a high correspondence between the sign of Π and the sign of $\mathcal{S}_{\Pi,Re_{\delta_0}}$, i.e., regions of negative $\mathcal{S}_{\Pi,Re_{\delta_0}}$ appear to overlap regions of negative Π and visa versa; whereas in terms of vorticity, ω remains negative over the entire domain while $\mathcal{S}_{\omega,Re_{\delta_0}}$ alternates sign according to the two-blade structure discussed previously in Chap.2. Based on the first order Taylor series approximation (see Sec. 2.6), one can say that regions of positive Π and positive $\mathcal{S}_{\Pi,Re_{\delta_0}}$ indicate enhanced forward energy dissipation (higher positive Π) at higher Re_{δ_0}; and, similarly regions of negative Π and negative $\mathcal{S}_{\Pi,Re_{\delta_0}}$ indicate enhanced backward energy dissipation (higher negative Π) at higher Re_{δ_0}. Note, both the dissipation and corresponding sensitivity fields at $Re_{\delta_0} = 100$ exhibit slightly differed topology compared to the $Re_{\delta_0} = 300$ and $Re_{\delta_0} = 500$ results. Specially, the first pairing is not formed completely at $Re_{\delta_0} = 100$ as a consequence of low Reynolds number effects. This highlights the care that must be exercised when performing the *a priori* study at very low Re_{δ_0}, as flow behavior may not be adequately representative of that at higher Reynolds numbers.

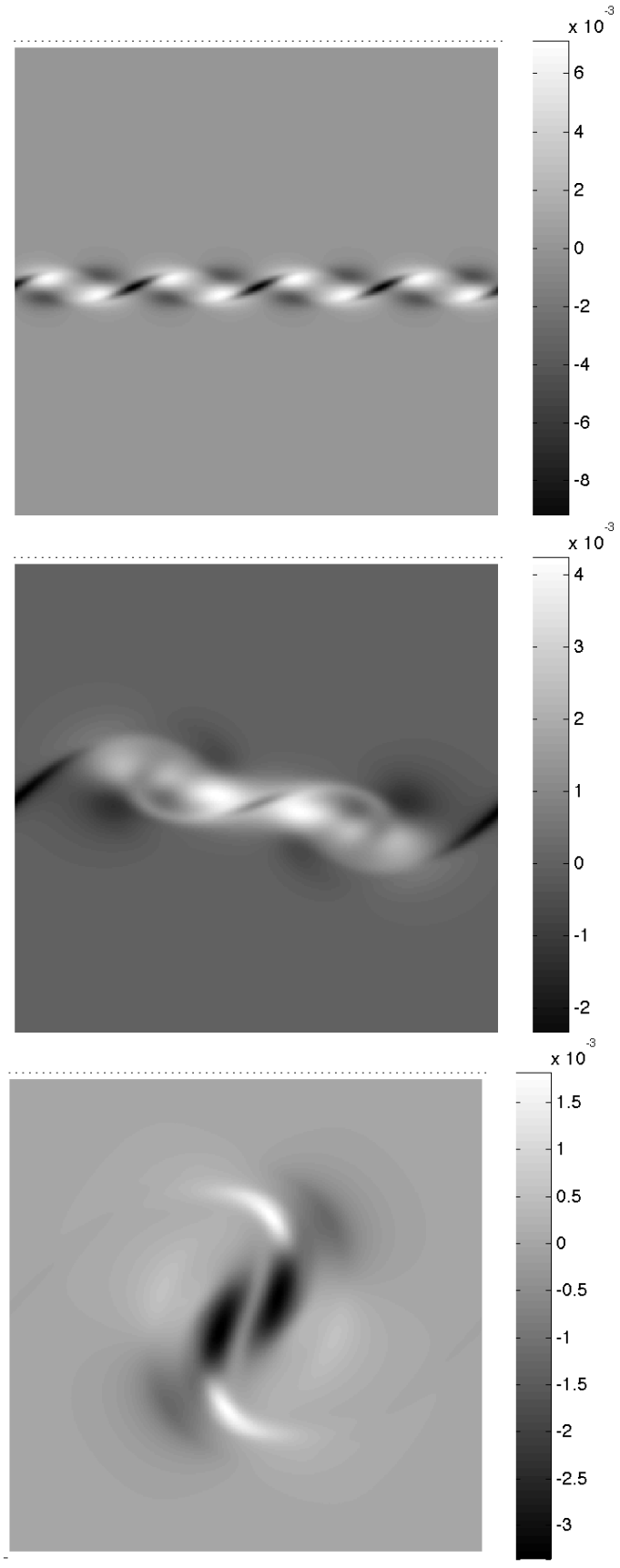

Figure 4.3. Π, at $Re_{\delta_0} = 100$. From top to bottom: the formation stage, first pairing and second pairing.

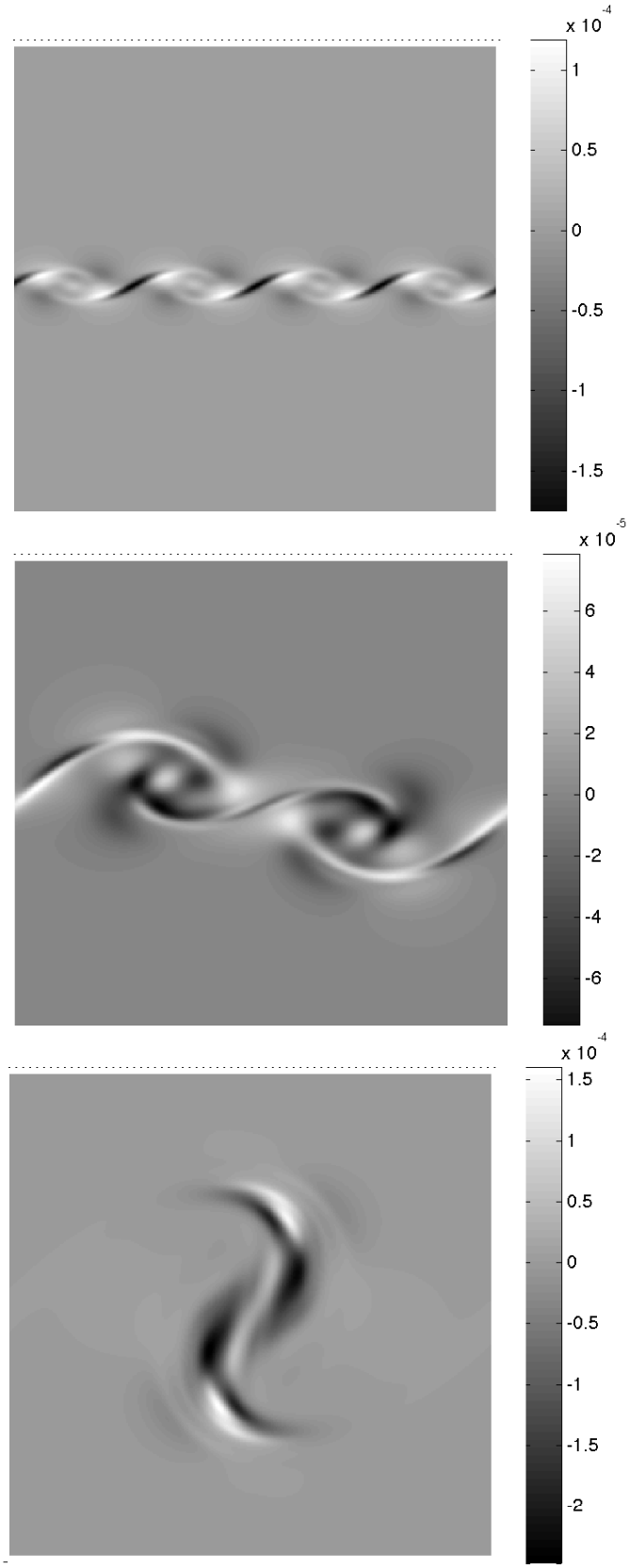

Figure 4.4. $\mathcal{S}_{\Pi,Re_{\delta_0}}$, at $Re_{\delta_0} = 100$. From top to bottom: the formation stage, first pairing and second pairing.

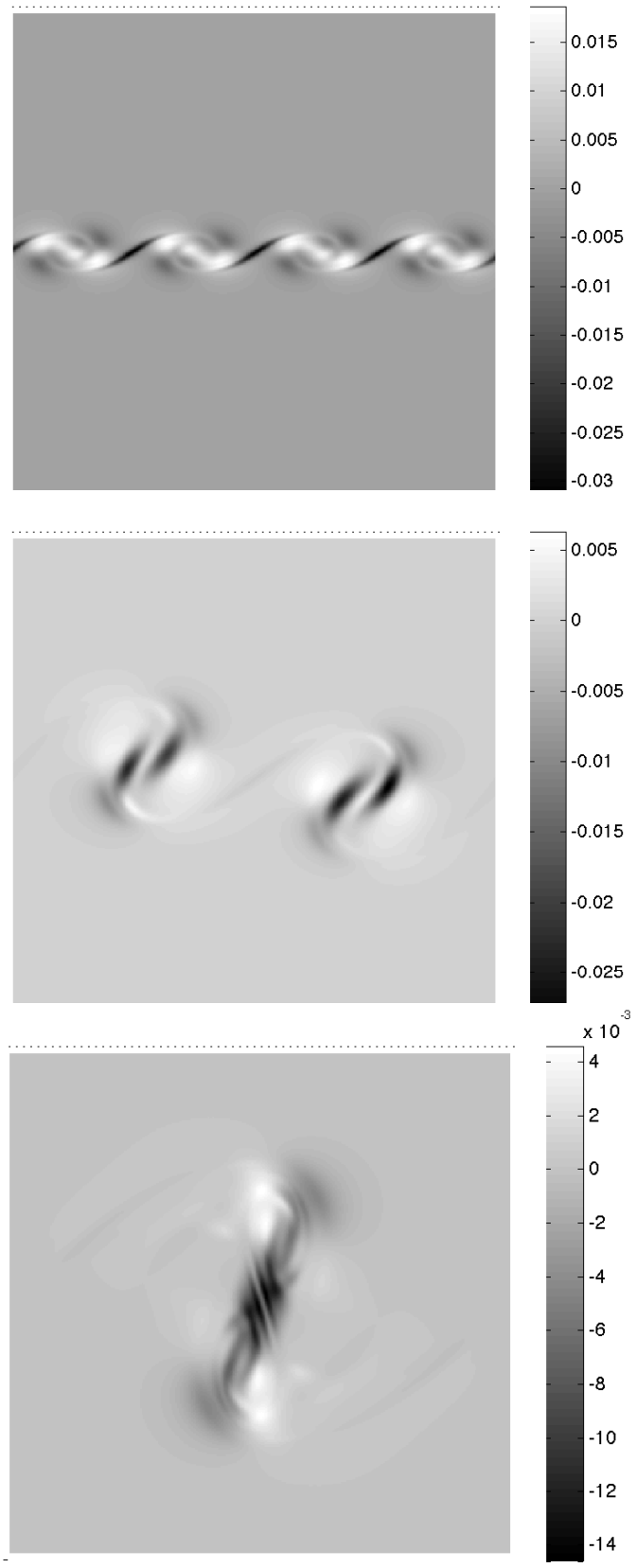

Figure 4.5. Π, at $Re_{\delta_0} = 300$, for the same stages of evolution shown in Fig. 4.3.

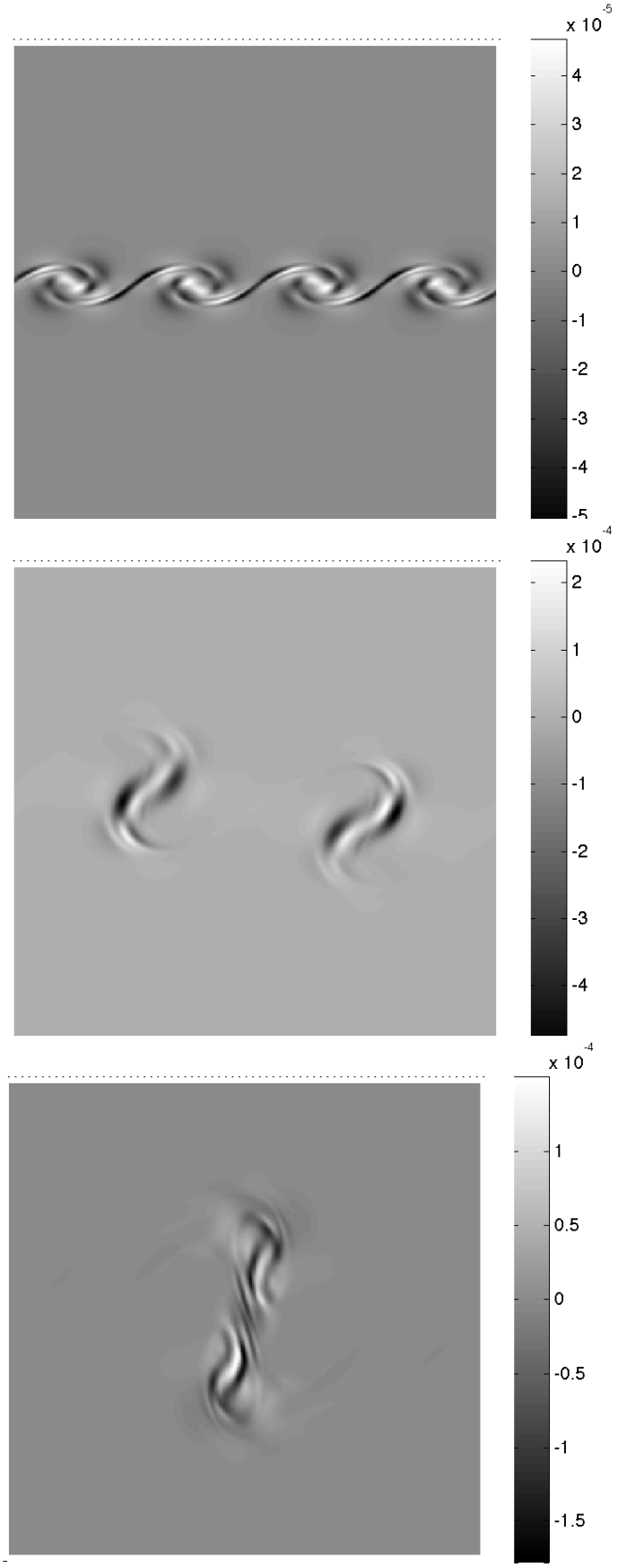

Figure 4.6. $\mathcal{S}_{\Pi,Re_{\delta_0}}$, at $Re_{\delta_0} = 300$, for the same stages shown in Fig. 4.3.

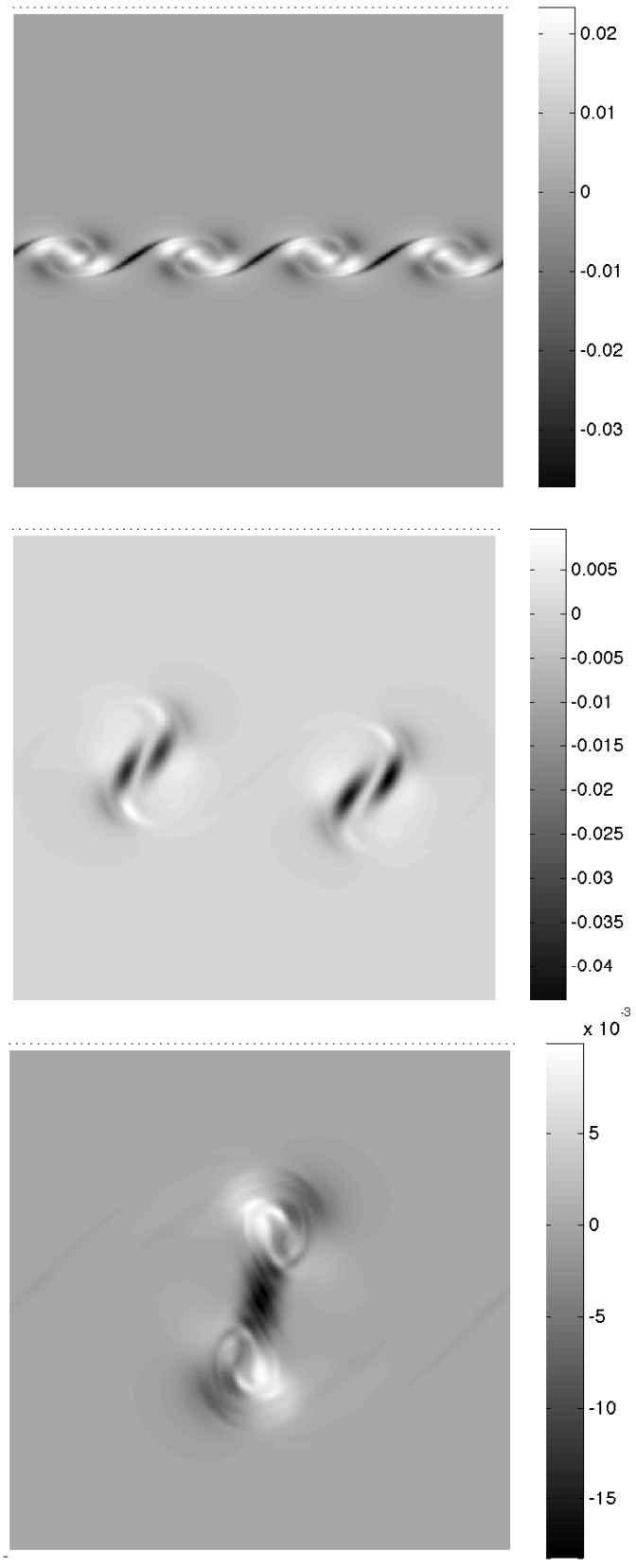

Figure 4.7. Π, at $Re_{\delta_0} = 500$, for the same stages of evolution shown in Fig. 4.3.

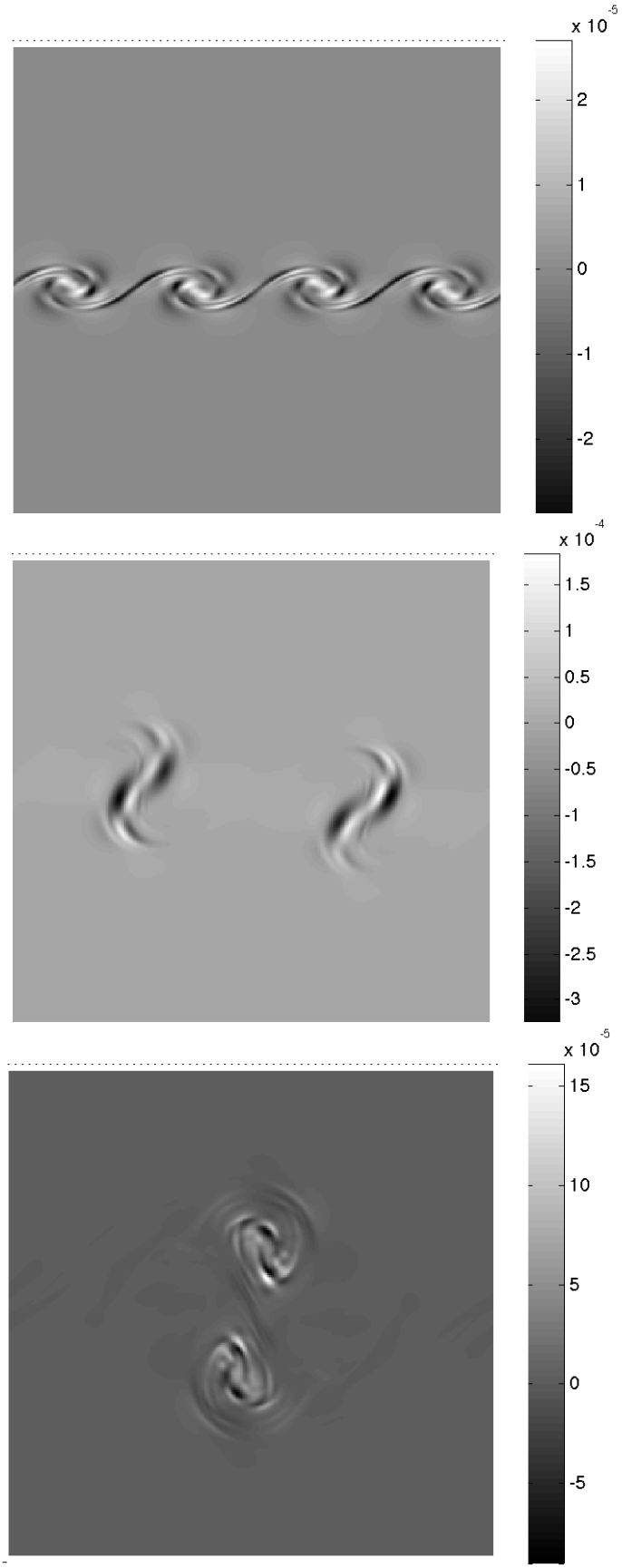

Figure 4.8. $\mathcal{S}_{\mathrm{II},Re_{\delta_0}}$, at $Re_{\delta_0} = 500$, for the same stages shown in Fig. 4.3.

During the formation stage at $Re_{\delta_0} \geqslant 300$ (first row of Fig. 4.5 and 4.7), Π possesses threads of high negative sensitivity that link the four vortices . One can see how these initially high concentrated dark bands of $\mathcal{S}_{\Pi,Re_{\delta_0}}$ between vortices become paired during the process resulting in striations of high positive (white) $\mathcal{S}_{\Pi,Re_{\delta_0}}$ sandwiched between two bands of high negative (black) $\mathcal{S}_{\Pi,Re_{\delta_0}}$, rarely exactly mimicking the topology in the Π field at the same t^*. As the flow continues to evolve through the second pairing process, the two dark bands of negative Π coalesce into one large elongated area of high negative Π in the core of the final vortex that resides after the second pairing. At opposite ends of this dark elongated region sit two circular regions of high positive (white) Π, similar to the shape of a barbell. In contrast, the corresponding sensitivity field, $\mathcal{S}_{\Pi,Re_{\delta_0}}$, maintains its striated pattern through the second pairing process. In fact, one can observe nearly circular regions containing concentrated bands of high positive/negative $\mathcal{S}_{\Pi,Re_{\delta_0}}$, which are coincident with the bulbs of positive (white) dissipation at the ends of the "barbell" pattern in the Π fields, joined together by a small band of negative sensitivity in between. Therefore, at the time of the second pairing, the $\mathcal{S}_{\Pi,Re_{\delta_0}}$ field may be described as a "*bi-core*" sensitivity pattern. The places where dark regions of $\mathcal{S}_{\Pi,Re_{\delta_0}}$ overlap dark regions of Π indicate area of more intense backscatter with increasing Reynolds number. It is important to emphasize that the *bi-core* sensitivity, indicative of enhanced backscatter at higher Re_{δ_0}, occurs in the same areas containing maximum vorticity (see Fig. 4.6 and 4.8). This type of information is helpful for purpose of developing a LES model that accurately captures the expected behavior in the dissipation at higher Re_{δ_0}.

4.5.3 Linear Correlation Coefficients

An alternative tool for measuring the performance of the LES model is the linear correlation coefficient between different components of the SFS stress tensor obtained from the filtered DNS data, τ_{ij}, and modeled as τ_{ij}^M, i.e.,

$$\rho_{ij}(\tau_{ij},\tau_{ij}^M) = \frac{cov(\tau_{ij},\tau_{ij}^M)}{\sigma_{\tau_{ij}}\sigma_{\tau_{ij}^M}} = \frac{\sum_p \sum_q (\tau_{ij}-\overline{\tau_{ij}})(\tau_{ij}^M-\overline{\tau_{ij}^M})}{\sqrt{\left(\sum_p \sum_q (\tau_{ij}-\overline{\tau_{ij}})^2\right)\left(\sum_p \sum_q (\tau_{ij}^M-\overline{\tau_{ij}^M})^2\right)}}, \quad (4.13)$$

where *cov* and σ stand for the covariance and standard deviation, respectively, and p, q denote the indices in the computational grid. In general, $-1 \leqslant \rho_{ij} \leqslant +1$.

Note, an "ideal" LES model would exhibit perfect correlation between the model and physical field, i.e., $\rho = +1$. On the other extreme, a poor model would yield $\rho = 0$. It is important to emphasize that *good* LES models are expected to be somewhat correlated to the corresponding filtered DNS data. In fact, a class of LES models called *similarity models* (Bardina et al., 1980) has been designed specially to have good correlation with physical data. In this research, it is hypothesized that not only should the LES model introduce, a SFS stress tensor with reasonable correlation to physical data, but also should demonstrate reasonable correlation between the *sensitivity* of the SFS stresses to Reynolds number and the actual sensitivity of the physical SFS stress tensor. This will help ensure proper model performance as the Reynolds number of the simulation is increased from a relatively low value as used in the *a priori* study to much higher magnitudes typically of most LES applications.

To examine the correlation between sensitivities, the sensitivity of the real SFS stress tensor to Re_{δ_0} is obtained using (3.45), along with (4.11) to determine $\mathcal{S}_{\tau_{ij},Re_{\delta_0}}$. Note, (3.45) is calculated from the SEM/DNS data by directly filtering the $\mathcal{S}_{u_i}$ and u_i fields. The resulting linear correlation coefficient is defined as

$$\rho^*_{ij}(\mathcal{S}_{\tau_{ij},Re_{\delta_0}}, \mathcal{S}_{\tau^M_{ij},Re_{\delta_0}}) = \frac{\sum_p \sum_q (\mathcal{S}_{\tau_{ij},Re_{\delta_0}} - \overline{\mathcal{S}_{\tau_{ij},Re_{\delta_0}}})(\mathcal{S}_{\tau^M_{ij},Re_{\delta_0}} - \overline{\mathcal{S}_{\tau^M_{ij},Re_{\delta_0}}})}{\sqrt{\left(\sum_p \sum_q (\mathcal{S}_{\tau_{ij},Re_{\delta_0}} - \overline{\mathcal{S}_{\tau_{ij},Re_{\delta_0}}})^2\right)\left(\sum_p \sum_q (\mathcal{S}_{\tau^M_{ij},Re_{\delta_0}} - \overline{\mathcal{S}_{\tau^M_{ij},Re_{\delta_0}}})^2\right)}}. \tag{4.14}$$

Before examining the correlation data based on (4.13) and (4.14) for the present case involving the standard Smagorisnky model in the planar mixing layer, it should be restated that the main goal of this research is not to investigate a particular LES model, but instead to outline a new methodology and framework for evaluating the performance of the SFS models using the computational sensitivity analysis. The expectation is that the additional sensitivity information may potentially lead to the development of more robust and accurate LES models. A brief discussion of this for the simple case of the standard Smagorinsky model is provided later in Sec. 4.5.4.

The linear correlation coefficients between the physical and modeled stress tensor and their corresponding sensitivities are shown in Fig. 4.9, 4.10, and 4.11 for $Re_{\delta_0} = 100, 300$ and 500, respectively. The left columns of each figure presents the three

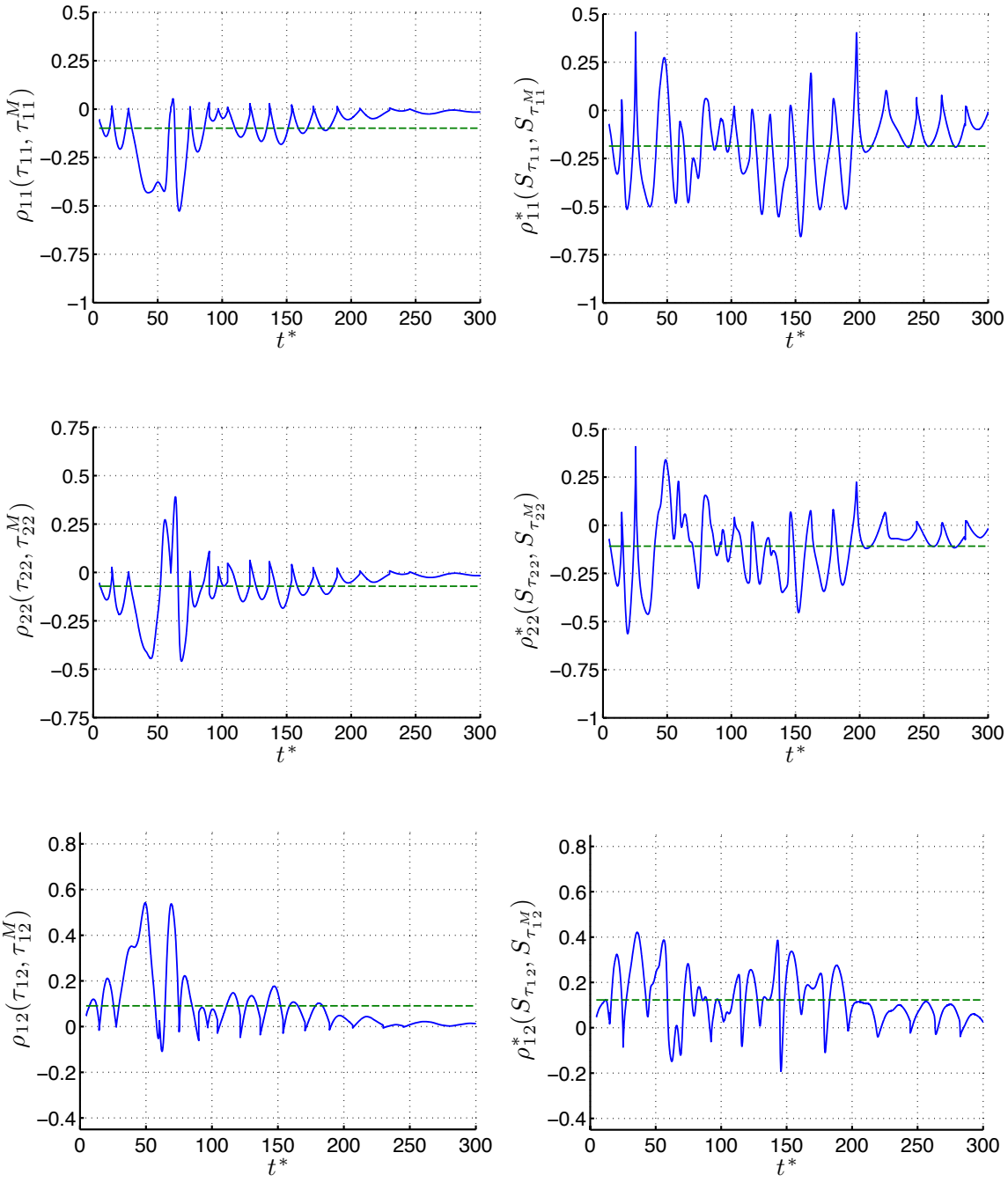

Figure 4.9. The correlation coefficients between the three components of the SFS stress tensors from the filtered DNS data and the model, ρ_{11}, ρ_{22}, and ρ_{12}, shown from top to bottom, respectively (left column), and the corresponding correlation coefficients between the sensitivity of the three components of SFS stress tensor to Re_{δ_0}, ρ_{11}^*, ρ_{22}^*, and ρ_{12}^*, shown from top to bottom, respectively (right column), obtained at $Re_{\delta_0} = 100$. The dashed line indicates the time-average value.

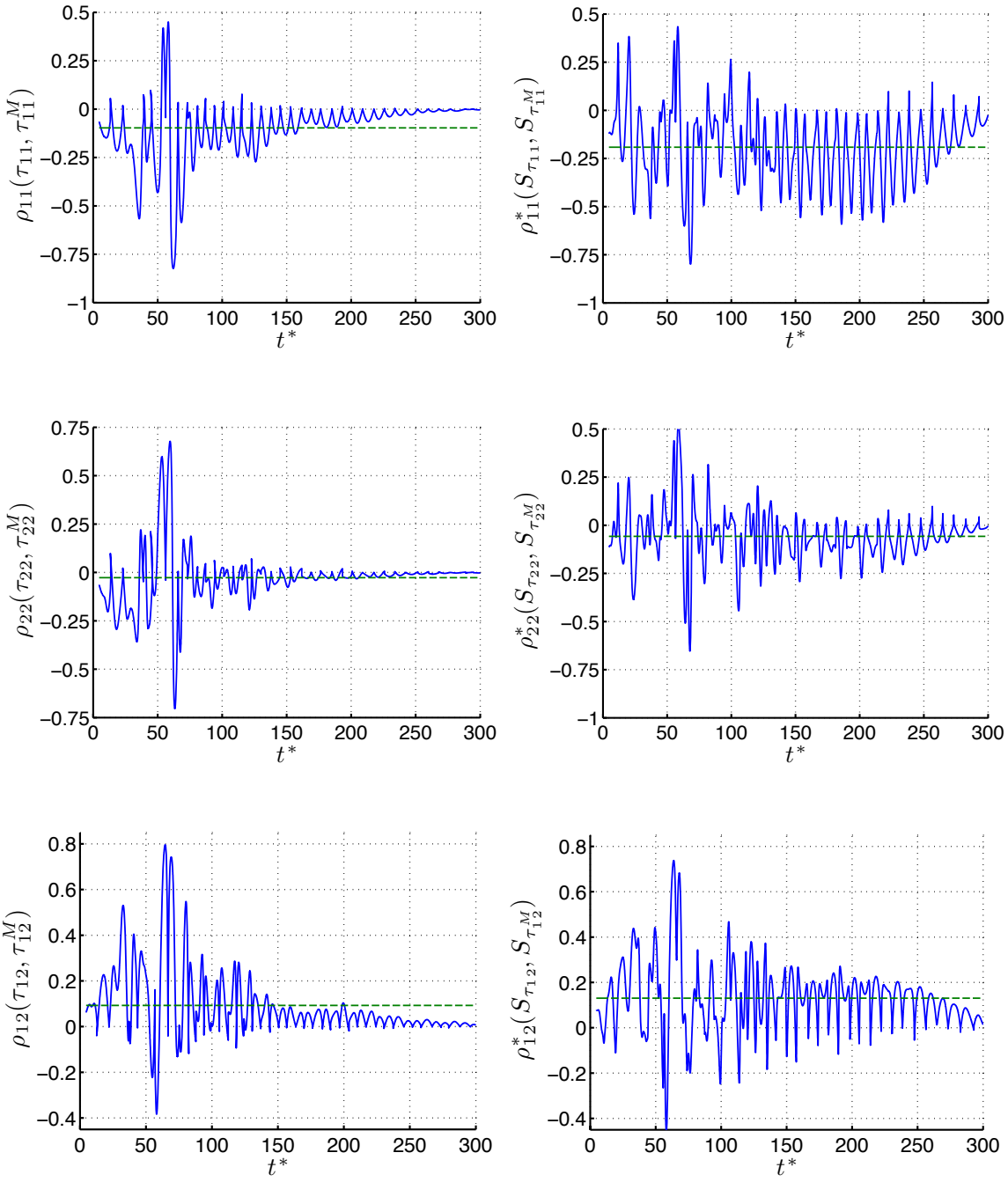

Figure 4.10. The correlation coefficients between the three components of the SFS stress tensors from the filtered DNS data and the model, ρ_{11}, ρ_{22}, and ρ_{12}, shown from top to bottom, respectively (left column), and the corresponding correlation coefficients between the sensitivity of the three components of SFS stress tensor to Re_{δ_0}, ρ_{11}^*, ρ_{22}^*, and ρ_{12}^*, shown from top to bottom, respectively (right column), obtained at $Re_{\delta_0} = 300$. The dashed line indicates the time-average value.

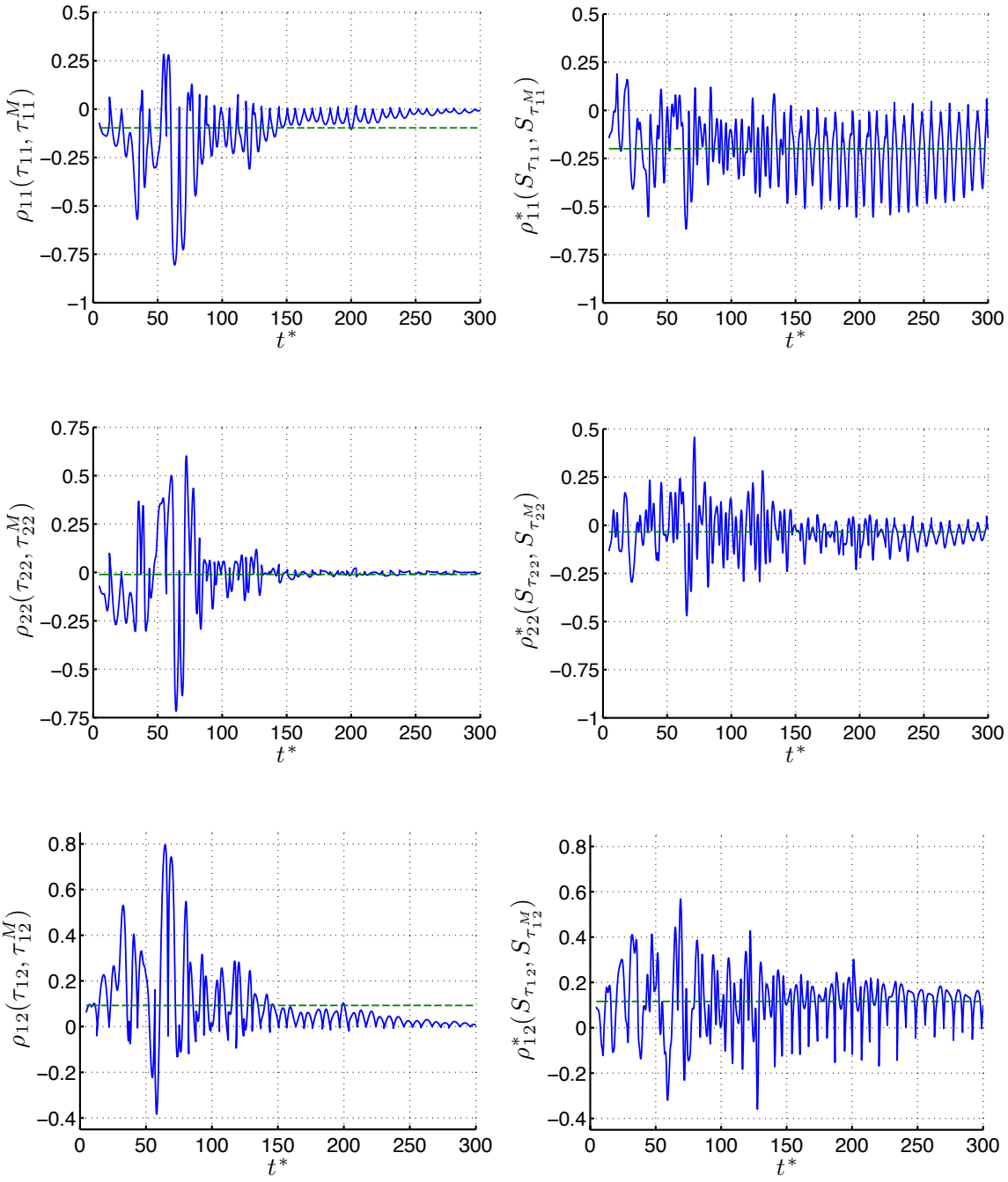

Figure 4.11. The correlation coefficients between the three components of the SFS stress tensors from the filtered DNS data and the model, ρ_{11}, ρ_{22}, and ρ_{12}, shown from top to bottom, respectively (left column), and the corresponding correlation coefficients between the sensitivity of the three components of SFS stress tensor to Re_{δ_0}, ρ_{11}^*, ρ_{22}^*, and ρ_{12}^*, shown from top to bottom, respectively (right column), obtained at $Re_{\delta_0} = 500$. The dashed line indicates the time-average value.

components of the linear correlation coefficients: ρ_{11}, ρ_{22}, and ρ_{12}; while the right column displays the three components of the sensitivity correlation coefficients: ρ^*_{11}, ρ^*_{22}, and ρ^*_{12}. The time-averaged values of ρ_{ij} and ρ^*_{ij} are listed in Tables 4.1 and 4.2, respectively. In terms of $\overline{\rho}_{ij}$, both the horizontal and shear components ($\overline{\rho}_{11}$ and $\overline{\rho}_{12}$) provide slightly better correlation than the vertical component ($\overline{\rho}_{22}$). However, in all cases, $\overline{\rho}_{ij} < 0.1$ indicating the relatively poor correlation between the different components of the SFS stress obtained from the filtered data and that form the Smagorinsky model. In terms of the sensitivity, $\overline{\rho^*}_{ij} < 0.2$ in all cases, with again the horizontal and shear components ($\overline{\rho^*}_{11}$ and $\overline{\rho^*}_{12}$) demonstrating slightly better correlation compared to the vertical component ($\overline{\rho^*}_{22}$), across the three Re_{δ_0} cases studied here.

It is important to note that the linear correlation coefficients between a modeled SFS stress tensor and that obtained from the filtered DNS data in the *a priori* study typically give an excessively pessimistic view of modeling (Meneveau, 1993). It has been emphasized that the low correlation between the stresses does not result in poor results when a model is implemented in a simulation (Reynolds, 1990).

Table 4.1. Time-averaged linear correlation coefficient $\overline{\rho_{ij}}(\tau_{ij}, \tau^M_{ij})$ at $Re_{\delta_0} = 100, 300$ and 500. The overbar denotes a time-average over the period $0 \leqslant t^* \leqslant 300$.

$\overline{\rho_{ij}}$	$Re_{\delta_0} = 100$	$Re_{\delta_0} = 300$	$Re_{\delta_0} = 500$
$\overline{\rho_{11}}$	-0.0983	-0.0970	-0.0971
$\overline{\rho_{22}}$	-0.0714	-0.0273	-0.0109
$\overline{\rho_{12}}$	0.0907	0.0904	0.0925

Table 4.2. Time-averaged linear correlation coefficient $\overline{\rho^*_{ij}}(\mathcal{S}_{\tau_{ij},Re_{\delta_0}}, \mathcal{S}_{\tau^M_{ij},Re_{\delta_0}})$ at $Re_{\delta_0} = 100, 300$ and 500. The overbar denotes a time-average over the period $0 \leqslant t^* \leqslant 300$.

$\overline{\rho^*_{ij}}$	$Re_{\delta_0} = 100$	$Re_{\delta_0} = 300$	$Re_{\delta_0} = 500$
$\overline{\rho^*_{11}}$	-0.1855	-0.1918	-0.1993
$\overline{\rho^*_{22}}$	-0.1087	-0.0576	-0.0343
$\overline{\rho^*_{12}}$	0.1227	0.1305	0.1160

4.5.4 Nearby *A Priori* Study

One of the important purposes of the sensitivity information obtained in the *a priori* study is to predict the appropriate value of the model coefficient that should be used at higher Reynolds numbers. This can be done via a nearby flow analysis, as described in Sec. 2.6.2. Specifically, the Smagorinsky coefficient at a *nearby* Reynolds number may be estimated based on a first order Taylor series as

$$\langle C_s^2 \rangle \Big|_{Nearby} = \langle C_s^2 \rangle \Big|_{Re_{\delta_0}} + \frac{\partial \langle C_s^2 \rangle}{\partial Re_{\delta_0}} \Big|_{Re_{\delta_0}} \Delta Re_{\delta_0}, \tag{4.15}$$

$$\langle C_s^2 \rangle \Big|_{Nearby} = \langle C_s^2 \rangle \Big|_{Re_{\delta_0}} + \mathcal{S}_{\langle C_s^2 \rangle, Re_{\delta_0}} \Big|_{Re_{\delta_0}} \Delta Re_{\delta_0}, \tag{4.16}$$

The right hand side of (4.16) is obtained from the SEM/DNS data run at Re_{δ_0}; while, the left hand side is the estimate at $Re_{\delta_0} + \Delta Re_{\delta_0}$. Taking the time average of both the sides yields

$$\overline{\langle C_s^2 \rangle|_{Nearby}} = \overline{\langle C_s^2 \rangle|_{Re_{\delta_0}} + \mathcal{S}_{\langle C_s^2 \rangle, Re_{\delta_0}}|_{Re_{\delta_0}} \Delta Re_{\delta_0}}, \tag{4.17}$$

$$\overline{\langle C_s^2 \rangle|_{Nearby}} = \overline{\langle C_s^2 \rangle|_{Re_{\delta_0}}} + \overline{\mathcal{S}_{\langle C_s^2 \rangle, Re_{\delta_0}}|_{Re_{\delta_0}}} \Delta Re_{\delta_0}. \tag{4.18}$$

Figure 4.12 shows the average Smagorinsky coefficients $\overline{\langle C_s^2 \rangle}$ and corresponding average sensitivity $\overline{\mathcal{S}_{\langle C_s^2 \rangle, Re_{\delta_0}}}$ versus Reynolds number from the DNS/SEM *a priori* study. The average Smagorinsky model coefficient appears to be approaching an asymptotic value as Reynolds number increases, which means that for high enough Reynolds number the sensitivity of $\overline{\langle C_s^2 \rangle}$ to further changes in Re_{δ_0} should be approximately zero. Indeed, the sensitivity data, $\overline{\mathcal{S}_{\langle C_s^2 \rangle, Re_{\delta_0}}}$, appear to be decreasing toward zero with higher Reynolds number, in support of the behavior of $\overline{\langle C_s^2 \rangle}$. Note, this is significant because $\overline{\langle C_s^2 \rangle}$ and $\overline{\mathcal{S}_{\langle C_s^2 \rangle, Re_{\delta_0}}}$ are obtained independently from the separate DNS and SEM algorithms. Using the results from Fig. 4.12 along with (4.18), a nearby flow analysis was performed in order to assess, at least for a simple example, the extent to which computational sensitivity analysis implemented in the context of the *a priori* study can provide meaningful information for LES model development. The specific question of interest here is whether the appropriate high Reynolds number values of $\overline{\langle C_s^2 \rangle}$ can be accurately predicted from the SEM/DNS at lower Re_{δ_0}. Table 4.3 presents the calculations.

The actual values of $\overline{\langle C_s^2 \rangle}$ obtained from the filtered DNS data are listed along with the predicted values calculated from the nearby flow analysis using the SEM/DNS

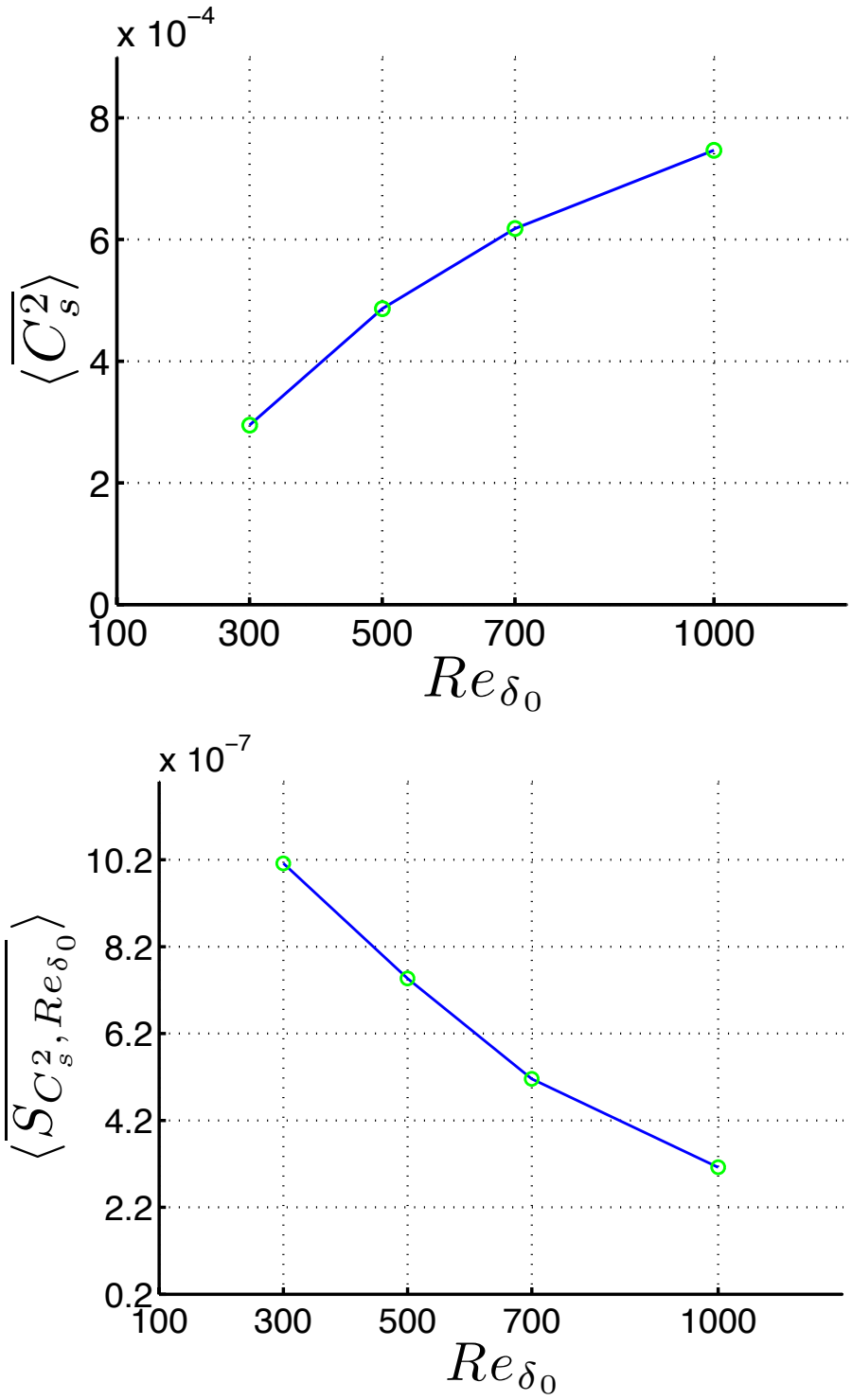

Figure 4.12. The average Smagorinsky coefficient $\overline{\langle C_s^2 \rangle}$ (top), and corresponding sensitivity to Re_{δ_0}, $\overline{\mathcal{S}_{\langle C_s^2 \rangle, Re_{\delta_0}}}$ (bottom) versus Reynolds number obtained from the SEM/DNS results of the *a priori* study.

Table 4.3. Comparison of actual and predicted average Smagorinsky coefficient. The actual values of $\overline{\langle C_s^2 \rangle}$ are obtained from the filtered DNS data. The predicted $\overline{\langle C_s^2 \rangle}$ values are calculated from a nearby flow analysis using the SEM/DNS data from the previous Reynolds number. For example, the nearby $\overline{\langle C_s^2 \rangle}$ at $Re_{\delta_0} = 300$ is determined from the simulation run at $Re_{\delta_0} = 100$ in conjunction with (4.18).

Re_{δ_0}	DNS $\overline{\langle C_s^2 \rangle}$	Nearby $\overline{\langle C_s^2 \rangle}$	error $\%\epsilon$
300	2.95×10^{-4}	2.60×10^{-4}	12
500	4.86×10^{-4}	4.97×10^{-4}	2.3
700	6.20×10^{-4}	6.35×10^{-4}	2.4
1000	7.47×10^{-4}	7.73×10^{-4}	3.5

data at the previous Re_{δ_0}. For example, the predicted $\overline{\langle C_s^2 \rangle}$ at $Re_{\delta_0} = 300$ is obtained using DNS data from $Re_{\delta_0} = 100$ simulation. At the higher Reynolds number and using relatively small step sizes (ΔRe_{δ_0}), the error between the actual and predicted $\overline{\langle C_s^2 \rangle}$ values remains about 3%. Whereas, the error in the prediction at $Re_{\delta_0} = 300$ is considerably larger at 12%. This may be attributed to (i) nonlinear behavior of $\overline{\langle C_s^2 \rangle}$ at low Re_{δ_0}, and (ii) the relatively large step size taken between $Re_{\delta_0} = 100$ and $Re_{\delta_0} = 300$, i.e., $\Delta Re_{\delta_0}/Re_{\delta_0} \approx 67\%$. Nevertheless, the present results are encouraging in terms of the potential to use computational sensitivity analysis within the framework of the *a priori* study for purpose of LES model enhancement and development.

CHAPTER 5

SENSITIVITY OF MIXING LAYER TO INITIAL CONDITIONS

Direct numerical simulations (DNS) and large eddy simulation (LES) of turbulent flows are strongly influenced by initial or inflow conditions. In a canonical test case such as the mixing layer, a thorough understanding of the flow evolution and corresponding dependencies on its initial/inflow conditions is important, because the formation and nonlinear interaction of large-scale, energy-containing coherent structures has a considerable impact on the overall mixing efficiency. This chapter describes the implementation of the complex-step differentiation (CSD) method, to discover the sensitivities of the evolution of the flow to its initial conditions (ICs) in a temporal frame work. The ICs are generated using the *supergrid modeling* method, which involves a noise function superposed on to a hyperbolic tangent shaped mean flow. Two different approaches have been utilized here to define the noise function:(i) stochastic method that incorporates a prescribed integral length scale $\mathcal{L}$, and (ii) linear stability theory, in which a noise modulation factor c_{noise} may be adjusted to set the magnitude of the turbulence intensity. Results form the CSD simulations reveal a switch in the sensitivity pattern at the stage of the first pairing for values of $\mathcal{L}$ and c_{noise} above a critical threshold. Beyond that critical threshold, the evolution of the flow is effected to such a strong extent the fewer than four fundamental K-H vortices maybe observed in the formation stage. The present study shows how the sensitivity fields serve as a useful indicator in stablishing this critical noise threshold.

5.1 Supergrid Modeling

Nowadays, direct numerical simulation (DNS) and large eddy simulation (LES) of turbulent flows have become interesting and attractive tools to capture the details of turbulent flows by utilizing the increasing power of computers. The biggest advantage of these approaches is that they can simulate features such as higher order moments

of the statistics and the motion of coherent structures that cannot be captured with Reynolds-Averaged Navier-Stokes (RANS) simulations, for example. For this reason, these approaches require appropriate initial and boundary conditions for all the resolved scales, which must be specified at the boundaries of the problem or as initial conditions. In other words, the turbulence has to be properly prescribed at the inflow or as an initial condition in the numerical simulations. In contrast, RANS simulations only need first-order statistics, such as k and ϵ or Reynolds stresses, at the boundaries or initial conditions. Consequently, DNS and LES generally demand more realistic prescription of boundary and initial conditions, which leads to a better representation of the main features of an actual turbulent flows. This issue will be denoted as *supergrid modeling* (Grinstein, 2004). In temporally evolving flows, supergrid modeling has a large influence on the long-term or asymptotic state of the flow-field development (Dziomba and Fiedler, 1985; Holmes et al., 1996). This profound effect of the upstream or initial conditions on the turbulent flow field development is believed to be largely influenced by the characters of coherent structures (Rogers and Moser, 1992; Moser and Rogers, 1993). Therefore, it is critical in supergrid modeling to correctly specify those field structures at the inflow or as initial conditions. The more the initial and/or inflow conditions mimic the real statistics of the turbulence, the more reliable and realistic simulations of turbulent flows can be achieved.

One the most common methods of defining the initial condition in turbulence simulations is through pseudo-perturbation superposed on a mean flow. The perturbation maybe prescribed by: (i) utilizing the detailed experimental data or prior DNS or LES calculations, (ii) using stochastic methods, or (iii) using linear stability theory (LST) applied to the Navier-Stokes equations. The first approach is extremely expensive and was not implemented in this research. As far the second approach, a variety of stochastic methods have been developed involving candidate statistical quantities such as Reynolds stresses and energy spectra (Lee et al., 1992; Kondo et al., 1997; Lund et al., 1998; Maruyama et al., 1999; Smirnov et al., 2001; Kondo and Tsuchiya, 2002). In stochastic approaches, turbulent inflow or initial conditions are generated as random realizations of a selected *pdf* statistically equivalthat to an actual turbulent flow field. Practically, however, the imposed statistical information is often limited by the knowledge of the correlation function $R_{ij}(\mathbf{x}, \mathbf{r})$. The last approach using LST

is the simplest and least expensive. In this method, velocity perturbations are the result of unstable eigenfunction of the linearized Navier-Stokes equations (Michalke, 1964; Ragab and Wu, 1989). Both supergrid modeling approaches involving stochastic method and LST are considered in this chapter.

Lee et al. (1992) proposed a stochastic method by which a turbulent velocity field can be artificially generated based on a prescribed energy spectrum function, following the appropriate rescaling of a random white-noise field in wavenumber space. This method provides a simpler although less descriptive initial field compared to the correlation function. The disadvantage of this method lies in the fact that the phase angle of the initial (or inflow) field is generated randomly, which translates into a loss of all directional information. Therefore, one cannot effectively control the formation and evolution of the coherent structures. Furthermore, the extension to three-dimensional space becomes challenging because the difficulty in defining an appropriate three-dimensional energy spectrum function to generate the initial field form.

Lund et al. (1998) proposed a method to generate a turbulent velocity field with prescribed mean profile and Reynolds stresses. In this method, instead of the correlation function, the Reynolds stress tensor is decomposed as the kernel for the transformation. The advantage of this method stems form the fact that the one-point statistical information is readily available for most of cases. The disadvantage here again is that one has no direct control over the coherent structures during the generation of the initial flow field. It can also be shown that the corresponding energy spectrum for this type of the initial field is relatively flat (i.e., white noise), which remains a weakness of this approach.

Smirnov et al. (2001) improved the method of Lund by modifying the Fourier modes scaling procedure; Lund's transformation on a continuous analytical flow field generated as a superposition of harmonic functions. This approach permits one to introduce an anisotropy in the turbulence. Consequently, the outcome is a time-dependent flow field with prescribed Reynolds stresses and prescribed turbulent characteristic time-and length-scales. This improvement allows a weak description of coherent structures through the characteristic length scales, and makes the approach applicable to more complex flow fields.

Klein et al. (2003) proposed a new method based on the application of a digital filter to random data followed by Lund's transformation (Lund et al., 1998). This method is able to artificially generate the turbulent velocity field with a prescribed Reynolds stresses. Moreover, the generated velocity field has a locally prescribed autocorrelation coefficient function. Introducing information regarding the two-point statistics increases the description level for coherent structures.

5.2 Stochastic Initial Condition Generation: Digital Filtering

The digital filtering approach proposed by Klein et al. (2003) for generating initial conditions was implemented in the present study, because it provides more control in the specification of the coherent structures in the flow. In this approach, initial statistical quantities are defined based on experimental data or, alternatively, from heuristic estimates. Here, the two-point correlation function is used. Let r_m represent a series of random data with $\overline{r_m} = 0$, and $\overline{r_m r_n} = 1$, then

$$u_m = \sum_{n=-N}^{N} b_n r_{m+n} \tag{5.1}$$

defines the convolution operation associated with a digital linear non-recursive filter, where b_n denote the filter coefficients and N is connected to the support of the filter. Because $\overline{r_m r_n} \neq 0$ for $m \neq n$, it follows

$$\frac{\overline{u_m u_{m+k}}}{\overline{u_m u_m}} = \sum_{j=-N+k}^{N} b_j b_{j-k} \Big/ \sum_{j=-N}^{N} b_j^2, \tag{5.2}$$

which yields a relation between the filter coefficients and the autocorrelation function of u_m. For the case of homogenous turbulence, it can be shown (Batchelor, 1953) that the autocorrelation function obeys

$$R_{uu}(r) = \exp(-\frac{\pi r^2}{4\mathcal{L}^2}), \tag{5.3}$$

where $\mathcal{L}$ represents the integral length scale of the turbulence. Note, this functional dependence fulfills some basic properties, like $R_{uu}(0) = 1$ and $\lim_{r\to\infty} R_{uu}(r) = 0$.

Suppose Δx represents the grid spacing, which in this case is uniform, and $\mathcal{L} = n\Delta x$ denotes the imposed length scale, then (5.3) can be written in discretized form as

$$\frac{\overline{u_m u_{m+k}}}{\overline{u_m u_m}} = R_{uu}(k\Delta x) = \exp\left(-\frac{\pi(k\Delta x)^2}{4(n\Delta x)^2}\right) = \exp\left(-\frac{\pi k^2}{4n^2}\right), \tag{5.4}$$

and the filter coefficients are

$$b_k \approx \tilde{b}_k \Big/ \sum_{j=-N}^{N} b_j^2 \quad \text{and} \quad \tilde{b}_k \equiv exp\left(-\frac{\pi k^2}{4n^2}\right). \tag{5.5}$$

Equation 5.5 is only approximately valid, but numerically the following error estimate can be given

$$\max_k \left| \exp\left(-\frac{\pi k^2}{4n^2}\right) - \sum_{j=-N+k}^{N} b_j b_{j-k} \Big/ \sum_{j=-N}^{N} b_j^2 \right| \leqslant 0.001 \tag{5.6}$$

for $N \geqslant 2n$ and $n = 1, 2, 3, ...$ The inequality in (5.6) simply states that the support of the filter should be large enough to capture twice the length scale, but essentially truncates to zero beyond that in all directions. In order to apply the digital filtering approach to supergrid modeling in the present study, the following steps were adopted:

1. Choose an integral length scale in the form of $\mathcal{L} = n\Delta$. The filter support is chosen according to the conditions $N \geqslant 2n$, which then defines the stencil used in the digital filter, i.e., $(4n + 1) \times (4n + 1)$ points.

2. Calculate the filter coefficients b_k using (5.5).

3. Generate a random set r_{ij} that fills the $(M \times M)$ computational domain and is sampled form a two-dimensional normal distribution.

4. Impose the proper boundary conditions by duplicating the r_{ij} on all sides of the computational domain.

5. Applying the following filter operation yields a two-dimensional field for the initial u-component velocity of spatially correlated to be superimposed to the mean flow as

$$u_{ij} = \sum_{i'=-N_x}^{N_x} \sum_{j'=-N_y}^{N_y} b_{i'j'} r_{i+i',j+j'}. \tag{5.7}$$

6. Multiply u_{ij} by a windowing function $\exp(-y^2/\delta_0^2)$ that confines the perturbation to a neighborhood along the x-axis of the computational domain with a width approximation equal to the initial vortex thickness δ_0.

7. Impose conservation of mass in order to calculate the corresponding v-component of the initial velocity field.

5.3 Application of Linear Stability Theory (LST) in Initial Conditions Generation

According to linear stability theory applied to the mixing layer problem, the *initial* velocity of the mixing layer is introduced as a basic mean flow plus a noise function (Michalke, 1964) as

$$u_0(x,y) = \bar{u}_0(y) + c_{noise}\,\frac{\partial \psi}{\partial y}\,, \tag{5.8}$$

where

$$\psi(x,y) = \exp\left(-y^2L^2/\delta_0^2\right)\,\left[\cos(8\pi x) + cos(20\pi x)\right]\,. \tag{5.9}$$

The nondimensional initial mean profile, $\bar{u}_0$, follows from Michalke (1964),

$$\bar{u}_0(y) = \tanh(2yL/\delta_0). \tag{5.10}$$

The turbulence modulation factor c_{noise} is typically chosen to be on the order of 1×10^{-3}, which guarantees that initial velocity perturbations remain a small percentage of the mean flow. In this chapter, c_{noise} serves as the parameter of interest; the main objective being to discover the effect of the initial turbulence level on the subsequent evolution of the coherent structures in the flow.

5.4 Sensitivity of the Shear Layer to Initial Conditions: Complex-Step Differentiation

Complex-step differentiation (CSD) in the context of low Re_{δ_0} DNS is used in the present chapter to examine the time-resolved sensitivity of the vorticity to instantaneous changes in both $\mathcal{L}$ and c_{noise}. Two sets of simulations were run at $Re_{\delta_0} = 200$ using two different approaches of initializing the mixing layer as outlined in Sec. 5.2 and 5.3. As mentioned before (see Sec.3.3.1.2), in CSD, the governing equations along with the velocity and pressure fields are treated as complex. The sensitivity

coefficients are estimated by dividing the imaginary part of the velocity field by a small perturbation in the parameter of interest. The main difference between the sensitivity analysis of this chapter and what was done Chap.3 is that the sensitive parameters do not explicitly appear in the governing equations. Here, the parameters of interest ($\mathcal{L}$ and c_{noise}) implicitly affect the initial conditions. Thus, differentiating the initial velocity field with respect to either $\mathcal{L}$ or c_{noise} (as the case maybe) leads to a nonhomogeneous initial condition for $\mathcal{S}_u$ and $\mathcal{S}_v$. In terms of CSD, this means that the imaginary part of the initial complex-valued velocity is nonzero.

5.5 Results

Sensitivity of the evolution of the planar incompressible mixing layer to the initial integral length scale $\mathcal{L}$ (in the stochastic approach) and the noise modulation factor c_{noise} (in the LST approach) from CSD in the context of DNS solved using a finite-volume based fractional-step method.

5.5.1 Sensitivity of the Vorticity to $\mathcal{L}$

The divergence-free initial velocity field generated using a prescribed integral length scale $\mathcal{L}$ and corresponding sensitivities of the initial velocity to $\mathcal{L}$ are presented in Fig. 5.1, 5.2, 5.3, and 5.4 for u and v-components of the velocity field. Results for three different integral lengths are shown: $\mathcal{L} = \Delta x, 2\Delta x$, and $4\Delta x$. Note, considering the fact that $\mathcal{L}$ measures one-fourth of the filter width (not support) along each direction, there are 25, 81, and 289 total grid points involved in the stencil of the digital filter, respectively, for the three $\mathcal{L}$ values examined.

Figure 5.1 illustrates the effect of $\mathcal{L}$ on the distribution of the perturbations in the initial u-velocity, with higher $\mathcal{L}$ values producing large "coherent" structures in the initial u-field. This same basic behavior may be observed in the initial $\mathcal{S}_{u,\mathcal{L}}$ field, although the extent of the coherency is reduced relative to that in the initial u-field. The v-component of the initial velocity field, shown in Fig. 5.3, is obtained from the initial u-velocity by imposing the incompressibility constraint. Note, both the u and v-components of velocity along with their corresponding sensitivities to $\mathcal{L}$ display similar order of magnitude.

In order to validate the sensitivity results, a nearby flow analysis has been performed using the first order Taylor series expansion about $\mathcal{L} = 4\Delta x$, and looking at

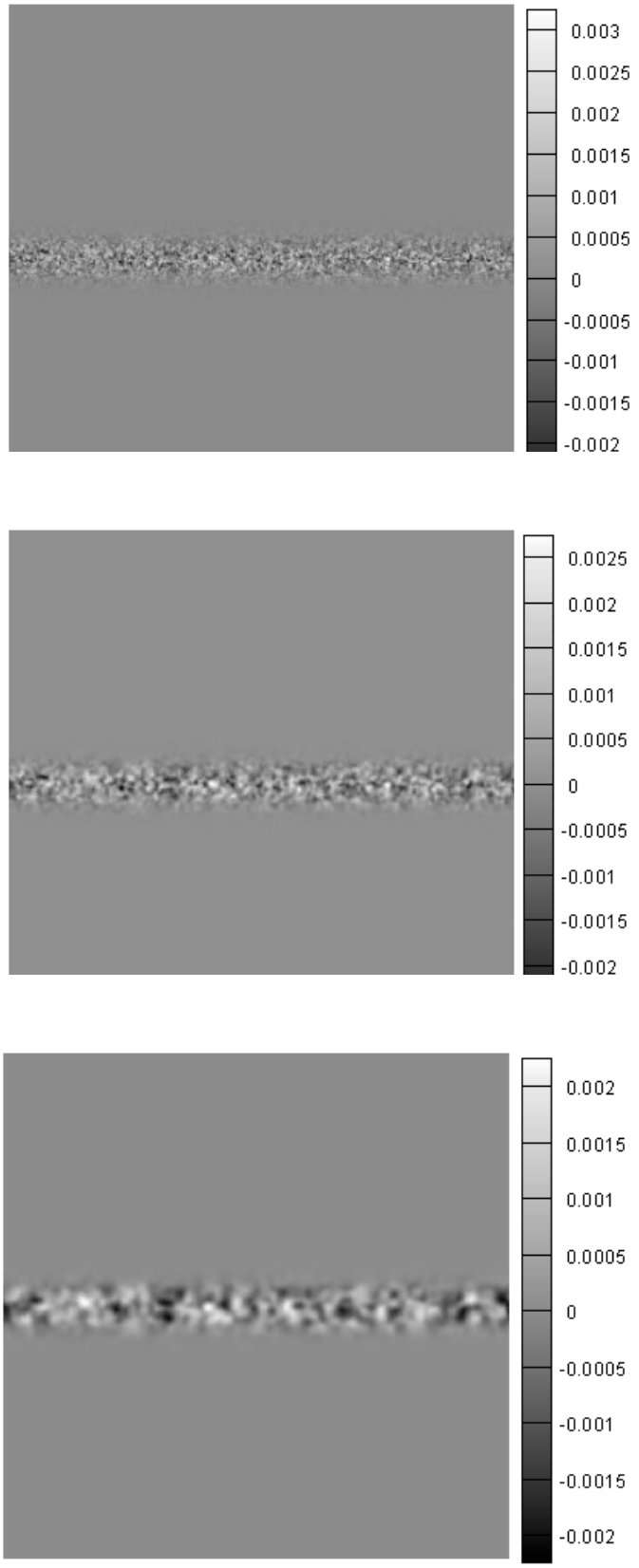

Figure 5.1. The initial u-velocity perturbation field for three different prespecified integral length scale: $\mathcal{L}=\Delta x$ (top), $2\Delta x$ (middle), and $4\Delta x$ (bottom).

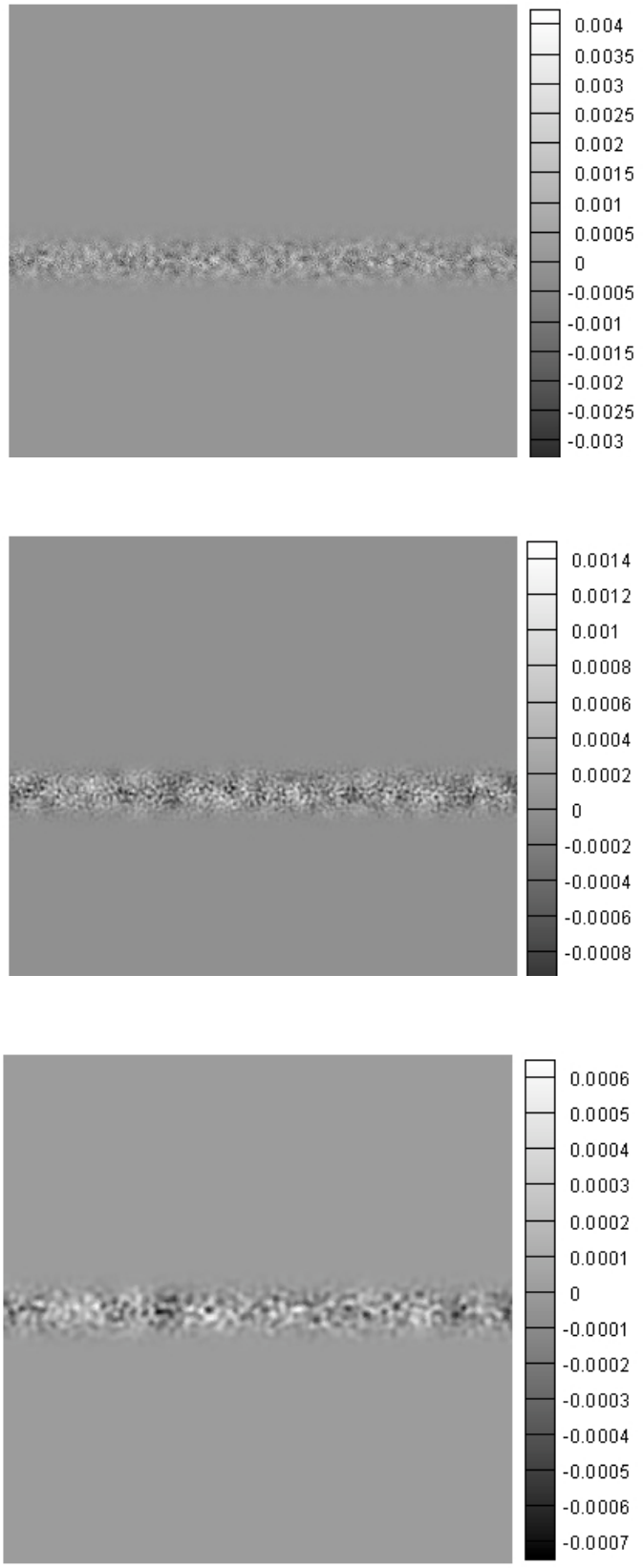

Figure 5.2. The initial sensitivity $\mathcal{S}_{u,\mathcal{L}}$ for three different prespecified integral length scale: $\mathcal{L}$=Δx (top), $2\Delta x$ (middle), and $4\Delta x$ (bottom).

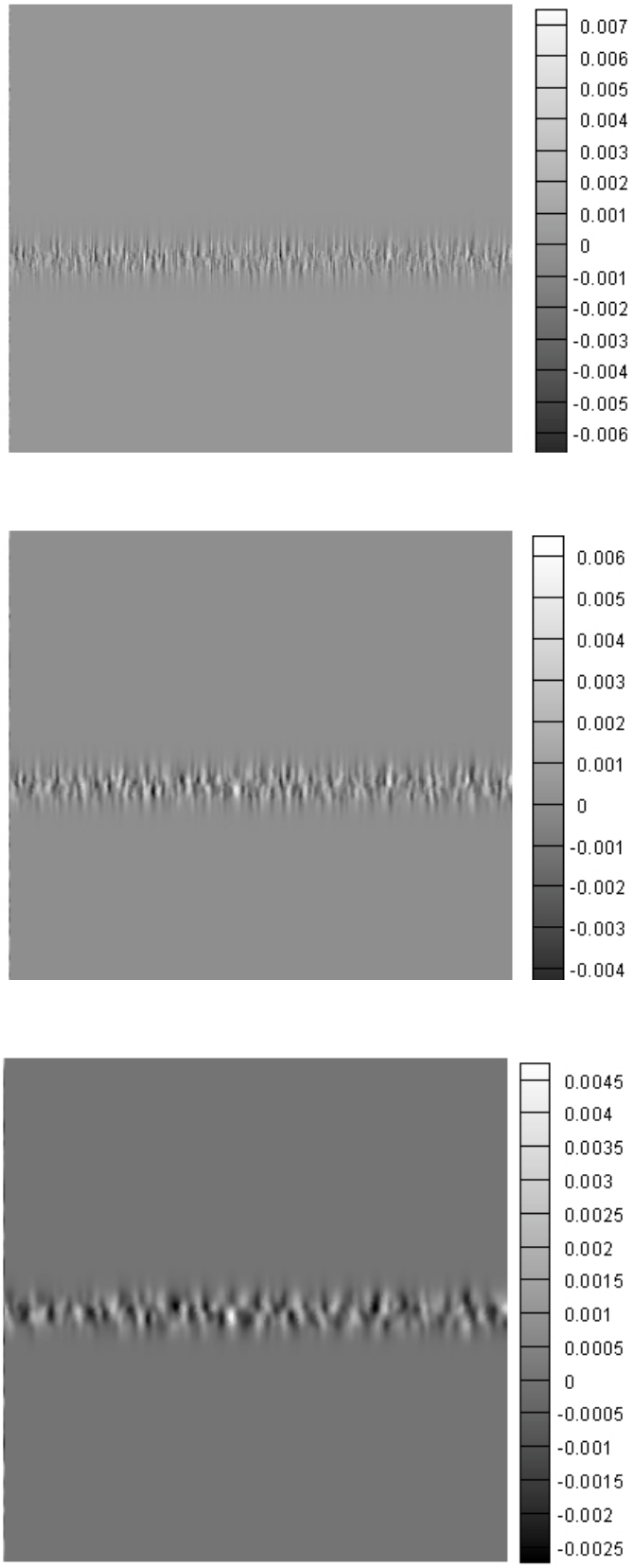

Figure 5.3. The initial v-velocity perturbation field for three different prespecified integral length scale: $\mathcal{L}=\Delta x$ (top), $2\Delta x$ (middle), and $4\Delta x$ (bottom).

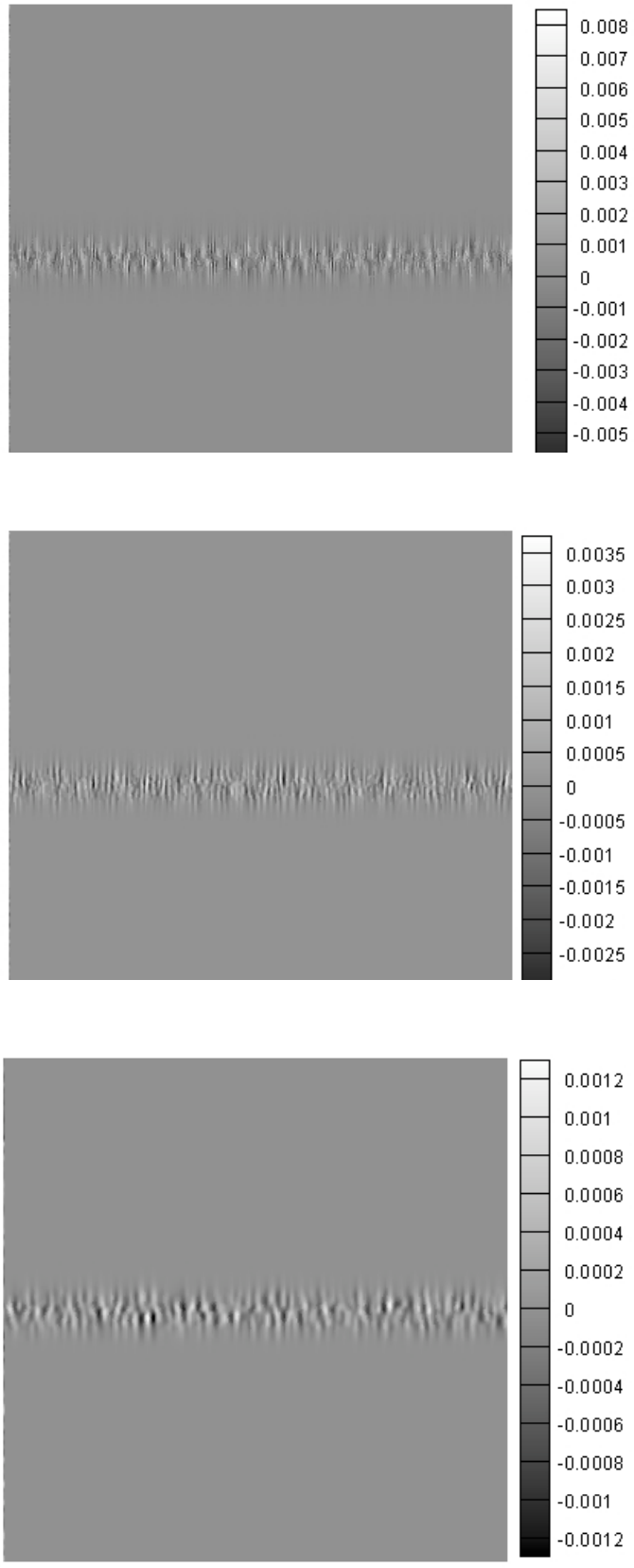

Figure 5.4. The initial sensitivity $\mathcal{S}_{v,\mathcal{L}}$ for three different prespecified integral length scale: $\mathcal{L}$=Δx (top), $2\Delta x$ (middle), and $4\Delta x$ (bottom).

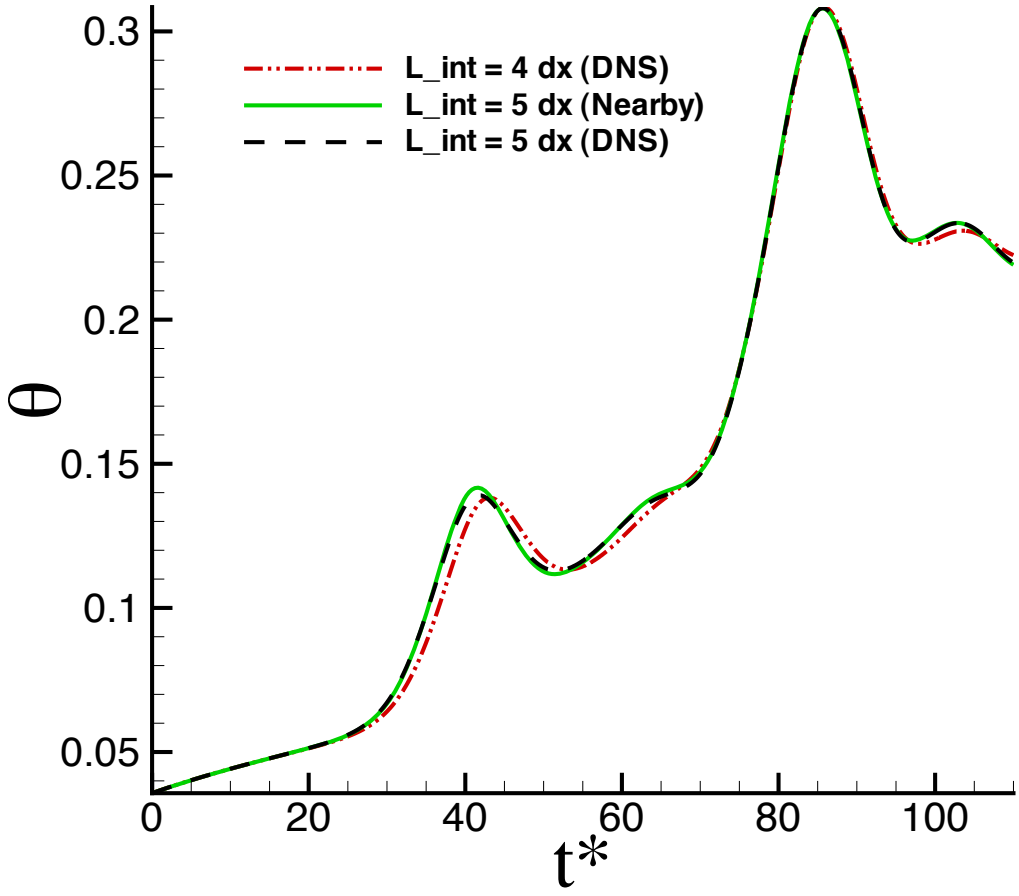

Figure 5.5. Momentum thickness as a function of the evolution of the flow for three cases: DNS using $\mathcal{L} = 4\Delta x$ $(- \cdot\cdot -)$, DNS using $\mathcal{L} = 5\Delta x$ $(--)$, and the nearby flow prediction for $\mathcal{L} = 5\Delta x$ using the CSD results at $\mathcal{L} = 4\Delta x$ $(—)$.

the growth of the momentum thickness,

$$\theta = \int_{-\infty}^{+\infty} (1 - \langle u \rangle^2) dy, \tag{5.11}$$

in which, $\langle u \rangle$ indicates the u-component of velocity averaged along the homogenous x-direction. By taking the partial derivative of θ with respect to $\mathcal{L}$, one obtains

$$\mathcal{S}_{\theta,\mathcal{L}} \equiv \partial\theta/\partial\mathcal{L} = -\int_{-\infty}^{+\infty} 2\langle u \rangle \; \mathcal{S}_{\langle u \rangle,\mathcal{L}} \; dy, \tag{5.12}$$

where $\mathcal{S}_{\theta,\mathcal{L}}$ represents a *secondary sensitivity coefficient* (as discussed in Sec. 2.7.4) obtained in terms of the primitive sensitivity coefficient $\mathcal{S}_{\langle u \rangle,\mathcal{L}}$. Figure 5.5 shows the results of the nearby flow prediction for a 25% increase in $\mathcal{L}$ (from $\mathcal{L} = 4\Delta x$ to $\mathcal{L} = 5\Delta x$). As observed, the *nearby* momentum thickness calculated using (5.12) along with the sensitivity data computed at $\mathcal{L} = 4\Delta x$ exhibits excellent agreement with the actual DNS run at $\mathcal{L} = 5\Delta x$, thereby validating the sensitivity code. Furthermore, Fig. 5.5 indicates that the sensitivity results correctly predict faster growth of the momentum thickness with increasing $\mathcal{L}$, at least up to the second pairing, in accordance with the parametric study of Fathali et al. (2008).

The evolution of the vorticity and corresponding sensitivity fields initialized utilizing three different integral length scales $\mathcal{L} = \Delta x, 2\Delta x$, and $4\Delta x$ are shown in Fig. 5.6, 5.7, 5.8, 5.9, 5.10, and 5.11. In the formation stage, the coherent vorticity structures, referred to earlier as Kelvin-Helmholtz vortices, are not as clearly formed as those reported in Chap. 2; and, this is attributed directly to the effect of the randomization via $\mathcal{L}$ in the initial condition on the subsequent evolution of the flow. As time evolves further, the four fundamental vortices still undergo first and second pairing, albeit with less than perfect symmetry in the vorticity field. In terms of the sensitivity, the structures in $\mathcal{S}_{\omega,\mathcal{L}}$ appear to mimic those in the vorticity field, analogous to what was observed in Chap. 2 for $\mathcal{S}_{\omega,Re_{\delta_0}}$. However, the two-blade pattern obtained in $\mathcal{S}_{\omega,Re_{\delta_0}}$ is not fully replicated here in the case of $\mathcal{S}_{\omega,\mathcal{L}}$. In particular, the $\mathcal{S}_{\omega,\mathcal{L}}$ sensitivity structures exhibits much more asymmetry than their corresponding counterparts in the vorticity field. This creates some challenges in trying to interpret instantaneous snapshots of $\mathcal{S}_{\omega,\mathcal{L}}$ for purpose of predicting mixing layer growth, for example, with increasing $\mathcal{L}$. In this incident, prediction is better accomplished using a nearby flow analysis as was was done for the momentum thickness calculation shown in Fig.

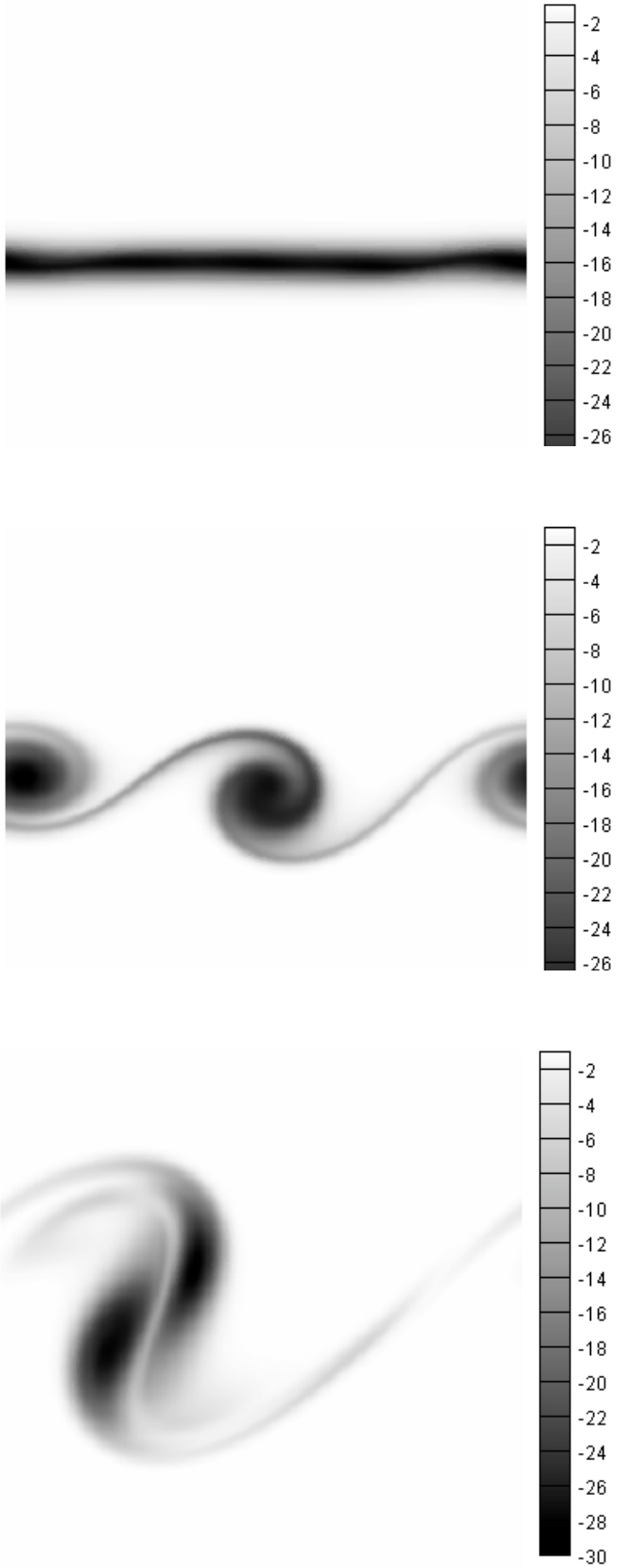

Figure 5.6. The evolution of the mixing layer for an initial integral length scale $\mathcal{L} = \Delta x$: vorticity, ω. Three snapshots are shown corresponding to the formation stage at (top), first pairing (middle), and second pairing (bottom).

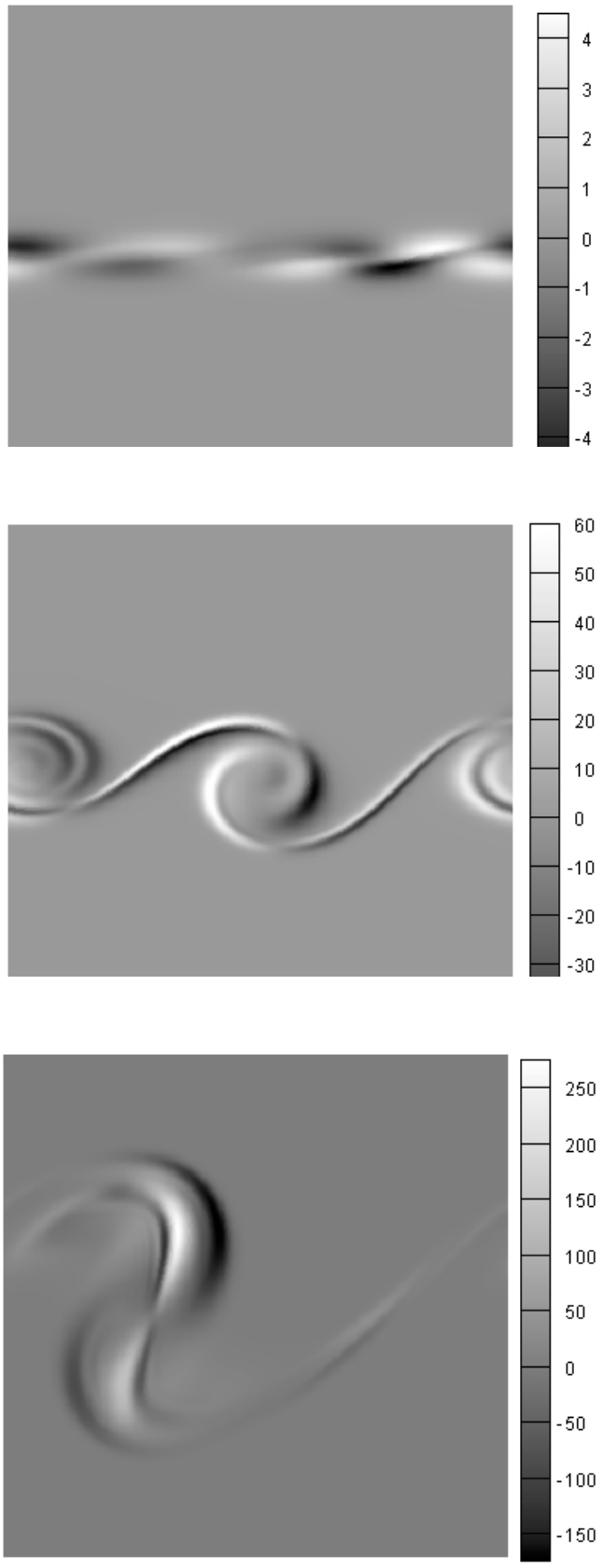

Figure 5.7. $\mathcal{S}_{\omega,\mathcal{L}}$ at $\mathcal{L} = \Delta x$ corresponding to the evolution stages shown in Fig. 5.6

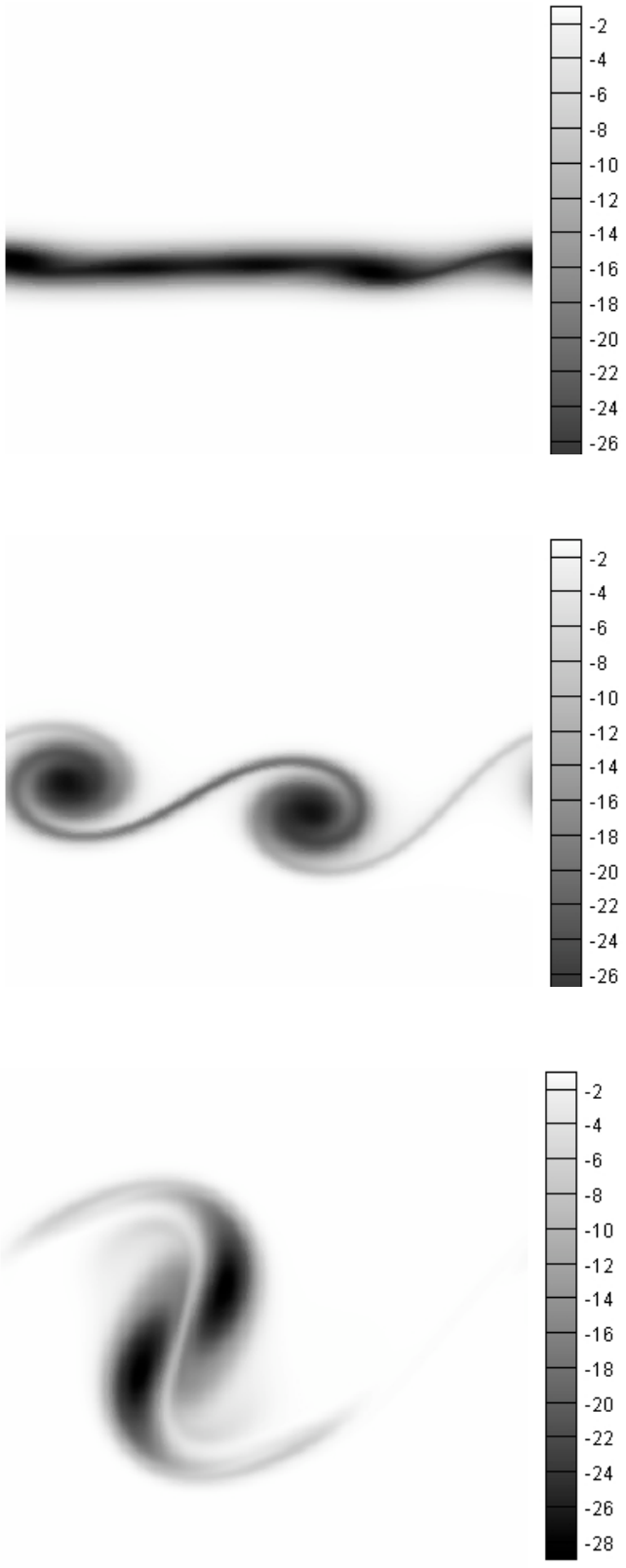

Figure 5.8. The evolution of the mixing layer for an initial integral length scale $\mathcal{L} = 2\Delta x$: vorticity, ω. Three snapshots are shown corresponding to the formation stage (top), first pairing (middle), and second pairing (bottom).

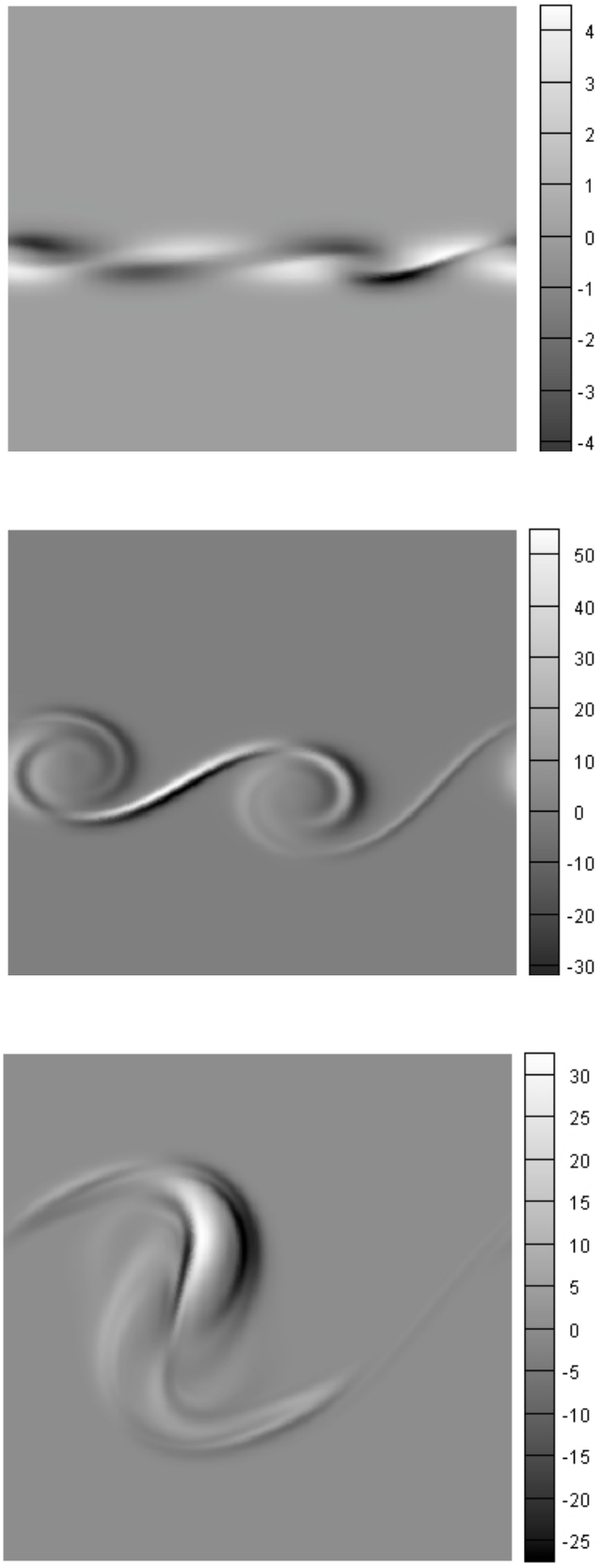

Figure 5.9. $\mathcal{S}_{\omega,\mathcal{L}}$ at $\mathcal{L} = 2\Delta x$ corresponding to the evolution stages shown in Fig. 5.8.

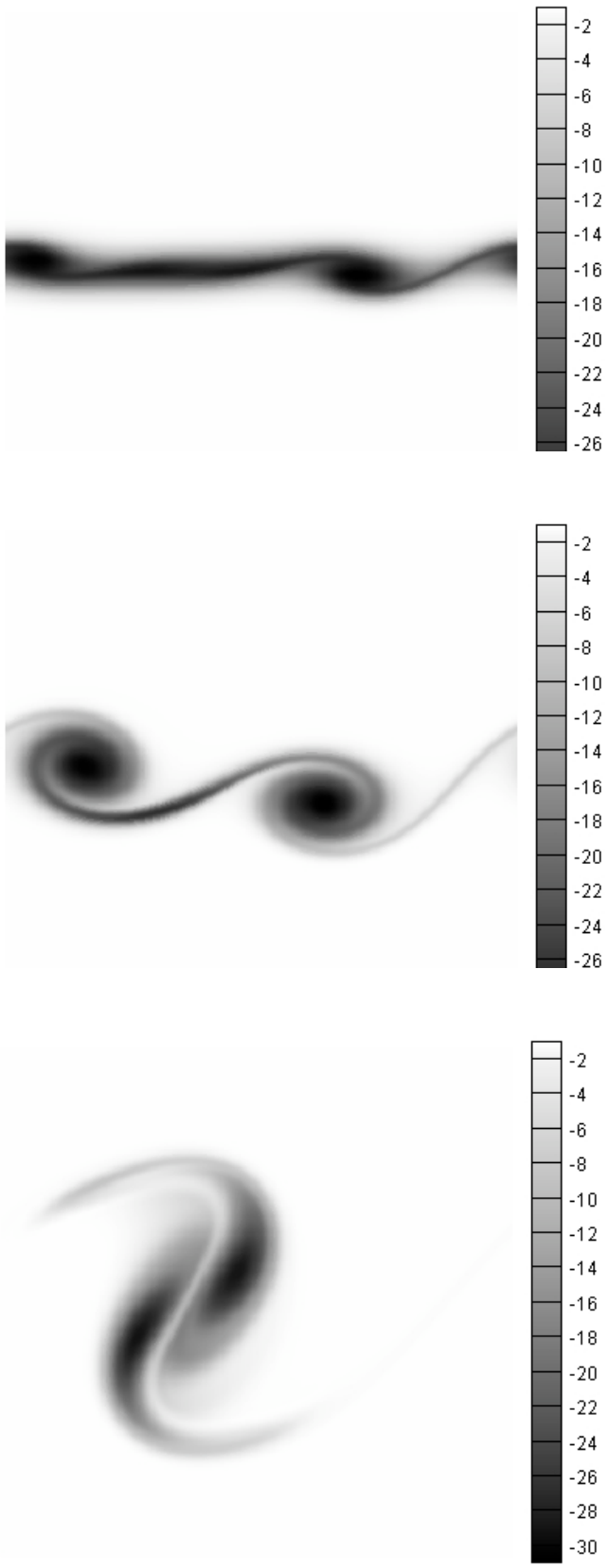

Figure 5.10. The evolution of the mixing layer for an initial integral length scale $\mathcal{L} = 4\Delta x$: vorticity, ω. Three snapshots are shown corresponding to the formation stage (top), first pairing (middle), and second pairing (bottom).

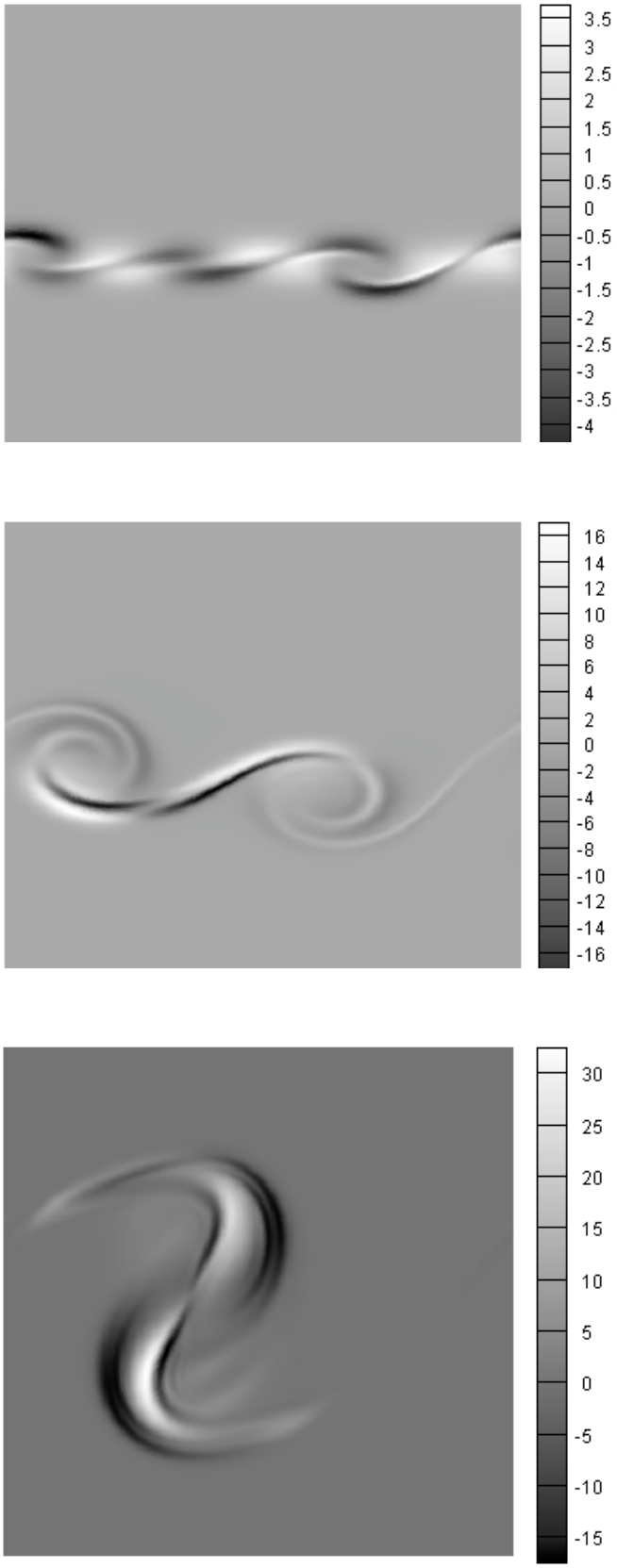

Figure 5.11. $\mathcal{S}_{\omega,\mathcal{L}}$ at $\mathcal{L} = 2\Delta x$ corresponding to the evolution stages shown in Fig. 5.10.

5.5. Nevertheless, several comments can be made regarding the expected change in the vorticity due to increasing $\mathcal{L}$, simply from visual inspection of the ω and $\mathcal{S}_{\omega,\mathcal{L}}$ snapshots presented in Figs. 5.6 through 5.11. The three different stages of evolution will be discussed in sequence.

First of all, in the formation stage, threads of positive (white) and negative (black) sensitivity are interwoven along the central region of the domain, for all three $\mathcal{L}$ investigated. This scenario in the sensitivity pattern suggests a shift or movement of the vortex structures across the weave in the direction of white to black sensitivity for increasing $\mathcal{L}$. The tendency would be for the central band of vorticity to develop undulations with higher $\mathcal{L}$ values. This occurs because $\omega < 0$ everywhere; therefore, black regions in the $\mathcal{S}_{\omega,\mathcal{L}}$ field indicates places where ω will become more negative with increasing $\mathcal{L}$, while regions of white in $\mathcal{S}_{\omega,\mathcal{L}}$ field indicates places where ω will become less negative. Based in part on consideration of ω one can surmise that the vorticity become redistributed with increasing $\mathcal{L}$, leaving the regions in space corresponding to the white $\mathcal{S}_{\omega,\mathcal{L}}$ replete of $-\omega$ and re-depositing that negative vorticity in regions corresponding to the black strips of $\mathcal{S}_{\omega,\mathcal{L}}$. Visual inspection of the waviness of the vorticity band at $\mathcal{L} = 4\Delta x$ (top image in Fig. 5.10) compared to the relatively straight band of vorticity $\mathcal{L} = \Delta x$ (top image in Fig. 5.6) supports this argument.

In the first pairing, one can observe (for example in the middle of Fig. 5.7) a narrow arc of *dark* $\mathcal{S}_{\omega,\mathcal{L}}$ at the nose or leading edge of the central vortex, with a narrow *white* $\mathcal{S}_{\omega,\mathcal{L}}$ at the back or the trailing edge of the central vortex. Between these two arcs, $\mathcal{S}_{\omega,\mathcal{L}} \approx 0$. Again, using the same reasoning as in the formation stage (that ω from white $\mathcal{S}_{\omega,\mathcal{L}}$ becomes re-deposited into regions of dark $\mathcal{S}_{\omega,\mathcal{L}}$), it is predicted that an increase in $\mathcal{L}$ will cause the entire vortex structure in the first pairing to shift from left to right. Figures, 5.7, 5.9, and 5.11 indeed confirm this. Notice, for example, in the middle image of Fig. 5.8 ($\mathcal{L} = 2\Delta x$) how the two paired vortices together reside more or less in the center of the domain and appear shifted relative to the corresponding image in Fig. 5.6 ($\mathcal{L} = \Delta x$) where one vortex lies in the middle of the domain while the other vortex is split across the boundary. Similar comments can be made between Fig. 5.11 ($\mathcal{L} = 4\Delta x$) and Fig. 5.9 ($\mathcal{L} = 2\Delta x$).

Finally, in the second pairing (lower rows of Figs. 5.7, 5.9, and 5.11), the white and dark bands of sensitivity again indicate an expected shift in the vortex structures

at higher $\mathcal{L}$. This can be seen most predominantly between $\mathcal{L} = 2\Delta x$ (Fig. 5.8, lower image), and $\mathcal{L} = 4\Delta x$ (Fig. 5.10, lower image). The sensitivity pattern at $\mathcal{L} = 2\Delta x$ (lower right image), following the same reasoning as before, predicts that the top lobe of the vortex will move slightly to the right, while the lower lobe will remain essentially constant. This will in effect cause the second-paired vortex structure to appear more tilted at $\mathcal{L} = 4\Delta x$, which is exactly the case observed in Fig. 5.10 ($\mathcal{L} = 4\Delta x$, lower image).

Therefore, in summary, it has been demonstrating that the instantaneous $\mathcal{S}_{\omega,\mathcal{L}}$ snapshots can be interpreted to correctly yield the expected behavior at higher $\mathcal{L}$. However, in terms of assessing the effect of $\mathcal{L}$ on mixing layer growth, it is necessary to consider a nearby flow analysis of the momentum thickness, rather than instantaneous snapshots of the $\mathcal{S}_{\omega,\mathcal{L}}$.

5.5.2 Sensitivity of the Vorticity to c_{noise}

As mentioned in Sec. 5.3, c_{noise} represents an amplifier factor that sets the initial turbulence intensity level. In The present study, two values of c_{noise} (10^{-4} and 10^{-3}) are employed and their effects on the structures of $\mathcal{S}_{\omega,c_{noise}}$ examined. In fact, the choice of $c_{noise} = 10^{-4}$ is consistent with the initial velocity defined in the stochastic method, in terms of yielding similar order of magnitude of the perturbations, which allows a fair comparison between the sensitivity results. Validation of the sensitivity code in this case is again done using the nearby flow analysis of the momentum thickness θ, as shown in Figs. 5.12 and 5.13. The nearby θ calculated by projecting the sensitivity results at $c_{noise} = 10^{-4}$ to a higher c_{noise} value of 1.25×10^{-4} using a first order Taylor series, follows the θ obtained directly form the DNS run at $c_{noise} = 1.25 \times 10^{-4}$. The same can be said for the same nearby θ results at $c_{noise} = 1.25 \times 10^{-3}$; although some noticeable deviation between the nearby θ and the actual DNS can be observed for $t^* > 65$ after the second pairing.

The initial velocity and vorticity fields and corresponding sensitivities to c_{noise} and vorticity are shown in Fig. 5.14 and 5.15, respectively, for the case of $c_{noise} = 10^{-4}$. Note, the initial sensitivity fields remain unchanged with c_{noise}; whereas, the initial velocity fields for $c_{noise} = 10^{-3}$ look identical to those of $c_{noise} = 10^{-4}$ with a reduction in the magnitude only. Note, a value of $c_{noise} \leqslant 1 \times 10^{-3}$ has been suggested by Lesieur

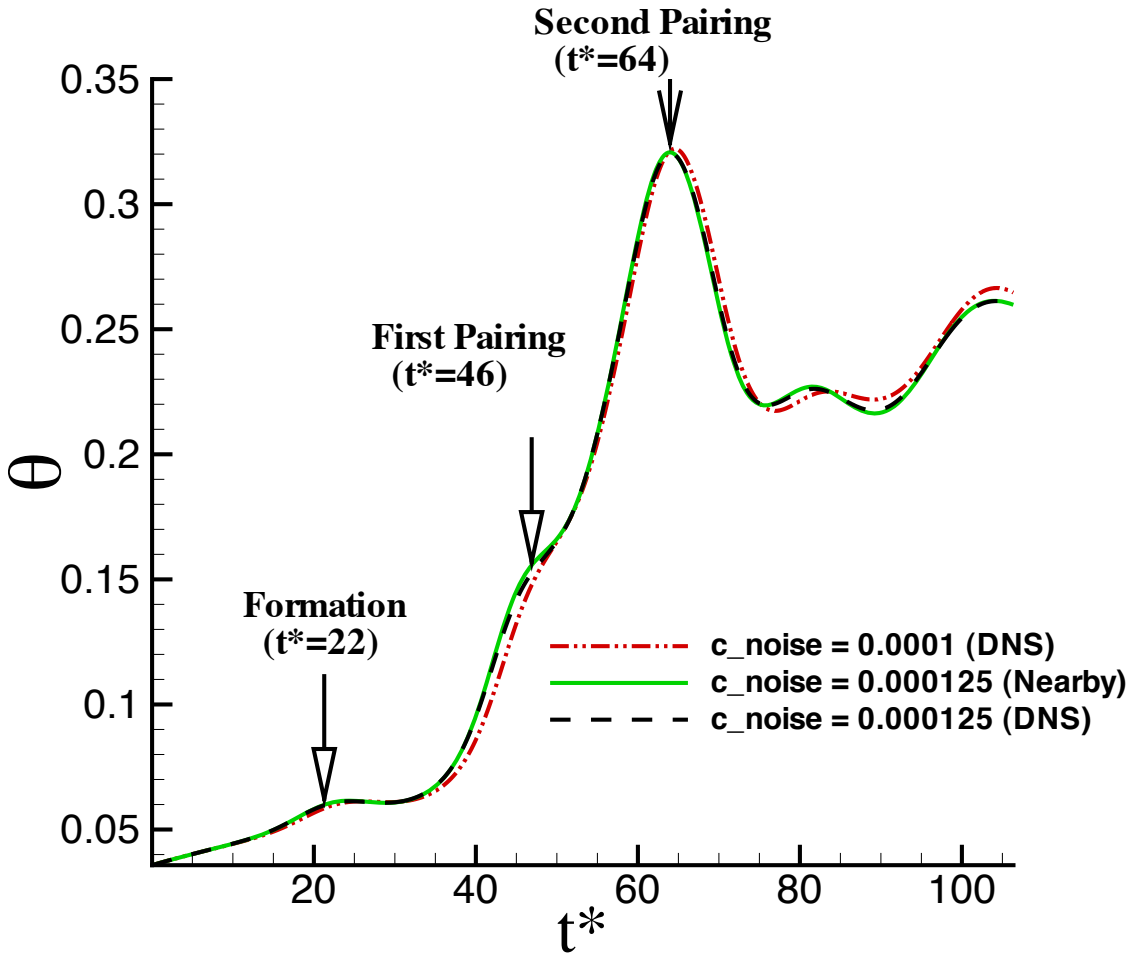

Figure 5.12. Momentum thickness as a function of flow evolution for three cases: DNS using $c_{noise} = 0.0001$ ($-\cdots-$), DNS using $c_{noise} = 0.000125$ ($--$), and the nearby flow prediction for $c_{noise} = 0.000125$ using the CSD results at $c_{noise} = 0.0001$ (—).

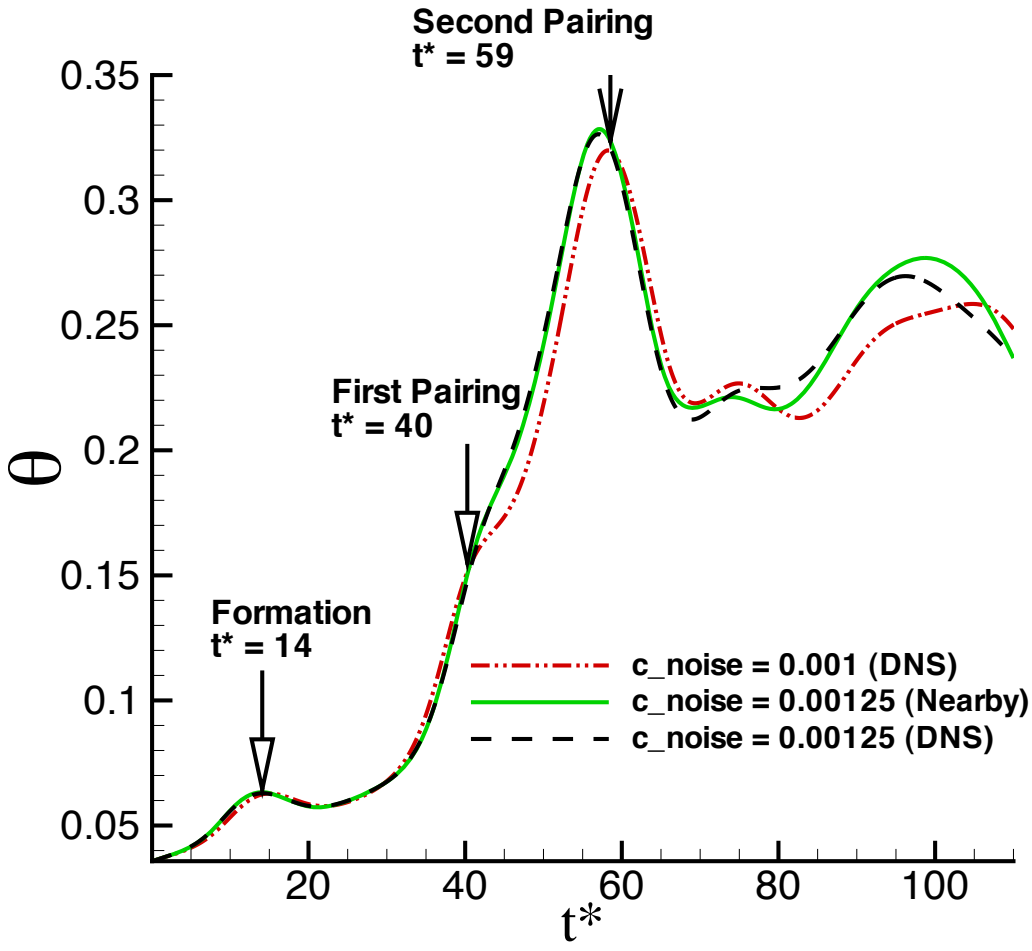

Figure 5.13. Momentum thickness as a function of flow evolution for three cases: DNS using $c_{noise} = 0.001$ ($- \cdot \cdot -$), DNS using $c_{noise} = 0.00125$ ($--$), and the nearby flow prediction for $c_{noise} = 0.00125$ using the CSD results at $c_{noise} = 0.001$ (—).

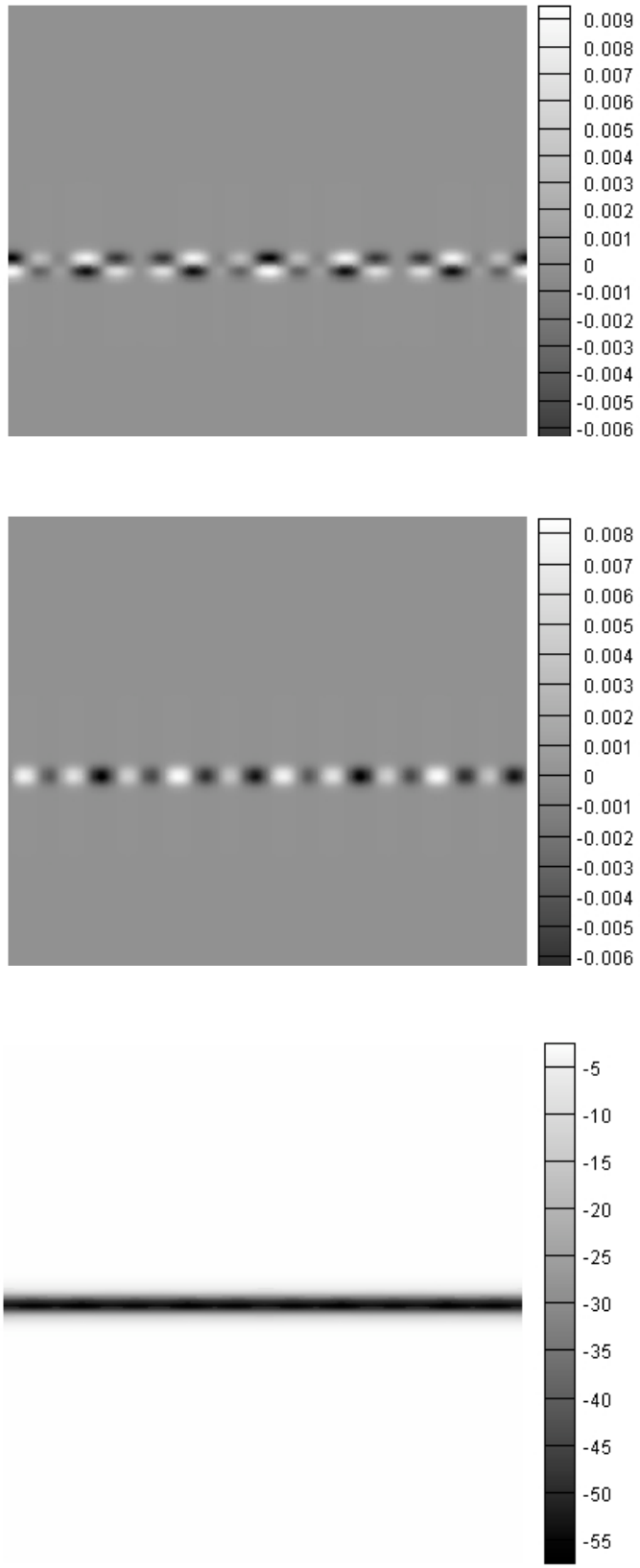

Figure 5.14. Initial velocity and vorticity using $c_{noise} = 1 \times 10^{-4}$, (top): horizontal component of the initial velocity, (middle): vertical component of the initial velocity, (bottom): initial spanwise vorticity field.

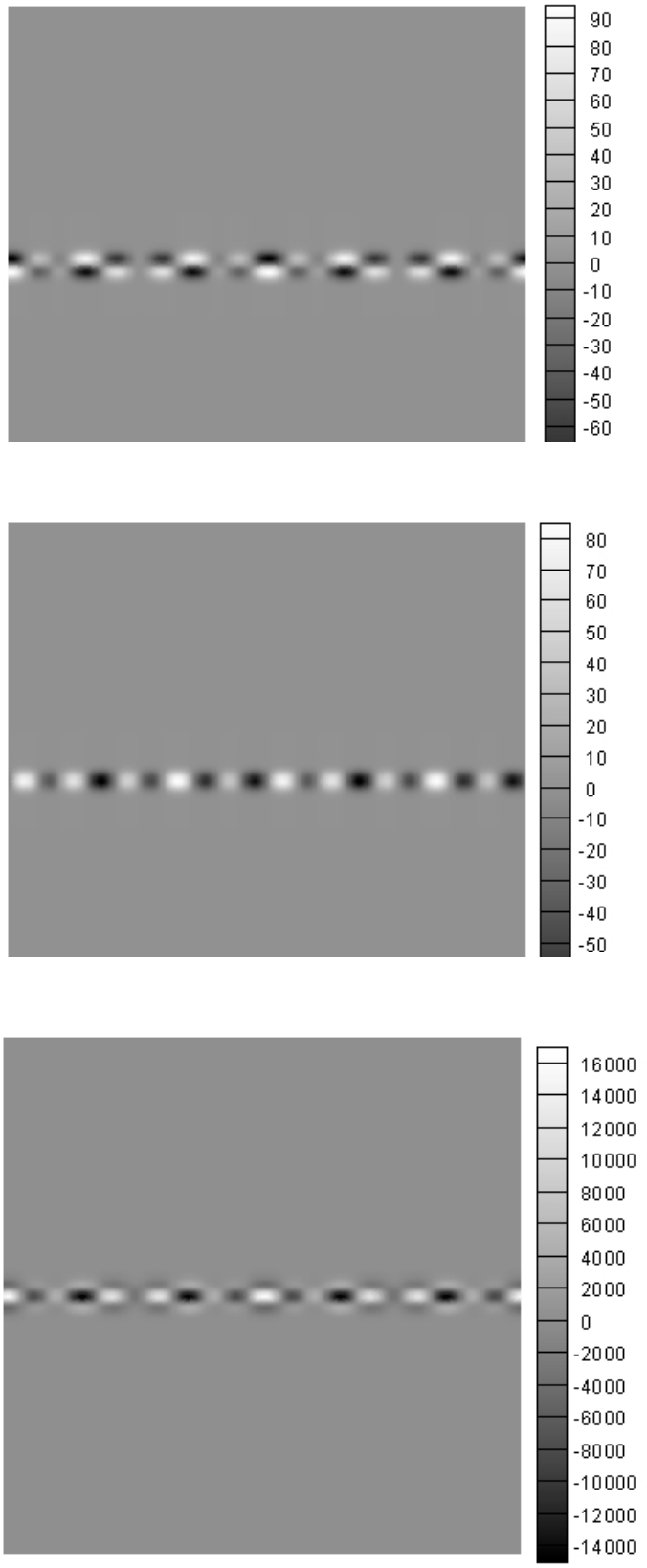

Figure 5.15. Initial sensitivity of velocity and vorticity to c_{noise} using $c_{noise} = 1 \times 10^{-4}$, corresponding to the snapshots shown in Fig. 5.14.

et al. (1988) in order to obtain suitably formed vortices. Values of c_{noise} higher than this tend to disrupt the development of the mixing layer causing fewer fundamental K-H vortices to form due to excessive turbulence intensity levels.

Figures 5.16 and 5.17 compares the evolution of $\mathcal{S}_{\omega,c_{noise}}$ for the two cases of $c_{noise} = 1 \times 10^{-4}$ (left panels) and 1×10^{-3} (right panels). It can be seen that the sensitivity snapshots $c_{noise} = 1 \times 10^{-4}$ are consistent with the two-blade structure discovered in Chap. 2. Recall that the two-blade structure indicates enlargement of the coherent vortices with an increase in the parameter, implying faster growth of the mixing layer. This interpretation of the sensitivity field is indeed confirmed in Fig. 5.18, which displays the evolution of the momentum thickness using both $c_{noise} = 1 \times 10^{-4}$ and 1×10^{-3}. The stark shift between the two lines clearly means that the mixing layer grows faster comparatively for $c_{noise} = 1 \times 10^{-3}$.

In terms of the sensitivity fields for the case of $c_{noise} = 1 \times 10^{-3}$, Fig. 5.17 reveals a noticeable change in the pattern of $\mathcal{S}_{\omega,c_{noise}}$ during the first paring stage. Instead of the original two-blade structure that occurred at lower c_{noise}, a reverse two-blade structure appears at $c_{noise} = 1 \times 10^{-3}$. Here, reverse refers to the opposite sign sensitivity, so that black regions (negative $\mathcal{S}_{\omega,c_{noise}}$) at $c_{noise} = 1 \times 10^{-4}$ switch to white (positive $\mathcal{S}_{\omega,c_{noise}}$) at $c_{noise} = 1 \times 10^{-3}$, and visa versa. This transformation in the sensitivity structure is important and signifies a critical change in the behavior and evolution of the mixing layer. Specifically, it was found (not shown) that for $c_{noise} > 1 \times 10^{-3}$, the formation of the initial K-H vortices becomes erratic. In this manner, $\mathcal{S}_{\omega,c_{noise}}$ serves as a useful indicator for establishing this critical threshold for c_{noise}.

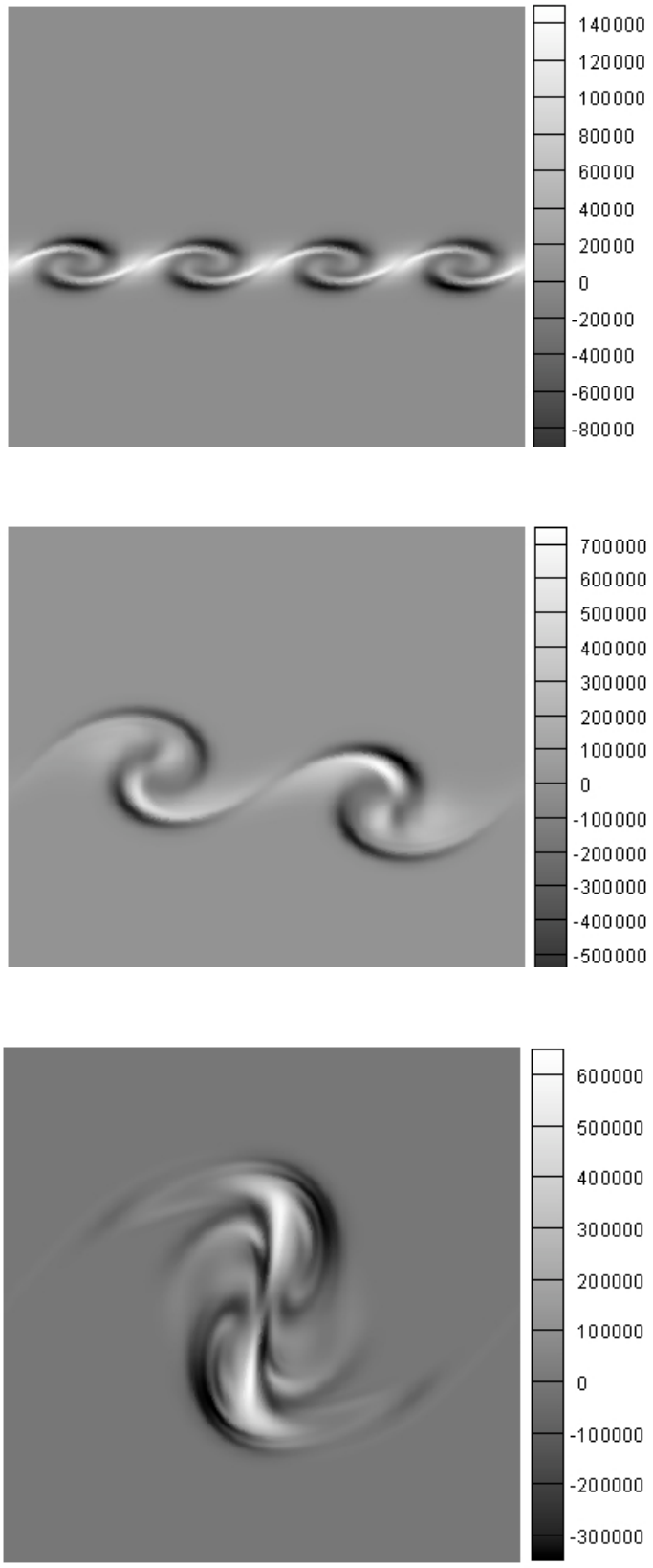

Figure 5.16. Sensitivity of vorticity to c_{noise}, $\mathcal{S}_{\omega,c_{noise}}$ for the case of $c_{noise} = 1 \times 10^{-4}$.

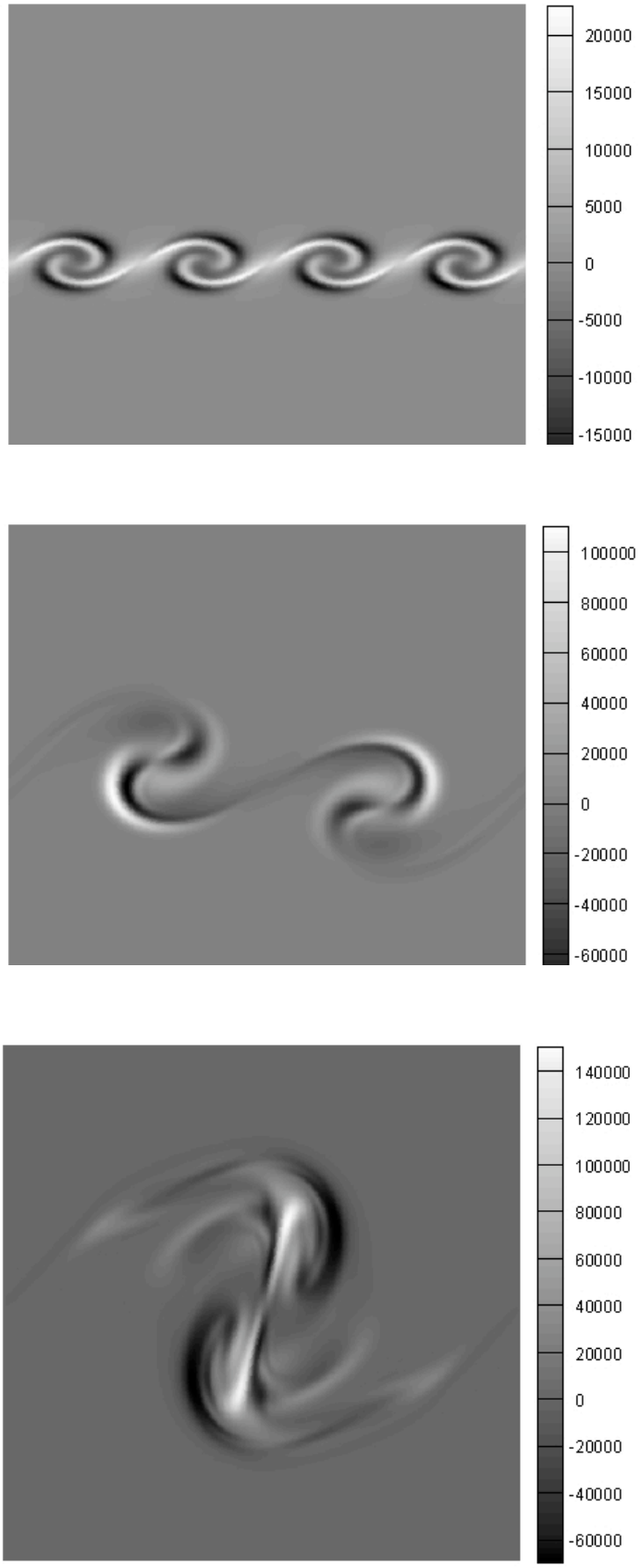

Figure 5.17. Sensitivity of vorticity to c_{noise}, $\mathcal{S}_{\omega,c_{noise}}$ for the case of $c_{noise} = 1 \times 10^{-3}$.

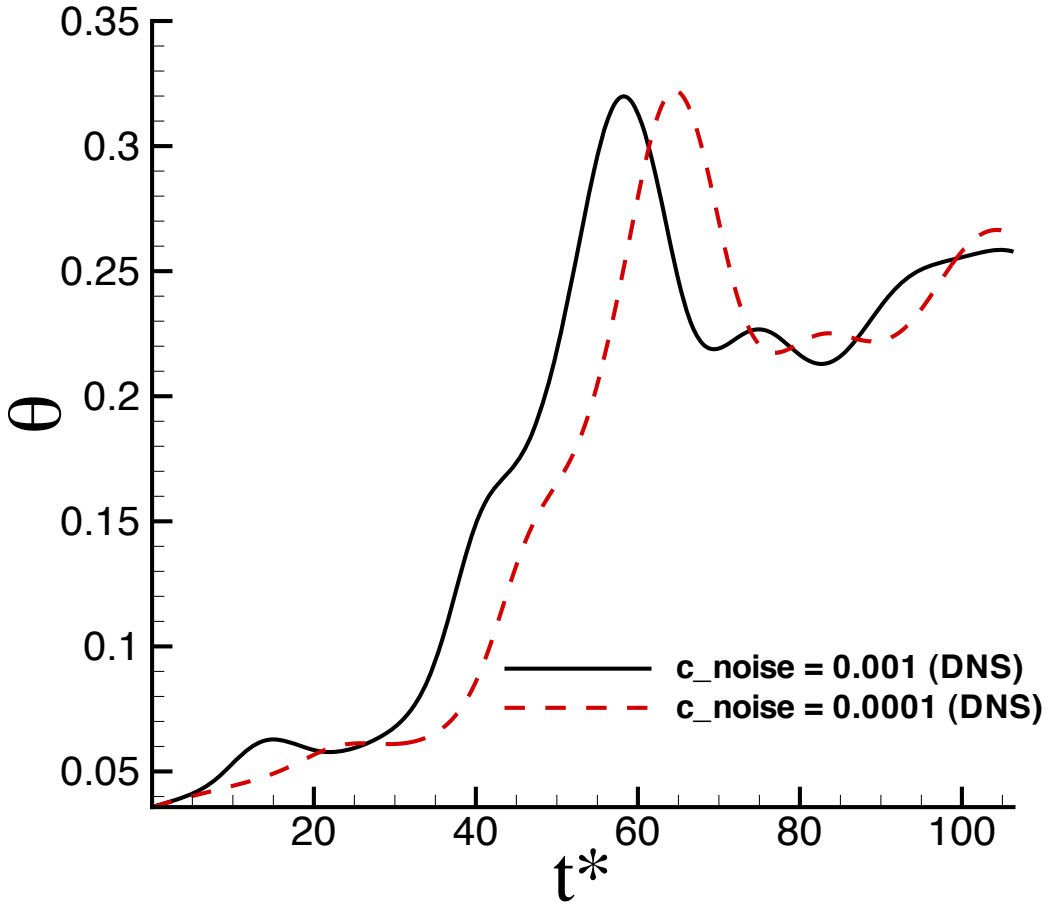

Figure 5.18. Comparison between the evolution of the momentum thickness using: $c_{noise} = 1 \times 10^{-3}$ $(-)$, and $c_{noise} = 1 \times 10^{-4}$ $(--)$.

CHAPTER 6

SUMMARY

Computational sensitivity analysis is a modern technique that has many real world applications. In fluid mechanics, it can be used to further our understanding of the turbulent flows. When applied to the engineering world, it can help optimize fluid systems. In this approach, sensitivity coefficients relevant to the problem are computed. Sensitivity coefficients are defined as the partial derivatives of the objective function (function whose behavior is to be understood) with respect to the design parameters of interest.

In the present work, two computational sensitivity analysis tools, namely, the sensitivity equation method (SEM) and complex-step differentiation (CSD), are used. The primary objective of this research is to examine and quantify the functional relationship between changes in the dynamics of turbulent shear layer flows and perturbations in certain flow parameters. The temporal mixing layer is chosen as the canonical test case as it appears in a variety of engineering applications. The spatial mixing layer was not considered as its analysis is more computationally expensive in direct numerical simulation (DNS) and large eddy simulation (LES). However, by satisfying Taylor's hypothesis, the results obtained from temporal mixing layer can be easily extended to its spatial counterpart.

The fundamental feature of mixing layers is the formation of Kelvin-Helmholtz (K-H) vortices, and their roll-up process. Sensitivity analysis of the planar mixing layer is performed at a Reynolds number based on the initial vortex thickness (Re_{δ_0}) of 200 in Chap.2. The continuous sensitivity equations with the corresponding boundary and initial conditions were derived by taking the partial derivatives of the momentum and temperature equations (as well as their boundary/initial conditions) with respect to Re_{δ_0} and the Prandtl number (Pr). Direct numerical simulations (DNS) of the equations governing both the primitive variables and the sensitivity coefficients were

performed using a finite-volume, fractional-step algorithm. Sensitivity results are presented from a baseline DNS/SEM simulation run at $Re_{\delta_0} = 200$ and $Pr = 0.71$. Three sensitivity coefficients are examined: (i) $\mathcal{S}_{\omega,Re_{\delta_0}}$, which is the sensitivity of vorticity to changes in Re_{δ_0}, (ii) $\mathcal{S}_{T,Pr}$, which is the sensitivity of temperature to changes in Pr, and (iii) $\mathcal{S}_{T,Re_{\delta_0}}$, which is the sensitivity of temperature to changes in Re_{δ_0}. Using SEM, the coherency of the instantaneous sensitivity field was captured. The instantaneous sensitivity fields shed light on the physical mechanisms responsible for Re_{δ_0} and Pr effects on the vorticity and temperature fields. SEM is introduced as a powerful tool to obtain quantitative predictions of *nearby flows*, i.e., those with Re_{δ_0} and Pr values near the baseline case. The SEM results reveal that coherent structures not only exist in the sensitivity field but also mimic those in the vorticity and temperature fields. Following the roll-up process in the vorticity field, the sensitivity field undergoes the same four main stages of evolution as the vorticity field: (i) the formation of the fundamental K-H vortices, (ii) first pairing, (iii) second pairing, and (iv) saturation. The $\mathcal{S}_{\omega,Re_{\delta_0}}$ field obtained from the baseline SEM exhibits a two-blade pattern characterized by a highly negative band of $\mathcal{S}_{\omega,Re_{\delta_0}}$ along the outer edges of the vortices, coupled with a highly positive band of $\mathcal{S}_{\omega,Re_{\delta_0}}$ in the vortex cores. From the two-blade sensitivity pattern, growth in both the size and vorticity magnitude of the vortices at higher Re_{δ_0} can be predicted. From the pattern of $\mathcal{S}_{T,Pr}$, it can be predicted that the temperature in the core region of the vortices becomes less homogeneous with increasing Pr, which implies less scalar mixing at higher Pr. In contrast, the configuration of $\mathcal{S}_{T,Re_{\delta_0}}$ reveals a negligible Re_{δ_0} effect on scalar mixing, at least up to the second pairing. However, $\mathcal{S}_{T,Re_{\delta_0}}$ predicts growth in the size of the coherent temperature structures with increasing Re_{δ_0}, due to the Reynolds number effect on the vorticity field. In addition, the normalized sensitivity coefficients show that the temperature field is an order of magnitude more sensitive to perturbations in Re_{δ_0} compared to Pr. In the last part of Chap.2, an expression is derived for the sensitivity of the vortex thickness (δ/δ_0) to Re_{δ_0}. This can be treated as a secondary sensitivity coefficient. Evaluating this expression using the baseline SEM results helped successfully predict δ/δ_0 at 20% higher Re_{δ_0}. The coherent sensitivity structure at higher Reynolds numbers is investigated in Chap.3.

A posteriori tests in capturing the unsteady coherent features in the sensitivity

field of the planar mixing layer are done in Chap.3. The study of two non-parametric sensitivity analysis methods CSD and SEM is performed in the context of the two-dimensional temporal mixing layer. The simulations were run at a baseline $Re_{\delta_0} = 500$ using DNS and LES by implementing the standard and dynamic Smagorinsky models. The characteristic coherent feature in the sensitivity of vorticity to Re_{δ_0}, called the *two-blade sensitivity structure* (discussed in Chap.2), is generalized to higher Reynolds numbers with some modifications. The coherent pattern of the instantaneous sensitivity field observed during the roll-up process (including the second pairing) in Chap.2 is shown to switch to another chaotic structure in the second pairing snapshot, beyond $Re_{\delta_0} = 350$. The new sensitivity structure is indicative of a faster self-similar and fully developed turbulent state in the mixing layer at higher Reynolds numbers. It is shown that CSD and SEM are in excellent agreement in capturing the instantaneous sensitivity fields until the first pairing in the DNS sense. The probability density function (*pdf*) of the sensitivity field is used as a tool to quantify the performance of the methods. The error in the *pdf* increases in both methods and CSD performs better with about 5.8% less error in the *pdf* of sensitivity field at the second pairing compared to SEM. An important contribution of this chapter is the successful implementation of CSD in the context of LES using the standard and dynamic Smagorinsky models for the first time. It is shown that coherent structures of the sensitivity of resolved vorticity to Re_{δ_0} exist in LES of the mixing layer. In fact, CSD/LES and SEM/LES methods successfully reproduce the coherent two-blade structure of sensitivity of the resolved vorticity to Re_{δ_0}. However, these methods underestimate the range of sensitivity in comparison to the filtered DNS data. As opposed to DNS, it is shown that the error in the *pdf* from CSD/LES and SEM/LES increases up to a maximum error at the first paring snapshot, and then decreases until the end of the simulation, when standard Smagorinsky model is used. It is observed that although CSD/LES and SEM/LES produce similar results until the formation snapshot, there is appreciable difference in their performance. CSD/LES simulated the coherent sensitivity field with 10.1% less error in comparison to SEM/LES using the standard model. However, both methods have similar errors at the second pairing snapshot. Implementing the dynamic model resultes in improvement in the range of the sensitivity field compared to the filtered

DNS data. The *pdf* error variation in both methods and the DNS results behave similarly and increase as the flow evolves, when dynamic model is used. Surprisingly, the peak of *pdf* error decreased from 8.1% to 4% in CSD/LES, and from 18.2% to 3.9% in SEM/LES, when the standard model was replaced by the dynamic Smagorinsky model. Implementing CSD is shown to be easier than SEM as no additional sensitivity equation for the parameters of interest needs to be derived and solved. Also, it is shown that the CSD solution is five times faster than SEM in DNS case, and more than 4 times faster than SEM in LES studies. Furthermore, the sensitivity field of resolved vorticity to SFS length scale (l^*), $\mathcal{S}_{\omega,l^*}$, at $Re_{\delta_0} = 500$ is obtained using both CSD and SEM. The effect of increase in l^* on the flow dynamics is shown to be equivalent to effect of decreasing Re_{δ_0}. It is concluded that by increasing the l^*, the growth of the mixing layer decreases.

In Chap.4, *a priori* study is performed in the context of LES for the incompressible planar temporal mixing layer. This is done by implementing the Smagorinsky model to evaluate the subfilter scale (SFS) tensor. Time evolution of the Smagorinsky constant, $\langle C_s^2 \rangle$, was obtained by matching the spatially averaged SFS energy dissipation rate from the filtered DNS data set and that modeled using the LES calculations of the flow field at each time step. The correlation coefficients of SFS stress tensor, $\rho_{ij}(\tau_{i,j}^{\Delta}, \tau_{i,j}^{\Delta,M})$, show poor correlations between values calculated from the filtered DNS data and those obtained from the Smagorinsky model except for the shear component. In addition, SFS dissipation rate field and corresponding sensitivity field (to Re_{δ_0}) obtained from the filtered DNS data, are shown at different simulation times to visualize the source and sink loci in the SFS energy dissipation rate field. Also, a new criterion is developed in the *a priori* study of LES models using which, further assessment of LES models in reproducing the physical features of the flow would be possible. The new criterion demands that an ideal LES model introduces not only SFS stress tensor, τ_{ij}^M, with good correlation to physical data, τ_{ij}, but should also introduce the sensitivity of τ_{ij} to Reynolds number, $\mathcal{S}_{\tau_{ij}^M,Re_{\delta_0}}$, well-correlated to the real sensitivity of the SFS stress tensor, $\mathcal{S}_{\tau_{ij},Re_{\delta_0}}$. To do so, the sensitivity of SFS stress tensor from standard Smagorinsky model was derived in a similar form as τ_{ij}^M. Finally, the idea of *nearby a priori* study is introduced in this chapter. It is motivated by performing the traditional *a priori* study at low-to-moderate Reynolds

numbers. Computational sensitivity analysis provided the sensitivity coefficients necessary for predicting the appropriate values of the model parameter(s) at higher Reynolds number, in the nearby *a priori* study.

In Chap.5, CSD is implemented to calculate the sensitivities of evolution of the mixing layer to its initial conditions. The initial conditions are generated using the supergrid modeling method. Two approaches are utilized: (i) the stochastic method, and (ii) linear stability theory (LST). The parameters of interest in this chapter are the initial integral length scale $\mathcal{L}$ (introduced in the stochastic method), and the initial noise factor c_{noise} (used by the LST approach). It is shown that an increase in the initial length scale $\mathcal{L}$ (if it does not exceed the the size of initial vortex thickness) results in faster growth of the momentum thickness grows. The same observation is made in the case of LST generation of the initial velocity field. It is shown that increasing c_{noise} results in faster evolution of the mixing layer.

APPENDIX

DERIVATIONS

A.1 Sensitivity of the Vortex Thickness, δ/δ_0, to Re_{δ_0}

The sensitivity of δ/δ_0 to Re_{δ_0} is obtained by taking the partial derivative of the vortext thickness introduced in (2.36). Based on definition, vortex thickness is obtained by

$$\frac{\delta(t)}{\delta_0} = \frac{2U/\delta_0}{\zeta}, \tag{A.1}$$

where $\zeta \equiv [d\langle u\rangle/dy]_{max}$. The sensitivity of the nondimensional vortex thickness (to Re_{δ_0}) is derived as

$$\mathcal{S}_{(\delta/\delta_0),Re_{\delta_0}} \equiv \partial(\delta/\delta_0)/\partial Re_{\delta_0} = \partial\left(\frac{2U/\delta_0}{\zeta}\right)/\partial Re_{\delta_0}, \tag{A.2}$$

where $\delta_0 = \nu Re_{\delta_0}/U$, and therefore,

$$\mathcal{S}_{(\delta/\delta_0),Re_{\delta_0}} = \partial\left(\frac{2U^2}{\nu Re_{\delta_0}\zeta}\right)/\partial Re_{\delta_0} = -\frac{2U^2\left[\nu\zeta + \nu Re_{\delta_0}\partial\zeta/\partial Re_{\delta_0}\right]}{(\nu Re_{\delta_0}\zeta)^2}. \tag{A.3}$$

By fraction separation, one can show that

$$\mathcal{S}_{(\delta/\delta_0),Re_{\delta_0}} = -\left(\frac{2U^2}{\nu Re_{\delta_0}^2\zeta} + \frac{2U^2\partial\zeta/\partial Re_{\delta_0}}{\nu Re_{\delta_0}\zeta^2}\right), \tag{A.4}$$

where $\partial\zeta/\partial Re_{\delta_0} \equiv \mathcal{S}_{\zeta,Re_{\delta_0}}$. Rearranging of (A.4) and using the definition of the Reynolds number based on the initial vortex thickness (i.e., $Re_{\delta_0} = U\delta_0/\nu$) yields

$$\mathcal{S}_{(\delta/\delta_0),Re_{\delta_0}} = -\left[(\frac{2U/\delta_0}{\zeta})\ Re_{\delta_0}^{-1} + (\frac{2U/\delta_0}{\zeta})\ \frac{\mathcal{S}_{\zeta,Re_{\delta_0}}}{\zeta}\right]. \tag{A.5}$$

Since $\frac{2U/\delta_0}{\zeta} = \delta/\delta_0$ (see A.1) the sensitivity of the vortex thickness to Re_{δ_0} is derived as

$$\mathcal{S}_{(\delta/\delta_0),Re_{\delta_0}} = -\left(Re_{\delta_0}^{-1} + \frac{\mathcal{S}_{\zeta,Re_{\delta_0}}}{\zeta}\right)(\delta/\delta_0). \tag{A.6}$$

The beauty of (A.6) is that it yields the sensitivity of vortex thickness to Reynolds number as a secondary sensitivity coefficient, for which no additional SEM equations

are solved. In fact, the sensitivity of the momentum thickness to Re_{δ_0} is obtained as the product of a new Re_{δ_0} dependent expression, $-(Re_{\delta_0}^{-1}+\mathcal{S}_{\zeta,Re_{\delta_0}}/\zeta)$, to the function of interest, δ/δ_0. Sensitivity of ζ to Re_{δ_0} (i.e., $S_{\zeta,Re_{\delta_0}}$) is approximted through a nearby flow analysis as follows:

1. The nearby velocity field at $Re_{\delta_0}^{new}$ is evaluated from

$$u_i\big|_{Nearby} = u_i\big|_{Re_{\delta_0}} + S_{u_i}\Delta Re_{\delta_0}. \tag{A.7}$$

2. The corresponding nearby ζ is determined from the nearby velocity field, i.e.,

$$\zeta\big|_{Nearby} = \Big[d\langle u\big|_{Nearby}\rangle/dy\Big]_{max}. \tag{A.8}$$

3. Finally, $\partial\zeta/\partial Re_{\delta_0}$ can be approximated using a finite difference as

$$S_{\zeta,Re_{\delta_0}} \approx (\zeta\big|_{Nearby} - \zeta\big|_{Re_{\delta_0}})/\Delta Re_{\delta_0}. \tag{A.9}$$

It is important to emphasize that the whole quantities associated with $Re_{\delta_0}^{new}$ are estimated from the *nearby* velocity field, which is obtained from a *single* DNS/SEM simulation run at Re_{δ_0}.

A.2 Sensitivity of the Resolved Momentum Equations

Sensitivity of the filtered momentum equations shown in Chap.3 and obtained by taking the partial derivative of (3.14) with respect to $P_k = \{P_1, P_2\} = \{Re_{\delta_0}, l^*\}$ as

$$\frac{\partial\mathcal{S}_{\widetilde{u}_i,P_k}}{\partial t} + \frac{\partial(\widetilde{u}_j\mathcal{S}_{\widetilde{u}_i,P_k})}{\partial x_j} = -\frac{\partial\mathcal{S}_{\widetilde{p},P_k}}{\partial x_i} + \frac{1}{Re_L}\frac{\partial}{\partial x_j}\left[\left(\frac{\partial\mathcal{S}_{\widetilde{u}_i,P_k}}{\partial x_j} + \frac{\partial\mathcal{S}_{\widetilde{u}_i,P_k}}{\partial x_i}\right)\right] - \frac{\partial(\mathcal{T}_{ijk})}{\partial x_j}, \tag{A.10}$$

where $l^* = C_s\Delta$ is called SFS length scale, $\mathcal{S}_{\widetilde{u}_i,P_1}$ ($\equiv \partial\widetilde{u}_i/\partial Re_{\delta_0}$) is the sensitivity of resolved velocity to Re_{δ_0}, and $\mathcal{S}_{\widetilde{u}_i,P_2}$ ($\equiv \partial\widetilde{u}_i/\partial l^*$) is the sensitivity of resolved velocity to l^*. Similarly, $\mathcal{S}_{\widetilde{p},P_1}$ and $\mathcal{S}_{\widetilde{p},P_2}$ are sensitivities of resolved pressure to Re_{δ_0} and l^*, respectively. In this context, $\mathcal{T}_{ijk}$ in (A.10) is originally a *closed* term explicitly obtained based on the resolved velocity and sensitivity fields as

$$\mathcal{T}_{ijk} = \widetilde{u}_i\mathcal{S}_{\widetilde{u}_j,P_k} + \frac{\delta_{1k}2\widetilde{s}_{ij}}{(N\lambda_a/\delta_0)Re_{\delta_0}^2} + \mathcal{S}_{\tau_{ij}^M,P_k}, \tag{A.11}$$

where $\widetilde{u}_i\mathcal{S}_{\widetilde{u}_j}$ is originated from the differentiation of the convection term due to the chain rule, $\delta_{1k}2\widetilde{s}_{ij}/\big[(N\lambda_a/\delta_0)Re_{\delta_0}^2\big]$ is appeared due to existence of Re_{δ_0} in the diffusion term in (A.10), and $\mathcal{S}_{\tau_{ij}^M,P_k}$ is the sensitivity of the modeled SFS stress τ_{ij} to P_k.

A.2.1 Derivation of $\mathcal{S}_{\tau_{ij}^M,P_k}$

Sensitivity of the modeled SFS stress tensor to the parameters of interest $P_k = Re_{\delta_0}, l^*$ i.e., $\mathcal{S}_{\tau_{ij}^M,P_k}$ is derived by taking the partial derivative of τ_{ij}^M with respect to P_k as

$$\mathcal{S}_{\tau_{ij}^M,P_k} \equiv \frac{\partial \tau_{ij}^M}{\partial P_k} = \frac{\partial \left(-2\nu_\tau \widetilde{s}_{ij}\right)}{\partial P_k} = \frac{\partial \left(-2(C_s\Delta)^2|\widetilde{S}|\widetilde{s}_{ij}\right)}{\partial P_k}, \tag{A.12}$$

where $\widetilde{s}_{ij} = \frac{1}{2}(\partial\widetilde{u}_i/\partial x_j + \partial\widetilde{u}_j/\partial x_i)$ is the resolved strain-rate tensor, and $|\widetilde{S}| = \sqrt{2\widetilde{s}_{ij}\widetilde{s}_{ij}}$. The sensitivity of the modeled SFS stress tensor to $P_1 = Re_{\delta_0}$ is first derived as

$$\mathcal{S}_{\tau_{ij}^M,Re_{\delta_0}} = \frac{\partial \left(-2(C_s\Delta)^2|\widetilde{S}|\widetilde{s}_{ij}\right)}{\partial Re_{\delta_0}}. \tag{A.13}$$

It can be shown that the filter width Δ is independent of Re_{δ_0} in a nondimensional grid, and C_s is assumed to be constant in the standard Smagorinsky model. Therefore,

$$\mathcal{S}_{\tau_{ij}^M,Re_{\delta_0}} = -2(C_s\Delta)^2\frac{\partial \left(|\widetilde{S}|\widetilde{s}_{ij}\right)}{\partial Re_{\delta_0}} = -2(C_s\Delta)^2\left(|\widetilde{S}|\frac{\partial \widetilde{s}_{ij}}{\partial Re_{\delta_0}} + \widetilde{s}_{ij}\frac{\partial|\widetilde{S}|}{\partial Re_{\delta_0}}\right), \tag{A.14}$$

where $\partial\widetilde{s}_{ij}/\partial Re_{\delta_0} \equiv \mathcal{S}_{\widetilde{s}_{ij},Re_{\delta_0}}$ obtained as

$$\mathcal{S}_{\widetilde{s}_{ij},Re_{\delta_0}} = \frac{1}{2}\left[\partial\mathcal{S}_{\widetilde{u}_i,Re_{\delta_0}}/\partial x_j + \partial\mathcal{S}_{\widetilde{u}_j,Re_{\delta_0}}/\partial x_i\right], \tag{A.15}$$

where $\mathcal{S}_{\widetilde{u}_i,Re_{\delta_0}}$ is the sensitivity of the *resolved* velocity to Re_{δ_0} obtained from (3.25), and $\partial|\widetilde{S}|/\partial Re_{\delta_0}$ is obtained as

$$\frac{\partial|\widetilde{S}|}{\partial Re_{\delta_0}} = \frac{\partial}{\partial Re_{\delta_0}}(\sqrt{2\widetilde{s}_{ij}\widetilde{s}_{ij}}) = \frac{2\widetilde{s}_{ij}\mathcal{S}_{\widetilde{s}_{ij},Re_{\delta_0}}}{|\widetilde{S}|}. \tag{A.16}$$

Plugging (A.15) and (A.16) into (A.14) yields

$$\mathcal{S}_{\tau_{ij}^M,Re_{\delta_0}} = -2(C_s\Delta)^2\left(|\widetilde{S}|\mathcal{S}_{\widetilde{s}_{ij},Re_{\delta_0}} + |\widetilde{S}|\mathcal{S}_{\widetilde{s}_{ij},Re_{\delta_0}}\right) = -2\underbrace{(C_s\Delta)^2|\widetilde{S}|}_{\nu_\tau}(2\mathcal{S}_{\widetilde{s}_{ij},Re_{\delta_0}}), \tag{A.17}$$

and therefore,

$$\mathcal{S}_{\tau_{ij}^M,Re_{\delta_0}} = -2\nu_\tau\widetilde{\Lambda}_{ij1}, \tag{A.18}$$

where

$$\widetilde{\Lambda}_{ij1} = 2\mathcal{S}_{\widetilde{s}_{ij},Re_{\delta_0}} = \frac{\partial\mathcal{S}_{\widetilde{u}_i,Re_{\delta_0}}}{\partial x_j} + \frac{\partial\mathcal{S}_{\widetilde{u}_j,Re_{\delta_0}}}{\partial x_i}. \tag{A.19}$$

Similarly, the sensitivity of the modeled SFS stress tensor to $P_2 = l^* = C_s\Delta$ is derived as

$$\mathcal{S}_{\tau_{ij}^M, l^*} = -2\nu_\tau \widetilde{\Lambda}_{ij2}, \tag{A.20}$$

where

$$\widetilde{\Lambda}_{ij2} = 2\left(\mathcal{S}_{\widetilde{s}_{ij}, l^*} + \frac{1}{l^*}\widetilde{s}_{ij}\right) = \frac{\partial \mathcal{S}_{\widetilde{u}_i, l^*}}{\partial x_j} + \frac{\partial \mathcal{S}_{\widetilde{u}_j, l^*}}{\partial x_i} + \frac{2}{l^*}\widetilde{s}_{ij} \tag{A.21}$$

A.3 Sensitivity of the Filtered Momentum Equations to Re_{δ_0}

A.3.1 Proof of $\mathcal{S}_{\widetilde{u}_i, Re_{\delta_0}} = \widetilde{\mathcal{S}}_{u_i,, Re_{\delta_0}}$

One needs to first show that $\mathcal{S}_{\widetilde{u}_i, Re_{\delta_0}} = \widetilde{\mathcal{S}}_{u_i,, Re_{\delta_0}}$. By definition, it can be shown that

$$\mathcal{S}_{\widetilde{u}_i, Re_{\delta_0}} \equiv \frac{\partial \widetilde{u}_i}{\partial Re_{\delta_0}} = \frac{\partial}{\partial Re_{\delta_0}} \int_\Omega u_i(\mathbf{x}) G(\mathbf{x} - \xi) d\xi. \tag{A.22}$$

Since $\Omega \in [-0.5, 0.5]^2$ is a nondimensional domain and independent of Re_{δ_0}, it is possible to take the partial derivative into the integral as

$$\mathcal{S}_{\widetilde{u}_i, Re_{\delta_0}} = \int_\Omega \frac{\partial \left[u_i(\mathbf{x}) G(\mathbf{x} - \xi)\right]}{\partial Re_{\delta_0}} d\xi.$$

Since $G(\mathbf{x} - \xi)$ (defined on Ω) is nondimensional, the kernel filter is independent of Re_{delta_0} and therefore

$$\mathcal{S}_{\widetilde{u}_i} = \int_\Omega \frac{\partial u_i(\mathbf{x})}{\partial Re_{\delta_0}} G(\mathbf{x} - \xi) d\xi,$$

and by definition $\partial u_i(\mathbf{x}) / \partial Re_{\delta_0} \equiv \mathcal{S}_{u_i, Re_{\delta_0}}$, and therefore

$$\mathcal{S}_{\widetilde{u}_i, Re_{\delta_0}} = \int_\Omega \mathcal{S}_{u_i, Re_{\delta_0}} G(\mathbf{x} - \xi) d\xi \tag{A.23}$$

The right hand side of (A.23) denotes the filtered sensitivity coefficient, i.e.,

$$\mathcal{S}_{\widetilde{u}_i, Re_{\delta_0}} = \widetilde{\mathcal{S}}_{u_i,, Re_{\delta_0}} \tag{A.24}$$

.

A.3.2 Proof of $\mathcal{S}_{\widetilde{s}_{ij},Re_{\delta_0}} = \widetilde{\mathcal{S}}_{s_{ij},Re_{\delta_0}}$

In order to show that $\mathcal{S}_{\widetilde{s}_{ij},Re_{\delta_0}} = \widetilde{\mathcal{S}}_{s_{ij},Re_{\delta_0}}$, one needs to start from the definition of this sensitivity coefficient as

$$\mathcal{S}_{\widetilde{s}_{ij},Re_{\delta_0}} \equiv \partial \widetilde{s}_{ij}/\partial Re_{\delta_0}. \tag{A.25}$$

Substituting the definition of the strain rate tensor yields

$$\mathcal{S}_{\widetilde{s}_{ij},Re_{\delta_0}} = \frac{1}{2}\partial\left[\widetilde{\frac{\partial u_i}{\partial x_j} + \frac{\partial u_j}{\partial x_i}}\right]/\partial Re_{\delta_0}. \tag{A.26}$$

By considering the linearity property of the kernel filter and commutive behavior of the kernel filter with respect to the spatial derivations, (A.26) can be rewritten as

$$\mathcal{S}_{\widetilde{s}_{ij},Re_{\delta_0}} = \frac{1}{2}\partial\left[\frac{\partial \widetilde{u}_i}{\partial x_j} + \frac{\partial \widetilde{u}_j}{\partial x_i}\right]/\partial Re_{\delta_0}.$$

Again, by switching the order of spatial differentiation with the differentiation with respect to Re_{δ_0} as

$$\mathcal{S}_{\widetilde{s}_{ij},Re_{\delta_0}} = \frac{1}{2}\left[\partial(\frac{\partial \widetilde{u}_i}{\partial Re_{\delta_0}})/\partial x_j + \partial(\frac{\partial \widetilde{u}_j}{\partial Re_{\delta_0}})/\partial x_i\right].$$

Using the definition of the sensitivity coefficients $\partial\widetilde{u}_i/\partial Re_{\delta_0}$ and $\partial\widetilde{u}_j/\partial Re_{\delta_0}$,

$$\mathcal{S}_{\widetilde{s}_{ij},Re_{\delta_0}} = \frac{1}{2}\left[\partial\mathcal{S}_{\widetilde{u}_i,Re_{\delta_0}}/\partial x_j + \partial\mathcal{S}_{\widetilde{u}_j,Re_{\delta_0}}/\partial x_i\right] \tag{A.27}$$

Plugging (A.24) into (A.27) yields

$$\mathcal{S}_{\widetilde{s}_{ij},Re_{\delta_0}} = \frac{1}{2}\left[\partial\widetilde{\mathcal{S}}_{u_i,Re_{\delta_0}}/\partial x_j + \partial\widetilde{\mathcal{S}}_{u_j,Re_{\delta_0}}/\partial x_i\right] \tag{A.28}$$

Using the linearity property of the kernel filter as mentioned earlier, one can take the tilde averaging over both terms as

$$\mathcal{S}_{\widetilde{s}_{ij},Re_{\delta_0}} = \frac{1}{2}\widetilde{\left[\partial\mathcal{S}_{u_i,Re_{\delta_0}}/\partial x_j + \partial\mathcal{S}_{u_j,Re_{\delta_0}}/\partial x_i\right]} \tag{A.29}$$

The term under the tilde is basically the sensitivity of the strain rate tensor to Re_{δ_0} and therefore

$$\mathcal{S}_{\widetilde{s}_{ij},Re_{\delta_0}} = \widetilde{\mathcal{S}}_{s_{ij},Re_{\delta_0}}. \tag{A.30}$$

A.3.3 Derivation of $\mathcal{S}_{\tau_{ij},Re_{\delta_0}}$

The subfilter scale (SFS) stress tensor τ_{ij} appears in the filtered momentum equations as a result of filtering process. The sensitivity of τ_{ij} to Re_δ (i.e., $\mathcal{S}_{\tau_{ij},Re_{\delta_0}}$) is an important term that appears in the SEM equation for the sensitivity of the *resolved* or *filtered* velocity field to Re_{δ_0}. To derive $\mathcal{S}_{\tau_{ij},Re_{\delta_0}}$, the definition of $\mathcal{S}_{\tau_{ij},Re_{\delta_0}}$ is written as

$$\mathcal{S}_{\tau_{ij},Re_{\delta_0}} = \frac{\partial}{\partial Re_{\delta_0}}(\widetilde{u_i u_j} - \widetilde{u}_i\widetilde{u}_j) = \underbrace{\frac{\partial(\widetilde{u_i u_j})}{\partial Re_{\delta_0}}}_{\mathcal{A}} - \underbrace{\frac{\partial(\widetilde{u}_i\widetilde{u}_j)}{\partial Re_{\delta_0}}}_{\mathcal{B}}. \tag{A.31}$$

The inner term of $\mathcal{A}$ can be substituted by the convolution of $u_i u_j$ to the kernel filter as

$$\mathcal{A} := \frac{\partial}{\partial Re_{\delta_0}} \int_\Omega (u_i u_j) G(\mathbf{x}-\xi) d\xi. \tag{A.32}$$

Since the nondimensional domain Ω and the kernel filter G are independent of Re_{δ_0}, $\mathcal{A}$ can be rewritten as

$$\mathcal{A} = \int_\Omega \frac{\partial(u_i u_j)}{\partial Re_{\delta_0}} G(\mathbf{x}-\xi) d\xi = \int_\Omega \left[u_i \frac{\partial u_j}{\partial Re_{\delta_0}} + u_j \frac{\partial u_i}{\partial Re_{\delta_0}} \right] G(\mathbf{x}-\xi) d\xi,$$

hence

$$\mathcal{A} = \int_\Omega (\underbrace{u_i \mathcal{S}_{u_j,Re_{\delta_0}}}_{f} + \underbrace{u_j \mathcal{S}_{u_i,Re_{\delta_0}}}_{g}) G(\mathbf{x}-\xi) d\xi = \int_\Omega f G(\mathbf{x}-\xi) d\xi + \int_\Omega g G(\mathbf{x}-\xi) d\xi = \widetilde{f} + \widetilde{g}.$$

Therefore,

$$\mathcal{A} = \widetilde{u_i \mathcal{S}}_{u_j,Re_{\delta_0}} + \widetilde{u_j \mathcal{S}}_{u_i,Re_{\delta_0}}. \tag{A.33}$$

The second term in the r.h.s. of (A.31) is obtained as

$$\mathcal{B} := \frac{\partial(\widetilde{u}_i\widetilde{u}_j)}{\partial Re_{\delta_0}} = \widetilde{u}_i \frac{\partial \widetilde{u}_j}{\partial Re_{\delta_0}} + \widetilde{u}_j \frac{\partial \widetilde{u}_i}{\partial Re_{\delta_0}}, \tag{A.34}$$

where $\frac{\partial \widetilde{u}_i}{\partial Re_{\delta_0}} \equiv \mathcal{S}_{\widetilde{u}_i,Re_{\delta_0}}$ and $\frac{\partial \widetilde{u}_j}{\partial Re_{\delta_0}} \equiv \mathcal{S}_{\widetilde{u}_j,Re_{\delta_0}}$. Using (A.30), one can obtain the term $\mathcal{B}$ in its final form

$$\mathcal{B} = \widetilde{u}_i \widetilde{\mathcal{S}}_{u_j,Re_{\delta_0}} + \widetilde{u}_j \widetilde{\mathcal{S}}_{u_i,Re_{\delta_0}}. \tag{A.35}$$

Plugging (A.33) and (A.35) into (A.31) yields

$$\mathcal{S}_{\tau_{ij},Re_{\delta_0}} = \left(\widetilde{u_i \mathcal{S}}_{u_j,Re_{\delta_0}} + \widetilde{u_j \mathcal{S}}_{u_i,Re_{\delta_0}} \right) - \left(\widetilde{u}_i \widetilde{\mathcal{S}}_{u_j,Re_{\delta_0}} + \widetilde{u}_j \widetilde{\mathcal{S}}_{u_i,Re_{\delta_0}} \right) \tag{A.36}$$

By rearranging the four terms in (A.36), the sensitivity of the SFS stress tensor to Re_{δ_0} is obtained as an unclosed term in the momentum sensitivity equation as

$$\mathcal{S}_{\tau_{ij},Re_{\delta_0}} = \mathcal{L}_{ij} - \mathcal{L}_{ij}^T, \tag{A.37}$$

where

$$\mathcal{L}_{ij} = \widetilde{u_i \mathcal{S}}_{u_j,Re_{\delta_0}} + \widetilde{u}_i \widetilde{\mathcal{S}}_{u_j,Re_{\delta_0}}. \tag{A.38}$$

REFERENCES

Anderson, W. K., J. C. Newmann, D. L. Whitefield, and E. J. Nielsen, 1999: Sensitivity analysis for the navier-stokes equations on unstructured meshes using complex variables. *AIAA Journal*, **99–3294**.

Bardina, J., J. H. Ferziger, and W. C. Reynolds, 1980: Improved subgrid scale models for large eddy simulation. *AIAA Journal*, **80 1357**.

Batchelor, G., 1953: *The theory of homogenous turbulence*. Cambridge University Press.

Bell, J. H. and R. D. Mehta, 1990: Development of a two-stream mixing layer from tripped and tripped boudary layers. *AIAA Journal*, **28**, 2034–2042.

Betchov, R. and G. Szewczyk, 1963: Stability of shear layer between parallel streams. *Physics of Fluids*, **6**, 1391–1396.

Bischof, C., P. Khademi, A. Mauer-Oats, and A. Carle, 1996: Adifor 2.0: Automatic differentiation of Fortran 77 program. *IEEE Computational Science and Engineering*.

Bischof, C., B. Land, and A. Vehreschild, 2003: Automatic differentiation for matlab program. *Proceeding in Applied Mathematics and Mechanics*, 2:50–53.

Bischof, C., L. Roh, and A. Mauer-Oats, 1997: Adic: an extensible automatic differentiation tool for ansi-c. *Software Practice and Experience*.

Blackwell, B. F. and K. J. Dowding, 2002: Sensitivity and uncertainty analysis for thermal problems. *4th International Conference on Inverse Problems in Engineering*, Rio de Janeiro, Brazil.

Borggaard, J. and J. Burns, 1997: A PDE sensitivity equation method for optimal aerodynamic design. *Journal of Computational Physics*, **136**, 366–384.

Borggaard, J. and A. Verma, 2000: On efficient solutions to the continuous sensitivity equation using automatic differentiation. *SIAM Journal of Scientific Computing*, **22**, 39–62.

Brown, G. and A. Roshko, 1974: On density effects and large structure in turbulent mixing layers. *Journal of Fluid Mechanics*, **64**, 775–816.

Champagne, F. H., Y. H. Pao, and I. J. Wygnanski, 1976: On the two dimensionl mixing region. *Journal of Fluid Mechanics*, **74**, 209–250.

Chorin, A., 1968: Numerical solution of the navier-stokes equations. *Mathematics of Computation*, **22**, 745–762.

Clarksean, R. and P. McMurtry, 1991: Analysis of mixing within two-dimensional planar mixing layers using direct numerical simulation. *Computational Fluid Dynamics Conference, 10th*, AIAA, Honolulu, HI.

Colin, E., S. Etienne, D. Pelletier, and J. Borggaard, 2005: Application of a sensitivity equation method to turbulent flows with heat transfer. *International Journal of Thermal Sciences*, **44**, 1024–1038.

Deardorff, J. W., 1970: A numerical study of three dimensional channel flow at large reynolds numbers. *Journal of Fluid Mechanics*, **41**, 453–480.

Dimotakis, P. E. and G. L. Brown, 1976: The mixing layer at high reynolds numbers: large scale dynamics and entrainment. *Journal of Fluid Mechanics*, **78**, 535–560.

Domoratdski, J. A., W. Liu, and M. E. Brachet, 1993: An analysis of subgrid-scale interactions in numerically simulated isotropic turbulence. *Physics of Fluids*, **A5–1747**.

Dowding, K. J. and B. F. Blackwell, 1998: Joint experimental/computational techniques to measure thermal properties of solids. *Meas. Sci. Technol.*, **9**, 877–887.

Duvigneau, R. and D. Pelletier, 2006: On accurate boundary conditions for a shape sensitivity equation method. *International Journal for Numerical Methods in Fluids*, **50**, 147–164.

Dziomba, B. and H. E. Fiedler, 1985: Effecs of initial conditions on two-dimensional free shear flows. *Journal of Fluid Mechanics*, **152**, 419–442.

Fathali, M., J. Meyers, G. Rubio, S. Smirnov, and M. Baelmansa, 2008: Sensitivity analysis of initial condition parameters on the transitional temporal turbulent mixing layer. *Journal of Turbulence*, **9**, 1–28.

George, W. K. and L. Davidson, 2004: Role of initial conditions in stabilishing asymptotic flow behavior. *AIAA Journal*, **42**, 438–447.

Germano, M., U. Piomelli, P. Moin, and H. W. Cabot, 1991: A dynamic subgrid-scale eddy viscosity model. *Physics of Fluids A*, **3**, 1760–1765.

Ghosal, S. G., T. S. Lund, P. Moin, and K. Akselvoll, 1995: A dynamic localization model for large-eddy simulation of turbulent flows. *Journal of Fluid Mechanics*, **286**, 229–255.

Grinstein, F., 2004: Boundary conditions for large eddy simulation. *AIAA Journal*, **42**, 437.

Gunzburger, M., 1999: Sensitivities, adjoints, and flow optimization. *International Journal of Numerical Methods in Fluids*, **31**, 53–78.

— 2002: *Perspectives of Flow Control and Optimization*. SIAM, Philadelphia, PA.

Harlow, F. and J. Welch, 1965: Numerical calculation of time-dependent viscous incompressible flow of fluid with free surface. *Physics of Fluids*, **8(12)**, 2182–2189.

Hartel, K. and L. Kleiser, 1993: Energy transfer between large and small scales in wall-bounded turbulent fows, in engineering applications of large eddy simulaitons. *ASME, New York City*.

Holmes, P., J. L. Lumley, and G. Berkooz, 1996: *Turbulence, Coherent Structures, Dynamical systems and Symmetry*. Cambridge University Press, New York, NY.

Hristova, H., S. Étienne, D. Pelletier, and J. Borggaard, 2006: A continuous sensitivity equation method for time-dependent incompressible laminar flows. *International Journal for Numerical Methods in Fluids*, **50**, 817–844.

Jimenez, C., L. Valino, and C. Dopazo, 2001: A priori and a posteriori tests of subgrid scale models for scalar transport. *Physics of Fluids*, **13, 2433**.

Kerstein, A. R., 1988: A linear-eddy model of turbulent scalar transport and mixing. *Combustion science and technology*, **60**, 391–421.

Kim, J. and P. Moin, 1985: Application of of a fractional-step method to incompressible navier-stokes equations. *Journal of Computational Physics*, **59**, 308–323.

Kirkman, R. and M. Metzger, 2008a: Direct numerical simulation of sensitivity coefficients in low-Reynolds number turbulent channel flow. *aiaap*, **2008–4242**.

— 2008b: Sensitivity analysis of low Reynolds number channel flow using the finite volume method. *International Journal for Numerical Methods in Fluids*, **57**, 1023–1045.

— 2009: Direct numerical simulaiton of sensitivity coefficients in low reynolds number turbulent channel flow. *Journal of Turbulence*, **10, No.23**, 1–21.

Klein, M., A. Sadiki, and J. Janicka, 2003: A digital filter based generation of inflow data for spatially developing direct numerical or large eddy simulations. *Journal of COmputational Physics*, **186**, 652–665.

Kline, S. J., W. C. Reynolds, F. A. Schaub, and P. W. Runstadler, 1967: The structure of turbulent boundary layer. *Journal of Fluid Mechanics*, **30**, 741–773.

Ko, J., D. Lucor, and P. Sagaut, 2008: Sensitivity of two-dimensional spatially developing mixing layers with respect to uncertain inflow conditions. *Journal of Physics of Fluids*, **20**, 077102–2–077102–20.

Kondo, K., A. Mochida, and S. Murakami, 1997: Generation of velocity fluctuations for inflow boundary conditions of LES. *Journal of Wind Engineering and Industrial Aerodynamics*, **67–68**, 51–64.

Kondo, K. and M. Tsuchiya, 2002: Generation of inflow turbulent boundary layer for les computation. *Journal of Wind Engineering and Industrial Aerodynamics*, **4(2–4)**, 209–226.

Lee, S., S. Lele, and P. Moin, 1992: Simulation of spatially evolving turbulence and the applicability of taylor's hypothesis in compressible flow. *Physics of Fluids*, **4(7)**, 1521–1530.

Lesieur, M., 1997: *Turbulence in Fluids*, volume 40 of *Fluid Mechanics and its Applications*. Kluwer, Dordrecht, Netherlands, 3rd edition.

Lesieur, M., J. P. Comte, and P. L. Roy, 1988: Numerical simulation of the coherent structures in free shear flows. *Mathemtical Modeling in Combustion and Related Topic*, 131–150.

Li, N., E. Balaras, and U. Piomelli, 2000: Inflow conditions for large-eddy simulations of mixing layers. *Physics of fluids*, **12**, 935.

Liepmann, H. W. and J. Laufer, 1947: Investigation of the free turbulent mixing layer. Technical Report TN 1257, NACA.

Lilly, D. K., 1992: A proposed modification of the germano subfilter-scale closure method. *Physics of FLuids A*, **4**, 633–635.

Lu, H., C. J. Rutland, and L. M. Smith, 2007: A priori tests of one-equation les modeling of rotating turbulence. *Journal of Turbulence*, **8, N37**.

Lu, H. and L. M. Smith, 2008: A posteriori tests of one-equation les modeling of rotating turbulence. *International Journal of Modern Physics C*, **19, No.12**, 1949–1964.

Lund, T. S., X. Wu, and K. D. Squires, 1998: Generation of turbulent inflow data for spatially-developing boundary layer simulations. *Journal of Computational Physics*, **140**, 233–258.

Lyness, J. N., 1967: Numerical algorithm based on the theory of complex variables. *Proc. ACM 22nd Nat. Conf. Thomas Book Co.*

Lyness, J. N. and C. B. Moler, 1967: Numerical differentiation of analytic functions. *SIAM J. Numer. Anal.*.

Mahieu, J., S. Etienne, D. Pelletier, and J. Borggaard, 2005: A second-order sensitivity equation method for laminar flow. *International Journal of Computational Fluid Dynamics*, **19**, 143–157.

Martins, J., I. Kroo, and J. Alonso, 2000: An automated method for sensitivity analysis using complex variables. *Proceedings of the 38th Aerospace Sciences Meeting*, Reno, NV, AIAA 2000–0689.

Maruyama, T., W. Rodi, Y. Maruyama, and H. Hiraoka, 1999: Large eddy simulation of the turbulent boundary layer behind roughness elements usi ng an artificially generated inflow. *Journal of Wind Engineering and Industerial Aerodynamics*, **83**, 381–392.

Mason, P. J. and D. J. Thomson, 1992: Stochastic backscatter in large-eddy simulation of boundary layer. *JFM*, **242**, 51–78.

McMillan, O. J. and J. H. Ferziger, 1979: Direct testing of subgrid-scale models. *AIAA Journal*, **17–1340**.

Mehta, R. D. and R. V. Westphal, 1986: Near-field turbulence properties of single and two-stream plane mixing layers. *Experiments in Fluids*, **4**, 257–266.

— 1989: Effect of velocity ratio on plane mixing layer development. *Proceeding of the Seventh Symposium on Turbulent Shear Flows*, Stanford University, 3.2.1–3.2.6.

Meneveau, C., 1993: Statistics of turbulent subgrid-scale stresses: Necessary conditions and experimental tests. *Physics of Fluids*, **6 (2)**, 815–833.

Michalke, A., 1964: On the inviscid instability of the hyperbolic tangent velocity profile. *Journal of Fluid Mechanics*, **19**, 543–556.

Moser, R. D. and M. M. Rogers, 1993: The three-dimensional evolution of a plane mixing layer: pairing and transition to turbulence. *Journal of Physics of fluids*, **247**, 275–320.

Patel, R. P., 1978: Effect of the stream turbulence on free shear flows. *Aeronautical Quarterly*, **29**, 33–43.

Piomelli, U., P. Moin, and J. H. Ferziger, 1988: Model consistency in large eddy simulation of turbulent channel flows. *Physics of Fluids*, **31–1884**.

Pope, S., 2000: *Turbulent Flows*. Cambridge University Press, New York, NY.

Ragab, S. and J. Wu, 1989: Linear instabilities in two-dimensional compressible mixing layers. *Physics of fluids*, **1**, 957–966.

Reynolds, W. C., 1990: The potential and limitations of direct and large eddy simulations. *Lecture Notes in Physics*, **357**, 313–343.

Roache, P., 1997: Quantification of uncertainty in computational fluid dynamics. *Annual Review of Fluid Dynamics*, **29**, 123–160.

Rogers, M. M. and R. D. Moser, 1992: The three-dimensional evolution of a plane mixing layer: the kelvin-helmholtz rollup. *Journal of Physics of Fluids*, **243**, 183–226.

— 1993: Direct simulation of a self-similar turbulent mixing layer. *Physics of Fluids*, **6**, 903–923.

Sagaut, P., 2006: *Large Eddy Simulation for Incompressible Flows*. Springer, 3rd edition.

Schlüter, J., H. Pitsch, and P. Moin, 2003: Boundary conditions for LES in coupled simulations. *AIAA paper*, **2003–0069**.

Scotti, A. and C. Meneveau, 1999: A fractal model for large eddy simulation of turbulent flow. *Physica D*, **127**, 198–232.

Smagorinsky, J., 1963: General circulaiton experiments with the primitive equation. *Mon. Weath. Rev.*, **91**, 99–164.

Smirnov, A., S. Shi, and I. Celik, 2001: Random flow generattion technique for large eddy simulations and particle-dynamics modeling. *Journal of Fluid Mechanics*, **123**, 359–371.

Sobieski, J. S., 1990: Sensitivity of complex, internally coupled systems. *AIAA Journal*.

Spencer, B. W. and B. J. Jones, 1971: Statistical investigation of pressure and velocity fields in the turbulent two-stream mixing layer. *AIAA paper*, **71–613**.

Squire, W. and G. Trapp, 1998: Unsing complex variables to estimate derivatives of real functions. *SIAM Review*.

Stanley, L. and D. Stewart, 2002: *Design Sensitivity Analysis*. Society for Industrial and Applied Mathematics, Philadelphia, PA.

Townsend, A. A., 1976: *Structure of turbulent shear flow*. Cambridge University Press.

Turgeon, E., D. Pelletier, and J. Borggaard, 2000: A continuous sensitivity equation approach to optimal design in mixed convection. *Numerical Heat Transfer, Part A*, **38**, 869–885.

— 2002: A general continuous sensitivity equation formulation for complex flows. *Numerical Heat Transfer, Part B*, **42**, 485–498.

— 2003: Applications of continuous sensitivity equations to flows with temperature-dependent properties. *Numerical Heat Transfer, Part A*, **44**, 611–624.

Verman, B., B. Geurts, and H. Kuerten, 1995: A priori tests of large eddy simulation of the compressible plane mixing layer. *Journal of Engineering Mathematics*, **29**, 299–327.